Topological spin structures on superconducting surfaces

Dissertation by Felix Nickel
Kiel 2025

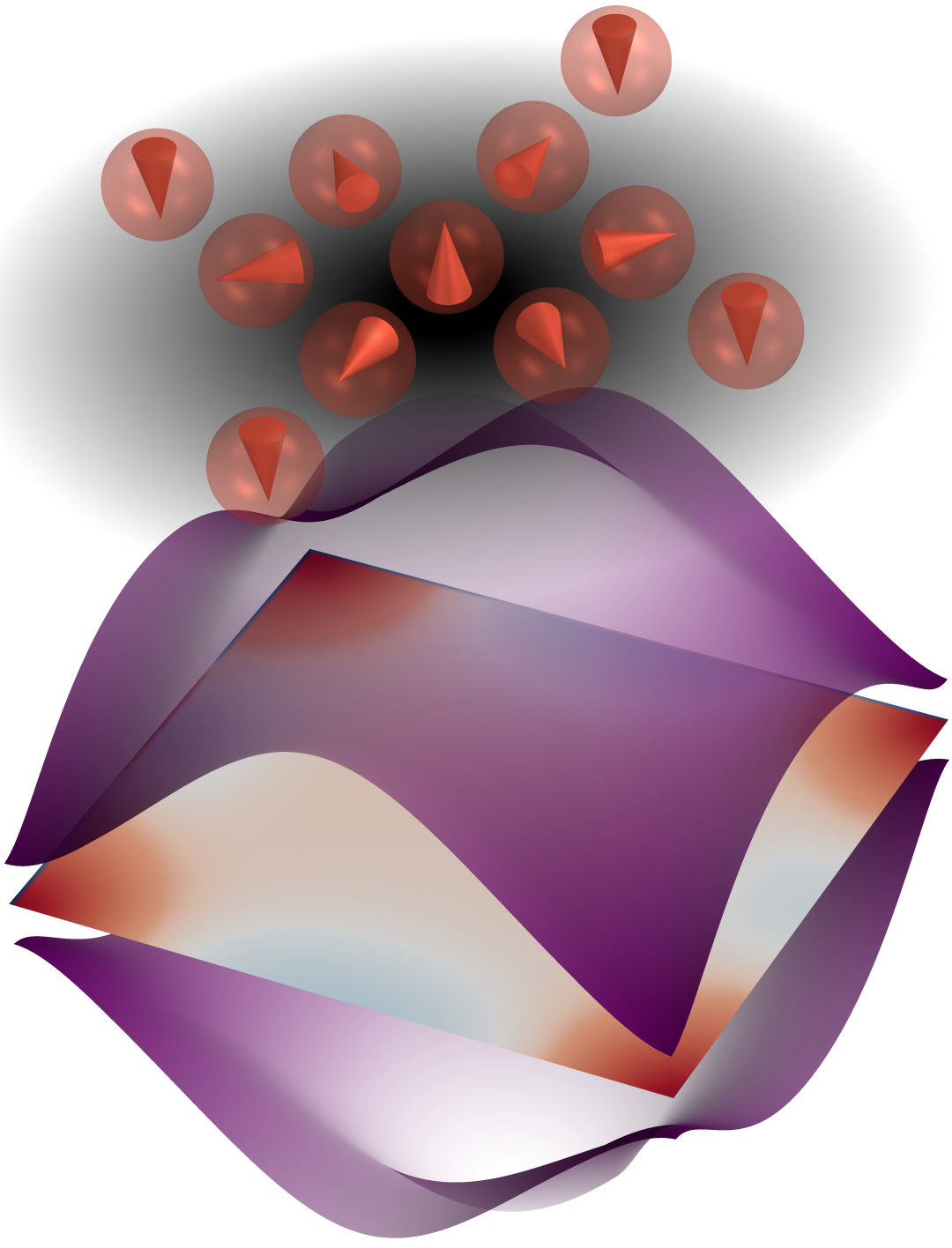

Topological spin structures on superconducting surfaces

Dissertation
zur Erlangung des Doktorgrades
der Mathematisch-Naturwissenschaftlichen Fakultät
der Christian-Albrechts-Universität zu Kiel

vorgelegt von
Felix Nickel

Kiel, 2025

Erster Gutacher: Prof. Dr. Stefan Heinze
Zweite Gutachterin: PD Dr. Kirsten von Bergmann
Dritter Gutachter: Prof. Dr. Samir Lounis

Tag der mündlichen Prüfung: 14.10.2025

Inhaltsangabe

In topologischen Supraleitern können Majorana Nullmoden existieren, diese können für Quantencomputer genutzt werden. Magnet-Supraleiter-Hybrid (MSH) Systeme, hergestellt aus konventionellen Supraleitern, bilden eine vielversprechende Basis, da die magnetische Struktur topologische Supraleitung induzieren kann. Ebenso kann die magnetische Struktur dabei eine nicht-triviale Spin-Topologie aufweisen.

In dieser Arbeit werden realistische MSH-Systeme im Hinblick auf die magnetische Struktur sowie auf induzierte topologische Supraleitung untersucht, wobei der Schwerpunkt auf der Beziehung zwischen der Spin-Topologie und der Topologie des Supraleiters liegt.

Ultradünne magnetische Filme auf der Re(0001)-Oberfläche werden als Modellsysteme für MSH Systeme betrachtet. Komplexe magnetische Strukturen werden mittels Dichtefunktionaltheorie (DFT) identifiziert. Die Wechselwirkungen, welche den Grundzustand stabilisieren, werden anschließend mittles eines parametrisierten atomistischen Spinmodells analysiert. Die Auswirkung der Spinstruktur auf die elektronischen Eigenschaften des supraleitenden Substrats wird mit einem Tight-Binding-Modell untersucht. Simulationen von spinpolarisierten Rastertunnelmikroskopie-Aufnahmen (SP-STM) erlauben einen direkten Vergleich zwischen den theoretisch vorhergesagten magnetischen Grundzuständen oder Randzuständen in Supraleitern und experimentellen Beobachtungen. Diese wurde von Partnern der Universität Hamburg durchgeführt.

Für Pd/Mn- und Rh/Mn- Doppellagen auf einer Re(0001)-Oberfläche wird der ideale 3Q-Zustand – eine nicht-koplanare magnetische Struktur mit Tetraederwinkeln zwischen benachbarten magnetischen Momenten – über DFT als Grundzustand gefunden und experimentell durch SP-STM nachgewiesen. Es wird gezeigt, dass der Spinzustand in einer spezifischen, hochsymmetrischen Orientierung an das atomare Gitter durch den anisotropen symmetrischen Austausch koppelt. Aufgrund der Symmetrie des magnetischen Zustands tragen andere Wechselwirkungen nicht zu der Orientierung bei. Eine Verzerrung des idealen 3Q-Zustandes, z.B. durch frustrierte Austauschwechselwirkungen höherer Ordnung, verringert die Symmetrie. In diesem Fall kann auch die magnetokristalline Anisotropie zu der Orientierung beitragen, was zu einer anderen Ausrichtung führt. Dies zeigt eine Verbindung zwischen der Verzerrung und der Orientierung des 3Q-Zustands, wodurch eine mögliche Verzerrung durch SP-STM Experimente nachgewiesen werden kann.

Die nicht-koplanare Spinausrichtung im 3Q-Zustand führt zu topologisch orbitalen Momenten (TOM). Diese treten selbst ohne Spin-Bahn-Kopplung auf und bilden eine ferromagntische Ordnung. In Fe/Ir-3/Re(0001) stabilisieren Austauschwechselwirkungen höherer Ordnung skyrmionische Gitter auf atomarer Skala im Vergleich zu Spinspiral-Zuständen. Verschiedene skyrmionische Gitter werden als mögliche magnetische Grundzustände betrachtet und mit experimentellen Messungen verglichen. Die Ordnung der TOM ist bei allen diesen Gittern antiferromagnetisch, kann entweder kompensiert oder nicht kompensiert sein. Das heißt, die gesamte skalare Spinchiralität verschwindet oder ist von Null verschieden.

Durch kontinuierliche Transformation eines der skyrmionischen Gitter in ein anderes kann die skalare Spinchiralität zwischen Null und einem endlichen Wert variiert werden. Es zeigt sich für diese Systeme, dass starke topologische Supraleitung mit einer nicht-verschwindenen skalaren Spichiralität korreliert. Des Weiteren nimmt die Größe der supraleitenden Bandlücke mit zunehmender skalarer Spinchiralität zu.
Trotz einer geschlossenen Bandlücke, können antiferromagnetische Spintrukturen, mit verschwindender skalarer Spinchiralität, topologische Knotenpunkt Supraleitung (TNPSC – engl.: topologigal nodal point superconductivity) induzieren. Hier wird gezeigt, dass Randzustände nicht nur an dem Übergang zu trivialen Domänen sondern auch zwischen zwei unterschiedlichen TNSCPs auftreten können. Im Allgemeinen klingen Randzustände dabei unterschiedlich in beide Domänen ab, was zu einer Spinpolaisation des Randzustandes führt.
Experimente an Mn Mono- und Bilagen auf der Ta(110) Oberfläche stimmen gut mit den theoretischen Ergebnissen überein. Die Monolage und Bilage repräsentieren dabei zwei Domänen unterschiedlicher TNPSC.

Abstract

Topological superconductivity can lead to the formation of Majorana zero-modes, which could be harnessed for topological quantum computing. Magnet-superconductor-hybrid (MSH) systems, built with conventional superconductors, are a promising host platform as the magnetic structure can induce topological superconductivity. Also, the magnetic state itself can exhibit a non-trivial spin topology. In this thesis realistic MSH systems are investigated with regard to the magnetic structure as well as induced topological superconductivity, focusing on the connection between the spin topology and the topology of the superconductor.
Ultra-thin magnetic films on the Re(0001) surface are considered as model MSH systems. Complex magnetic structures are identified via density functional theory (DFT) calculations. The stabilizing mechanisms are revealed by mapping the obtained total DFT energies of various collinear and non-collinear spin states onto an atomistic spin model. The effect of the spin structure on the electronic properties of the superconducting substrate is investigated by a tight-binding model. Spin-polarized scanning tunneling microscopy (SP-STM) simulations allow a direct comparison between theoretically predicted magnetic ground states or edge states in superconductors and experimental observations, performed by collaborators of the University of Hamburg.
For Pd/Mn and Rh/Mn bilayers on a Re(0001) substrate the ideal 3Q state – a non-coplanar magnetic texture with tetrahedron angles between adjacent magnetic moments – is found via DFT as the ground state and revealed experimentally via SP-STM. It is shown that the spin state couples in a specific, highly-symmetric orientation to the atomic lattice by the anisotropic symmetric exchange. All other interactions are not contributing to the orientation due to the symmetry of the magnetic state. A distortion of the ideal 3Q structure, e.g. by frustrated higher-order exchange interactions, lowers the symmetry. In this case the magnetocrystalline anisotropy energy can also contribute, resulting in a different orientation. This showcases a link between the distortion and the orientation of the 3Q state, making a possible distortion detectable by SP-STM experiments.
The non-coplanar spin alignment in the 3Q state leads to topological orbital moments. These occur even without spin-orbit coupling and order ferromagnetically. In Fe/Ir-3/Re(0001) higher-order exchange interactions stabilize atomic-scale skyrmionic lattices over spin spiral states. Different skyrmionic lattices are considered as potential magnetic ground states and compared to experimental data. The topological orbital moments order in an antiferromagnetic pattern for all lattices but can either be compensated or non-compensated, i.e. have a vanishing or non-zero total scalar spin chirality, respectively. By continuously transforming one skyrmionic lattice into the other, the scalar spin chirality can be tuned between zero and some finite value. By quantifying the topology of the superconductor for the transforming spin textures it is indicated that non-zero total scalar spin chirality can induce strong topological superconductivity. Further the size of the superconducting bandgap increases with larger scalar spin chirality.
Antiferromagnetic spin textures with vanishing scalar spin chirality can still induce topological nodal point superconductivity, although the system is gapless. It is demonstrated

here that edge modes can not only occur on boundaries to trivial states, but also between two different domains of topological nodal point superconductors. These edge modes in general decay differently into both domains, which leads to a spin-polarization of the edge state. For Mn mono- and bilayer on Ta(110) as the two domains of different topological nodal point superconductors, the theoretical findings are in good agreement with experimental data.

List of publications

The results of this thesis are contained in four publications, which are reprinted in the chapters 5 to 8. Throughout this thesis the publications are referred to by roman numerals.

I Coupling of the triple-Q state to the atomic lattice by anisotropic symmetric exchange
Felix Nickel, André Kubetzka, Soumyajyoti Haldar, Roland Wiesendanger, Stefan Heinze, Kirsten von Bergmann
Physical Review B **108**, L180411 (2023)

II Antiferromagnetic order of topological orbital moments in atomic-scale skyrmion lattices
Felix Nickel, André Kubetzka, Mara Gutzeit, Roland Wiesendanger, Kirsten von Bergmann, Stefan Heinze
npj Spintronics **3**, 7 (2025)

III Topological properties of magnet-superconductor hybrid systems due to atomic-scale non-coplanar spin textures
Felix Nickel, Stefan Heinze
npj Spintronics **3**, 13 (2025)

IV Spin-polarized edge modes between different magnet-superconductor-hybrids
Felix Zahner*, **Felix Nickel***, Roberto Lo Conte, Tim Drevelow, Roland Wiesendanger, Stefan Heinze, Kirsten von Bergmann
* These authors contributed equally.
Submitted for peer-review. Preprint available: arXiv:2506.16869 (2025)

Further publication that are not part of this thesis:

V Exchange and Dzyaloshinskii-Moriya interaction in Rh/Co/Fe/Ir multilayers: towards skyrmions in exchange-frustrated multilayers
Felix Nickel, Sebastian Meyer, Stefan Heinze
Physical Review B **107**, 174430 (2023)

Contents

1 Introduction

Technological development, which has an impact on everyone's life, is closely linked to the resources and scientific tools available. While most of today's technology is constantly being improved, some advances open fundamentally new path and lead to a fast acceleration of research. The invention of the computer revolutionized the possibilities of performing large-scale calculations and lead to the new field of computer simulations. The discovery of the giant magneto resistance (GMR) effect [1, 2] allowed to construct hard-disk drives with a large information density, small size and fast access. This discovery has created the field of spintronics [3, 4], where the spin degree of freedom of electrons influences transport properties and can lead to the formation of complex spin structures with non-trivial topology [5–8]. The field of spintronics offers a wide variety of possible applications, such as improved and energy-efficient computing hardware [9] or neuromorphic computing [10]. The next revolutionary step might be the usage of fully operational quantum computers [11]. These could solve problems, that are simply unsolvable for classical computers, even in centuries. Quantum computers have already been built, but are right now very limited in their usage. However, a lot of research is dedicated to their improvement [12]. Different physical concepts are used for the construction of qubits, which form the basis of a quantum computer [13–20]. While for most approaches many qubits are necessary for error corrections [21–23], topological quantum computers are stable against local perturbations, which gives them an intrinsic benefit [24–28]. Topological qubits could be realized by spatially separated Majorana states, that can emerge in topological superconductors [29]. Topological superconductors form promising host platforms for Majorana states. Advances have been made in semiconductor-superconductor [30–33] systems and magnet-superconductor-hybrid (MSH) systems [34–39]. While this research field is relatively young and a definite proof of the existence of Majorana states is still lacking, already advances are made to fabricate devices [40]. This makes the combination of magnetic and superconducting materials a highly interesting branch of solid-state physics and motivates the research of this thesis.

Isolated non-collinear spin textures such as skyrmions can lead to fascinating effects, which depend on their non-trivial topology [42–46]. Such a magnetic skyrmion is shown in Fig. 1.1a. On one hand, isolated skyrmions are metastable states that can be created, moved and annihilated [47–51]. On the other hand, the non-coplanar arrangement of

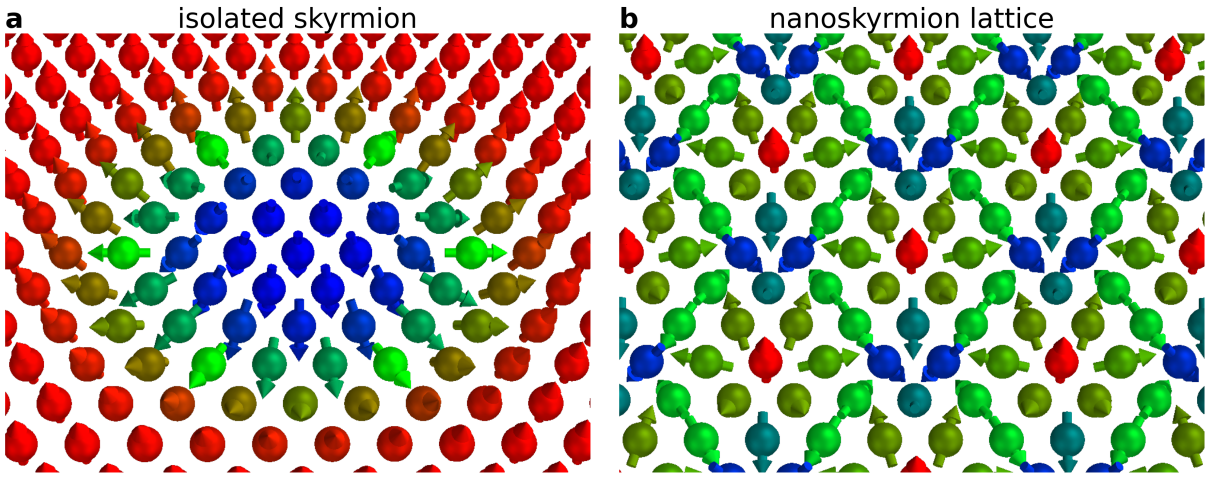

Figure 1.1: Isolated skyrmion and nanoskyrmion lattice. Each sphere with an arrow represents the local magnetic moment of an atomic site in a hexagonal lattice. **a** Isolated skyrmion in a ferromagnetic background. **b** Nanoskyrmion lattice as found in Fe/Ir(111) [41].

magnetic moments leads to transport phenomena, such as the topological Hall effect [52, 53], or could induce topological superconductivity [54]. For both effects large tilting angles between neighboring spins are beneficial. Large tilting angles can be achieved in skyrmion lattices, in which many skyrmions form a periodic arrangement. The diameter and distance of the individual skyrmions is controlled by the magnetic interactions, mostly the Heisenberg exchange and Dzyaloshinskii-Moriya interaction. For certain combinations of interactions the skyrmions can come so close and become so small, that each skyrmion only consist of a few lattice sites. These atomic-scale skyrmionic lattices share some key properties, such as the non-coplanar spin texture or a non-trivial topology, with the larger isolated skyrmions. The non-coplanar spin alignment is an exceptional feature, since it breaks the time-reversal symmetry for electron moving through the magnetic layer, even when the magnetic moments are compensated [55]. A physical consequence of the broken time-reversal symmetry is the topological orbital moment (TOM) [56]. It occurs even without spin-orbit coupling (SOC) and is directly linked to the topology of the spin texture. Therefore, it can be seen as a measure of the spin topology in complex atomic-scale spin textures [57]. An atomic-scale skyrmionic lattice, as shown in Fig. 1.1b has firstly been reported for a Fe monolayer on an Ir(111) substrate [41]. Also in other materials skyrmionic lattices of a small scale could be found [58, 59]. Important interactions for the stabilization of atomic-scale skyrmion lattices are higher-order exchange interactions (HOI) [41, 60] , which also enhance the stability of isolated skyrmions [61]. Such atomic-scale skyrmionic lattices on superconducting substrates could induce topological superconductivity [62].

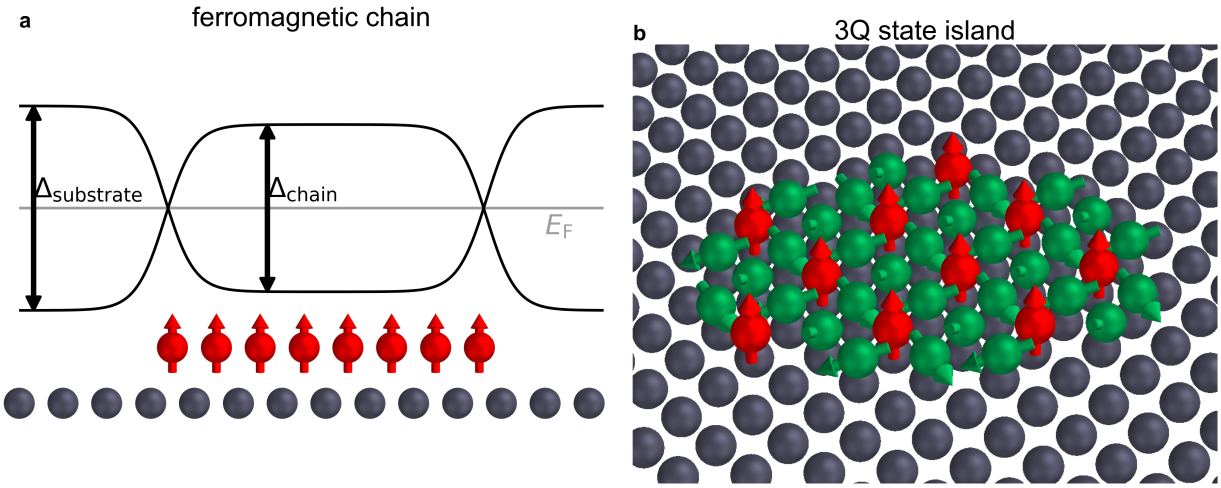

Figure 1.2: Magnet-superconductor-hybrid systems. The black spheres represent a superconducting substrate. The spheres with arrows mark atoms with local magnetic moments of a magnetic adlayer. **a** Ferromagnetic chain of magnetic atoms. A schematic spatially varying band gap is sketched. The chain is assumed to be in a topological phase, while the uncovered surface is in a trivial phase. At the end of the chain the band gap is closed due to the phase transition. The Fermi energy is indicated by a gray line. **b** A magnetic island hosting the non-coplanar 3Q state.

Topological superconductivity has become a field of great interest as it might allow the creation of Majorana quasi-particles [63]. In contrast to the idea, that each particle has a distinct antiparticle Ettore Majorana proposed already in 1937 a particle, which is its own anti-particle [64]. Since particles and antiparticles have an opposite charge this Majorana-particle would need to be charge-less. While elementary particle Majorana fermions could not been found so far, the research is more focused on Majorana quasi-particles in condensed matter systems [65]. Quasi-particles are an excitation of a system, which exhibit particle-like behavior [66]. For example, they can be created, annihilated and moved. One example of quasi-particles are the already discussed magnetic skyrmions, which are an excitation in a uniform magnetic field. In the case of Majorana quasi-particles they have to fulfill the properties that elementary Majorana particles would have to.
In solid state-physics superconducting materials form a promising starting point for the search of Majorana quasi-particles, since they have particle-hole symmetry, formed by the Cooper pairs [29, 67]. At the transition between a topological and a conventional superconductor with trivial topology Majorana quasi-particles can form as a superposition of electron and hole states [68]. Topological superconductors are a special phase of superconductivity. Topological and trivial superconductors have a superconducting band gap [1], which separates occupied and unoccupied states. When a topological and trivial superconductor are brought in contact, the band gap has to close. This is called bulk-boundary correspondence [69, 70]. At the interface between both areas zero-energy Majorana modes occur. These states consist formally of half of an electronic and half of

[1] Note, that also gap-less topological superconductors exists. These are discussed later.

a hole state. Therefore, they always have to occur in pairs. In Fig. 1.2a a ferromagnetic (FM) chain on a superconducting substrate is sketched. The spatially varying size of the bandgap is schematically indicated. In general the band gap of the uncovered surface and the magnetic chain can differ. The magnetic chain is assumed to be in a non-trivial phase. At both ends of the chain the band gap closes and zero-energy Majorana states can exist.

This makes topological superconductors a promising system to find Majorana quasi-particles. The arising problem is now to find topological superconductors – ideally tunable between topological and trivial phase. A conventional superconducting pairing forms Cooper pairs from spin-up and spin-down electrons [67, 71]. Topological superconductors can arise for unconventional superconducting pairing [29, 72]. Here Cooper pairs can be formed by electrons with the same spin orientation. A great route towards topological superconductors is the usage of a conventional superconductor, which are brought in vicinity of a thin magnetic layer. The magnetism in these so-called magnet-superconductor-hybrid (MSH) systems can induce effective unconventional pairing [73]. Usually magnetism and superconductivity are known to exclude each other. Conventional superconductors are perfect diamagnets, which expel magnetic fields. If the magnetic field is strong enough to penetrate into the superconductor it suppresses the superconductivity. A spin mixing can circumvent this problem, so that superconductivity can exist even in the presence of a magnetic field. Finding a system with suitable interactions to induce topological superconductivity turns out to be challenging. Various approaches have been taken to obtain MSH systems. A good overview is given in Ref. [54].

Motivated by the thought experiment of the so-called Kitaev-chain [68], monoatomic chains on superconducting substrates were investigated experimentally and theoretically [74–82]. As displayed in Fig. 1.2a magnetic adatoms are arranged on a superconducting substrate. At each end of the chain a Majorana zero mode can exist. FM islands in systems with large SOC were applied on superconducting substrates [34, 35, 74, 83]. Also isolated spin textures, such as skyrmions are predicted to couple to superconducting vortices [84–87]. Interesting systems are also formed by non-coplanar spin textures, where the mixing of the spin-channels occurs even without SOC [73, 88, 89]. As an example an island hosting the 3Q state is shown in Fig. 1.2b. Zero energy edge modes can form at the boundary of the island [83].

Besides gapped topological superconductors also gapless superconductors, so-called topological nodal point superconductor (TNPSC) came into focus [29, 90]. Here edge modes can occur only at boundaries with certain crystallographic orientations. These TNPSC can occur in antiferromagnet (AFM) spin textures [39, 91] or be induced by spin spirals [73, 92]. Also gapped topological superconductors exist, which have edge modes only at specific edges, which is called weak topological superconductivity [93]. For a so-called higher order topological superconductor (HOTSC) zero modes exist only at corners of islands [93–96].

Besides the fact, that the spin structure can influence the superconductor, the magnetic ground state can also be influenced by the superconductor, which is investigated in Ref. [97, 98]. Topological superconductivity can also be induced by nanoskyrmion lattices in formerly not superconducting materials [99, 100].

A variety of atomic scale spin textures has been investigated in recent years. However, only a few of them have been considered in the regard of topological superconductivity in MSH systems. This work aims to systematically vary spin textures and study the effect on a superconducting substrate.

Experimentally feasible film systems on Re(0001) substrates are considered. Re becomes superconducting below 1.7 K. This makes the investigated systems potential candidates for the experimental realization of topological superconductivity in MSH systems. The low critical temperature of Re is a hurdle, but approaches exist to use proximity induced superconductivity of materials with a higher T_c, e.g. Nb, to achieve a larger band gap [101, 102].

Different theoretical methods are used in this thesis. Density functional theory (DFT) calculations are used to find the magnetic ground state of specific materials and parameterize an atomistic spin model. This atomistic spin model is used to analyze the stabilizing interactions and examine their general behavior. Within this thesis a tight-binding model was implemented in order to study the interplay of magnetism and superconductivity. Spin-polarized scanning tunneling microscopy (SP-STM) simulations are used for a direct comparison of theoretical data and experiments performed by collaborators from the University of Hamburg [2].

Here a Pd/Mn and a Rh/Mn bilayer on the Re(0001) surface were investigated via DFT, where the non-coplanar ideal triple-Q state was identified as the magnetic ground state. Therefore, DFT calculations and SP-STM simulations were performed and compared to SP-STM experiments. Previously a distorted 3Q state has been proposed as the ground state of Mn/Re(0001) [103, 104]. A parameterized atomistic model reveals, that the stabilization of the 3Q state and possible distortions originate from HOI. Further the coupling of the spin-structure to the atomic lattice in a highly symmetric orientation is found. This coupling originated from the anisotropic symmetric exchange (ASE), while other SOC effects cancel due to symmetry as shown here. A distortion of the 3Q state would lower the symmetry. As a consequence also the magnetocrystalline anisotropy energy (MAE) influences the coupling, which leads to different orientations. Therefore, the distortion and orientation of the 3Q state are linked, which allows to distinguish the ideal and distorted 3Q state via SP-STM, even when the distortion angles are not resolvable directly in the images.

[2] Dr. K. von Bergmann *et al.*

The non-coplanar orientation of the 3Q state leads to the formation of ferromagnetic ordered topological orbital moments (TOMs). The TOM occurs even in the absence of SOC and can lead to unusal transport properties. Due to large tilting angles significant TOM can also be expected for atomic scale skyrmion lattices. In Fe/Ir-3/Re(0001) HOI stabilize such atomic scale skyrmion lattices. Due to skyrmionic and antiskyrmionic structures an antiferromagnetic ordering of the TOM occurs. The opposite sign of the TOM for skyrmionic and antiskyrmionic structures coincides with an opposite topological charge for isolated skyrmions and antiskyrmions. This shows, that properties of larger isolated spin textures can be transferred to atomic-scale lattices. The benefit of atomic-scale lattices are the large tilting angles, which lead to larger TOM per unit area, than for e.g. an isolated nanometer-scale skyrmion.

Some non-coplanar spin textures are predicted to induce topological superconductivity even in the absence of SOC [73, 88, 89]. Here it is shown that large tilting angles induce comparably large super conducting band gaps. To realize topological superconductivity in MSH systems the size of the band gap is a crucial factor, because only large enough band gaps allow for an experimental detection of topological in-gap states. For atomic-scale skyrmionic lattices it is demonstrated in this thesis, that the total scalar spin chirality can be seen as a precursor of topological superconductivity.

Edge states cannot only occur for gapped topological superconductors but also in TNPSC. For Mn mono- and bilayers on a Ta(110) surface it is shown here, that edge modes occur not only between TNPSC and trivial states but also between two different TNPSC. Further edge states induced by AFM spin textures can be spin-polarized, which is a result of different decay length of the edge mode into both TNPSC domains, as demonstrated here.

This thesis is structured as follows: Firstly the used theoretical methods are discussed.

In Sec. 2.1 the basics of conventional and topological superconductivity are discussed and how it can be modeled in electronic structure calculations. Also, basic principles of Majorana zero modes (MZM), which can occur in topological superconductors, are described.

Within this work a tight-binding model has been implemented. In Sec. 2.2 the model and all investigated quantities are described. This section should allow anyone to implement the same model Hamiltonian and reproduce all calculations of this thesis. Explicit examples are given, which can be used for comparison.

A broad overview over the key concepts of DFT and some details over the used features are introduced in Sec. 2.3. An atomistic spin model has been parameterized by DFT calculations and is used for physical interpretations. All magnetic interactions are shortly discussed in Sec. 2.4. Special emphasis is given to the comparison of the topological charge of spin textures and the scalar spin chirality. The latter is used to classify topological atomic scale spin textures in this work.

A good comparison of theoretical predictions and experimental data can be made via SP-STM simulations. In Sec. 2.5 the basic principles of an STM, the Tersoff-Harmann model [105] and an extension to spin-polarization [106, 107] are described. Further it is shown, how SP-STM simulations can be performed based on an atomistic model, a tight-binding model or directly from DFT.
In Chap. 3 an overview is given over the key finding of this thesis. Followed by a short summary in Chap. 4. A detailed description of the results can be found in the four publications, which are part of this work. These papers can be found in chapters Chap. 5, Chap. 6, Chap. 7 and Chap. 8. Each of these chapters consists of the publication and supplementary information.

2 Theoretical background

This chapter presents the theoretical background for the publications that are given in the chapters 5 to 8. Firstly an overview over topological superconductivity and related phenomena is given. Afterwards the methods, which were used in this work, are presented. These include a tight-binding model, density functional theory (DFT) calculations, an atomistic spin model and spin-polarized scanning tunneling microscopy (SP-STM) simulations.

2.1 Superconductivity

Topological superconductivity is a fascinating phenomenon, which is a promising candidate for fault tolerant-quantum computing [25, 108, 109]. One route towards topological superconductors is the combinations of magnetic structures with conventional superconductors. A superconducting material is resistance free for electronic current [110–112]. In the Bardeen-Cooper-Schrieffer (BCS) [113, 114] theory this phenomenon is explained by the formation of so-called Cooper pairs [67]. In a Cooper pair two electrons with opposite wave vector $\mathbf{k}$ are coupled by a weak attractive interaction. While the BCS theory does not require a specific origin of this attractive interaction, it is often viewed as an interaction mediated by a phonon. Note, that a Cooper pair is an effective description for weak attractive interactions between many electrons. Each pair of distinct electrons interacts only for a short time, since both are moving through the lattice [115]. The Cooper pair, consisting of two electrons, has an integer spin, as both electrons are spin-1/2 particles. Usually in conventional superconductors both electrons have an opposite spin, which is called a spin-singlet, but also a spin-triplet for electrons with the same spin could exist [71]. Due to their integer spin Cooper pairs classify as bosons in contrast to their fermionic building blocks. Under the right conditions, especially low temperatures, the bosonic Cooper pairs can form a Bose-Einstein-condensate [116]. Here all bosons can be in the same ground state, which can be described by a single wavefunction. This bosonic wavefunction does not depend on the number of Cooper pairs. Therefore, the particle number of Cooper pairs is not preserved. This allows for example for the annihilation of a Cooper pair, which creates two electrons, that are no longer bound in a Cooper pair, without altering the ground state. This property is reflected in the electron-hole symmetry. Via creation or annihilation of a Cooper pair an electron can be transformed into a hole or vice versa.

The formation of Cooper pairs at energies close to the Fermi energy creates a superconducting band gap. The width of this gap depends on the coupling of the Cooper pairs, which is material dependent. At a critical temperature T_c a phase transition occurs, where the superconducting properties vanish for $T > T_c$ [111].

A second property of superconductors is, that they are perfect diamagnets [117], i.e. they expel magnetic fields [1]. When the external magnetic field becomes too large, the superconducting state is suppressed. Here two distinct mechanisms exist. For type-I superconductors [119], the superconducting properties vanish in the whole sample at once. In type-II superconductors [120] so-called vortices can exist above a critical magnetic field B_1, where the superconducting properties are only suppressed within a vortex. Schematically this can be viewed as holes in the superconducting state. In a vortex a quantized magnetic flux exists. If the magnetic field is further increased to a second critical field $B_2 > B_1$ a second phase transition occurs, where superconductivity is completely suppressed.

While magnet-superconductor-hybrid (MSH) systems might seem contradictory, they offer a great platform for topological superconductivity. An unconventional pairing can arise due to spin-mixing mechanisms, such as Rashba-SOC or non-collinear magnetism [29, 54, 73] . When parameters of the system, like the spin-mixing effect are varied phase transitions can occur between topological and conventional, i.e. trivial, phases. These phase transitions can happen in the time domain, e.g. for a magnetic field varying with time, or spatially. This thesis focuses on spatially varying properties, especially varying magnetic structures.

To model boundaries, like magnetic islands, often the Bogoliubov de Gennes (BdG) formalism is used [121, 122]. Here a mean-field approximation is made for the superconductivity. A simple Hamiltonian in the BCS theory can be given by [29]

$$H = \sum_{\mathbf{k}\,\sigma_1\,\sigma_2} \epsilon_{\sigma_1\sigma_2}(\mathbf{k}) c^\dagger_{\mathbf{k}\sigma_1} c_{\mathbf{k}\sigma_2} + \frac{1}{2} \sum_{\mathbf{k}\,\mathbf{k}'\,\sigma_1\,\sigma_2\,\sigma_3\,\sigma_4} V_{\sigma_1\sigma_2\sigma_3\sigma_4}(\mathbf{k},\mathbf{k}') c^\dagger_{-\mathbf{k}\sigma_1} c^\dagger_{\mathbf{k}\sigma_2} c_{-\mathbf{k}'\sigma_3} c_{\mathbf{k}'\sigma_4} \quad , \tag{2.1}$$

where $\epsilon_{\sigma_1\sigma_2}(\mathbf{k})$ gives the non-superconducting energy dispersion. The superconducting pairing is given by $V_{\sigma_1\sigma_2\sigma_3\sigma_4}(\mathbf{k},\mathbf{k}')$, where the creation of two electrons with opposite wave vector $c^\dagger_{-\mathbf{k}\sigma_1} c^\dagger_{\mathbf{k}\sigma_2}$ can be interpreted as the annihilation of a Cooper pair. Now a pair potential

$$\Delta_{\sigma_1\sigma_2}(\mathbf{k}) = -\sum_{\mathbf{k}'\sigma_3\sigma_4} V_{\sigma_1\sigma_2\sigma_3\sigma_4}(\mathbf{k},\mathbf{k}') \langle c_{-\mathbf{k}'\sigma_3} c_{\mathbf{k}'\sigma_4} \rangle \tag{2.2}$$

can be defined, where $\langle c_{-\mathbf{k}'\sigma_3} c_{\mathbf{k}'\sigma_4} \rangle$ is the expectation value of $c_{-\mathbf{k}'\sigma_3} c_{\mathbf{k}'\sigma_4}$. Using a mean field-approximation the pairing potential can be approximated as the $\mathbf{k}$-dependent function

[1] The magnetic field strength is exponentially decaying into the superconductor. The decay length is material specific [118].

$\Delta_{\sigma_1\sigma_2}(\mathbf{k})$ [29]. The resulting Hamiltonian has the form

$$H = \sum_{\mathbf{k}\sigma_1\sigma_2} \epsilon_{\sigma_1\sigma_2}(\mathbf{k}) c^\dagger_{\mathbf{k}\sigma_1} c_{\mathbf{k}\sigma_2} + \frac{1}{2} \sum_{\mathbf{k}\sigma_1\sigma_2} \left[\Delta_{\sigma_1\sigma_2}(\mathbf{k}) c^\dagger_{\mathbf{k}\sigma_1} c^\dagger_{-\mathbf{k}\sigma_2} + \text{h.c.} \right] \tag{2.3}$$

where h.c. marks the hermitian conjugate. This form is often called the BdG Hamiltonian [29, 123]. It can now be written in a matrix form, where the vectors contain only single orbitals

$$H = \frac{1}{2} \sum_{\mathbf{k}} \begin{pmatrix} c^\dagger_{\mathbf{k}\uparrow} & c^\dagger_{\mathbf{k}\downarrow} & c_{-\mathbf{k}\uparrow} & c_{-\mathbf{k}\downarrow} \end{pmatrix} \begin{pmatrix} \epsilon_{2\times2}(\mathbf{k}) & \Delta_{2\times2}(\mathbf{k}) \\ -\Delta^*_{2\times2}(-\mathbf{k}) & -\epsilon^*_{2\times2}(-\mathbf{k}) \end{pmatrix} \begin{pmatrix} c_{\mathbf{k}\uparrow} \\ c_{\mathbf{k}\downarrow} \\ c^\dagger_{-\mathbf{k}\uparrow} \\ c^\dagger_{-\mathbf{k}\downarrow} \end{pmatrix} , \tag{2.4}$$

where $\epsilon_{2\times2}(\mathbf{k})$ and $\Delta_{2\times2}(\mathbf{k})$ are (2×2) matrices in the spin-space. This BdG Hamiltonian is in the following used to describe topological superconductivity.
The eigen values of the matrix

$$\underline{H} = \begin{pmatrix} \epsilon_{2\times2}(\mathbf{k}) & \Delta_{2\times2}(\mathbf{k}) \\ -\Delta^*_{2\times2}(-\mathbf{k}) & -\epsilon^*_{2\times2}(-\mathbf{k}) \end{pmatrix} \tag{2.5}$$

are the eigen energies of the system.

2.1.1 Topological Superconductivity

Topology is a concept to group states of a system together, which can be transformed into each other by continuous deformations. All states, that can be transformed into each other by some continuous transformation, are called topologically equivalent. This concept can be applied to various systems, which can have different definitions of continuous transformations. A well known example is the transformation from a torus into a cup, where all deformations that do not involve gluing or ripping the surface do not alter the topological phase. Each topological phase hereby has a distinct number of holes, which defines the topological invariant. All deformations, that include a ripping or gluing change the number of holes and therefore the topological phase. For topological superconductors all transformations that do not involve a closing of the superconducting band gap are considered to not change the topological phase. Also here a topological invariant, like the Chern number, can be defined. When a parameter of the system is modified in a way, that the topological phase is changing, the band gap has to close at the phase transition. This transformation could exist in time, e.g. by applying external fields, or spatially, e.g. by changing some property of the material in a specific region of the sample. The later case is referred to as the bulk-boundary correspondence [69, 70]. Strictly speaking this means, on a boundary between two regions with different topological phase (different values of

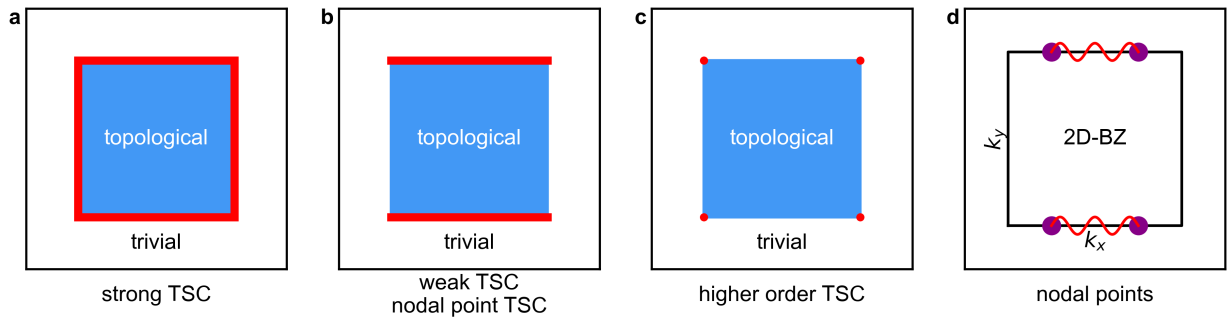

Figure 2.1: Schematic drawing of edge modes for different topological superconductivity. The blue square represents a magnetic island on a superconducting surface (white). The localization of zero energy modes are displayed in red. **a** A strong topological superconductor has edge modes at all boundaries. **b** For weak topological superconductors or nodal point superconductors edge modes appear only on specific edges. **c** For higher order topological superconductivity modes appear only at the corners. **d** Sketch of nodal points in a 2D-BZ. The purple circles mark the location of nodal points, where the superconducting bandgap is locally zero. Edge states, that occur for edges along the x-direction are indicated by red wavy lines. Along a y-edge no edge states would form, like indicated in **b**.

the topological invariant) the band gap has to be closed. The states occurring in the bulk band gap are called edge states. These edge states are protected by the topology of the two superconducting areas and cannot vanish due to local perturbations of the system. Further away from the interface the two regions develop bulk like properties including their band gap. This makes the zero-energy state localized at the boundary. Topological superconductors have come into focus as they are good host systems for Majorana zero modes [29].

Different kinds of topological phases can exist. In the so-called strong topological superconductivity zero energy edge modes occur all the way around a topological island on a trivial surface as a consequence of the bulk-boundary correspondence, as shown in Fig. 2.1a. In contrast, the weak topological phase exhibits zero-energy edge states only on specific edges, dependent on the geometry of the island [96]. This is exemplary sketched in Fig. 2.1b. Even if on none of the edges modes are propagating, localized modes can exist in the corners of the island, as shown in Fig. 2.1c, which is called higher order topological superconductivity [94, 124]. A comparison between strong-, weak- and higher order topological superconductivity can be found in refs. [93, 95].

While for strong topological superconductivity the bulk band gap is open across the whole Brillouin zone (BZ), also superconductors exist, which have a closed gap at specific $\mathbf{k}$-points, while the gap is open for the rest of the BZ (Fig. 2.1d). This phenomenon is called nodal point superconductivity [90, 94, 125–127]. Topological nodal points always appear in pairs. For certain edge orientations two nodal points are connected by an edge mode [39, 91, 125], as indicated by wavy lines in Fig. 2.1d. This can lead to edge states only on specific edges of an island, just like for the weak topological superconductivity (cf. Fig. 2.1b). If multiple pairs of topological nodal points exist it could also happen, that edge modes are located at all boundaries of an island, like for strong topological superconductivity. As a

consequence it is not possible to deduct the type of the topological superconductivity only from the existence of zero energy modes.

If topological superconductivity can exist in general in a system depends on the symmetries of the Hamilton operator. The symmetries can be easily investigated, when the Hamiltonian is written in a matrix from like Eq. (2.4). For general matrices symmetries can be represented by an antiunitary operator $\mathcal{O}$ [128], which can be written as a unitary operator $\mathcal{U}$ and the complex conjugation operator $\mathcal{K}$ as $\mathcal{O} = \mathcal{U}\mathcal{K}$. Based on three symmetries, the time-reversal symmetry, the charge-conjugation, also-called particle-hole-symmetry, and the chiral symmetry, a matrix can be grouped into one of ten topological classes [129, 130]. These classes, that are defined for any matrices, can be also related to the matrix representation of the Hamiltonian [131] (cf. Eq. (2.5)). The BdG Hamilton matrices, which are used to describe superconducting systems in tight-binding models, correspond to four of the ten classes [131], which are listed in Tab. 2.1. For each class, depending on the dimension of the physical system, topological invariants can be defined. Here $\mathbb{Z}_2$ is a binary invariant and $\mathbb{Z}$ is an integer invariant, like the Chern number. An entry of 0 means, that only trivial states exist. The class of the system depends on the symmetries of the Hamiltonian. The particle-hole symmetry is thereby fulfilled, when

$$C\underline{H}(\mathbf{k})C^{-1} = -\underline{H}(-\mathbf{k}) \quad . \tag{2.6}$$

is satisfied. The time reversal-symmetry requires

$$\mathcal{T}\underline{H}(\mathbf{k})\mathcal{T}^{-1} = \underline{H}(-\mathbf{k}) \quad . \tag{2.7}$$

Each of those symmetries is present if one finds anti-unitary operators C or $\mathcal{T}$, that obey these relations. To find the topological class now the operators are squared, which gives a unity matrix with positive or negative sign. These signs are denoted in Tab. 2.1. When no operator exists to obey Eq. (2.6) or Eq. (2.7) a zero is written. The third symmetry, the chiral symmetry, is fulfilled, when the system is symmetric under the combination of the first two symmetries.

The here used BdG Hamilton matrices contain electronic and hole states as well as spin-up and spin-down states (cf. Eq. (2.4)). Such a matrix has the general form of

$$\underline{H}(\mathbf{k}) = \begin{pmatrix} \underline{H}^{e}(\mathbf{k}) & \underline{H}^{(e-h)}(\mathbf{k}) \\ \underline{H}^{(h-e)}(\mathbf{k}) & \underline{H}^{h}(\mathbf{k}) \end{pmatrix} \quad , \tag{2.8}$$

called electron-hole space. Each of the entries is again a matrix of the form

$$\underline{H}^{\mu}(\mathbf{k}) = \begin{pmatrix} H^{\mu}_{\uparrow\uparrow}(\mathbf{k}) & H^{\mu}_{\uparrow\downarrow}(\mathbf{k}) \\ H^{\mu}_{\downarrow\uparrow}(\mathbf{k}) & H^{\mu}_{\downarrow\downarrow}(\mathbf{k}) \end{pmatrix} \quad , \tag{2.9}$$

	$\mathcal{T}$	$\mathcal{C}$	$\mathcal{S}$	1d	2d	3d
D	0	+1	0	$\mathbb{Z}_2$	$\mathbb{Z}$	0
DIII	-1	+1	+1	$\mathbb{Z}_2$	$\mathbb{Z}_2$	$\mathbb{Z}$
C	0	-1	0	0	$\mathbb{Z}$	0
CI	+1	-1	+1	0	0	$\mathbb{Z}$

Table 2.1: Four topological classes as defined by the tenfold way. The tenfold way allows a classification of ten topological classes [131], where the four classes, that can occur in a BdG Hamiltonian, are given here. The classification depend on the square of the operators $\mathcal{T}$, $\mathcal{C}$ and $\mathcal{S}$, which represent time-reversal symmetry, charge corrugation symmetry and the combination of the former two. A value of 0 shows, that this symmetry does not exist. If the symmetry exists, the sign of the square of the matrix, that fulfills this symmetry, is given. For up to three dimensions is denoted, which type of topological invariant can be defined. $\mathbb{Z}_2$ is a binary invariant, $\mathbb{Z}$ represents an integer invariant and 0 means, no topological invariant is defined. Table adapted from [131].

referred to as spin-space. The symmetry operators are often written in terms of the Pauli spin-matrices σ_x, σ_y, σ_z , where $\sigma_0 = \mathbb{1}_{2\times2}$ is additionally defined to get a full basis (see Appendix A for explicit matrices). These matrices act in spin space and the same matrices are used in electron-hole space, but labeled τ_0, τ_x, τ_y and τ_z, to indicate in which space they are acting.

For the here used BdG Hamiltonian the particle-hole symmetry operator $\mathcal{C}$ is acting in the electron-hole space and has the form

$$\mathcal{C} = \tau_x \otimes \sigma_0 \mathcal{K} = \begin{pmatrix} 0 & 0 & 1 & 0 \\ 0 & 0 & 0 & 1 \\ 1 & 0 & 0 & 0 \\ 0 & 1 & 0 & 0 \end{pmatrix} \mathcal{K} \quad , \tag{2.10}$$

which squares to $\mathcal{C}^2 = \mathbb{1}$. Here $\otimes$ is the Kronecker product. When no magnetic moments are considered the Hamiltonian used in this work obeys Eq. (2.7) with

$$\mathcal{T} = \tau_0 \otimes i\sigma_y \mathcal{K} = \begin{pmatrix} 0 & 1 & 0 & 0 \\ -1 & 0 & 0 & 0 \\ 0 & 0 & 0 & 1 \\ 0 & 0 & -1 & 0 \end{pmatrix} \mathcal{K} \quad . \tag{2.11}$$

Here $\mathcal{T}$ squares to $\mathcal{T}^2 = -\mathbb{1}$. For the BdG Hamiltonians the chiral symmetry is fulfilled, when the time-reversal and the particle-hole symmetry are present. Without magnetism the Hamiltonian corresponds therefore to class DIII (see Tab. 2.1), where a $\mathbb{Z}_2$ invariant can be defined. The magnetic moments break the time-reversal symmetry, so that the system falls into class D, where the Chern number can be defined in 2D. Note that for topological nodal point superconductors still no Chern number can be defined, as the band gap is closed. But other possibilities for classifications exist [132].

If a 2D system is for example in the topological class D it can be in a trivial or a topological phase, depending on the exact parameters. If the system is in a topological phase depends for example on the pair-potential (Eq. (2.2)). This is reflected by the matrix $\underline{H}^{(e-h)}(\mathbf{k})$ from Eq. (2.8), which is often named $\Delta(\mathbf{k})$. This matrix has four entries in the spin space and has the form

$$\underline{\Delta}(\mathbf{k}) = \begin{pmatrix} \Delta_{\uparrow\uparrow}(\mathbf{k}) & \Delta_{\uparrow\downarrow}(\mathbf{k}) \\ \Delta_{\downarrow\uparrow}(\mathbf{k}) & \Delta_{\downarrow\downarrow}(\mathbf{k}) \end{pmatrix} \quad . \tag{2.12}$$

Conventional superconductors have spin singlet pairing, which is given by [29]

$$\underline{\Delta}_{\text{singlet}}(\mathbf{k}) = \Delta_0(\mathbf{k}) \mathrm{i}\sigma_y \quad , \tag{2.13}$$

where Δ_0 is a scalar function. A triplet pairing can be written as [29]

$$\underline{\Delta}_{\text{triplet}}(\mathbf{k}) = \mathbf{d}(\mathbf{k}) \cdot \boldsymbol{\sigma} \mathrm{i}\sigma_y \quad , \tag{2.14}$$

with a vector $\mathbf{d}(\mathbf{k})$. Also, a combination of both is possible [71], leading to the total pairing of

$$\underline{\Delta}(\mathbf{k}) = \underline{\Delta}_{\text{singlet}}(\mathbf{k}) + \underline{\Delta}_{\text{triplet}}(\mathbf{k}) = [\Delta_0(\mathbf{k}) + \mathbf{d}(\mathbf{k}) \cdot \boldsymbol{\sigma}] \, \mathrm{i}\sigma_y \quad . \tag{2.15}$$

A singlet pairing has an even angular momentum of $l = 0, 2, 4, ...$, where the triplet pairing has an odd angular momentum of $l = 1, 3, 5, ...$ Dependent on the angular momentum the pairing is called s-wave ($l = 0$), p-wave ($l = 1$), d-wave ($l = 2$) and so on [29, 72]. A conventional s-wave superconductor is described by a constant, which is independent of the wave vector $\Delta_0(\mathbf{k}) = \Delta_0$. But due to a magnetic structure in a MSH system effective p-wave pairing can occur. In Ref. [73] this is demonstrated for non-collinear and non-coplanar spin textures. Here a simple example is given using a ferromagnetic structure and spin mixing due to SOC. This example demonstrates how the interplay of magnetism, mixing of the spin channels and conventional superconductivity can induce unconventional superconductivity. The explicit form of all terms is given in Appendix A.2. A Hamiltonian with the form of Eq. (2.8) and the entries

$$\underline{H}^{e}(\mathbf{k}) = \begin{pmatrix} JS & -2\alpha(\sin(k_y a) + \mathrm{i}\sin(k_x a)) \\ -2\alpha(\sin(k_y a) - \mathrm{i}\sin(k_x a)) & -JS \end{pmatrix} \tag{2.16}$$

and

$$\underline{H}^{(e-h)}(\mathbf{k}) = \begin{pmatrix} 0 & \Delta_0 \\ -\Delta_0 & 0 \end{pmatrix} \tag{2.17}$$

describes a periodic square lattice with lattice constant a, as sketched in Fig. 2.2a. The other two entries follow from $\underline{H}^{h}(\mathbf{k}) = -\underline{H}^{e*}(-\mathbf{k})$ and $\underline{H}^{(h-e))}(\mathbf{k}) = -\underline{H}^{(e-h)*}(-\mathbf{k})$. The lattice has FM oriented magnetic moments, which could also be interpreted as a uniform magnetic field. The coupling strength is given by the parameter JS. The parameter α represents a hopping between neighboring lattice sites, where the spin is flipped. This form of hopping

is given by Rashba-type SOC interactions. An s-wave superconducting pairing is given by Δ_0, which is independent of the wave vector. Now a unitary transformation

$$\widetilde{\underline{H}} = \mathcal{U}^{\dagger}\underline{H}\mathcal{U} \tag{2.18}$$

can be applied, which diagonalizes $\underline{H^e}(\mathbf{k})$ and $\underline{H^h}(\mathbf{k})$, but does not mix electronic and hole states (see Appendix A.2 for $\mathcal{U}$). The new pairing matrix then has the form

$$\widetilde{\underline{H}}^{(e-h)}(\mathbf{k}) = \Delta_0\zeta(\mathbf{k})\begin{pmatrix} JS & JS-\beta(\mathbf{k}) \\ JS+\beta(\mathbf{k}) & JS \end{pmatrix} \tag{2.19}$$

with the definitions

$$\beta(\mathbf{k}) = \sqrt{4a^2\sin^2(k_x a) + 4a^2\sin^2(k_y a) + (JS)^2} \quad \text{and} \quad \zeta(\mathbf{k}) = \frac{-1}{\alpha(\mathrm{i}\sin(k_x a) + \sin(k_y a))} \quad . \tag{2.20}$$

This new pairing matrix is now $\mathbf{k}$-dependent. The effective paring matrix from Eq. (2.19) can be written in terms of the vector $\mathbf{d}(\mathbf{k})$ and $\Delta_0(\mathbf{k})$, following Eq. (2.15) as

$$\Delta_0(\mathbf{k}) = -\Delta_0\beta(\mathbf{k})\zeta(\mathbf{k}) \quad \text{and} \quad \mathbf{d}(\mathbf{k}) = \Delta_0\begin{pmatrix} 0 \\ -\mathrm{i}\zeta(\mathbf{k})JS \\ \zeta(\mathbf{k})JS \end{pmatrix} \quad . \tag{2.21}$$

The effective pairing is now a combination of singlet pairing and triplet pairing, as shown by the non-zero vector $\mathbf{d}(\mathbf{k})$. The uniform s-wave pairing from Eq. (2.17) in the $\mathbf{k}$-space is shown in Fig. 2.2b. The effective pairing from one of the diagonal elements of $\widetilde{\underline{H}}^{(e-h)}(\mathbf{k})$ is displayed in Fig. 2.2c. This pairing has the symmetry of p-orbitals yielding the name p-wave superconductivity [72]. The real value of the pairing is thereby aligned with the k_y direction and the imaginary part with the k_x direction. Therefore, this pairing can be called $p_y + \mathrm{i}p_x$-pairing. Up to a phase it is equivalent to $p_x + \mathrm{i}p_y$-pairing. This effective unconventional p-wave pairing can lead to topological superconductivity [133, 134]. This simple example demonstrates how MSH systems, built from conventional superconductors, can host topological superconductivity.

2.1.2 Majorana zero mode

Majorana fermions, predicted by Ettore Majorana [64], are particles, which are their own antiparticles. The existence of Majorana fermions as elementary particles could not been proven so far. A different approach to find Majorana particles is the construction of quasi-particles, which are excitations that behave in a particle like fashion. Such Majorana quasi-particles are theoretically proposed in condensed matter physics, when superconductivity is involved [68]. However, a doubt free experimental observation of the Majorana quasi-particles still remains an open issue. In many cases signatures of

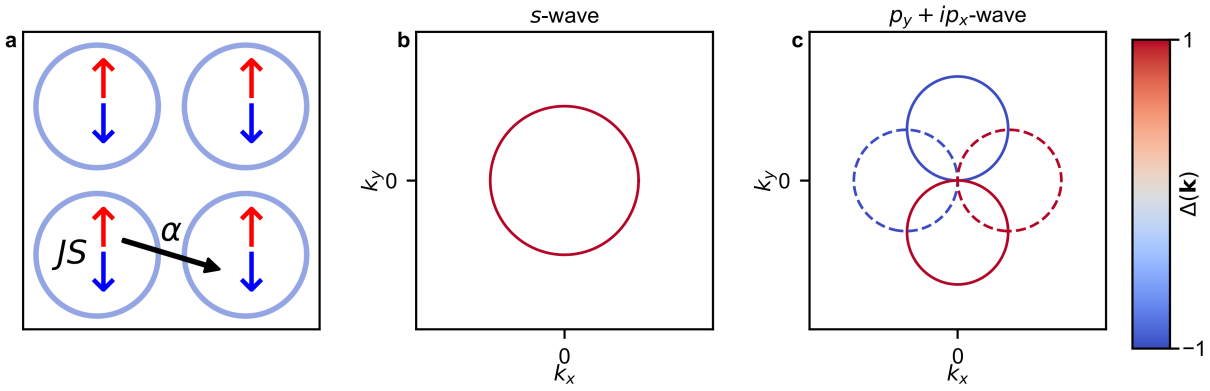

Figure 2.2: Effective p-wave pairing. **a** Square lattice with a uniform magnetic field of strength JS, rashba-SOC α and s-wave superconductivity Δ_0. **b** Isoline for one value of $\Delta(\mathbf{k})$ for conventional s-wave pairing. **c** Isoline for effective p-wave pairing obtained by a unitary transformation. The pairing has the symmetry of p_x and p_x orbitals. The p_x-components (p_y) have imaginary (real) values.

Majorana modes could be observed in experiments [31, 32, 34–36] . But in all cases up to date the experimental finding could alternatively be explained by other phenomena [30, 135, 136], not allowing for a definite proof of Majorana modes. Especially so-called Andreev bound states [137, 138] are hard to differentiate from Majorana states. Andreev states occur on boundaries or defects and are also located in the bulk band gap. In contrast to Majorana states they are not located at zero energy, but can exist at very small energies. This makes a really fine energy resolution necessary to distinguish between both. However, a lot more research is expected in the next years, making also theoretical investigations interesting. These Majorana quasi-particles in condensed matter systems are often referred to as Majorana zero modes (MZM), as the state needs to be located at zero energy in order to be its own antiparticle. Majorana states always have to appear in pairs, where a pair of Majorana states is called often a Majorana bound state (MBS). In the following the main idea for the construction of MZM in condensed matter systems is given. One can define two operators γ_1 and γ_2 using fermionic creation and annihilation operators $c^\dagger$ and c as

$$\gamma_1 = \tfrac{1}{2}(c + c^\dagger) \qquad \gamma_2 = \tfrac{\mathrm{i}}{2}(c - c^\dagger) \tag{2.22}$$

Both of these operators are hermitian and fulfill $\gamma_1 = \gamma_1^\dagger$ and $\gamma_2 = \gamma_2^\dagger$. Therefore, the creation operator is the same as the annihilation operators for γ_1 and γ_2. Subsequently, both new particles can be viewed as their own antiparticles, fulfilling the requirement for Majorana states. The definition is up to now very artificial, as the construction of γ_1 and γ_2 is a superposition of fermionic creation and annihilation operators, meaning fermionic particles and antiparticles. How this can be realized is discussed later. For now these definitions should be used to recreate a well known thought experiment called the Kitaev chain [68]. The chain consists of a row of N electrons, as sketched in Fig. 2.3a. Following

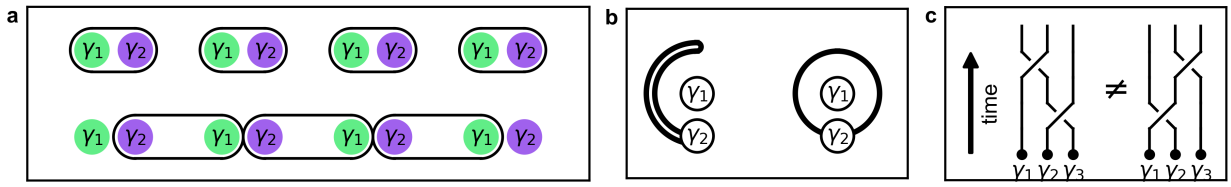

Figure 2.3: Kitaev chain and exchange of anyons. **a** Schematic representation of the Kitaev chain. **b** Trivial and non-trivial exchange of two anyons. **c** Schematic drawing of non-equal anyon braiding operations.

Eq. (2.22) the electronic creation and annihilation operators can be written as

$$c^\dagger = \gamma_1 + \mathrm{i}\gamma_2 \qquad c = \gamma_1 - \mathrm{i}\gamma_2 \tag{2.23}$$

Using this basis transformation each electron can be viewed as a superposition of two Majorana states γ_1 and γ_2. Consequently, the chain consists of $2N$ Majorana states, where γ_1 and γ_2 are alternating. In the thought experiment this chain of Majorana states can now be regrouped to a chain with $N-1$ electrons and two unpaired Majorana states at each end of the chain. The length of the chain prevents the two Majorana states from overlapping and annihilating. This spatial separation is crucial for the stabilization of a pair of Majorana states, due to their main property, being their own antiparticle. While this seems like a very naive model a similar approach has been used in many experiments, where a chain of magnetic atoms was arranged on a superconducting surface. Superconductors are thereby a natural choice, as superconductors have a particle-hole symmetry, where electrons and holes behave like antiparticles. This existence of particles and holes at zero energy does theoretically allow for the construction of Majorana states following Eq. (2.22). The zero energy is here referring to the Fermi energy. The Fermi energy is not the zero-energy for electrons, but for quasi-particle excitations, which are e.g. described by the BdG Hamiltonian. These quasi-particles are formed by superpositions of electronic and hole states. MZM in two-dimensional systems have another interesting property. They follow non-Abelian exchange statistics and are therefore classified as anyons [139].

2.1.3 Non-abelian Anyons

The wavefunction of bosons and fermions behave different under the exchange of two particles. The wavefunction for bosons ψ_b is symmetric, when two particles are exchanged

$$\psi_\mathrm{b}(\mathbf{r}_2, \mathbf{r}_1) = \psi_\mathrm{b}(\mathbf{r}_1, \mathbf{r}_2) \quad , \tag{2.24}$$

where the wavefunction of fermions ψ_f is antisymmetric

$$\psi_\mathrm{f}(\mathbf{r}_2, \mathbf{r}_1) = -\psi_\mathrm{f}(\mathbf{r}_1, \mathbf{r}_2) \quad , \tag{2.25}$$

which is represented by a change of the sign. This change of sign can also be written as a complex phase

$$\psi_f(\mathbf{r}_2, \mathbf{r}_1) = e^{i\theta}\psi_f(\mathbf{r}_1, \mathbf{r}_2) \quad , \tag{2.26}$$

where $\theta = \pi$. The execution of two exchanges consequently leads to the exact same wavefunction, represented by a phase of 2π as

$$\psi'_f(\mathbf{r}_1, \mathbf{r}_2) = e^{i\pi}\psi_f(\mathbf{r}_2, \mathbf{r}_1) = e^{i\pi}e^{i\pi}\psi_f(\mathbf{r}_1, \mathbf{r}_2) = \psi_f(\mathbf{r}_1, \mathbf{r}_2) \quad . \tag{2.27}$$

In three spatial dimensions only these two cases of a symmetric or antisymmetric wavefunction exist. However in two dimensions also a third case exists, where the phase for an exchange of particles can change at any amount. Particles following these exchange statistics are called anyons [25, 140]. The composition of two exchanges in clockwise fashion leads to a phase for the anyon wavefunction

$$\psi'_a(\mathbf{r}_1, \mathbf{r}_2) = e^{i2\theta}\psi_a(\mathbf{r}_1, \mathbf{r}_2) \quad , \tag{2.28}$$

where $\theta \neq \pi$ and $\theta \neq 0$ (the $\theta = \pi$ case would make the particles fermions and $\theta = 0$ would be bosons). The clockwise fashion means, that in the coordinate frame of one anyon the other anyon is following a full circle around the first anyon, as shown in Fig. 2.3b. If the second anyon would perform a half rotation clockwise and a half rotation counterclockwise the anyons would be back in the initial state. The choice of a full clockwise rotation over a full counterclockwise rotation is arbitrary. The important point is, that the rotational sense does not change for the second exchange. From a topological viewpoint the full rotation of one particle around another leads to a path encapsulating the second particle, where in the back and forth rotation the second particle is not encapsulated in the path, making both paths topological different. As a consequence a state after two exchange operations is now distinguishable from the initial state [141]. In Fig. 2.3c three anyons are shown. For three particles now also the order of exchanges is important. The exchange of anyon 1 and 2, followed by an exchange of 1 and 3 leads to a different wavefunction, than the exchange of particles 2 and 3 followed by an exchange of 1 and 3 . In other words the exchanges of particles do not commute as it would be the case for fermions or bosons. The non-commutation of exchanges allows for the so-called braiding of anyons, where the final state depends on the history of exchange operations, which is indicated by the lines. Anyon braiding is proposed to allow for unconventional computing operations [25, 141–144].

2.2 Tight-binding model

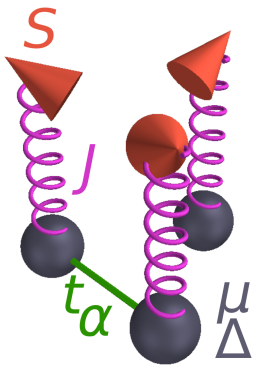

Figure 2.4: Sketch of the interactions included in the tight-binding model. The gray spheres represent atoms of a superconducting substrate. The superconducting lattice sites are coupled via the hopping parameter t and the Rashba-SOC α. Each lattice site has the chemical potential μ and the superconducting order parameter Δ. The cones represent the magnetic structure with a magnetic moment S. The parameter J gives the coupling to the magnetic moment.

A tight-binding model describes the electronic structure of a condensed matter system by expanding the systems wavefunction as a superposition of localized basis functions. In this thesis a tight-binding model was implemented to investigate topological superconductivity in MSH systems. This self-written code has been used for all calculations. In this chapter the here used tight-binding Hamiltonian for a MSH system is presented. Further it is described how physical properties such as the Chern number or local density of states (LDOS) can be calculated from the solutions of the Hamiltonian. The focus is to give a description which allows anyone to implement the same model and reproduce the results of this thesis. In some cases explicit matrices or small examples are given, which can be used to compare own implementations to the one used here. For many examples an atomic-scale skyrmionic lattice (SkX), presented in Pub. II (called s-SkX state here) and Pub. III, is used. The magnetic moments for this spin structure are explicitly given in Appendix A.4. A more general description of the tight-binding model can be found in Refs. [145–148] and in Appendix A.3.

2.2.1 Hamiltonian for magnet-superconductor hybrids

The tight-binding model, used for this thesis, includes five different contributions, each represented by an interaction parameter. The parameters acting only on one lattice site, so-called one-site parameters, are the chemical potential μ, the coupling to a magnetic moment JS and the superconducting order parameter Δ. The superconducting pairing is treated in a mean-field approximation as described in Sec. 2.1. By a coupling strength J the lattice site $\mathbf{r}_i$ is coupled to a magnetic moment $\mathbf{S}_i$ with magnitude S and direction $\mathbf{s}_i$. For the interaction between two lattice sites, so-called two-site terms, the hopping parameter t and the Rashba-type SOC parameter α are considered. The later one represents a hopping with a spin-flip, while t preserves the spin. The Hamiltonian containing these five parameters is

given by [73, 83, 88, 89, 149, 150]

$$H = -\mu \sum_{i,\sigma} c^{\dagger}_{i,\sigma} c_{i,\sigma} + \Delta \sum_{i} (c^{\dagger}_{i,\uparrow} c^{\dagger}_{i,\downarrow} + c_{i,\downarrow} c_{i,\uparrow}) + \sum_{i,j,\sigma} t_{i,j} c^{\dagger}_{i,\sigma} c_{j,\sigma} - \mathrm{i} \sum_{i,j,\sigma,\sigma'} \alpha_{i,j} c^{\dagger}_{i,\sigma} (\mathbf{e}_{\mathbf{r}_i - \mathbf{r}_j} \times \boldsymbol{\sigma}_{\sigma\sigma'}) \cdot \mathbf{e}_z c_{j,\sigma'} + J \sum_{i,\sigma,\sigma'} S_i c^{\dagger}_{i,\sigma} (\mathbf{s}_i \cdot \boldsymbol{\sigma}_{\sigma\sigma'}) c_{i,\sigma'} \quad (2.29)$$

where $c^{\dagger}_{i,\sigma}$ and $c_{i,\sigma}$ are the electronic creation and annihilation operators at the position $\mathbf{r}_i$ with spin σ and $\boldsymbol{\sigma}$ is the vector of the Pauli spin matrices $\boldsymbol{\sigma} = (\sigma_x, \sigma_y, \sigma_z)^T$ (see Appendix A.1 for Pauli matrices). $\mathbf{e}_{\mathbf{r}_i - \mathbf{r}_j}$ is the unit vector of the connection between lattice sites i and j and $\mathbf{e}_z$ the unit vector in z-direction. The summation indices i and j represent the lattice sites and σ and σ' represent the spin channel. Usually all parameters, including the energy E, are written in units of the hopping parameter t. All interactions are marked in Fig. 2.4, where a superconducting layer is represented by gray spheres. The one-site interactions μ and Δ are denoted in gray and the two site interactions t and α in green. The directions of the magnetic moments are displayed by cones and their magnitude is given by S. As J and S have the same effect on the superconducting substrate mostly just their product JS is given. Each lattice site from the superconducting substrate is connected to exactly one magnetic moment. If for example a bilayer system is modeled, the magnetic moment S has to represent the effective moment at the superconducting lattice site. Note, that in this thesis only a single layer with superconducting and magnetic properties is considered. An extension to more than one layer is straight forward. The biggest challenge here would be to chose physically reasonable parameters.

In principle, all interactions could vary over the lattice. In the scope of this thesis the chemical potential μ and superconducting order parameter Δ are constant over the lattice. The hopping parameter t_{ij} and Rashba-SOC parameter α_{ij} are assumed to be isotropic and therefore only dependent on the distance between the two interacting lattice sites. For hexagonal lattices only nearest-neighbor interactions were considered and for the bcc(110) surface up to next-next-nearest neighbors. For the latter a decrease of the coupling strength over the distance is assumed. The magnitude of the magnetic moment S is in some calculations spatially varied, to model for example a magnetic island. The direction of the magnetic moment $\mathbf{s}_i$ is unique to each lattice site in the magnetic unit cell and depends on the considered spin structure.

The Hamiltonian in Eq. (2.29) can be rewritten in a matrix form, when the creation and annihilation operators are written in a vector form. For the lattice site i these have the

vector form

$$\mathbf{c}_i^\dagger = \begin{pmatrix} c_{i,\uparrow}^\dagger & c_{i,\downarrow}^\dagger & c_{i,\uparrow} & c_{i,\downarrow} \end{pmatrix} \quad \text{and} \quad \mathbf{c}_i = \begin{pmatrix} c_{i,\uparrow} \\ c_{i,\downarrow} \\ c_{i,\uparrow}^\dagger \\ c_{i,\downarrow}^\dagger \end{pmatrix} \quad , \tag{2.30}$$

where the annihilation of an electron $c_{i,\sigma}$ with spin σ corresponds to the creation of a hole, due to the particle-hole symmetry. Therefore, the first two entries of $c_i^\dagger$ can be understood as electronic creation operators and the later two as hole creation operators. For all lattice sites the operators can be written in a vector of the form

$$\mathbf{c}^\dagger = \begin{pmatrix} \mathbf{c}_1^\dagger & \mathbf{c}_2^\dagger & \dots & \mathbf{c}_N^\dagger \end{pmatrix} \quad \text{and} \quad \mathbf{c} = \begin{pmatrix} \mathbf{c}_1 \\ \mathbf{c}_2 \\ \vdots \\ \mathbf{c}_N \end{pmatrix} \quad . \tag{2.31}$$

Now the Hamiltonian from Eq. (2.29) can be written as

$$H = \mathbf{c}^\dagger \underline{H} \mathbf{c} \quad , \tag{2.32}$$

where $\underline{H}$ is a matrix containing the contributions of all parameters. This matrix is of dimension $(4N \times 4N)$, where N is the number of lattice sites. The explicit form of $\underline{H}$ is later given for some examples.

In many calculations infinitely expanded samples are described via periodic boundary conditions. With the Fourier transform of the creation and annihilation operators

$$c_i(\mathbf{r}) = \frac{1}{\sqrt{N}} \sum_{\mathbf{k} \in BZ} c_i(\mathbf{k}) \mathrm{e}^{\mathrm{i}\mathbf{k}\cdot\mathbf{r}} \tag{2.33}$$

$$c_i(\mathbf{k}) = \frac{1}{\sqrt{N}} \sum_{\mathbf{r}} c_i(\mathbf{r}) \mathrm{e}^{-\mathrm{i}\mathbf{k}\cdot\mathbf{r}} \tag{2.34}$$

the calculation can be carried out in the magnetic unit cell, while it also has to be integrated over the BZ. Here N is the number of lattice sites. For the numerical calculations the integration is substituted by a summation over discrete k-points, which sample the BZ. Using Eq. (2.33) the Hamiltonian from Eq. (2.32) can be written as

$$H = \sum_{\mathbf{k} \in BZ} \mathbf{c}^\dagger(\mathbf{k}) \underline{H}(\mathbf{k}) \mathbf{c}(\mathbf{k}) \quad , \tag{2.35}$$

where the exponential functions are absorbed into $\underline{H}(\mathbf{k})$. As the entries of Eq. (2.30) can be interpreted as electronic and hole states, also the entries of the Hamilton matrix from Eq. (2.32) and Eq. (2.35) can be grouped into an electronic matrix $\underline{H^e}$ and a hole matrix $\underline{H^h}$

as

$$\underline{H}(\mathbf{k}) = \begin{pmatrix} \underline{H}^{e}(\mathbf{k}) & \underline{\Delta}^{(e-h)}(\mathbf{k}) \\ \underline{\Delta}^{(h-e)}(\mathbf{k}) & \underline{H}^{h}(\mathbf{k}) \end{pmatrix} \quad . \tag{2.36}$$

The off-diagonal blocks describe a transition from electronic to hole states and vice versa. The transitions can be interpreted as the respective creation and annihilation of a Cooper pair. The entry $\underline{\Delta}^{h-e}$ describes the annihilation of a hole and creation of an electron, which resembles the annihilation of a Cooper pair. The hole and one electron of the Cooper pair with the same spin can annihilate, as they are antiparticles. Thereby the other electron of the Cooper pair is left. In the case of spin singlet Cooper pairs, this electron has the opposite spin of the hole (cf. Sec. 2.1). $\underline{\Delta}^{e-h}$, on the other hand, describes the opposite process, where an electron is annihilated and a hole is formed. Here an electron-hole pair is created, both electrons form a Cooper pair and the hole is left. The diagonal blocks obey the relation

$$\underline{H}^{h}(\mathbf{k}) = -\underline{H}^{e*}(-\mathbf{k}) \tag{2.37}$$

which reflects the particle-hole symmetry (cf. Sec. 2.1). Due to this symmetry, for every eigenvalue ϵ at $\mathbf{k}$ there exists an eigenvalue $-\epsilon$ at $-\mathbf{k}$. Accordingly, also the off-diagonal elements fulfill

$$\underline{\Delta}^{(h-e)}(\mathbf{k}) = -\underline{\Delta}^{(e-h)*}(-\mathbf{k}) \quad . \tag{2.38}$$

Each of the entries of Eq. (2.36) is a (2×2) matrix in spin space. When the model contains N types of orbitals, the matrix form of the Hamiltonian looks like

$$H = \begin{pmatrix} \mathbf{c}_1^\dagger & \mathbf{c}_2^\dagger & \dots & \mathbf{c}_N^\dagger \end{pmatrix} \underbrace{\begin{pmatrix} \underline{H}_{11} & \underline{H}_{12} & \cdots & \underline{H}_{1N} \\ \underline{H}_{21} & \underline{H}_{22} & & \underline{H}_{2N} \\ \vdots & & \ddots & \\ \underline{H}_{N1} & \underline{H}_{N2} & & \underline{H}_{NN} \end{pmatrix}}_{\underline{H}} \begin{pmatrix} \mathbf{c}_1 \\ \mathbf{c}_2 \\ \vdots \\ \mathbf{c}_N \end{pmatrix} \quad , \tag{2.39}$$

where each of the entries of $\underline{H}$ has the form of Eq. (2.36). Each type of orbitals consists actually of four orbitals in the spin space and particle-hole space. Different types of orbitals could correspond to different lattice sites or multiple orbitals at one lattice site with different character, e.g. s and p_x. In this thesis each lattice site is described by one entry of $\underline{H}$ from Eq. (2.39), representing one type of orbital per lattice site. The one-site interactions are contained in the diagonal elements $\underline{H}_{ii}$. The electronic (2×2) matrices for the chemical potential and the coupling to a magnetic structure with the local magnetic moment $\mathbf{S}_i = (S_i^x, S_i^y, S_i^z)^T$ are given by

$$\underline{H}^{e}_{\text{chem. pot.}} = \begin{pmatrix} -\mu & 0 \\ 0 & -\mu \end{pmatrix} \quad \text{and} \quad \underline{H}^{e}_{\text{magnetic}} = \begin{pmatrix} JS_i^z & J(S_i^x - \mathrm{i}S_i^y) \\ J(S_i^x + \mathrm{i}S_i^y) & -JS_i^z \end{pmatrix} \quad , \tag{2.40}$$

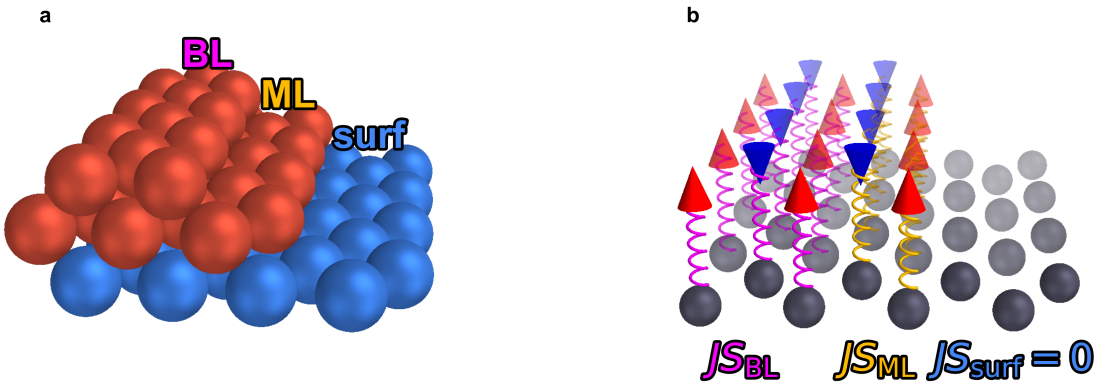

Figure 2.5: Setup to model different domains in the tight-binding model. a Sketch of magnetic layers (red) on a superconducting surface (blue). Three different regions exist: a magnetic bilayer (BL), a magnetic monolayer (ML) and an uncovered superconducting surface (surf). **b** Setup of the tight-binding model to simulate the structure from (**a**). Also here three different domains exist, which differ only in the parameter JS, which is indicated by springs. The effective magnetic moments, forming an AFM structure, are sketched as cones.

where the contributions of the hole-like orbitals follow directly from Eq. (2.37). The two-site interactions, the hopping parameter and Rashba-SOC, for the entries $\underline{H}_{ij}$ from Eq. (2.39) are

$$\underline{H}^{e}_{\text{hopping}} = \begin{pmatrix} t & 0 \\ 0 & t \end{pmatrix} \quad \text{and} \quad \underline{H}^{e}_{\text{Rashba}} = \begin{pmatrix} 0 & \alpha(-e^{x}_{ij} + \mathrm{i}e^{y}_{ij}) \\ \alpha(e^{x}_{ij} + \mathrm{i}e^{y}_{ij}) & 0 \end{pmatrix} , \tag{2.41}$$

where $\mathbf{e}_{ij} = (e^{x}_{ij}, e^{y}_{ij}, e^{z}_{ij})^{T}$ is the normalized connection vector between the lattice sites $\mathbf{r}_i$ and $\mathbf{r}_j$. Note, that also the two-site interactions can be contained in the matrix elements $\underline{H}_{ij}$ with $i = j$ due to periodic boundary conditions. In this work only an one-site spin singlet s-wave superconductivity is considered, which is an appropriate model for most conventional superconductors (cf. Sec. 2.1). S-wave superconductivity can be written as (cf. Eq. (2.15))

$$\Delta^{(e-h)} = \begin{pmatrix} 0 & \Delta \\ -\Delta & 0 \end{pmatrix} \tag{2.42}$$

for the one-site contributions $\underline{H}_{ii}$. The contribution $\underline{\Delta}^{(h-e)}$ is given by Eq. (2.38). An extension to other forms of Cooper pair pairing, e.g. spin triplet pairing, is given by Eq. (2.15). From these (2×2) matrices the Hamilton matrix Eq. (2.39) can be constructed.

2.2.2 Sample geometries

In this thesis MSH systems are modeled by a single atomic layer, which is superconducting and magnetic. This layer can either be interpreted as the magnetic layer with proximity induced superconductivity or as a superconducting layer with induced magnetic moments. In either way the simplicity of this model allows to investigate fundamental features of

MSH systems without relying on specific electronic interactions between superconducting and magnetic layers [39, 73, 83, 88, 89, 91]. To give a more accurate electronic representation of a specific system, the tight-binding model can straightforwardly be expanded to multiple layers. However, in that setup more interactions parameters exist, which have to be chosen in a way to represent the realistic system. Therefore, detailed information about the electronic structure from first-principles calculations or experiments would be needed. In the setup used here, which contains a single atomic layer, different domains are described by unique sets of interaction parameters. As an example a superconducting substrate (blue) with two magnetic layers (red) is sketched in Fig. 2.5a . Thereby three regions are formed, one with a magnetic bilayer, one with a magnetic monolayer and the uncovered superconducting surface. Fig. 2.5b shows the setup used for the tight-binding calculations to model the three domains and their boundaries from Fig. 2.5a. The hopping parameter t, the chemical potential μ, the superconducting order parameter Δ and the Rashba-SOC term α are set to values representing the uncovered superconducting surface. The coupling to the magnetic layer $JS_{\mathrm{surf}} = 0$ is zero in this region, as no magnetic layer is present. For the magnetic monolayer the parameter JS_{ML} is set to some finite value. All other parameters are the same as for the uncovered superconducting layer. For the bilayer a different value JS_{BL} is chosen. This parameter reflects the effective magnetization from both of the magnetic layers. As an approximation one could use the induced magnetic moments in the first superconducting layer, calculated by DFT, as it has been done in Pub. IV. While the tight-binding parameters in general can be chosen freely, the model should reflect key properties of the system that is simulated, e.g. known from experimental observations or first-principle calculations.
To calculate various properties, different geometries can be used for the tight-binding calculations. Periodic or open boundary conditions can be assumed in each direction. For periodic boundary conditions, lattice sites at one boundary of the unit cell are connected to lattice sites on the opposite boundary of the unit cell. For open boundary conditions, the lattice sites at a boundary of the unit cell have fewer binding partners, than lattice sites in the center. In this work open boundary conditions are always assumed in the z-direction as thin films are investigated. The plane of the thin film is spanned by two lattice vectors, which depend on the investigated lattice and in general do not have to be perpendicular. These lattice vectors $\mathbf{a}_1$ and $\mathbf{a}_2$ span the chemical unit cell. The sample can be periodic in none, one or both of these directions. A system with uniform parameters, which is periodic in two directions is in the sense of the tight-binding calculations also referred to as the 2D bulk or bulk for short.

Bulk setup

The bulk represents an infinitely expanded sample of one magnetic state, as sketched in Fig. 2.6a. All tight-binding parameters are the same over the lattice. The calculations are performed in the magnetic unit cell with periodic boundary conditions and have to

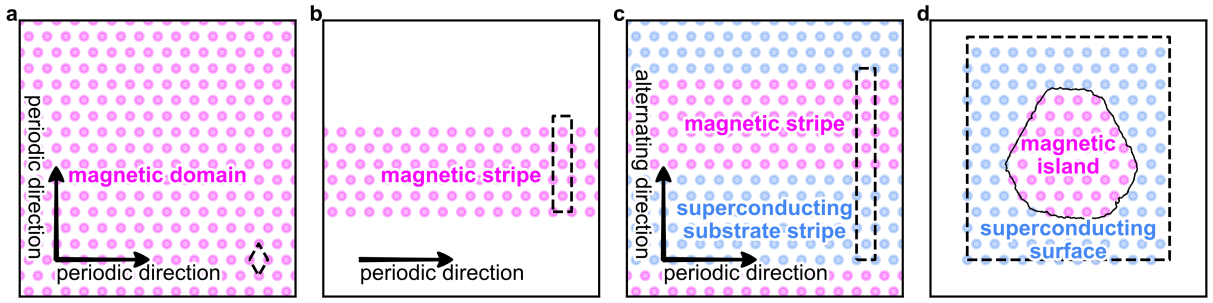

Figure 2.6: Sketches of different setups using periodic or open boundary conditions. Three regions are displayed. A magnetic island is represented by one set of parameters. The uncovered superconducting substrate is reflected by a different set of parameters. A vacuum corresponds to the absence of lattice sites. **a** Bulk magnetic domain periodically repeated in both directions. **b** A magnetic stripe, periodic in one direction and with a finite width in the other direction. **c** Alternating stripes of magnetic and superconducting substrate domains. The unit cell is periodically repeated in both directions. **d** A magnetic island on a superconducting surface without periodic boundary conditions. The magnetic unit cell is marked by dashed black lines for each setup.

be performed for a mesh of discrete k-points in the first BZ. As an example a square lattice with one atom in the magnetic unit cell is sketched in Fig. 2.7a. The hopping and Rashba-SOC parameters for interactions between nearest neighbors are denoted, where the exponential functions originate from Eq. (2.33). As only one atom is in the magnetic unit cell, the Hamilton matrix from Eq. (2.39) contains only the element $\underline{H}_{11}$. The electronic part of the matrix is

$$\underline{H}^e = \begin{pmatrix} \mu + JS + 2t(\cos(k_x a) + \cos(k_y a)) & 2\alpha(-\sin(k_y a) - \mathrm{i}\sin(k_x a)) \\ 2\alpha(-\sin(k_y a) + \mathrm{i}\sin(k_x a)) & \mu - JS + 2t(\cos(k_x a) + \cos(k_y a)) \end{pmatrix} , \tag{2.43}$$

where $\cos(x) = (\mathrm{e}^{\mathrm{i}x} + \mathrm{e}^{-\mathrm{i}x})/2$ and $\mathrm{i}\sin(x) = (\mathrm{e}^{\mathrm{i}x} - \mathrm{e}^{-\mathrm{i}x})/2$ were used. The BZ for this square lattice is displayed in Fig. 2.7b. In the BZ a (10×10) grid of k-points is sketched, which can be used for the numerical calculations. For all calculations the convergence with respect to the number of k-points has to be checked. An evenly spaced grid of k-points can be created by

$$\mathbf{k}_{\mu\nu} = \frac{\mu}{N_1}\mathbf{b}_1 + \frac{\nu}{N_1}\mathbf{b}_2 \quad (\mu = 0, 1, 2, ..., N_1 - 1 \quad \text{and} \quad \nu = 0, 1, 2, ..., N_2 - 1) \quad , \tag{2.44}$$

where $\mathbf{b}_1$ and $\mathbf{b}_2$ are the unit vectors of the reciprocal lattice. Such a mesh of k-points is shown for a hexagonal lattice in Fig. 2.7c in blue. By this definition it is ensured, that the $\overline{\Gamma}$-point is always one of the sampled points. Alternatively the Monkhorst-Pack mesh [151] could be used.

Not all points of the mesh defined by $\mathbf{k}_{\mu\nu}$ are located in the first BZ. However, these points $\mathbf{k}_{\mu\nu}$ can always be folded back into the first BZ by finding the minimal distance $\min_G(d_G)$ of $d_G = |\mathbf{k}_{\mu\nu} - \mathbf{k}_G|$, where $\mathbf{k}_G$ can be any integer linear combination of the reciprocal lattice

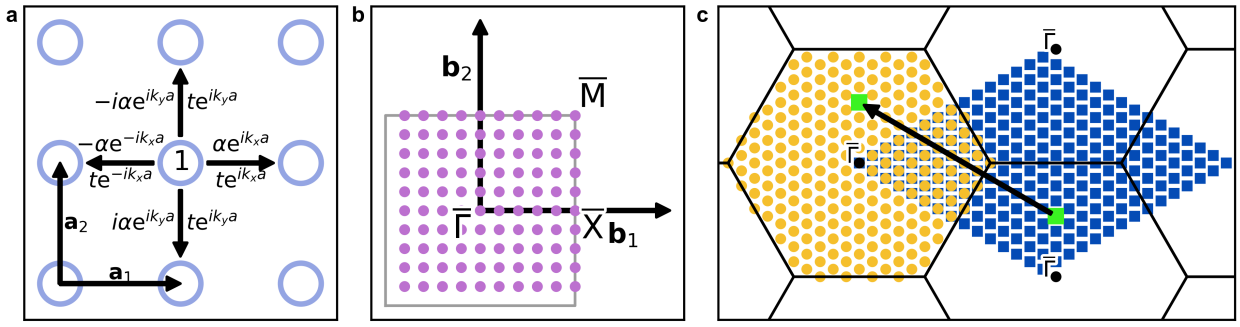

Figure 2.7: Hopping and Rashba-SOC parameters for a periodic square lattice and k-point distributions. a A periodic square lattice with one atom in the magnetic unit cell. The hopping and Rashba-SOC elements for the nearest neighbors are denoted. The Rasba-SOC elements are given for a hopping from a ↑ to a ↓ orbital. **b** BZ for the lattice in **a**. A uniform grid of k-points, which can be used for the numerical calculations is marked by purple points. **c** BZ for a hexagonal lattice. A uniform mesh of k-points generated by Eq. (2.44) (blue) and uniform grid of k-points in the first BZ (orange), obtained by shifting of k-points by reciprocal lattice vectors. The shift of one point is sketched in green.

vectors $\mathbf{b}_1$ and $\mathbf{b}_2$. The k-point $\mathbf{k}_{\mu\nu}$ is shifted by the lattice vector $\mathbf{k}_G$, which is closest to it. This is indicated by the two green marked k-points in Fig. 2.7c. This procedure creates an evenly spaced grid of k-points in the first BZ as shown by the orange mesh in Fig. 2.7c. In the first BZ the bulk band structure can be calculated. The superconducting band gap, which is occurring here, is referred to as the bulk band gap. Also other properties, such as the Chern number, can be calculated in the bulk setup.

Stripe geometry

For the calculation of edge states quasi-1D systems are useful [88, 152–154], where an infinite long stripe with finite width is formed, as sketched in Fig. 2.6b. This is sometimes also referred to as a ribbon. In the periodic direction $\mathbf{a}_\mu$, which is one of the lattice vectors, the Bloch condition is fulfilled, leading to

$$\Psi(\mathbf{r}) = \mathrm{e}^{\mathrm{i}\mathbf{k}_\mu n \mathbf{a}_\mu} u(\mathbf{r}) \quad , \tag{2.45}$$

where n is the distance in units of the lattice vector and $\mathbf{k}_\mu \| \mathbf{a}_\mu$. As this geometry has only one periodic direction, the reciprocal vector $\mathbf{k}$ can only be chosen along this periodic direction. To calculate the complex phase shift between two lattice sites, their distance has to be known in units of the real space lattice vectors. If not known, these can be calculated from the distance in cartesian units. The position in cartesian units is given by

$$\mathbf{r} = n\mathbf{a}_1 + m\mathbf{a}_2 = n \begin{pmatrix} a_1^x \\ a_1^y \\ a_1^z \end{pmatrix} + m \begin{pmatrix} a_2^x \\ a_2^y \\ a_2^z \end{pmatrix} = \begin{pmatrix} r^x \\ r^y \\ r^z \end{pmatrix} \quad , \tag{2.46}$$

which yields

$$n = \frac{a_2^y r_x - a_2^x r_y}{a_1^x a_2^y - a_1^y a_2^x} \quad m = \frac{a_1^x r_y - a_1^y r_x}{a_1^x a_2^y - a_1^y a_2^x} \quad . \tag{2.47}$$

In the non-periodic direction the stripe can have a certain width. For a hexagonal lattice with lattice vectors $\mathbf{a}_1 = (1, 0, 0)^T$ and $\mathbf{a}_2 = \frac{1}{2}(1, \sqrt{(3)}, 0)^T$ such a stripe is sketched in Fig. 2.8. The unit cell contains four atoms and the stripe has a width of only two rows, but it is infinitely long in the horizontal direction. The connection vectors to the nearest neighbors of lattice site 1 are marked in units of the lattice vectors. The lattice site 4′ represents the periodic repetition of lattice site 4. The contributions from $1 \to 4$ and $1 \to 4'$ are both contained in element $\underline{H}_{14}$ from Eq. (2.39), due to the periodic boundary conditions. The hopping parameters and the Rashba-SOC parameters for a hopping from the ↑ orbital to a ↓ orbital are given in Tab. 2.2. The Rashba-contributions for a hopping from ↓ to ↑ orbitals follow by complex conjugation and multiplying with −1. From these contributions and the one-site terms the Hamilton matrix for this stripe geometry can be constructed. To investigate topological properties the width of the stripe has to be larger, so that the stripe has bulk-like properties in the middle of the stripe. The necessary width of the stripe depends thereby on the electronic structure.

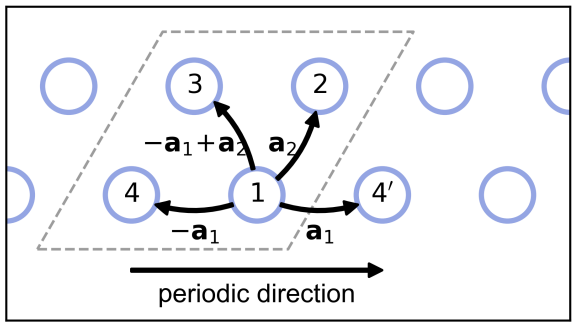

Figure 2.8: Sketch of a stripe with a magnetic unit cell of four lattice sites. The magnetic unit cell is marked by a gray dashed line. The lattice sites in the unit cell are numerated and correspond to different orientations of the magnetic moment. The periodic repetition of the lattice site 4 is marked as 4′. The connection vectors to the nearest neighbors from lattice site 1 are given in unit of the lattice vectors. The hopping and Rashba-SOC matrix elements for these connections are given in Tab. 2.2.

	hopping	Rashba-SOC
$1 \to 2$	t	$\alpha(\frac{1}{2} - \mathrm{i}\frac{\sqrt{3}}{2})$
$1 \to 3$	$t\mathrm{e}^{-\mathrm{i}ka}$	$\alpha(-\frac{1}{2} - \mathrm{i}\frac{\sqrt{3}}{2})\mathrm{e}^{-\mathrm{i}ka}$
$1 \to 4$	$t\mathrm{e}^{-\mathrm{i}ka}$	$-\alpha\mathrm{e}^{-\mathrm{i}ka}$
$1 \to 4'$	$t\mathrm{e}^{\mathrm{i}ka}$	$\alpha\mathrm{e}^{\mathrm{i}ka}$

Table 2.2: Hopping and Rashba-SOC parameters for nearest neighbors of a small stripe. The stripe wit a four atomic unit cell is sketched in Fig. 2.8. The matrix elements are given for a hopping from lattice site 1 to the nearest neighbors. The Rashba-SOC parameters are given for a hopping from a ↑ to a ↓ orbital. The matrix elements for a hopping from a ↓ to a ↑ state follow from a complex conjugation and multiplying by −1.

Outside of the stripe is a vacuum, which is a trivial state. If the stripe is in a topological superconducting phase, edge modes will occur on both sides of the stripe. Fig. 2.9a presents the bulk band structure of the SkX state. The green sheet represents the Fermi energy and the bulk band gap is between $-0.4\,t \leq E \leq 0.4\,t$. Fig. 2.9b shows the band structure for a stripe geometry of the same state, where vacuum is on both sides of the stripe (cf. Fig. 2.6b).

This band structure contains also states in the bulk band gap. For a direct comparison the projected bulk band structure is displayed together with the band structure of the ribbon in Fig. 2.9c. The bulk band structure, calculated in the 2D-BZ (cf. Fig. 2.9a) is thereby projected onto the periodic direction of the stripe. The states outside of the energy interval $E \in [-0.4\,t, 0.4\,t]$ coincide with the bulk energy bands. The modes, crossing the superconducting gap, can therefore be accounted to the edges. The stripe has a width of ten magnetic unit cells, which seems sufficient to reflect bulk properties in the middle of the stripe. A drawback of this approach is, that the edge modes cannot be assigned to one of the two edges. This problem can be solved, when the spectral function (cf. Sec. 2.2.5) is calculated, which gives a k-resolved LDOS. The spectral function for two rows of atoms at one boundary of the stripe is displayed in Fig. 2.9d. Here only one of the edge modes from Fig. 2.9b is visible. The spectral function for the other boundary shows the other edge mode. The asymmetry of the edge modes originates from different terminations of the magnetic texture. In the middle of the stripe the spectral function would show an open band gap (see Pub. III for the data). Via the spectral function it could be confirmed, that at each edge one edge mode exists, while the middle of the stripe has a band gap. The edge modes have an opposite slope, which represents a chirality of the edge modes.
Apart from a boundary to the vacuum, one might want to calculate edge modes for a boundary to other trivial or non-trivial domains. Such a geometry is sketched in Fig. 2.6c. In this case the wide ribbons can be repeated in the formerly non-periodic direction, where the properties are alternating from stripe to stripe. This leads to a setup, which is periodic in two directions. As the stripes are very wide, the energy dispersion in the alternating direction is approximately flat. This condition can also be used to check for the convergence of the width of the stripes. Edge modes in this setup can be investigated equivalent to the quasi-1D stripe.

Finite sample

While the ribbon geometry allows to calculate the dispersion relation of edge modes, also edge states for odd shaped islands can be calculated. Fig. 2.6d shows a magnetic island on a superconducting surface. The shape of the magnetic island is inspired by an island found in a STM measurement (see Ref. [155] and Pub. II). As this island has no periodicity, all lattice sites have to be included explicitly in the calculation. The magenta points represent lattice sites within the magnetic islands and the blue points lattice sites outside of the island. Properties such as the LDOS (cf. Sec. 2.132) or the supercurrent (cf. Sec. 2.2.6) can be calculated in order to investigate the boundary of the magnetic island. Via the LDOS the existence of zero-energy edge states can be obtained, where the chirality is reflected in the supercurrent. Besides the boundary at the magnetic island a second boundary exists at the border of the simulation box, where the superconducting surface is adjacent to the vacuum. In the case of a trivial superconducting surface no topological edge modes would arise there, but the LDOS can still be altered compared to the bulk superconducting surface.

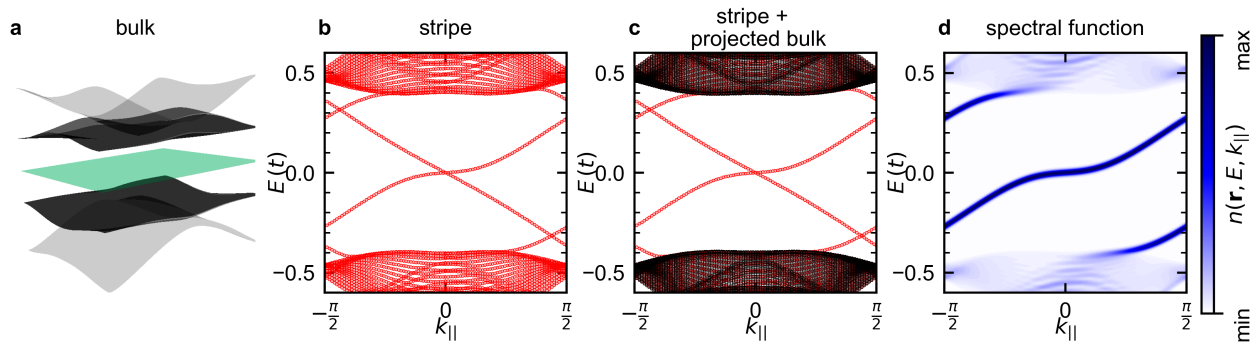

Figure 2.9: Band structure for different geometries and spectral function. The magnetic structure is given by the SkX state (see Appendix. A.4). **a** Bulk band structure. The green sheet marks the Fermi energy. **b** Band structure in the periodic direction of a stripe with as width of 10 magnetic unit cells. **c** Band structure of a stripe (red) and projected band structure of the bulk (black). **d** Spectral function for two rows at one boundary of the stripe. The parameters for the calculations are $t = 1, \mu = 1.5, JS = 3, \Delta = 0.7, \alpha = 0$.

To avoid effects from this boundary, periodic boundary conditions can be applied but the calculation is still restricted to $\mathbf{k} = 0$. When this trick is used, it has to be made sure, that the area of the uncovered superconducting surface is large enough, so that interactions of the magnetic island with itself over the periodic boundaries are avoided.

2.2.3 Quantization axis

In the previously shown Hamilton matrix the quantization axis is chosen along the z-direction. Spins aligned along the z-axis are therefore diagonal in spin space, while x and y components are on the off-diagonal. The global quantization axis could be rotated to any axis by a unitary transformation. Also a local rotation of the quantization axis at each lattice site is possible [88, 89]. The local quantization axis could for example be aligned with each magnetic moment. This would make all magnetic contributions diagonal in spin space. Hopping elements between lattice sites with different quantization axis can now contain off-diagonal elements, even if they were diagonal for a global uniform quantization axis. These off-diagonal elements represent spin-flip events. In the following is demonstrated how a local quantization axis can be obtained by unitary transformations. Global quantization axis, differing from the z-direction can be obtained, when the same unitary transformation is applied to all lattice sites. The Hamiltonian H_{ij} for interactions between the lattice sites i and j can be written in different bases, which can be transformed into each other by unitary transformations as

$$H_{ij} = \mathbf{c}_i^\dagger \underline{H}_{ij} \mathbf{c}_j = \mathbf{c}_i^\dagger \mathcal{U}_i^\dagger \mathcal{U}_i \underline{H}_{ij} \mathcal{U}_j^\dagger \mathcal{U}_j \mathbf{c}_j = \tilde{\mathbf{c}}_i^\dagger \underline{\widetilde{H}}_{ij} \tilde{\mathbf{c}}_j \quad . \tag{2.48}$$

The unitary transformations $\mathcal{U}_i$ and $\mathcal{U}_j$ describe a rotation from the z-axis to the axis of the local magnetic moment of i and j respectively. The unitary transformation for the lattice

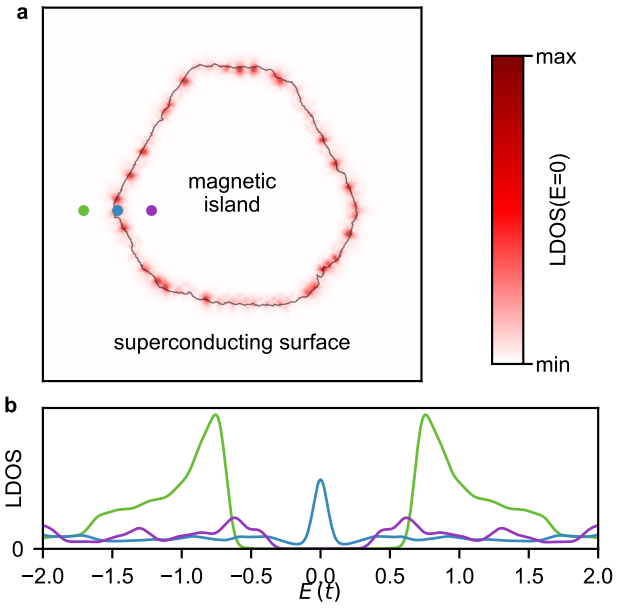

Figure 2.10: LDOS for a magnetic island on a superconducting substrate. The magnetic layer contains the SkX state (cf. Appendix A.4). **a** Spatially resolved LDOS at zero energy. **b** Energy resolved LDOS for the tree lattice sites, marked in **a**. These are located on the superconducting substrate (green), at the boundary (blue) and on the magnetic island (purple). The green and purple lattice sites have a distance of ten lattice constants from the boundary. The parameters for the calculation are $t = 1, \alpha = 0, \mu = 1.5, \Delta = 0.7$, $JS = 3.0$ on the magnetic island and $JS = 0$ on the superconducting surface. The broadening parameter for the LDOS is $\sigma = 0.05\,t$. The figure is adapted from Pub. III.

site i is given by

$$\mathcal{U}_i = \sigma_0 \cos\left(\frac{\Theta_i}{2}\right) + \mathrm{i}(\boldsymbol{\sigma} \cdot \mathbf{n}_i) \sin\left(\frac{\Theta_i}{2}\right) \quad , \tag{2.49}$$

where $\boldsymbol{\sigma}$ is the vector of the Pauli spin matrices, σ_0 the (2×2) unity matrix, $\mathbf{n}_i$ the rotation axis and Θ_i the rotation angle. The rotation axis and the angle can be derived from the unit vector in z-direction $\mathbf{e}_z$ and the local quantization axis $\mathbf{s}_i$ as

$$\mathbf{n}_i = \frac{\mathbf{s}_i \times \mathbf{e}_z}{|\mathbf{s}_i \times \mathbf{e}_z|} \tag{2.50}$$

and

$$\Theta_i = \arccos\left(\frac{\mathbf{s}_i}{|\mathbf{s}_i|} \cdot \mathbf{e}_z\right) \quad . \tag{2.51}$$

2.2.4 Local density of states

The density of states (DOS) is the integration over all states in the BZ for a given energy E. This DOS can be projected onto an orbital located at lattice site $\mathbf{r}_i$ leading to the local density of states (LDOS). If more than one orbital exists per lattice site, the projected DOS can be calculated for each orbital individually or all contributions from a lattice site can be summed. Using the BdG Hamiltonian each lattice site has at minimum four orbitals, the electronic $\uparrow, \downarrow$ and the hole $\uparrow, \downarrow$ states. In the following one specific orbital is represented by the multi indices $m = (i, \sigma, \tau)$ or $n = (j, \sigma', \tau')$. Here i represents a lattice site, σ a spin channel and τ the electron or hole character. The LDOS can be calculated from the diagonal elements of the retarded Greens function $G^r_{mn}(E)$ as

$$\eta_m(E) = -\frac{1}{\pi} \Im(G^r_{mm}(E)) \quad , \tag{2.52}$$

where $\Im$ denotes the imaginary part. The orbital index m is given as an index here, as the LDOS can be only calculated at lattice sites in the used tight-binding framework. For other approaches the LDOS could also be calculated in between lattice sites. The retarded Greens function has the form [156]

$$G_{mn}(E) = \sum_{\nu} \frac{\langle m|\Psi_\nu\rangle\langle\Psi_\nu|n\rangle}{E - \epsilon_\nu + \mathrm{i}\delta} \quad , \tag{2.53}$$

where $\delta \to 0^+$ is an infinitesimal positive number, ν is the band index and ϵ_ν the corresponding eigenenergy of the wavefunction Ψ_ν. The poles of this retarded Greens function corresponds to the eigenvalues of the Hamiltonian. Using Eq. (2.52) the LDOS has the form [157]

$$\eta_m(E) = \sum_{\nu} \delta(E - \epsilon_\nu)\langle m|\Psi_\nu\rangle\langle\Psi_\nu|m\rangle \quad . \tag{2.54}$$

The state $|m\rangle$ is in the tight-binding simulation simply a vector with a 1 at the component that represents the state m. All other components are zero. For the electronic spin-down state in a system with only one lattice site, the vector would have the form

$$|m\rangle = \begin{pmatrix} 0 \\ 1 \\ 0 \\ 0 \end{pmatrix} \tag{2.55}$$

following Eq. (2.30). For a periodic system each state has an additional parameter $\mathbf{k}$ and for the total LDOS an integration over the BZ has to be performed. For the numerical calculation, where the BZ integration is substituted by a summation over all k-points, the LDOS is calculated as

$$\eta_m(E) = \sum_{\mathbf{k}} \sum_{\nu} \delta(E - \epsilon_{\nu,\mathbf{k}})\langle m|\Psi_{\nu,\mathbf{k}}\rangle\langle\Psi_{\nu,\mathbf{k}}|m\rangle \quad . \tag{2.56}$$

For the numerical calculation of the LDOS a challenge arises due to the finite number of k-points. For a given energy E no eigenvalue might exist with the same energy, because the respective k-point is not in the set of sampled points. For this problem two common approaches exist, either the eigen energy $\epsilon_{\nu,\mathbf{k}}$ is interpolated between neighboring k-points or a broadening is applied on all eigen energies. While a dense mesh of k-points is beneficial for the accuracy of both methods, especially the second method requires a relatively large number of k-points. In this work the approach of a broadening of all states was used together with a fine mesh of k-points leading to

$$\eta_m(E) = \sum_{\mathbf{k}} \sum_{\nu} g(E - \epsilon_{\nu,\mathbf{k}})\langle m|\Psi_{\nu,\mathbf{k}}\rangle\langle\Psi_{\nu,\mathbf{k}}|m\rangle \quad , \tag{2.57}$$

where $g(E - \epsilon_{\nu,\mathbf{k}})$ is the Gaussian distribution

$$g(x) = \frac{1}{\sigma\sqrt{2\pi}} \exp\left(\frac{-(E-\epsilon_{\nu,\mathbf{k}})^2}{2\sigma^2}\right) \tag{2.58}$$

with σ being the standard derivation defining the broadening. The LDOS can also be calculated, when the state is only in one direction periodic or even, when it is not periodic at all.

Fig. 2.10 shows the LDOS for a magnetic island hosting a SkX state on a superconducting surface. The island is modeled as shown in Fig. 2.6d. Fig. 2.10a displays the spatially resolved LDOS at zero energy. Zero-energy states are located all around the boundary of the magnetic island. Along the boundary the intensity of the zero energy states is varying. Reasons for this are the irregular-shaped boundary and the non-coplanar spin structure (see Pub. III for details).

For three lattice sites the energy resolved LDOS is given in Fig. 2.10b. One lattice site is located on the superconducting surface (green), which shows a band gap, that is defined by the superconducting order parameter Δ of the calculation. States within the energy interval $E \in [-\Delta, \Delta]$ exist only due to the broadening (cf. Eq. (2.58)). The lattice site on the magnetic island (purple) has also a band gap, which is reduced in respect to the superconducting substrate. The LDOS directly at the boundary (blue) has a peak at zero energy, representing the edge state. While the LDOS can be used to find edge states, it still has to be investigated if these are topological edge states, e.g. by calculating the supercurrent.

2.2.5 Spectral function

Compared to the LDOS, the spectral function resolves also the $\mathbf{k}$ dependence of a state with energy E for a specific orbital ν. The spectral function is given by

$$A_m(\mathbf{k}, E) = \sum_{\nu} \delta(E_{\mathbf{k}} - \epsilon_{\nu,\mathbf{k}}) \langle m|\Psi_{\nu,\mathbf{k}}\rangle\langle\Psi_{\nu,\mathbf{k}}|m\rangle \quad . \tag{2.59}$$

This spectral function can be used to determine at which lattice sites modes, occurring in the band structure, are mostly localized. Edge modes, which are localized at the boundaries of an island, can cross the superconducting gap. In the center of the sample the band structure should be similar to the bulk band structure. This can be examined by calculating the spectral function for all k-points, for a lattice site at the edge and a lattice site in the middle of the sample. The spectral function at the boundary of a stripe is shown in Fig. 2.9d. Here the spectral function sums over electronic, hole, spin-up and spin-down states. These could also be calculated individually. For non-coplanar spin textures the spectral function can vary from lattice site to lattice site. Therefore, the spectral function in Fig. 2.9d sums also over two rows of atoms, which are closest to the boundary. The spectral function shows, that one of the edge modes from Fig. 2.9b is located at the investigated edge.

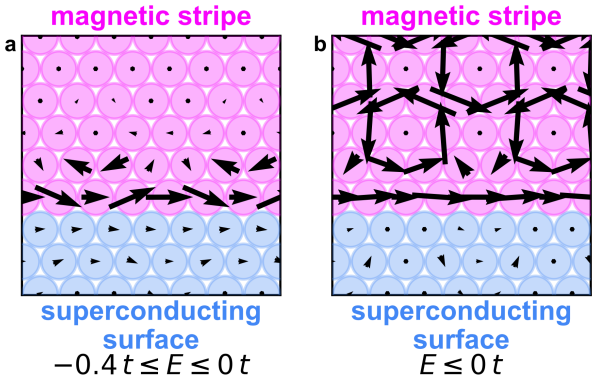

Figure 2.11: Supercurrent at the boundary of a magnetic stripe. The magnetic stripe contains the SkX state (cf. Appendix A.4). Adjacent to the magnetic stripe is a stripe representing an uncovered superconducting surface. In the horizontal direction the stripes are infinitely long. In the vertical direction each stripe has a width of 10 magnetic unit cells. **a** Supercurrent of states in the bulk band gap. **b** Supercurrent of all occupied states. The parameters for the calculation are $t = 1, \alpha = 0, \mu = 1.5, \Delta = 0.7, JS = 3.0$ on the magnetic island and $JS = 0$ on the superconducting surface.

2.2.6 Supercurrent

The current between two lattice sites i and j with spin σ and σ' can be calculated via [83]

$$I_{ij}^{\sigma\sigma'} = -2g_s\frac{e}{\hbar}\int_{-\infty}^{\infty}\frac{\mathrm{d}E}{2\pi}\Re[T_{ij}^{\sigma\sigma'}G^<(i,\sigma;j,\sigma';E)] \quad , \tag{2.60}$$

where g_s is the gyromagnetic ratio, e the electronic charge, $G^<$ is the lesser Greens-function, $T^{\sigma\sigma'}$ is the matrix element for both orbitals, $\Re$ marks the real part and the integration is over the whole energy. The matrix element is either the hopping parameter $T^{\sigma\sigma'} = t$, when $\sigma = \sigma'$ representing the current without a spin flip, or it is the Rashba parameter $T^{\sigma\sigma'} = \alpha$, when $\sigma \neq \sigma'$ representing a spin flip. The current can be calculated for all sites, that are connected by a two-site interaction, such as the hopping term or Rashba-SOC.

Similar to the LDOS the Greens function can be calculated from the solutions of the Hamilton matrix. Further the current can only be evaluated for a certain energy range. Therefore, the current between the lattice sites $\mathbf{r}_i$ and $\mathbf{r}_j$ from states in the energy interval $[E_{\min}, E_{\max}]$ can be written as [158]

$$\mathbf{I}_{ij}^{\sigma\sigma'} = \frac{2eT_{ij}^{\sigma\sigma'}}{\hbar}\Im\left[\sum_{E_{\min}\leq\epsilon_n\leq E_{\max}}\langle i,\sigma'|\Psi_n\rangle\langle\Psi_n|j,\sigma\rangle\right]\frac{\mathbf{r}_i-\mathbf{r}_j}{|\mathbf{r}_i-\mathbf{r}_j|} \quad , \tag{2.61}$$

where $\Im$ marks the imaginary part. The whole current between two lattice sites can be calculated from the contributions of all orbitals. The summation over the spin channels is given by $I_{ij} = \sum_{\sigma\sigma'} I_{ij}^{\sigma\sigma'}$. This now includes currents from the $\uparrow$ and $\downarrow$ orbitals as well as currents with a spin flip. The current I_{ij} has been calculated between two orbitals of the lattice sites i and j and therefore has the direction $\mathbf{I}_{ij} = I_{ij}\frac{\mathbf{r}_i-\mathbf{r}_j}{|\mathbf{r}_i-\mathbf{r}_j|}$. For a better visualization the currents between the lattice site i and all neighboring lattices sites n can be summed via

$$\mathbf{I}_i = \sum_n I_{in}\frac{\mathbf{r}_i-\mathbf{r}_n}{|\mathbf{r}_i-\mathbf{r}_n|} \tag{2.62}$$

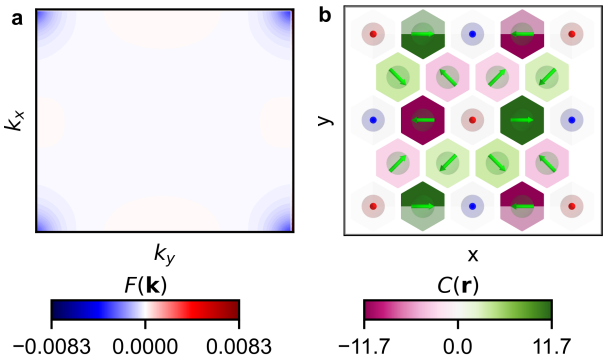

Figure 2.12: Berry curvature and real space Chern marker. **a** Berry curvature of all occupied bands for the SkX state. The integration over the 2D-BZ leads to the Chern number of −1. **b** Real space Chern markers, obtained by projecting the Berry curvature onto the real space orbitals. The spin structure of the SkX state is indicated by colored arrows. The used parameters are $t = 1, \alpha = 0, \mu = 1, \Delta = 0.7, JS = 3$.

to obtain a single current located at the lattice site i. The index n is over all lattice sites, that have a non-vanishing current to or from the lattice site i. In practice, these are all lattice sites with a non-vanishing matrix element $T_{in} \neq 0$.

The supercurrent can be used to investigate the chirality of an edge state. Fig. 2.11 shows the supercurrents for a stripe geometry, where a magnetic stripe is adjacent to a non-magnetic stripe. This could resemble the boundary between an uncovered superconducting surface and a magnetic island. The magnetic stripe contains the SkX state. In Fig. 2.11a the supercurrent for states with an energy $-0.4\,t \leq E \leq 0$ is shown. These states are in the bulk band gap. Therefore, only edge states, which can be located in the bulk band gap, can contribute to the supercurrent. In the row of the magnetic stripe directly at the boundary a current is flowing from the left to the right. In the next row a smaller current is flowing in the opposite direction. In the non-magnetic stripe smaller currents are also flowing from left to right. A few lattice sites away from the edge the currents are neglegibly small, due to the decay of the edge state away from the boundary. Overall a net current is flowing from the left to the right. If the current on the other edge of the stripe flows in the opposite direction, this would showcase a chirality of the edge mode.

Fig. 2.11b shows the supercurrents for all occupied states $E \leq 0$ for the same system. A similar current from left to right exists directly at the boundary. Additionally circular currents exist around some lattice sites. These lattice sites are the centers of atomic-scale skyrmionic structures of the magnetic state. More details about these circular supercurrents can be found in Pub. III.

2.2.7 Chern number

The topological phase of gapped class D superconductors in two dimensions can be described by the Chern number C (cf. Tab. 2.1). The Chern number is an integer value, where zero corresponds to a trivial state. The Chern number depends beside the magnetic texture also on the parameters of the calculation. If the parameters of the calculations are varied, either in time or in space, the Chern number can change. A change in the Chern number reflects a change in the topological phase. This phase transition has to be accompanied by the closing of the band gap (cf. Sec. 2.1). In this work spatial changes of

the magnetic texture are considered. Two domains, which are large enough to develop bulk-like properties, can be in different topological phases, reflected by different Chern numbers. On the boundary between both domains the band gap has to close, resulting in zero energy edge modes, which are protected by topology. This phenomenon is called bulk-boundary correspondence [69, 70].

The Chern number is defined as the integral over the 2D-BZ of the Berry-curvature $F(\mathbf{k})$ as [159]

$$C = \frac{1}{2\pi \mathrm{i}} \int_{\text{2D-BZ}} \mathrm{d}^2 k \, F(\mathbf{k}) \quad . \tag{2.63}$$

As the calculation of the Chern number includes an integration over the 2D-BZ it needs to be calculated from the bulk band structure. The Berry curvature $F(\mathbf{k})$ can be calculated from the Berry connection $\mathbf{A}(\mathbf{k})$ via [159]

$$F(\mathbf{k}) = \frac{\partial A_y(\mathbf{k})}{\partial k_x} - \frac{\partial A_x(\mathbf{k})}{\partial k_y} \quad , \tag{2.64}$$

where the Berry connection depends on the wave function $|\Psi(\mathbf{k})\rangle$ via [159]

$$A_\mu = \langle \Psi(\mathbf{k}) | \frac{\partial}{\partial k_\mu} | \Psi(\mathbf{k}) \rangle \quad (\mu = x, y, z) \quad . \tag{2.65}$$

For large enough islands bulk-like properties can be assumed in the center of the island. Therefore, the Chern number allows to predict the existence of topologically protected edge states. In principle the Chern number can be calculated for each band individually, but when two bands cross or are close, the compound Chern number for both bands has to be calculated [160]. As the contributions from individual bands are not of interest and in general many bands cross in a band structure it is most handy to calculate the compound Chern number of all occupied bands. The Chern number of all unoccupied bands would thereby give the exact opposite value due to the particle-hole symmetry. In a numerical calculation the BZ integration will be substituted by a summation over k-points for which the Schrödinger equation is solved. The BdG Hamiltonian has a freedom of gauge due to the U(1) symmetry [161], resulting in possibly different gauges for each k-point of the simulation. This is a challenge for the numerical calculation of the Chern number. The Chern number is not gauge dependent, but the gauge needs to be the same over the whole BZ, which is easy to achieve for analytical solutions, but can be challenging for numerical calculations. If the gauge is constant over the BZ, the Chern number can be calculated with a small amount of k-points as described in Ref. [159]. Otherwise, the projector approach can be used, which is gauge independent. The projector can be calculated from all eigenfunctions of the Hamilton matrix $|\Psi_\mathbf{k}\rangle$ by

$$\mathbf{P}_\mathbf{k} = \sum_{E_\mathbf{k} < E_\mathrm{F}} |\Psi_\mathbf{k}\rangle\langle\Psi_\mathbf{k}| \quad , \tag{2.66}$$

where the summation is over all states $E_{\mathbf{k}}$ below the Fermi energy E_{F}, meaning all occupied states. Note that at the Fermi energy no states exist due to the band gap, leading to $E_{\mathbf{k}} < E_{\mathrm{F}}$ instead $E_{\mathbf{k}} \leq E_F$. Using this projector the Chern number can be calculated as

$$C = \frac{1}{2\pi \mathrm{i}} \int_{BZ} \mathrm{d}^2 k \mathrm{Tr}(P_{\mathbf{k}}[\partial_{k_x} P_{\mathbf{k}}, \partial_{k_y} P_{\mathbf{k}}]) \quad . \tag{2.67}$$

For the numerical calculation the derivatives of the projector can be estimated by the finite difference, e.g.

$$\partial_{k_x} \mathbf{P}_{\mathbf{k}} = \frac{1}{\delta \mathbf{k}_x} \left[\mathbf{P}_{\mathbf{k}+\delta \mathbf{k}_\mathbf{x}} - \mathbf{P}_{\mathbf{k}} \right] = \frac{1}{\delta \mathbf{k}_x} \sum_{E_k < E_F} |\Psi_{\mathbf{k}+\delta \mathbf{k}_\mathbf{x}}\rangle\langle\Psi_{\mathbf{k}+\delta \mathbf{k}_\mathbf{x}}| - |\Psi_{\mathbf{k}}\rangle\langle\Psi_{\mathbf{k}}| \quad . \tag{2.68}$$

Here $\delta \mathbf{k}_x$ is a small displacement along $\mathbf{k}_x$. Also finite difference schemes of higher order could be used to improve the accuracy. In general a large number of k-points has to be used to approximate the integration over the BZ. Especially when the bandgap is small at a certain point of the BZ, the Berry-curvature often has a large contribution localized at this point of the smallest band gap. This makes an even finer sampling of the k-points necessary. One can avoid regions in the parameter space with small band gaps. As the Chern number cannot change as long as the bang gap does not close, the Chern number can be calculated in a region of the parameter space, where the Berry curvature is relatively homogeneous. The Chern number stays constant for all parameter transformations, where the band gap does not close. If one uses this approach a very good knowledge over the closing of the band gap is necessary, which could be easier to obtain than calculating the Chern number directly for a small band gap. In general the convergence of the Chern number with the number of k-points needs to be tested. The Chern numbers for the 3Q state have for example been calculated on a (1000×1000) mesh of k-points.

Fig. 2.12a shows the Berry curvature for a $C = -1$ phase. The parameters are chosen in a way, that the system is close to a phase transition and the bandgap is relatively small. Comparably large contributions exist in the corners of the BZ, where also the band gap is the smallest. The Chern number can also be projected on the lattice positions in real space [83, 89, 162]

$$C(\mathbf{r}) = \frac{L_1 L_2}{2\pi \mathrm{i}} \int_{BZ} \mathrm{d}^2 k \sum_{\tau,\sigma} \langle \mathbf{r}, \tau, \sigma | P_{\mathbf{k}}[\partial_{k_x} P_{\mathbf{k}}, \partial_{k_y} P_{\mathbf{k}}] | \mathbf{r}, \tau, \sigma \rangle \quad . \tag{2.69}$$

Here the sum is over electronic and hole states τ as well as over both spin channels σ. The state $|\mathbf{r}, \tau, \sigma\rangle$ represents an orbital at lattice site $\mathbf{r}$, with electron or hole character τ and spin σ. In the here used tight-binding approach this will be a vector with one entry equal to 1 and all other entries zero. This projection gives a real space representation of the Chern number at a lattice site $\mathbf{r}$. The sum of $C(\mathbf{r})$ over all lattice sites is again the Chern number of the system. The real space projection of the Berry curvature from Fig. 2.12a is shown in Fig. 2.12b. The spin structure of the SkX state is marked by colored arrows and the

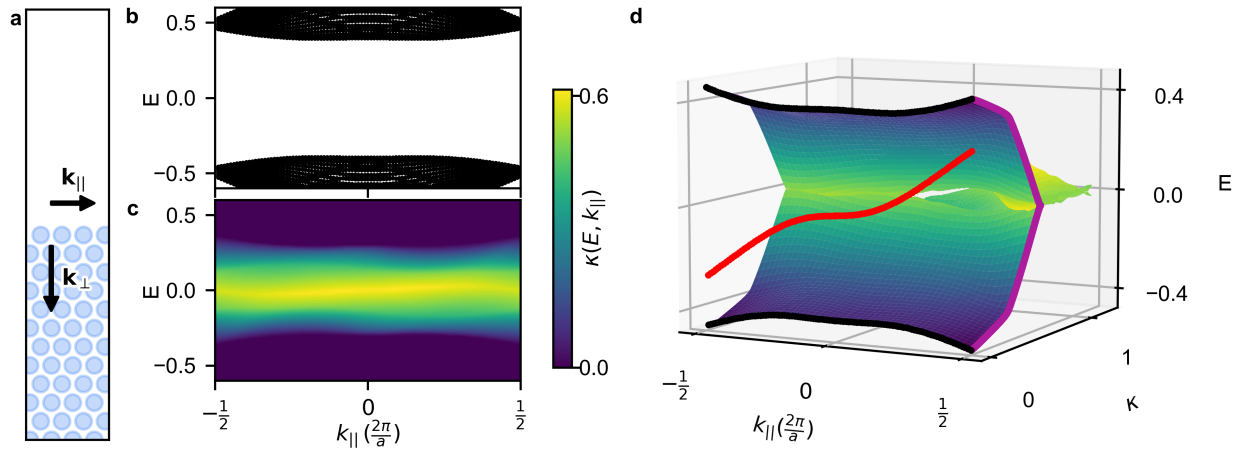

Figure 2.13: Complex band structure for the SkX state. **a** Propagation directions of $\mathbf{k}_{||}$ and $\mathbf{k}_{\perp}$. **b** Bulk band structure of the SkX state projected on the $k_{||}$ direction of a stripe. **c** Decay constants $\kappa(\mathbf{k}_{||}, E)$ for surface states. **d** Energies in dependency of $\mathbf{k}_{||}$ and κ. The bulk bands, closest to the Fermi energy are marked in black. The purple line displays the decay constants for $\mathbf{k}_{||} = \frac{\pi}{a}$. The red line represents an edge mode for the stripe geometry (cf. Fig. 2.9b).

magnetic unit cell is highlighted. The contribution of the real space Chern marker varies over the lattice.

2.2.8 Complex band structure

The complex band structure allows to calculate how edge states decay into the bulk [163]. The wavefunction for two symmetry equivalent lattice sites varies by a complex phase $e^{i\theta}$. This complex phase can be written as $e^{i\mathbf{k}\cdot\mathbf{r}}$, where $\mathbf{k}$ is a reciprocal vector and $\mathbf{r}$ the real space distance between both lattice sites. According to the Bloch theorem [164] the wavefunction can be written as

$$\Psi_{\mathbf{k}}(\mathbf{r}) = e^{i\mathbf{k}\cdot\mathbf{r}} u(\mathbf{r}) \quad , \tag{2.70}$$

where $u(\mathbf{r})$ has the periodicity of the lattice. When the Schrödinger equation

$$\hat{H}(\mathbf{k})\Psi_{\mathbf{k}} = E(\mathbf{k})\Psi_{\mathbf{k}} \tag{2.71}$$

is solved, the band structure is obtained. States can only exist in the energy bands $E(\mathbf{k})$. These states can propagate through the whole bulk. If a state exists outside of the bulk band structure, e.g. due to a defect, a surface or some interface to a different material, this state is exponentially decaying into the bulk.
This behavior is described by a complex contribution to $\mathbf{k}$ [165, 166]. When a generally complex valued $\mathbf{k}$ is assumed, it can be written as $\mathbf{k} = \mathbf{k}_{Re} + \mathbf{k}_{Im}$, where $\mathbf{k}_{Re}$ marks the real part and $\mathbf{k}_{Im}$ the imaginary part. With this Eq. (2.70) becomes

$$\Psi_{\mathbf{k}}(\mathbf{r}) = \left(e^{i\mathbf{k}_{Re}\cdot\mathbf{r}} \cdot e^{i\mathbf{k}_{Im}\cdot\mathbf{r}}\right) u(\mathbf{r}) \quad . \tag{2.72}$$

If one further writes the imaginary part as $\mathbf{k}_{Im} = \mathrm{i}\boldsymbol{\kappa}$, where i is the imaginary number and $\boldsymbol{\kappa}$ is real, the wavefunction can be written as a periodic and a decaying part as

$$\Psi_{\mathbf{k}}(\mathbf{r}) = \left(\underbrace{\mathrm{e}^{\mathrm{i}\mathbf{k}_{Re}\cdot\mathbf{r}}}_{\text{periodic}} \cdot \underbrace{\mathrm{e}^{-\boldsymbol{\kappa}\cdot\mathbf{r}}}_{\text{decaying}} \right) u(\mathbf{r}) \quad . \tag{2.73}$$

In general no restrictions exist for $\mathbf{k}_{Re}$ and $\boldsymbol{\kappa}$. A surface or interface has a periodic direction $\mathbf{a}_{\parallel}$ parallel to the interface and a non-periodic direction $\mathbf{a}_{\perp}$ perpendicular to the interface, as sketched in Fig. 2.13a. Further away from the surface, the band structure in the periodic direction $\mathbf{k}_{\parallel}$ corresponds to the bulk band structure, projected onto the $\mathbf{k}_{\parallel}$-direction. For the SkX state this projected band structure is shown in Fig. 2.13b, which exhibits a superconducting band gap around the Fermi energy. In the bulk-like region, away from the surface, states can only exist in these energy bands. At the surface, where the sample is not bulk-like, states can also exist in the gaps between the energy bands. Most interesting in the context of this work are states in the superconducting band gap, but states can occur between all bands. However, these states have to decay exponentially into the bulk-like region. The decay of these states can be calculated from the bulk band structure. Here it is useful to use a supercell, containing several magnetic unit cells, perpendicular to the surface. The size of the supercell should be chosen in a way, that the states are dispersion-less in the $\mathbf{k}_{\perp}$ direction, i.e. all energy band are flat in this direction. Periodic boundary conditions are applied in all directions, but the band structure has only to be calculated along $\mathbf{k}_{\parallel}$. The bands closest to the Fermi energy of Fig. 2.13b are shown in black in Fig. 2.13d. For each $\mathbf{k}_{\parallel}$ one can now also introduce a $\boldsymbol{\kappa} \perp \mathbf{k}_{\parallel}$, which describes the decay perpendicular the propagation direction, where $\kappa = |\boldsymbol{\kappa}|$ is the norm of $\boldsymbol{\kappa}$. The energies can be calculated via the Schrödinger equation

$$\hat{H}(\mathbf{k}_{\parallel}, \kappa)\Psi_{\mathbf{k}_{\parallel},\kappa} = E(\mathbf{k}_{\parallel}, \kappa)\Psi_{\mathbf{k}_{\parallel},\kappa} \quad . \tag{2.74}$$

For each $\mathbf{k}_{\parallel}$ the energy can be calculated for various κ. This is marked by a colored surface in Fig. 2.13d. The color corresponds to the value of κ. The two bulk bands, which are closest to the Fermi energy are shown as black lines. The energies of these bands are the solutions for $\kappa = 0$, which means they are not decaying. Energies slightly closer to the Fermi energy are solutions for a small non-zero κ. As an example the dispersion for $\mathbf{k}_{\parallel} = \frac{\pi}{a}$ is highlighted in purple. The smaller the energy is, the larger is the corresponding κ. For this example surface states closer to the Fermi energy have to decay faster into the bulk than surface states, which are close in energy to the bulk states. These decay parameters are calculated from the bulk band structure and universal for all possible occurring states. As an example one of the edge modes is marked in red, which arises in a SkX stripe (cf. Fig. 2.9b). All energies of the edge mode exist only for $\kappa \neq 0$, which showcases, that this

mode has to decay into the bulk. Thereby the edge mode does not have a universal decay constant, but it can vary for each $\mathbf{k}_{\parallel}$.
Now the function $E(\mathbf{k}_{\parallel}, \kappa)$ can be inverted to obtain $\kappa(\mathbf{k}_{\parallel}, E)$. This function now gives the decay constant κ for each energy E and parallel wave vector $\mathbf{k}_{\parallel}$. The analytical determination of $\kappa(E, \mathbf{k}_{\parallel})$ can be challenging, although different approaches exist [167]. In this work a numerical approach was used. Therefore, the energies $E(\kappa, \mathbf{k}_{\parallel})$ have to be calculated for one $\mathbf{k}_{\parallel}$ and a varying κ, where the sampling size of the κ has to be very fine and in an interval such that the energies in the range of interest are solutions of the Schrödinger equation. The actual range, that has to be calculated, can vary between systems. A good step size $\Delta\kappa$ can be determined by convergence tests.
The values for $\kappa(\mathbf{k}_{\parallel}, E)$ are displayed in Fig. 2.13c. The darkest areas correspond to the bulk energy bands. The value of κ now shows, how each state is decaying into the bulk.

2.3 Density functional theory

DFT is an ab-initio method, meaning that the calculations are based on the fundamental interaction of the system and no external parameters have to be given [168]. [2] Traditional methods of solving many-body Hamiltonians, like Hartree-Fock [169], are computationally costly due to the number of particles. DFT uses thereby the electronic density of a system together with effective single-particle orbitals, which allows for a self-consistent calculation of the ground state electronic density and all involved properties like the total energy or local magnetic moments. This approach reduces the computational cost dramatically, which allows for calculations of larger systems sizes.
In this chapter a short overview over the conceptual basics of DFT is given and the basis sets for the wave functions of the two used codes, `FLEUR` and `VASP`, are shortly described. For a more detailed description of the DFT method Ref. [170–172] are recommended.

2.3.1 General framework

The Hamiltonian of a condensed matter system contains the kinetic energy of electrons T_e and of the atomic nucleus T_n as well as interactions between electrons V_{e-e}, between electrons and the nucleus V_{e-n} and between the nuclei V_{n-n}. The Hamilton operator is given by

$$\hat{H} = \hat{T}_e + \hat{T}_n + \hat{V}_{e-e} + \hat{V}_{e-n} + \hat{V}_{n-n} \quad . \tag{2.75}$$

The Born-Oppenheimer-approximation [173] utilizes that the nuclei have a larger mass and assumes that the electrons follow the movement of the nuclei adiabatic. When the kinetic energy of the cores is approximated as zero, the interactions between the cores becomes a constant, which is neglected. Using this approximations Eq. (2.75) becomes

$$\hat{H} = \hat{T}_e + \hat{V}_{e-e} + \hat{V}_e(\mathbf{r}) \quad , \tag{2.76}$$

where $\hat{V}_e(\mathbf{r})$ describes the potential of the nuclei, in which the electrons are moving. For this Hamiltonian the wavefunction can be calculated by solving the stationary Schrödinger equation. Despite the Born-Oppenheimer approximation the computational effort is still not feasible for larger systems. The theorems of Hohenberg and Kohn [174] allow to describe a system in dependency of the electronic density instead of the wavefunction. The theorems state:

1. Two Potentials, which differ by more than a constant cannot map on the same density. Therefore, the potential is uniquely defined by the density. [174]

$$E_0 = E_0[n] \tag{2.77}$$

[2] Although DFT uses an exchange-correlation (XC)-functional which is in many cases obtained by other methods like quantum monte-carlo calculations, it is still widely considered as an ab-initio method. This can be justified as the XC-functional is not unique to a specific system.

2. The ground state electron density n_0 minimizes the Energy [174].

$$E_{V_0}[n] \geq E_{V_0}[n_0] \tag{2.78}$$

Due to this theorems the energy can be written in dependency of the electronic density of the many-body system, which can be calculated from the wavefunctions via

$$n(\mathbf{r}) = N \int ... \int |\Psi(\mathbf{r}, \mathbf{r}_,..., \mathbf{r}_N)|^2 \mathrm{d}\mathbf{r}_2 ... \mathrm{d}\mathbf{r}_N \quad , \tag{2.79}$$

where N is the total number of electrons. Further it has been shown by Kohn and Sham [175] that a single-body wavefunction with an effective potential can lead to the same ground state density as the many body system.
The total energy of the many body system can be written as

$$E[n] = \langle \hat{T} \rangle + \langle \hat{W} \rangle + V[n] \quad , \tag{2.80}$$

where $\langle \hat{T} \rangle$ is the kinetic energy of the interacting many body system, $\langle \hat{W} \rangle$ the interactions between the electrons and $V[n]$ the external potential given by the nuclei. An exchange-correlation (XC) functional

$$E_{XC}[n] = \langle \hat{T} \rangle - T_S[n] + \langle \hat{W} \rangle - V_H[n] \tag{2.81}$$

can be defined by the difference of the many body kinetic energy $\langle \hat{T} \rangle$ and the single body kinetic energy $T_S[n]$ and the difference between the many body interaction $\langle \hat{W} \rangle$ and the Hartree-energy $V_H[n]$. The Hartree energy is given by

$$V_{\mathrm{H}}[n] = \frac{1}{2} \int \int \frac{n(\mathbf{r}) n(\mathbf{r}')}{|\mathbf{r} - \mathbf{r}'|} \mathrm{d}\mathbf{r} \mathrm{d}\mathbf{r}' \, . \tag{2.82}$$

This new defined $E_{XC}[n]$ contains the exchange and correlation effects of the many body system, which are not contained in the single-body Kohn-Sham equations. Now Eq. (2.80) be written as

$$E[n] = T_S[n] + V_H[n] + V[n] + E_{XC}[n] \quad . \tag{2.83}$$

The density can now be calculated from the single particle wavefunctions φ_i as

$$n(\mathbf{r}) = \sum_i |\varphi_i(\mathbf{r})|^2 \mathrm{d}\mathbf{r} \quad . \tag{2.84}$$

The conservation of the particle number requires the normalization of the single-particle wavefunction $\int |\varphi_i(\mathbf{r})|^2 = 1$. This leads to the Kohn-Sham equations

$$-\frac{1}{2} \nabla^2 \varphi_i + V_{\mathrm{eff}} \varphi_i = \epsilon_i \varphi_i \tag{2.85}$$

with the Lagrange parameters ϵ_i and the effective potential

$$V_{\text{eff}} = V_{\text{ext}} + V_{\text{H}} + V_{\text{XC}} \quad , \tag{2.86}$$

where

$$V_{\text{XC}} = \frac{\delta E_{\text{XC}}[n(\mathbf{r})]}{\delta n(\mathbf{r})} \quad . \tag{2.87}$$

This equation has the form of a single-particle Schrödinger equation, which has the same ground state density as the many-body problem. The Kohn-Sham equations form a self-consistency problem with the electronic density and the wavefunction. The density can be calculated from the wavefunction, which can be calculated from the Schrödinger equation, where the potential depends on the density. This problem can iteratively be solved. One makes a first guess about the density, calculates the wavefunction via Eq. (2.85) and a new density with Eq. (2.84). Then both densities are mixed and the procedure is repeated until a convergence is achieved. Different mixing algorithms are discussed in Ref. [176].

Besides the ground state density, other parameters like the eigen energies of the Kohn-Sham system ϵ_i can not be directly connected to the many-body system. However many investigations show, that the Kohn-Sham band structure can provide some understanding of the physical many body system, although this is formally not given.

The total energy of the system can accurately be described, when some correction term to the sum of Kohn-Sham eigenvalues are added [177]. The sum over all eigenenergies of the Kohn-Sham system is

$$\sum_i \epsilon_i = T_{\text{S}}[n] + \int n(\mathbf{r}) v(\mathbf{r}) \mathrm{d}\mathbf{r} + 2V_{\text{H}}[n] + \int v_{\text{XC}}(\mathbf{r}) n(\mathbf{r}) \mathrm{d}\mathbf{r} \,, \tag{2.88}$$

while the total energy of the many-body system is

$$E_{\text{total}} = T_{\text{S}}[n] + \int n(\mathbf{r}) V(\mathbf{r}) \mathrm{d}\mathbf{r} + V_{\text{H}}[n] + E_{\text{XC}}[n] \,. \tag{2.89}$$

By comparing both equations one can write the total energy of the many-body system in terms of the sum of eigenvalues of the Kohn-Sham system plus some additional terms

$$E_{\text{total}} = \sum_i^N \epsilon_i - V_{\text{H}}[n] + E_{\text{XC}} - \int n(\mathbf{r}) V_{\text{XC}}(\mathbf{r}) \mathrm{d}\mathbf{r} \quad . \tag{2.90}$$

For periodic system the sum over all lattice site can be replaced by an integration over the first BZ

$$\sum_i \epsilon_i \rightarrow \sum_j \frac{V}{(2\pi)^3} \int_{BZ} d^3\mathbf{k} \epsilon_j(\mathbf{k}) \,, \tag{2.91}$$

where j is the band index. In numerical calculations the Kohn-Sham equations can only be solved for discrete k-points $\mathbf{k}_\nu$. To approximate the integration over the BZ a mesh of discrete k-points is created and the integrations is substituted by a sum

$$\sum_j \frac{V}{(2\pi)^3} \int_{BZ} d^3\mathbf{k} \epsilon_j(\mathbf{k}) \to \sum_j \sum_{\mathbf{k}_\nu} \epsilon_j(\mathbf{k}_\nu) \quad . \tag{2.92}$$

Due to the symmetries of the lattice some k-points might be symmetry equivalent. Here only one of these k-points has to be calculated and additionally weighted with the number of equivalent k-points. The so-called irreducible part of the BZ is formed by all k-points that cannot be transformed into each other by symmetry operations.

So far the XC-functional E_{XC} was assumed to be known. If this is the case, the Kohn-Sham equations lead to the exact ground state density of the many body system. In reality this functional is not known and approximations have to be made. This still can lead to very good approximations of the density, since the single particle kinetic energy and the Hartree energy are usually larger than the correlation and exchange contributions. The two XC-functionals used in this thesis are presented in Sec. 2.3.5.

2.3.2 Magnetization in DFT

For a magnetic system the Hohenberg-Kohn theorem can be expanded to

$$E[n(\mathbf{r}), \mathbf{m}(\mathbf{r})] \geq E[n_0(\mathbf{r}), \mathbf{m}_0(\mathbf{r})] \quad , \tag{2.93}$$

where $\mathbf{m}$ and $\mathbf{m}_0(\mathbf{r})$ are the magnetization and ground state magnetization, respectively [176]. Alternatively the energy functional can be written in dependency of the density matrix

$$\boldsymbol{\rho} = \frac{1}{2} n \mathbb{1}_{2\times2} + \boldsymbol{\sigma}\mathbf{m} = \frac{1}{2} \begin{pmatrix} n + m_z & m_x - \mathrm{i}m_y \\ m_x + \mathrm{i}m_y & n - m_z \end{pmatrix} \quad , \tag{2.94}$$

where $\mathbb{1}_{2\times2}$ is the unity matrix and $\boldsymbol{\sigma}$ is a vector containing the Pauli spin matrices (for the matrices see Appendix A.1). In the same fashion a potential matrix

$$\mathbf{V} = V_{eff}\mathbb{1}_{2\times2} + \mu_{\mathrm{B}}\boldsymbol{\sigma}\cdot\mathbf{B} = \begin{pmatrix} V_{eff} + \mu_{\mathrm{B}}B_z & \mu_{\mathrm{B}}(B_x - \mathrm{i}B_y) \\ \mu_{\mathrm{B}}(B_x + \mathrm{i}B_y) & V_{eff} - \mu_{\mathrm{B}}B_z \end{pmatrix} \tag{2.95}$$

can be defined, where V_{eff} is given by Eq. (2.86). The magnetic field is given by the sum of the external field $\mathbf{B}_{ext}(\mathbf{r})$ and the exchange-correlation field $\mathbf{B}_{xc}(\mathbf{r})$, which is defined by [176]

$$\mathbf{B}_{xc}(\mathbf{r}) = \frac{\delta E_{xc}[n(\mathbf{r}), \mathbf{m}(\mathbf{r})]}{\delta \mathbf{m}(\mathbf{r})} \, . \tag{2.96}$$

With the potential matrix the Kohn-Sham equation can be written as [178]

$$\left\{-\frac{\hbar^2}{2m}\nabla^2\mathbb{1}_{2\times2} + \mathbf{V}\right\}\Psi_i\mathbf{r} = \epsilon_i\Psi_i(\mathbf{r}) \quad . \tag{2.97}$$

Here the wavefunction is a spinor of the form

$$\Psi_i(\mathbf{r}) = \begin{pmatrix} \Psi_{\uparrow,i}(\mathbf{r}) \\ \Psi_{\downarrow,i}(\mathbf{r}) \end{pmatrix} \quad . \tag{2.98}$$

By solving this spin dependent Kohn-Sham equation the ground state density and magnetization density can be obtained. The density and magnetization can be calculated by

$$n(\mathbf{r}) = \sum_{i=1}^{N} \Psi_i^\dagger(\mathbf{r})\Psi_i(\mathbf{r}) \quad \text{and} \quad \mathbf{m}(\mathbf{r}) = \sum_{i=1}^{N} \Psi_i^\dagger\boldsymbol{\sigma}(\mathbf{r})\Psi_i(\mathbf{r}) \quad . \tag{2.99}$$

The entries of the density matrix are

$$\rho_{\alpha\beta} = \sum_{i=1}^{N} \Psi_{i\alpha}^\dagger(\mathbf{r})\Psi_{i\beta}(\mathbf{r}) \quad \text{with} \quad \alpha,\beta \in 1,2 \quad . \tag{2.100}$$

In the here investigated system the magnetization is mostly localized in the vicinity of the nuclei. A local magnetic moment can be defined as

$$\mathbf{m}_i = \int_{\Omega_i} \mathbf{m}(\mathbf{r})\mathrm{d}\mathbf{r} \quad , \tag{2.101}$$

where Ω_i is the volume of the sphere around lattice site i. In general, the magnetization can be non-collinear. For collinear states, in the absence of SOC, the magnetization always can be aligned with the z-direction, which makes Eq. (2.95) a diagonal matrix in spin space. This allows to solve the Kohn-Sham equation for each spin channel independent, which reduces the computational cost significantly. Instead of finding the magnetization of minimal energy via Eq. (2.97), the magnetic moments at the lattice sites can be constrained in the direction. This allows to calculate the total energy for specific spin structures and parameterize an atomistic spin model.

2.3.3 Spin spirals

Often spin spirals are used to calculate magnetic interactions and parameterize an atomistic model [176]. In a spin spiral the magnetic moment is tilted from lattice site to lattice site by a fixed angle. In Fig. 2.14 a flat spin spiral, which is rotating in the xy-plane is shown. A conical spin spiral would rotate on the surface of a cone. For a spin spiral, rotating around

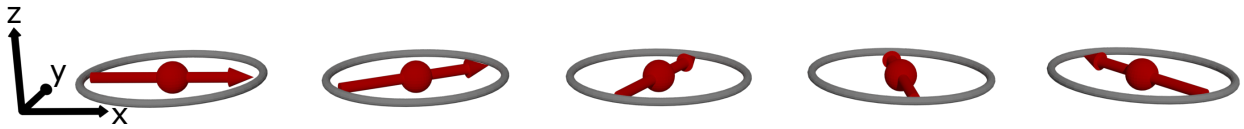

Figure 2.14: Flat spin spiral. The local magnetic moment is rotated by a fixed angle from lattice site to lattice site. The opening angle is $\theta = 90°$, the rational axis is the z-direction an the spin spiral is propagating along the x-direction.

the z-axis, the magnetization direction at lattice site i can be written by

$$\mathbf{S}_i = \begin{pmatrix} \cos(\varphi_i)\sin(\theta) \\ \sin(\varphi_i)\sin(\theta) \\ \cos(\theta) \end{pmatrix} \quad , \tag{2.102}$$

where θ is the opening angle and the angle φ_i is defined by the position $\mathbf{r}_i$ and a reciprocal lattice vector $\mathbf{q}$ by $\varphi_i = \mathbf{q} \cdot \mathbf{r}_i$. To use a different rotation axis, a global rotation can be applied to all magnetic moments. The reciprocal vector $\mathbf{q}$ defines the propagation direction of the spin spiral and the wavelength $\lambda = \frac{2\pi}{|\mathbf{q}|}$. Since $\mathbf{q}$ is a reciprocal lattice vector it can be described as a point in the BZ, where the high-symmetry points correspond to special spin spiral states. For a hexagonal lattice the BZ is shown in Fig. 2.15a. The $\overline{\Gamma}$ point represents the ferromagnetic state (Fig. 2.15b), the $\overline{\mathrm{M}}$-point the row-wise antiferromagnet (RW-AFM) state (Fig. 2.15c) and the $\overline{\mathrm{K}}$-point the Néel state (Fig. 2.15d). When the total energy is calculated for several spin spirals an atomistic spin model can be parameterized by a fit to these data. Although spin spirals, especially for small values of $|\mathbf{q}|$, can have large magnetic unit cells, the calculations can be performed in the chemical unit cell, as long as SOC is neglected. In this case an extension of the Bloch theorem in spin space can be used. The Bloch theorem states, that the wavefunction in a periodic lattice can be written as [164]

$$\Psi_{\mathbf{k}}(\mathbf{r}) = \mathrm{e}^{\mathrm{i}\mathbf{k}\cdot\mathbf{r}} u_{\mathbf{k}}(\mathbf{r}) \tag{2.103}$$

, where $u(\mathbf{r})$ is a function with the same periodicity as the lattice. The wavefunction of both spin channels can be written as a spinor and the Bloch theorem can be generalized to [176]

$$\begin{pmatrix} \Psi^{\uparrow}_{\mathbf{k}}(\mathbf{r}) \\ \Psi^{\downarrow}_{\mathbf{k}}(\mathbf{r}) \end{pmatrix} = \mathrm{e}^{\mathrm{i}\mathbf{k}\cdot\mathbf{r}} \begin{pmatrix} \mathrm{e}^{+\mathrm{i}\frac{\mathbf{q}\cdot\mathbf{r}}{2}} u^{\uparrow}_{\mathbf{k}}(\mathbf{r}) \\ \mathrm{e}^{-\mathrm{i}\frac{\mathbf{q}\cdot\mathbf{r}}{2}} u^{\downarrow}_{\mathbf{k}}(\mathbf{r}) \end{pmatrix} \quad . \tag{2.104}$$

Here the spin-up and the spin-down channel have a different phase, which represents a rotation of magnetic moments. This description of spin spirals can only be used, when the energy is invariant under the global rotation of all spins, meaning in the absence of SOC. The SOC contribution can be calculated in perturbation theory. Note, that in the first order perturbation theory the Dzyaloshinskii-Moriya interaction (DMI) is contained, but e.g. the magnetocrystalline anisotropy energy (MAE) and anisotropic symmetric exchange (ASE) occur only in higher orders.

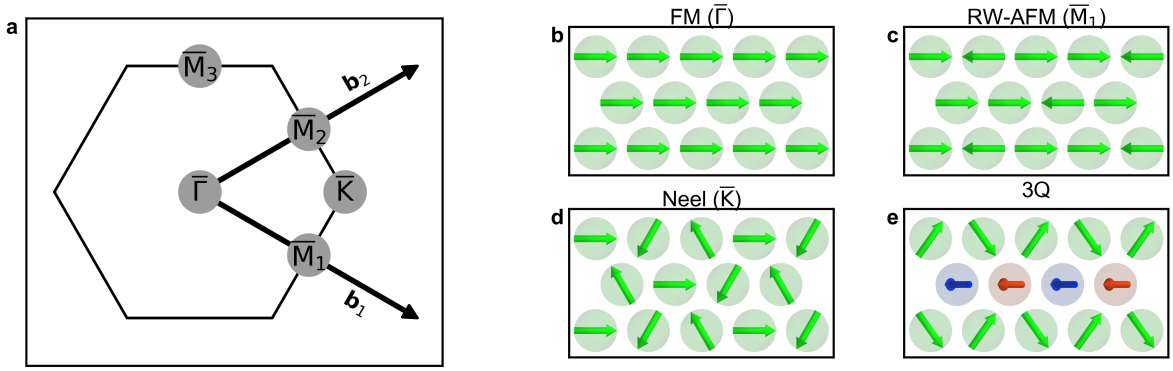

Figure 2.15: Spin spirals on a hexagonal lattice. **a** 2D-BZ of a hexagonal lattice, where the high-symmetry points and the reciprocal lattice vectors are marked. **b** Ferromagnetic state represented by the $\overline{\Gamma}$ point. **c** Row-vise antiferromagnetic state represented by the $\overline{M}_1$ point. **d** Neél state represented by the $\overline{K}$ point. **e** 3Q state, constructed by a superposition of the $\overline{M}_1$, $\overline{M}_2$ and $\overline{M}_3$ point. The green color represents magnetic moments which are oriented in a plane parallel to the surface, the red (blue) color indicates an outward (inward) orientation

Spin spirals sometimes are referred to as 1Q states, as they can be described by a single **q** value. For so-called multi-Q states a superposition of more than one spin spirals is created. For example the 3Q state is a superposition of three RW-AFM states represented by $\overline{M}$-points [179]. This 3Q or triple-Q state is shown in Fig. 2.15e.

2.3.4 Scalar-relativistic Hamiltonian and SOC contributions

Relativistic effects can be included in DFT calculations by using the relativistic Dirac equation instead of the non-relativistic Schrödinger equation. This is in detail discussed in Ref. [60, 176]. However the relativistic spin-orbit term couples spatial and spin coordinates and makes the calculation therefore much more demanding. A computationally more efficient approach is to use the so-called scalar-relativistic approximation [180]. Here all relativistic terms except the spin-orbit coupling (SOC) are included. The total Hamiltonian is therefore given by the sum of the scalar relativistic $\hat{H}_{\mathrm{SC}}$ and SOC Hamiltonian $\hat{H}_{\mathrm{SOC}}$

$$\hat{H}_{\mathrm{total}} = \hat{H}_{\mathrm{SR}} + \hat{H}_{\mathrm{SOC}} \tag{2.105}$$

The SOC contribution can approximately be written as [176]

$$H_{\mathrm{SOC}} = \zeta(r)\mathbf{L}\cdot\mathbf{S} \quad , \tag{2.106}$$

where $\zeta(r)$ is the SOC constant dependent on the distance to the nucleus r.
When the charge density is calculated with the scalar-relativistic approximations, the effect of SOC can be calculated in an additional step. As the energy contribution of SOC compared to all other contributions is small it is nearly always useful to first calculate the self-consistent charge density for the scalar relativistic approximation and to calculate the

effect of SOC based on these. To calculate the effect of SOC based on a converged charge density there are mainly three different approaches. In the so-called force theorem [181, 182] the SOC contribution is calculated based on the wavefunctions of the scalar-relativistic charge density in a single iteration. The SOC contribution is given by the difference in the sum of the Kohn-Sham eigenvalues. Alternatively the SOC contribution also can be calculated self-consistently, by including the corresponding term in the Hamiltonian. This approach is computationally more demanding, but also leads to more accurate results. For spin spirals, which can be calculated in the chemical unit cell, the SOC contribution can be calculated using first order perturbation theory without the need for a large unit cell [183]. Self-consistent calculations of the SOC for spin spirals are only possible for spin spirals with a relative short period. But even for magnetic supercells containing a few chemical unit cells is the computational effort drastically increased. Due to this the perturbation theory is the most widely used approach for spin spirals. Note, that contributions like the MAE and ASE do not occur in first order perturbation theory. Within the used atomistic spin model only the DMI appears in first order perturbation theory. In this work the perturbation theory approach was used for spin spirals and the self-consistent calculation for all other states.

2.3.5 Exchange correlation functional

The exchange-correlation (XC) functional contains by definition all interactions of the many body system, that can not be described by single-body orbitals (cf. Eq. (2.81)). So far it has been assumed, that the XC functional is known, leading to an exact description of the ground state density. But in general the XC functional is not know. Different approaches exist to make accurate approximations. Which approximation is used depends also on the investigated system and properties.
A variety of different approximations exist, where in many cases certain XC-functionals reflect some properties of the system better than others. For this reason the choice of the functional often depends on the type of system and on the quantities, that are computed. In the scope of this thesis the local density approximation (LDA) XC-functional VWN [184] and the generalized gradient approximation (GGA) functional PBE [185] were used.
The LDA approximates the density locally as the density of a homogeneous electron gas [175]. The XC-functional has the form

$$E_{XC}^{LDA}[n] = \int \mathrm{d}^3 r\, n(\mathbf{r}) \epsilon_{XC}^{hom}(n(\mathbf{r})) \tag{2.107}$$

, where $\epsilon_{XC}^{hom}(n(\mathbf{r})$ is the energy density of a homogeneous system. This concept can be expanded to the local spin density approximation (LSDA) to describe spin-polarized systems as

$$E_{XC}^{LSDA}[n, |\mathbf{m}(\mathbf{r})|] = \int \mathrm{d}^3 r\, n(\mathbf{r}) \epsilon_{XC}^{hom}(n(\mathbf{r}), |\mathbf{m}(\mathbf{r})|) \quad . \tag{2.108}$$

Due to the local definition of ϵ_{XC}^{hom} it depends only on the magnitude of the magnetization. In this work a LSDA functional in the parametrization from Vosko, Wilk and Nusair [184] based on Quantum-Monte-Carlo simulations by Ceperley and Alder [186] is used for most of the calculations.
For geometric relaxations a GGA XC-functional in the parametrization of Perdew, Burke and Ernzerhof [185] were used. Here also the gradient of the electronic density $\nabla n(\mathbf{r})$ is included for the energy density $\epsilon_{XC}^{GGA}(n(\mathbf{r}), |\nabla n(\mathbf{r})|)$ leading to

$$E_{XC}^{GGA}[n] = \int \mathrm{d}^3 r \, n(\mathbf{r}) \epsilon_{XC}^{GGA}(n(\mathbf{r}), |\nabla n(\mathbf{r})|) \quad . \tag{2.109}$$

This combination has shown to give often a good agreement with experimental results.

2.3.6 Basis of wavefunctions

For a numerical calculation the wavefunction has to be expanded in a some basis functions. The basis sets which are implemented in the `FLEUR` and `VASP` code are shortly introduced here.

FLAPW

In `FLEUR` [187, 188] the full-potential linearized augmented plane wave (FLAPW) method is used [189, 190]. The sample is divided into different regions, as sketched in Fig. 2.16. One region is the vicinity of the nuclei, which is called the muffin-tin sphere. The region outside of these spheres is referred to as the interstitial region. Also a third region, the vacuum-region, can be defined when the no periodic boundary conditions in the z-direction are assumed. For each of these regions different basis functions are defined. Inside of the muffin-tin sphere spherical harmonics are used. In the interstitial region plane waves are the basis functions. The vacuum region is represented by an exponential decay of the wavefunction. These basis functions allow for a very good description of the wavefunctions of the electrons as they are already reflecting the physical solution. Free moving electrons can be described by plane waves, where bound electrons of a free atom, would have spherical harmonics as solutions. With this spatial change in the basis functions all electrons can be adequately described. The challenges, that arise from this approach is, that the wavefunctions have to be smooth at the boundaries of the regions. The FLAPW method is an extension to the augmented plane wave (APW) and linearized augmented plane wave (LAPW) [191, 192] method. Thereby the APW method is exact, but contains an additional self-consistency problem for the solution of the radial Schrödinger equation inside the muffin-tin (MT) spheres. The LAPW method makes a linear approximation, which reduces the computational cost drastically and still provides very accurate results. A more detailed comparison between the three methods can be found in Ref. [176, 189]. Important parameters for calculations using the FLAPW method are the radius of the

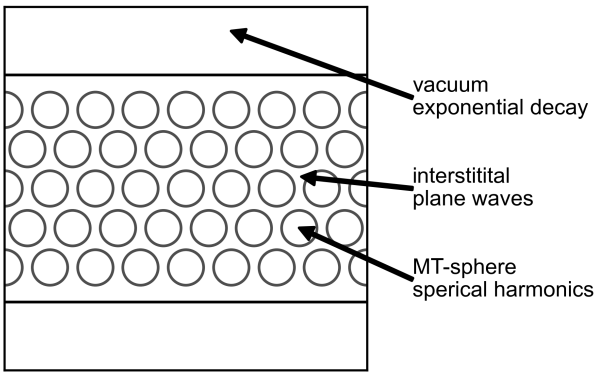

Figure 2.16: Visualization of FLAPW basis for a film calculation. The whole space is separated into three regions. The muffin-tin (MT) spheres are located at the lattice sites. The interstitial region fills the space in between the MT-spheres. On both sides of the film is a vacuum region. The basis for the wave function varies between the regions. Inside of the MT-spheres are spherical harmonics used. The interstitial region is represented by plane waves and the wavefunction is exponentially decaying into the vacuum. Figure inspired by Ref. [176].

MT-sphere and the cut-off parameter for the plane waves in the interstitial region. The MT-radius can differ for each element, where the radius should be large enough to contain the core states. The number of plane wave basis functions is determined by a cut-off parameter $k_{\max}$, which defines the maximal energy for the plane waves by

$$E_{\text{cut}} = \frac{\hbar^2 k_{\max}^2}{2m} . \tag{2.110}$$

While a larger cut-off parameter gives more accurate results, it is also computationally more costly. A good value can be found by convergence tests.

PAW

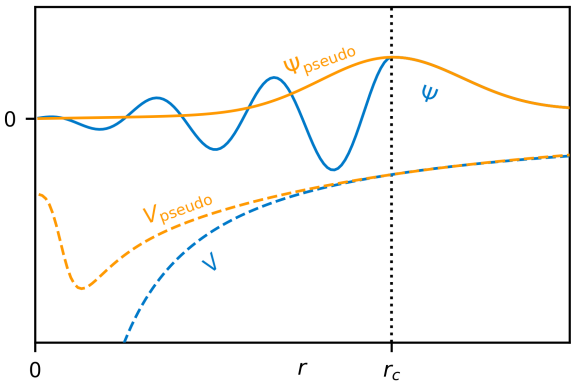

Figure 2.17: Sketch of a pseudo potential. The potential of an atom is sketched by a blue dashed line. The corresponding pseudo potential is marked by a dashed orange line. For $r > r_c$ both potentials are identical. The wavefunctions for both potential are shown by solid lines. The wavefunction for the real potential has some nodes for $r < r_c$, where the wavefunction for the pseudo potential has none. For $r > r_c$ also both wavefunctions are identical. Figure inspired from Ref. [190].

The code `VASP` [193, 194] has the projector augmented wave (PAW) [195–197] method implemented, which is a generalization of the pseudo potential method [198–200] and the LAPW method. The basis functions, used for expanding the Kohn-Sham wavefunction, are plane waves. Electrons close to the nucleus are localized and therefor many plane waves would be needed to expand these states. The pseudo potential method circumvents this problem by introducing a pseudo potential, which coincides with the real potential outside of a sphere with a specific radius around the nucleus. This is sketched in Fig. 2.17. Inside of the sphere the pseudo potential describes an effective potential from the core and the strongly bound electrons. This method is often combined with the frozen core

approximation, where the core electrons are not explicitly contained in the calculations, which leads to a significant decrease in computational cost. The wavefunction for the pseudo potential does not contain as many nodes as the wavefunction for the real potential. Therefore, far less plane waves are necessary to expand the wavefunction. Also for the PAW method the convergence with respect to the cut-off energy E_{cut} has to be ensured.

2.4 Atomistic spin model

DFT allows to accurately calculate the total energy for a given spin structure since in principle[3] all quantum mechanical interactions are included. However, these calculations require a large computational effort and allow only calculations for a relatively small number of atoms. An atomistic model, which can be parameterized by DFT, allows for the simulation of larger systems. In an atomistic model the magnetic moments are represented by classical vectors instead of quantum mechanical spins. The magnetic moment of lattice site i is given by $\mathbf{S}_i = S_i \mathbf{s}_i$, where S_i is the magnitude and $\mathbf{s}_i$ the normalized direction. Although this is a drastic simplification, the atomistic model has shown to give very good agreements with experiments in many cases [201]. Besides the larger number of atoms that can be included in the calculations, it also allows for a physical interpretation of the interactions which define the ground state of the system. Further the atomistic spin model allows to investigate the dynamics of a system [202].

The model is often referred to as the extended Heisenberg model, since the largest contributions typically stem from the Heisenberg exchange. Over the time more interactions, such as the Dzyaloshinskii-Moriya interaction (DMI), were considered. For some systems like the nanoskyrmion lattice in Fe/Ir(111) [41], higher-order exchange interactions (HOI) have a crucial effect for the stabilization of non-coplanar spin textures. Recently the HOI are more often considered [58, 61]. It is likely, that the model will be extended even further in the future. In this section all interactions, which are considered in this work, are shortly introduced.

2.4.1 Heisenberg exchange

Typically the largest contribution to the energy of a spin texture is the Heisenberg exchange [203, 204]. The exchange energy is given by [202]

$$E = -\sum_{ij} J_{ij}(\mathbf{s}_i \cdot \mathbf{s}_j) \quad , \tag{2.111}$$

where the sum is over all pairs of lattice sites and J_{ij} is the corresponding exchange constant. The directions of the normalized magnetic moments of each lattice site are given by $\mathbf{s}_i$ and $\mathbf{s}_j$. A positive constant J_{ij} favors a parallel, or ferromagnetic, alignment of magnetic moments. A negative value of J_{ij} leads to an antiparallel, or antiferromagnetic, alignment. This is sketched in Fig. 2.18a,b. The interaction constants are approximated to be isotropic, hence they depend only on the distance between two lattice sites. Using the isotropic approximation the energy contributions can be grouped into so-called shells. All lattice sites within one shell have the same distance to a reference atom and hence the same

[3] See Sec. 2.3 for more details.

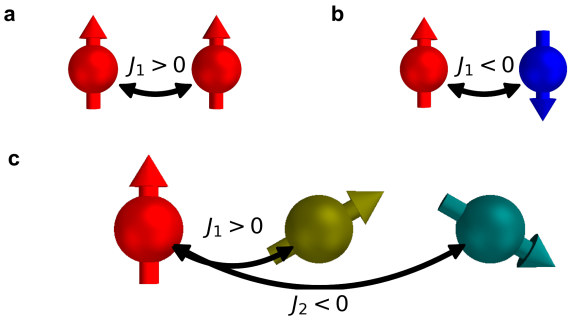

Figure 2.18: Sketch of the exchange interaction. **a** A ferromagnetic alignment is energetically favored for a positive value of J. **b** For a negative J an antiferromagnetic orientation is preferred. **c** A positive nearest neighbor interaction J_1 and a negative next nearest neighbor interaction J_2 can lead to a non-collinear ground state, like a spin spiral.

interaction parameter. For a reference spin $\mathbf{s}_0$ the exchange interaction can be written as

$$E_{\mathbf{s}_0} = -\sum_n \sum_{j_n} J_n(\mathbf{s}_0 \cdot \mathbf{s}_{j_n}) \quad , \tag{2.112}$$

where J_n is the exchange constant for the n^{th} shell and the index j_n runs over all lattice sites in the shell n. The absolute value of J_n will decrease with increasing distance. Therefore, only a finite number of shells N have to be considered. The sign of J_n can vary for each shell. For example the nearest neighbors could favor a ferromagnetic order ($J_1 > 0$) but the next nearest neighbors could favor an antiferromagnetic alignment ($J_2 < 0$). This so-called exchange frustration can stabilize non-collinear magnetic structures [205, 206], as shown in Fig. 2.18c.

Beside a direct interaction also the indirect Rudermann-Kittel-Kasuya-Yosida (RKKY) interaction exist [207–209], where magnetic moment couple via valence electrons. However, within the atomistic spin model this interaction is not distinguishable from the direct coupling and hence is absorbed into the coupling constants J_{ij}.

The sorting in shells with the same distance can be also done for all other interactions in the used atomistic model. For brevity this is not explicitly written in the following.

A good way to determine the exchange interaction constants J_n is to calculate the total energy of different spin spirals via DFT and perform a fit of the model to the DFT values, as discussed in Refs. [210, 211] in more detail.

2.4.2 Higher order exchange

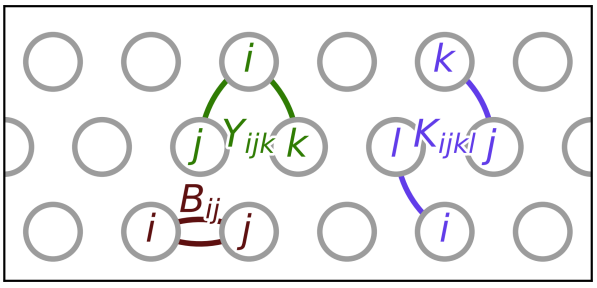

Figure 2.19: Sketch of the 4^{th} order HOI. The interacting lattices sites for the biquadratic interaction B_{ij}, the 4spin-3site interaction Y_{ijk} and the 4spin-4site interaction K_{ijkl} on a hexagonal lattice are marked. The connecting lines represent the scalar product. For the 4spin-4site interactions also a term with scalar products between i, k and j, l exists.

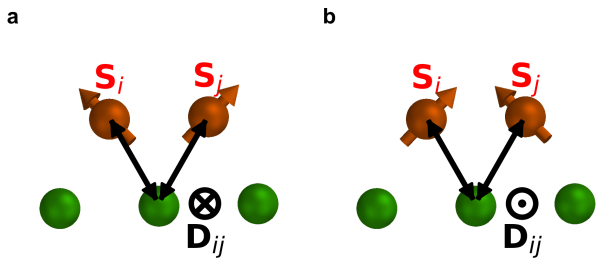

Figure 2.20: Sketch of the DMI. Shown are two magnetic atoms (red) on the substrate with large SOC constant (green). The interaction via the substrate is indicated by arrows. The rotational sense, favored by the DMI, depends on the direction of the vector $\mathbf{D}_{ij}$, which depends on the sign of D_0 (cf. Eq. (2.117)). **a** Energetically favored rotational sense for $D_0 > 0$. **b** Preferred orientation for $D_0 < 0$.

While spin spirals are solutions to the Heisenberg exchange, one can also create a superposition of more than one spin spiral, like the magnetic triple-Q (3Q) state [179, 212]. Considering the Heisenberg exchange both have the same energy. This energy degeneracy is lifted by the higher-order exchange interactions (HOI). These can therefore stabilize multi-Q states or other non-coplanar spin structures, like a nanoskyrmion lattice [41]. Compared to the Heisenberg exchange, the HOI consider more than two magnetic moments. A systematical derivation of the HOI using a Hubbard model is given in Ref. [213]. Interactions containing four magnetic moments in the scalar product are referred to the 4^{th} order, while interactions with six moments in the scalar product are called the 6^{th} order and so on. The 4^{th} order HOI can be further differentiated by the number of involved lattice sites. The biquadratic, 4spin-3site and 4spin-4site interactions connect two, three and four lattice sites respectively, as sketched exemplary in Fig. 2.19. For the Biquadratic term two lattice sites contribute and the energy is [213]

$$E_{\text{biquad}} = -\sum_{ij} B_{ij}(\mathbf{s}_i \cdot \mathbf{s}_j)^2 \quad . \tag{2.113}$$

Due to the square in the equation, each lattice site contributes twice. The Hubbard model assumes here two orbitals at each lattice site occupied by the majority spin. Therefore, this interaction can only occur for systems with a total spin greater or equal to 1 [213]. For the Mn or Fe based systems in this work, this is always fulfilled. The 4spin-3site interaction is given by [213]

$$E_{\text{4spin3site}} = -\sum_{ijk} Y_{ijk}[(\mathbf{s}_i \cdot \mathbf{s}_j)(\mathbf{s}_j \cdot \mathbf{s}_k) + (\mathbf{s}_j \cdot \mathbf{s}_i)(\mathbf{s}_i \cdot \mathbf{s}_k) + (\mathbf{s}_i \cdot \mathbf{s}_k)(\mathbf{s}_k \cdot \mathbf{s}_j)] \tag{2.114}$$

and involves three lattice sites. Four lattice sites contribute in the 4spin-4site interaction with the energy [213]

$$E_{\text{4spin4site}} = -\sum_{ijkl} K_{ijkl}[(\mathbf{s}_i \cdot \mathbf{s}_j)(\mathbf{s}_k \cdot \mathbf{s}_l) + (\mathbf{s}_i \cdot \mathbf{s}_l)(\mathbf{s}_j \cdot \mathbf{s}_k) - (\mathbf{s}_i \cdot \mathbf{s}_k)(\mathbf{s}_j \cdot \mathbf{s}_l)] \quad . \tag{2.115}$$

2.4.3 Dzyaloshinskii-Moriya-Interaction

The Dzyaloshinskii-Moriya interaction (DMI) is an interaction, that occurs due to spin-orbit coupling (SOC) and a broken inversion symmetry. In magnetic thin film systems the inversion symmetry is broken by the surface [214]. The DMI favors a non-collinear alignment of the spins with a specific rotational sense. The interaction between two magnetic lattice sites is mediated over a third lattice site. This interaction is typically stronger, when the SOC in the mediating lattice site is stronger. The contributions of all mediating lattice sites can be grouped into a vector $\mathbf{D}_{ij}$, which is unique for the pair of magnetic lattice sites i and j. The energy due to DMI is then given by [215]

$$E_{\mathrm{DMI}} = -\sum_{ij} \mathbf{D}_{ij} \cdot (\mathbf{s}_i \times \mathbf{s}_j) \quad . \tag{2.116}$$

The energy does not only depend on the angle between $\mathbf{s}_i$ and $\mathbf{s}_j$, but also on the orientation with respect to $\mathbf{D}_{ij}$. The interaction strength corresponds to the length of the vector. In contrast to the Heisenberg exchange or the HOI, a global spin rotation can change the energy due to the DMI. This can favor a certain orientation with respect to the atomic lattice. To determine the direction of $\mathbf{D}_{ij}$ one can use symmetry rules proposed by Dzyaloshinskii and Moriya [215, 216]. An approximation can also be calculated as proposed by Levy and Fert [217]

$$\mathbf{D}_{ij} = \frac{D_0}{d_{ij}} \sum_n \frac{\mathbf{d}_{in} \cdot \mathbf{d}_{jn} (\mathbf{d}_{in} \times \mathbf{d}_{jn})}{(d_{in} d_{jn})^{3/2}} \quad , \tag{2.117}$$

where the index n iterates over the mediating lattice sites and the vectors $\mathbf{d}_{ij} = \mathbf{r}_i - \mathbf{r}_j$ are the connections between two lattice sites with the length $d_{ij} = |\mathbf{d}_{ij}|$. For thin film systems it is often a good approximation to assume the vector $\mathbf{D}_{ij}$ to be perpendicular to the connection $\mathbf{d}_{ij}$ and only have an in-plane component. In Fig. 2.20a,b atoms of the substrate (green) and magnetic atoms (red) are shown. The direction of the $\mathbf{D}_{ij}$ vector is opposite in Fig. 2.20a and Fig. 2.20b, representing an opposite sign of the interaction. The direction of $\mathbf{D}_{ij}$ leads to a clockwise rotation in Fig. 2.20a and a counterclockwise rotation in Fig. 2.20b. Using the assumption of the in-plane oriented $\mathbf{D}_{ij}$, the DMI will favor spin spirals which have an out of plane component. To obtain DMI parameters from spin spiral energies calculated by DFT, the spin spirals have to be oriented accordingly. A good way to determine the DMI constants is by calculating the SOC contribution of spin spirals via first order perturbation theory. This SOC contribution can be mapped on the DMI since other considered interactions like the magnetocrystalline anisotropy energy (MAE) or anisotropic symmetric exchange (ASE) arise only in higher order perturbation theory.

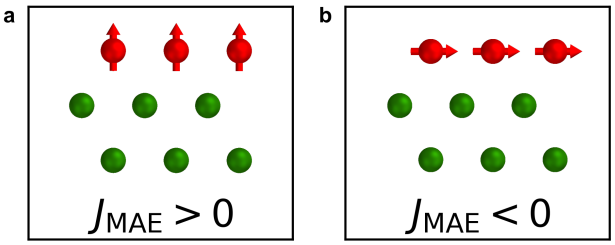

Figure 2.21: Sketch of the MAE interactions. Side view of a magnetic film (red) on a non-magnetic substrate (green). **a** For $J_{MAE} > 0$ the preferred orientation is perpendicular to the surface. **b** For $J_{MAE} < 0$ an alignment parallel to the surface in energetically favored.

2.4.4 Magnetocrystalline anisotropy

Another effect of SOC is the magnetocrystalline anisotropy energy (MAE), which favors a specific alignment of the magnetic moments with respect to the atomic lattice. In this work the MAE is assumed to be uniaxial, which leads to the energy [201]

$$E_{\mathrm{MAE}} = -K \sum_i (\mathbf{s}_i \cdot \mathbf{n})^2 \quad , \tag{2.118}$$

where $\mathbf{n}$ is the unit vector of the surface normal. A positive value of K represents an alignment with the surface normal (see Fig. 2.21a), where parallel and antiparallel alignments are degenerate. This is named easy-axis magnetization. A negative value of K leads to an orientation perpendicular to the surface normal (see Fig. 2.21b), called an easy-plane magnetization. Also, specific orientations within the plane of the magnetic layer can be energetically favored. This in-plane component of the MAE would need to have the symmetry of the lattice. For the systems in this work this effect was tested, but showed to be very small and is therefore neglected. The MAE could be calculated in second order perturbation theory, via the so-called force theorem or self-consistently. The first two approaches save computational time, since the scalar-relativistic calculation without SOC can be used to calculate the MAE. However, for a good accuracy all MAE energies in this work were calculated self-consistently.

2.4.5 Anisotropic symmetric exchange

The anisotropic symmetric exchange (ASE) is also an effect originating from SOC, where an interaction between two lattice sites is coupled to the connection vector [218, 219]. The energy contribution is given by [220]

$$E_{\mathrm{ASE}} = -J_{\mathrm{ASE}} \sum_{ij} (\mathbf{s}_i \cdot \mathbf{d}_{ij})(\mathbf{s}_j \cdot \mathbf{d}_{ij}) \quad , \tag{2.119}$$

where $\mathbf{d}_{ij}$ is the normalized connection vector between the lattice sites i and j. For a positive constant J_{ASE} a ferromagnetic alignment along the connection is energetically favored, where an antiferromagnetic alignment occurs for a negative J_{ASE}. For a positive sign the ASE leads to a similar orientation as the dipole-dipole interaction. Therefore, it is

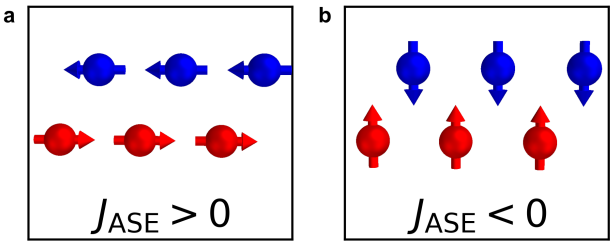

Figure 2.22: Sketch of the ASE. Top view on a hexagonal magnetic surface with a RW-AFM state. **a** The preferred orientation of the RW-AFM state for $J_{ASE} < 0$ is perpendicular to the FM rows. **b** For $J_{ASE} > 0$ the orientation is along the FM rows.

sometimes referred to as the pseudo-dipolar interaction. Within this work the ASE is only considered for nearest neighbors.
In Fig. 2.4.5 a top view on a magnetic layer, hosting an in-plane oriented RW-AFM state, is shown. For a positive value of J_{ASE} the magnetic moments align along to the ferromagnetic rows (Fig. 2.4.5a). For a negative value they align perpendicular the rows (Fig. 2.4.5b).

2.4.6 Dipole-dipole interaction

Compared to all other interactions the dipole-dipole interaction is usually very small. It does not have an interaction constant, but depends on the magnitude of the magnetic moment. The energy of the dipole-dipole interaction is [202]

$$E_{DD} = -\sum_{ij} \frac{\mu_0 S_i S_j}{4\pi} \frac{3(\mathbf{s}_j \cdot \mathbf{d}_{ij})(\mathbf{s}_i \cdot \mathbf{d}_{ij}) - (\mathbf{s}_i \cdot \mathbf{s}_j) d_{ij}^2}{d_{ij}^5} \quad , \tag{2.120}$$

where $\mathbf{d}_{ij} = \mathbf{r}_i - \mathbf{r}_j$ is the connection vector between the lattice sites i and j and $d_{ij} = |\mathbf{d}_{ij}|$ is the distance. The magnitude of the magnetic moment S_i is given in units of μ_B.

2.4.7 Topological orbital moments

Orbital moments emerge due to SOC, which leads to magnetic interactions like the DMI or MAE. Orbital moments can also emerge without SOC due to the topology of the spin structure [56]. Non-coplanar oriented magnetic moments, as sketched in Fig. 2.23, can lead to a preferred rotational sense for electrons (green arrow), which move in the plane of the magnetic layer. The orbital moment (blue arrow) originating from this preferred rotational sense is called the topological orbital moment (TOM), since it depends on the topology of the spin structure. The TOM for the lattice site i is defined as [56]

$$\mathbf{L}_i^{TO} = \sum_{(jk)} \kappa_{ijk}^{TO} \chi_{ijk} \boldsymbol{\tau}_{ijk} \quad . \tag{2.121}$$

Here the summation is over triplets of magnetic moments, which are nearest neighbors. κ_{ijk}^{TO} is the topological orbital susceptibility, a material specific parameter. $\boldsymbol{\tau} \propto (\mathbf{r}_j - \mathbf{r}_i) \times (\mathbf{r}_k - \mathbf{r}_i)$ defines the direction, which is perpendicular to the surface ($\boldsymbol{\tau} \propto \mathbf{e}_z$) for thin film systems.

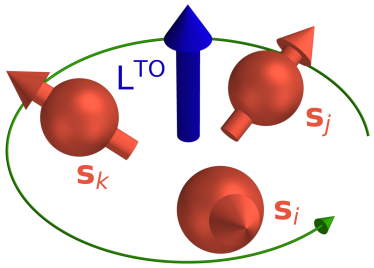

Figure 2.23: Sketch of the TOM. Three lattice sites with the non-coplanar oriented magnetic moments $\mathbf{s}_i$, $\mathbf{s}_j$ and $\mathbf{s}_k$ are shown by red arrows. A preferred chirality for electronic motion is indicated by a green round arrow. The resulting TOM is marked by a blue arrow. Figure inspired by Ref. [56].

χ_{ijk} is the scalar spin chirality defined as

$$\chi_{ijk} = \mathbf{s}_i \cdot (\mathbf{s}_j \times \mathbf{s}_k) \quad . \tag{2.122}$$

This scalar spin chirality is zero for collinear or coplanar magnetic textures. The topological orbital susceptibility depends on the electronic structure and can in principle vary over the lattice. However, for most materials a similar electronic structure for all lattice sites can be expected. Via first-principles calculations this can be verified by analyzing the electronic structure at each lattice site, e.g. via the LDOS. As a rough indicator the variation of the magnitude of the magnetic moments could be used. If the magnetic moments are strongly varying, the electronic structure will also differ between the lattice sites. The TOM can be calculated via DFT, when SOC is neglected, since in that case no other contributions to the orbital moment exist. Therefore, the whole orbital moment can be accounted to the TOM. However, the TOM could change, when SOC is considered, since SOC alters the electronic structure, which also influences the TOM via $\kappa^{\mathrm{TO}}_{ijk}$. In general this makes a clear separation of the TOM and the orbital moment due to SOC difficult. The change of the TOM due to SOC might be small, as the change in the electronic structure by SOC is usually small, as shown in calculations for a skyrmion [221].

When a TOM is present also an interaction between the TOM and the emergent magnetic field can occur. This interaction is called the chiral-chiral interaction [56]

$$E_{\mathrm{CCI}} = -\frac{1}{2}\sum_{ijk} \kappa^{\mathrm{CCI}}_{ijk} \left[\mathbf{s}_i \cdot (\mathbf{s}_j \times \mathbf{s}_k)\right]^2 \quad . \tag{2.123}$$

As an effect of SOC an interaction between a magnetic moment and the TOM, the so-called spin-chiral interaction, can arise [56]

$$E_{\mathrm{SCI}} = -\frac{1}{2}\sum_{ijk} \kappa^{\mathrm{SCI}}_{ijk} \left(\boldsymbol{\tau}_{ijk} \cdot \mathbf{s}_i\right)\left[\mathbf{s}_i \cdot (\mathbf{s}_j \times \mathbf{s}_k)\right] \quad . \tag{2.124}$$

2.4.8 Topological charge and scalar spin chirality

Topological spin textures can have interesting features like enhanced stability or transport properties. To measure the topology of spin textures like Skyrmions with diameters of a couple of nanometers or above often the topological charge is used. The topological charge is given by [222]

$$Q = \frac{1}{4\pi} \int \mathbf{m} \left(\frac{\partial \mathbf{m}}{\partial x} \times \frac{\partial \mathbf{m}}{\partial y} \right) \mathrm{d}x\mathrm{d}y \quad , \tag{2.125}$$

where $\mathbf{m}$ represents a spatially continuous magnetization and the integrand is called the topological density. For the atomistic model, where the magnetization is only defined at the lattice sites, the topological density can be calculated on a triangle between three lattice sites. The topological density is proportional to the area on the surface of a sphere, which is spanned by the three magnetic moments of the lattice sites. While this description works well for most isolated spin textures, it can break down for atomic-scale spin structures with large tilting angles between neighboring lattice sites.

This can be showcased for three lattice sites, where the tilting angles are continuously transformed. Fig. 2.24 shows the topological density for three magnetic moments, which are continuously rotated by the same angle ϑ, which is sketched in the inset. $\vartheta = 0°$ represents a FM alignment, where the topological density is zero. The topological density has a positive value in the range of $0° < \vartheta < 90°$. For $\vartheta = 90°$ all three magnetic moments are pointing away from the common center. Here the topological charge is not defined. Coming from the left or right the topological charge is approaching +0.5 or −0.5, respectively.

Additionally, the scalar spin chirality (cf. Eq. (2.122)) in dependency of ϑ is shown. It has the same sign as the topological charge, but is smoothly defined for all ϑ. As it is defined for all spin textures it can be used as a measure of the spin topology as proposed in Ref. [57]. Further, the scalar spin chirality has an intrinsic connection to the topology of the spin texture, as it breaks the time-reversal symmetry even for a zero net-magnetization [223]. The broken time-reversal symmetry leads to effects like the topological Hall effect [52, 53] or TOM [56].

Ref. [224] demonstrates using a simple model, how the scalar spin chirality can lead to a chiral current, which induces a TOM [56] or a Hall effect [225]. If a conduction electron is

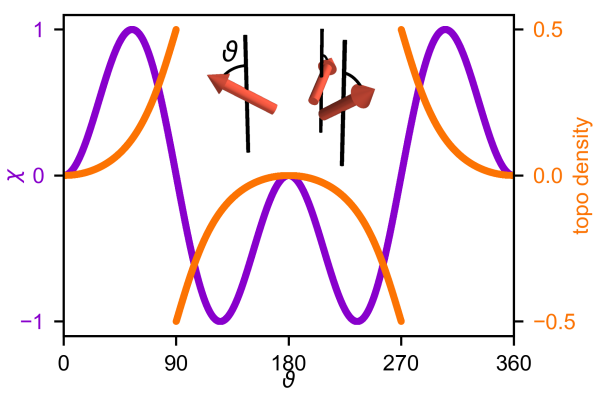

Figure 2.24: Scalar spin chirality and topological density for three magnetic moments. The three magnetic moments are positioned on the corners of a equilateral triangle. For a value of $\vartheta = 0°$ all magnetic moments are FM aligned upwards. For increasing ϑ they are rotating away from the center as sketched in the inset. The scalar spin chirality (purple) and the topological density (orange) are given for a 360° rotation of the magnetic moments. The values of $\vartheta = 90°$ and $\vartheta = 270°$ correspond to a coplanar in-plane alignment.

scattered on a lattice site $\mathbf{r}_n$ with magnetic moment $\mathbf{s}_n$ the wavefunction of the electron is multiplied by [224]

$$A(\mathbf{s}_n) = b\mathrm{e}^{\mathrm{i}b(\mathbf{s}_n\cdot\boldsymbol{\sigma})} \quad \text{with} \quad a, b \in \mathbb{C} \tag{2.126}$$

and $\boldsymbol{\sigma}$ is a vector containing the Pauli-spin matrices (see Appendix A.1). In general multiple scattering events do not commute $A(\mathbf{s}_k)A(\mathbf{s}_l) \neq A(\mathbf{s}_l)A(\mathbf{s}_k)$. This follows from the commutation relation of the Pauli-spin matrices [224]

$$[\sigma_k, \sigma_l] = 2\mathrm{i}\boldsymbol{\epsilon}_{klm}\sigma_m \quad , \tag{2.127}$$

where $\boldsymbol{\epsilon}_{klm}$ is the Levi-Civita symbol. However, the charge transport depends only on the trace , which is invariant for the order of two scattering events $\mathrm{tr}\left[A(\mathbf{s}_k)A(\mathbf{s}_l)\right] = \mathrm{tr}\left[A(\mathbf{s}_l)A(\mathbf{s}_k)\right]$ [224]. This leads to a vanishing net charge transport for two lattice sites. For a scattering at three lattice sites, the trace depends on the order of the scattering events as

$$\mathrm{tr}\left[A\left(\mathbf{s}_k\right)A\left(\mathbf{s}_l\right)A\left(\mathbf{s}_m\right)\right] - \mathrm{tr}\left[A\left(\mathbf{s}_m\right)A\left(\mathbf{s}_l\right)A\left(\mathbf{s}_k\right)\right] = 4a^3\sin^3(b)\mathbf{s}_k\cdot(\mathbf{s}_l\times\mathbf{s}_m) \quad . \tag{2.128}$$

The net charge transport is in general non-zero and depends on the scalar spin chirality. Note, that in special cases the current could be very small or even vanishing, depending on the electronic structure. The connection between the spin texture and an induced chiral current makes the scalar spin chirality an appropriate measure of the topology for atomic-scale spin textures. In Ref. [226] non-trivial transport properties are predicted for such atomic-scale spin textures with non-zero scalar spin chirality. While transport properties and TOM depends on the scalar spin chirality, a connection to topological superconductivity has not been shown so far. Pub. III shows, that the topological charge does not correlate with induced topological superconductivity but suggests, that the scalar spin chirality does.

2.5 Simulated scanning tunneling microscopy images

Scanning tunneling microscopy (STM) is a versatile and powerful experimental technique to directly probe the surface of a sample down to atomic resolution [227–232]. Simulated STM data are a direct way to compare theoretical calculations and experimental observations. This section describes the basic principle of STM and how STM data can be simulated based on DFT, a tight-binding model and an atomistic spin model.
In STM a sharp tip is brought close to the surface of the sample. The position of the tip can be controlled in all three spatial dimensions. Based on the quantum mechanical tunnel effect a small current I will flow between the tip and the sample, which is dependent on the distance between tip and sample, the electronic structure of the tip and the sample and the bias voltage V_B, which is applied between tip and sample.
When the tip is scanned across the surface a map of the electronic structure of the surface can be created, based on the spatial change in the tunnel current. The two most well known measurement modes are the constant-height mode, where the z-position of the tip is constant and the constant-current mode, where the z-position is constantly adjusted to keep the current constant. The z-position of the tip in dependency on the position (x, y) can be used to approximate the topography of the sample [4].
Magnetic properties can be probed with spin-polarized scanning tunneling microscopy (SP-STM), in which a spin-polarized tip is used [233–237]. Here the tunnel current depends also on the spin orientation of the sample. When the tip spin orientation is varied even non-coplanar spin textures can be resolved. Here it can be useful if multiple rotational domains of a spin texture exist. Even when probed with the same tip, the effective tip magnetization direction is different for the rotational domains.
Since magnetism influences the electronic structure, magnetic structures can also be detected without a spin-polarized tip, e.g. via the tunneling anisotropic magnetic resistance (TAMR) [238–241] or the non-collinear magneto resistance (NCMR) [242] effect. However, this work focuses on SP-STM.
When the bias voltage is varied scanning tunneling spectroscopy (STS) measurements can be performed [232, 243]. Here the differential conductance $\mathrm{d}I/\mathrm{d}V_\mathrm{B}$ can be measured, which gives an approximation of the LDOS of the sample $\rho_S(\mathbf{r}, E)$ [244]

$$\frac{\mathrm{d}I}{\mathrm{d}V_\mathrm{B}}(\mathbf{r}_\mathrm{T}, V_\mathrm{B}) \propto \rho_S(\mathbf{r}_\mathrm{T}, E_\mathrm{F} + eV_\mathrm{B}) \quad , \tag{2.129}$$

where E_F is the Fermi energy and $\mathbf{r}_\mathrm{T}$ the position of the tip. This can for example be interesting to resolve the superconducting band gap or zero-energy edge modes in MSH systems. The Tersoff-Hamann model [105] makes, based on the work of Bardeen [113], some assumptions for the tip to obtain an expression for the tunnel current, that only

[4] The topography can only be approximated, since the tunnel current depends on the electronic density, which is not only dependent on the topography. However, when probing different bias voltages, usually very good approximations of the topography can be made.

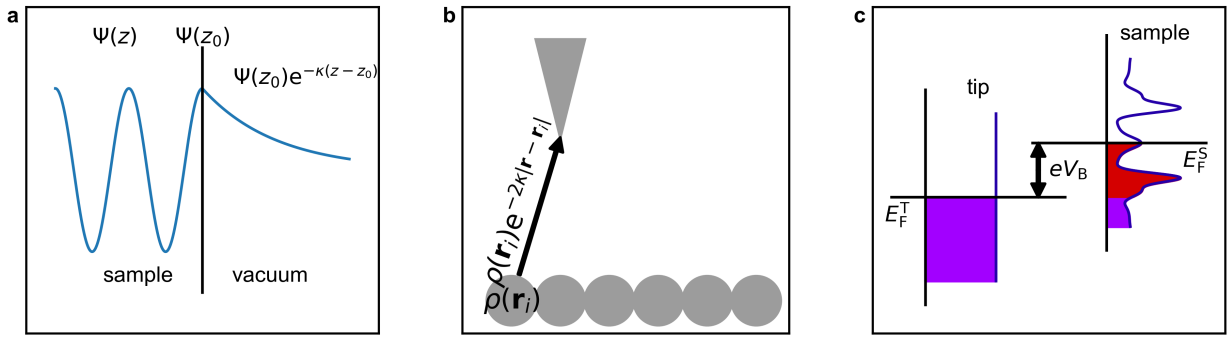

Figure 2.25: Sketch of the tunneling process in STM. **a** Sketch of the exponential decay of a wavefunction from the sample into the vacuum. **b** Sketch of surface atoms and a tip. The exponential decay of the LDOS is sketched. The total tunnel current results from a sum over the contributions of all lattice sites. **c** LDOS of the tip and the sample. The occupied states are marked by filled areas. The red area represents the electrons, that can tunnel from the sample into the tip for the given bias voltage V_B. The LDOS of the tip is assumed to be constant.

depends on properties of the sample. An extension to the model has been made by Lang [245] and Heinze *et al.* [106, 107, 233, 244], where the latter includes spin-polarization.

2.5.1 Tersoff-Hamann model

The tunnel probability for a single electron from a state μ of the sample to a state ν of the tip depends on the overlap of the wavefunctions Ψ_μ and Ψ_ν of the sample and tip, respectively. This overlap can be described by the matrix element $M_{\mu\nu}$.
The total tunnel current follows from a sum over all matrix elements, which are weighted with the Fermi function $f(E)$. The Fermi function ensures, that the state μ in the sample is occupied and the state ν in the tip is unoccupied.
Using first order perturbation theory the current is the given by [105]

$$I(V_B) = \frac{2\pi e}{\hbar} \sum_{\mu\nu} f(E_\mu)[1 - f(E_\nu + eV_B)]|M_{\mu\nu}|^2 \delta(E_\mu - E_\nu) \quad . \tag{2.130}$$

Here e is the charge of an electron and δ denotes the delta distribution. The bias voltage V_B shifts the energy of the tip state with respect to the sample (see Fig. 2.25c). Note, that for a negative bias voltage the current could also be flowing from the tip to the sample. For brevity only the case of positive bias voltage is treated in the following.
By relating the matrix element to the wave functions of a state of tip and sample [246] and approximating the wave function of the tip to be spherical symmetric the current can be written as [244]

$$I(\mathbf{r}_T) = \frac{16\pi^3 C^2 \hbar^3 e}{\kappa^2 m^2} \int \rho_T(E + eV_B)\rho_S(\mathbf{r}_T, E)[f(E - E_F^S) - f(E + eV_B - E_F^T)]\mathrm{d}E \quad . \tag{2.131}$$

Here C is a constant, ρ_T is the DOS of the tip and ρ_S is the LDOS of the sample. The LDOS can be calculated from the wavefunctions Ψ_μ by

$$\rho_S(\mathbf{r}, E) = \sum_\mu |\Psi_\mu(\mathbf{r})|^2 \delta(E_\mu - E) \quad , \tag{2.132}$$

where δ is the Delta distribution, μ corresponds to states of the sample.

Eq. (2.131) depends on the LDOS of the sample evaluated at the position of the tip $\rho_S(\mathbf{r}_T, E)$, i.e. in the vacuum a few Å above the surface. While this can be calculated directly via DFT, for simpler models such as the tight-binding approach used in this thesis the LDOS of the sample is only defined at the lattice sites of the sample. Generally a wavefunction decays exponentially into a potential barrier, when its energy is smaller than the potential. At a position z in the vacuum above the surface at z_0 the wavefunction of the sample is therefore given by

$$\Psi(z) = \Psi(z_0) \mathrm{e}^{-\kappa(z-z_0)} \qquad \kappa = \sqrt{\frac{2m\phi}{\hbar^2}} \quad , \tag{2.133}$$

where κ is the decay constant, dependent on the electron mass m and the work function ϕ. For small bias voltages κ can be assumed to be equal for all states [244]. This is sketched in Fig. 2.25a. The decay constant is approximately $\kappa = 0.51 \sqrt{\phi(eV)} \text{Å}^{-1}$ [231]. The work function can for example be calculated by DFT. If κ can not be determined by some ab-initio calculations, a value of $\kappa = 1 \text{Å}^{-1}$ can be a reasonable estimate. When further assuming an isotropic decay, the LDOS of the sample at the tip position is given by

$$\rho(\mathbf{r_T}, E) = \sum_\mu |\Psi_\mu(\mathbf{r_S})|^2 \, \mathrm{e}^{-2\kappa|\mathbf{r}_\mathrm{T} - \mathbf{r}_\mathrm{S}|} \, \delta(E_\mu - E) = \rho(\mathbf{r_S}, E) \, \mathrm{e}^{-2\kappa|\mathbf{r}_\mathrm{T} - \mathbf{r}_\mathrm{S}|} \quad , \tag{2.134}$$

as visualized in Fig. 2.25b. For low temperatures the Fermi function can be approximated by a Heaviside function, leading to

$$I(\mathbf{r}_T) \propto \int_{E_F - eV_\mathrm{B}}^{E_F} \rho_T(E + eV_B) \rho_S(\mathbf{r}_T, E) \mathrm{d}E \quad , \tag{2.135}$$

where the Heaviside functions are reflected in the integration boundaries. The LDOS of the tip is in general not easy to obtain and is assumed to be constant in the Tersoff-Harmann model $\rho_T(E) = const$. [105]. With the definition

$$\tilde{\rho}_S(\mathbf{r}_T, V_\mathrm{B}) := \int_{E_F - eV_\mathrm{B}}^{E_F} \rho_S(\mathbf{r}_T, E) \, \mathrm{d}E \tag{2.136}$$

the current becomes

$$I(\mathbf{r}_T) \propto \rho_T \tilde{\rho}_S(\mathbf{r}_T, V_\mathrm{B}) \quad . \tag{2.137}$$

In Fig. 2.25c the LDOS of the tip and the sample are sketched. The approximations for low temperatures and constant LDOS of the tip are used. Now all states above the Fermi

energy of the tip are assumed to be unoccupied. Due to the energy shift of eV_B between the Fermi energy of the tip and the sample, all states of the sample in the energy interval $E \in [-eV_B, 0]$ can contribute to the tunnel current.
For spin-polarized tips and samples two densities exist, one for the spin up channel $\rho^\uparrow$ and one for the spin down channel $\rho^\downarrow$. The total LDOS is now given by $\rho = \rho^\uparrow + \rho^\downarrow$ and the magnetization is $\mathbf{m} = (\rho^\uparrow - \rho^\downarrow)\mathbf{s}$, where $\mathbf{s}$ is the normalized direction of the tip magnetization or a surface atom. The current then becomes [106, 107, 233]

$$I(\mathbf{r}_T, V) = I_0(\mathbf{r}_T, V_B) + I_P(\mathbf{r}_T, V_B, \mathbf{s}_T) \propto \rho_T \tilde{\rho}_S(\mathbf{r}_T, V_B) + \mathbf{m}_T \tilde{\mathbf{m}}_S(\mathbf{r}_T, V_B) \quad , \tag{2.138}$$

where I_0 is the non-spin-polarized part and I_P the spin-polarized part. The tilde represents again the integration over the energy.

2.5.2 SP-STM simulations based on the atomistic spin model

The atomistic spin model uses classical vectors to represent the local magnetic moments. As a result this model does not contain any information of the LDOS apart from the spin-polarization, which is reflected in the magnetic moment. Therefore, also the LDOS of the sample is modeled by a constant value $\rho(E) = \rho_0 \Theta(E_F - E)$, where states are exactly occupied up to the Fermi energy, described by the Heaviside function Θ. Modeling the LDOS of the tip and the sample as constant makes the result completely independent on the bias voltage. Despite the simplicity of this model it still can give a quite good agreement for SP-STM images to more sophisticated simulations based on DFT, as shown in Sec. 2.5.4.
The LDOS at the tip position $\mathbf{r}_T$ follows from Eq. (2.134). The total current for the non-polarized part is then given by the summation over all lattice sites, as sketched in Fig. 2.25b

$$I_0 = \sum_i \rho_0 \mathrm{e}^{-2\kappa|\mathbf{r}_T - \mathbf{r}_i|} \quad . \tag{2.139}$$

Here ρ_0 is the constant LDOS. This sum contains in principle contributions from all lattice sites, where also periodic repetitions of the magnetic unit cell have to be considered. As the contributions become exponentially smaller with an increasing distance, only lattice sites up to a certain cut-off have to be considered. The cut-off distance can be determined by convergence tests. The spin-polarized part can be calculated in the same fashion by [233]

$$I_p = \sum_i \rho_0 P_T P_S \cos(\vartheta_i) \mathrm{e}^{-2\kappa|\mathbf{r}_T - \mathbf{r}_i|} \quad . \tag{2.140}$$

Here $P_{S/T} = \frac{\rho^\uparrow - \rho^\downarrow}{\rho^\uparrow + \rho^\downarrow}$ is the spin-polarization, which results, when the LDOS is assumed to be constant. ϑ_i is the angle between $\mathbf{s}_T$, the magnetization direction of the tip, and $\mathbf{s}_i$, the magnetization direction at the lattice site i.

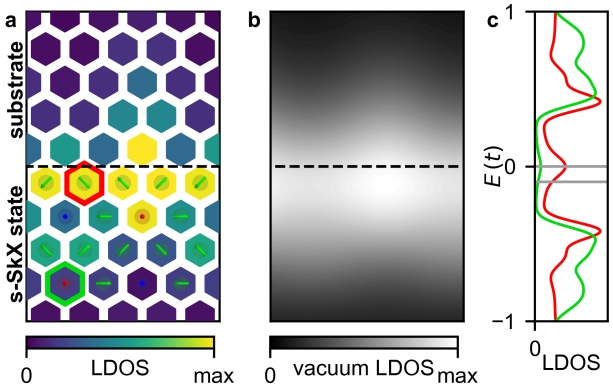

Figure 2.26: STM simulations for a edge state based on a tight-binding model. The boundary between a non-magnetic superconducting state and the SkX state for a stripe geometry is marked by a black dashed line. **a** LDOS integrated in the energy interval $E \in [-0.1, 0]$ as calculated by a tight-binding model. **b** Vacuum LDOS at a distance of 4 Å above the surface calculated from the LDOS in **a**. **c** Energy resolved LDOS for a lattice site at the boundary (red) and at a distance to the boundary (green). The positions of these lattice sites are marked in **a**. The parameters for the calculation are $t = 1, \alpha = 0, \mu = 1.5, \Delta = 0.7$, $JS = 3.0$ on the magnetic stripe and $JS = 0$ for the superconducting surface.

2.5.3 SP-STM simulations based on the tight-binding model

In contrast to the atomistic model the LDOS can be calculated explicitly via a tight-binding model. The tight-binding model used in this thesis allows only for a calculation at the lattice sites. The contribution at the position of the tip follows from Eq. (2.134).

The contributions of all atoms i are summed and the total current is given by

$$I = \int_{eV_B}^{E_F} \mathrm{d}E \sum_i \left[(\rho_i^{\uparrow}(E) + \rho_i^{\downarrow}(E)) + P_T(\rho_i^{\uparrow}(E) - \rho_i^{\downarrow}(E)) \right] \mathrm{e}^{-2\kappa d_i} \quad . \tag{2.141}$$

Note that also the current for unoccupied states could be calculated, when the bias voltage is inverted. Compared to Eq. (2.140), the angle dependency between the tip and the sample is not explicitly included, since the LDOS in the tight-binding model is already calculated with respect to the quantization axis of the tip. When tight-binding calculations are used to simulate SP-STM images in the post-processing, the LDOS has to be calculated for the quantization axis of the tip. Sec. 2.2.3 describes how the quantization axis can be adjusted in tight-binding calculations.

As the tight-binding model used in this work contains superconductivity, it allows to calculate related properties, such as emergent edge states at an interface between a topological and a trivial domain. With the spin-polarization of the tip even the spin-polarization of edge states can be modeled. An example for a STM simulation of an edge state is given in Fig. 2.26. The STM simulations were performed at an interface between a skyrmionic lattice (SkX) state and a non-magnetic stripe (cf. Fig. 2.6c). The width of each stripe is 10 unit cells, ensuring that the boundaries are sufficiently far apart.

In Fig. 2.26a the LDOS at the lattice sites integrated in the energy interval $E \in [-0.1, 0]$ is shown. This energy interval lies in the bulk band gap of the SkX state and also of the non-magnetic state. Therefore, only edge states, which exist in this energy interval (cf. Fig. 2.9), contribute to the LDOS. A large contribution exists on the first row of atoms at

the SkX side of the boundary. In Fig. 2.26b the vacuum LDOS at a height of 1.45 lattice constants is shown, which has been calculated by Eq. 2.134. With a lattice constant of 2.76 Å, as used in Pub. III, this corresponds to a height of 4 Å. This integrated vacuum LDOS represents the simulated tunnel current for a tip polarization of $P_T = 0$ (cf. Fig. 2.141). A spin-polarized SP-STM simulation would be done in the same fashion by adjusting the tip polarization. Fig. 2.26c displays the energy resolved LDOS for two lattice sites marked in Fig. 2.26a. One lattice site is located directly at the boundary (red) and one lattice site has a small distance to the boundary (green). For both a peak at zero energy is visible, while it is significantly smaller for the green-marked lattice site. The energy range, which has been used for the energy integration, is indicated by gray lines. To simulate STM measurements of edge states, the bias voltage should be chosen smaller, than the superconducting band gap. Also the robustness of the result in dependency of the bias voltage should be tested. In Pub. IV a small energy window symmetrical around the Fermi energy is used. This models a so-called zero-bias measurement, where a very small DC bias voltage is applied in the experiment. The signal is then averaged. This technique allows for measurements directly at the Fermi energy, which can be interesting to detect superconducting properties.

2.5.4 SP-STM simulations based on DFT

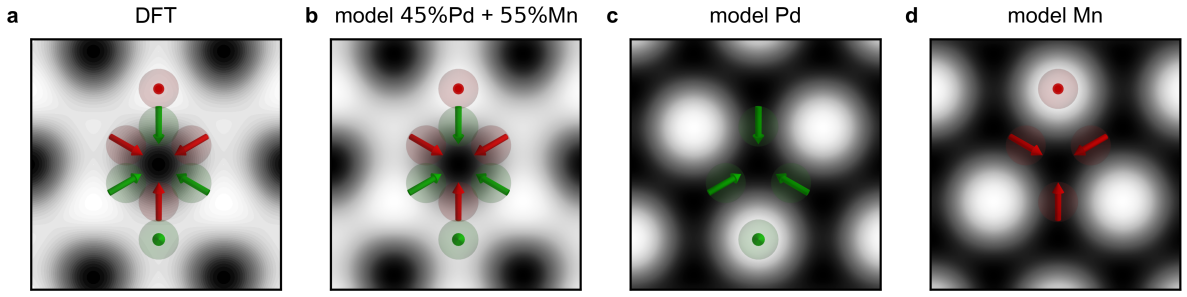

Figure 2.27: SP-STM simulations by an atomistic spin model and by DFT. The simulations are performed for a Pd/Mn bilayer on a Re(0001) substrate, hosting a 3Q state. The magnetization in the Mn layer is with 3.03 μ_B significantly larger than in the Pd layer with 0.1 μ_B. The tip magnetization is chosen perpendicular to the magnetic plane and pointing outward. The tip-sample distance is 6 Å for all calculations. **a** DFT calculated vacuum LDOS for a bias voltage of $V_B = -100$ meV.**b** superposition of **a, b**, where the Pd layer is contributing with 45% and the Mn layer with 55%. **c** atomistic model for the Pd layer. **d** atomistic model for the Mn layer.

In the previous methods the LDOS of the sample at the position of the tip $\rho(\mathbf{r}_T, E)$ was calculated from the LDOS at the sample position times an exponential function in the post-processing. The FLAPW method allows to directly calculate the wavefunction in the vacuum region due to the form of the basis wave functions. To perform a STM or SP-STM simulation first one starts with a converged charge density. Then a so-called energy slice can be created, where only energies in a certain range are considered. This energy range

needs to be set from the bias voltage to the Fermi energy which accounts for the integration in Eq. (2.136). The calculation is possible for occupied ($eV_B < 0$) and unoccupied ($eV_B > 0$) states. In the next step the charge and magnetization density on grid points in a plane can be calculated. The plane is chosen at the considered tip height. Assuming the constant LDOS and s-wave character of the tip, the non spin-polarized part is directly given by the calculated charge density. The spin-polarized contribution is given by the scalar product between the unit vector of the tip magnetization and the magnetization density, which is given as a vector by the `FLEUR` code.

In Fig. 2.27a the vacuum LDOS for a Pd/Mn bilayer on a Re(0001) substrate is shown (cf. Pub. I). The direction of the tip magnetization is perpendicular to the magnetic plane and pointing outwards. The tip spin-polarization is assumed as 100%. The Pd and the Mn layer, both host a 3Q state, where the induced magnetic moments of 0.10 μ_B in the Pd layer are significantly smaller, than the magnetic moments of 3.03 μ_B in the Mn layer. Here the question arises, which of the layers is mainly contributing to the spin-polarized tunnel current. Mn has the larger magnetic moment, but is covered by the Pd layer. For other systems it has been shown, that the main contribution does not have to originate from the top layer, but depends on shape of the occupied orbitals [247]. The SP-STM image from DFT can be interpreted by comparison with simulations using the atomistic model.

In Fig. 2.27c+d SP-STM images are simulated for a single Pd and Mn layer individually. Note, that the downward pointing magnetic moment from the Mn layer has a large contribution, although it is antiparallel to the tip magnetization. While the magnetic moment originates from the difference in the LDOS of all occupied states, it can differ in the small energy window around the Fermi energy probed by the SP-STM [248]. This can be pictured as an inversion of the spin-polarized contrast. When a superposition of the images of both layers with 45% Pd and 55% Mn is created, as shown in Fig. 2.27b, it is very similar to the SP-STM simulation by DFT. This showcases, that both layers have a similar contribution to the SP-STM signal.

Here only the spin-polarized contributions from the Mn and the Pd layer were used, although also the atomic contrast contributes to the vacuum LDOS. In general the spin-polarized contrast will be more prominent with increasing tip-sample distance. The magnetic unit cell is larger, than the chemical unit cell and the contrast of larger unit cells decays slower into the vacuum [106, 249]. In the example here, a good fit between the DFT and the atomistic model could be achieved even, when the atomic contrast is completely neglected.

The ratio of the contributions of the Mn and the Pd layer can be obtained by a fit. The atomistic model has to be calculated on the same grid as the DFT data. In Fig. 2.27 for example (100×100) grid points in the magnetic unit cell were used. For each grid point α the difference between the DFT value and the atomistic values is weighted with a constant

c_1 and c_2. The sum over the squares of these differences given by

$$\sum_{\alpha} \left(I^{\alpha}_{\mathrm{DFT}} - c_1 I^{\alpha}_{\mathrm{Pd}} - c_2 I^{\alpha}_{\mathrm{Mn}} \right)^2 \tag{2.142}$$

is the minimized with respect to c_1 and c_2. This least squares fit gives the contributions of the individual layers, and can be also expanded to more layers. For spin-polarized simulations the constants c_1 and c_2 can have negative values, since the spin-polarization in a small energy range close to the Fermi energy does not have to coincide with the spin-polarization of all occupied states [248].

3 Overview of results

This chapter gives a broad overview over the results obtained in this PhD thesis. A more detailed discussion can be found in the publications reprinted in Chap. 5 to 8. The results can be separated into two parts. In the first part the spin structures of realistic magnetic materials are investigated via density functional theory (DFT) and spin-polarized scanning tunneling microscopy (SP-STM) simulations, which are compared to experiments performed by our collaborators Dr. K. von Bergmann *et al.* from the University of Hamburg (Pub. I and Pub. II). These systems use a Re(0001) substrate, which becomes superconducting below 1.7 K.

The second part (Pub. III and Pub. IV) focuses on topological superconductivity in magnet-superconductor-hybrid (MSH) systems. Here a tight-binding model is used to investigate the effect of complex magnetic structures on the state of the superconducting substrate. Topological superconductivity can be induced by the spin textures even for conventional s-wave superconductors. A variety of non-coplanar spin textures, including those found in Pub. I and Pub. II, are investigated in Pub. III with respect to strong topological superconductivity. Pub. IV examines topological nodal point superconductivity (TNPSC), induced by a collinear antiferromagnetic (AFM) state and focuses also on properties of topological edge states such as spin-polarization and decay length.

The non-coplanar structure and large tilting angles of the magnetic triple-q (3Q) state [179] can lead to interesting phenomena [88, 250, 251], such as a topological Hall effect [252, 253] or topological superconductivity [88]. It has four magnetic moments in the unit cell, which form tetrahedral angles (Fig. 3.1c,d). Although the magnetic spin moments are compensated over the unit cell topological orbital moments (TOMs) arise and order with a ferromagnetic alignment. The topological orbital moment (TOM) depends on the scalar spin chirality $\chi_{ijk} = \mathbf{s}_i \cdot (\mathbf{s}_j \times \mathbf{s}_k)$, which can be viewed as a measure of the topology of a spin texture [57]. As the scalar spin chirality breaks time-reversal symmetry, it can lead to interesting transport properties, such as the topological Hall effect [225].

In Pub. I it is shown, that the ideal 3Q state will always orient in a specific highly-symmetric orientation with respect to the atomic lattice. This allows to differentiate ideal and distorted 3Q states. In the ultra-thin film system Mn/Re(0001) the 3Q state has been found on a surface, allowing for direct observation via SP-STM [103]. SP-STM measurements in comparison to simulations, which are shown in Fig. 3.1a, reveal a specific orientation of the 3Q state on the surface. Here the spin state couples in the so-called $3Q^3$ orientation, where two spins are oriented within the magnetic Mn layer. This is sketched in Fig. 3.1c and can

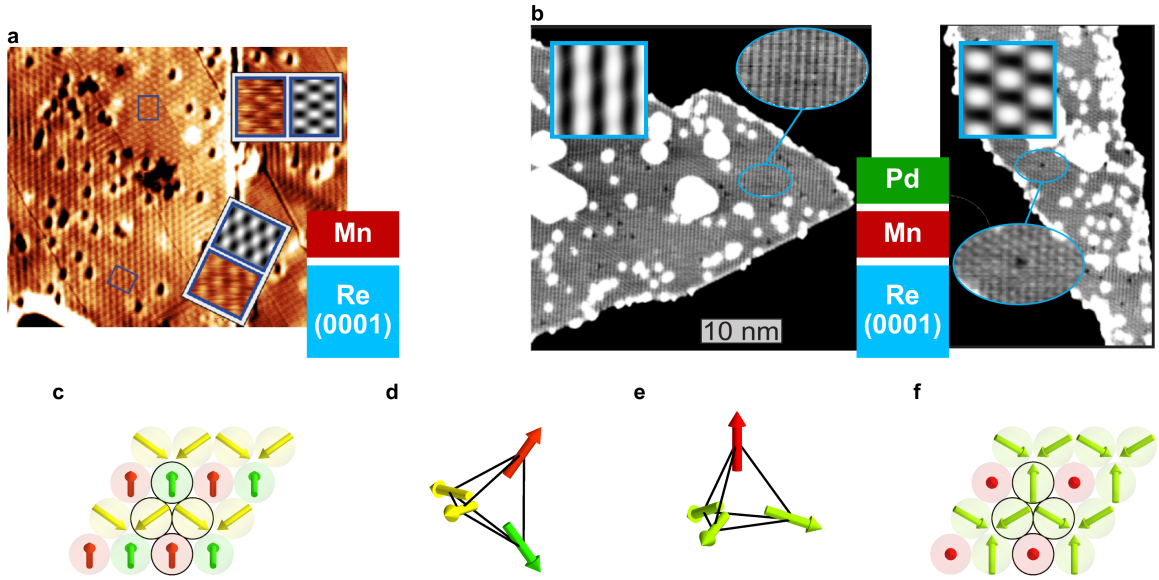

Figure 3.1: 3Q state in Mn/Re(0001) and Pd/Mn/Re(0001). **a** SP-STM measurements of a Mn monolayer on a Re(0001) substrate, showing two rotational domains of the $3Q^3$ state. **b** SP-STM images of two Pd/Mn/Re(0001) islands. Due to a step edge is the spin structure 180° rotated between both islands. The insets show SP-STM simulations for the $3Q^1$ state based on DFT. The orientation of the spin structures in the simulations reflect the two islands. **c** The $3Q^3$ state on a hexagonal lattice. **d** Tetrahedron representation of the $3Q^3$ orientation. **e** Tetrahedron representation of the $3Q^1$ orientation. **f** The $3Q^1$ state on a hexagonal lattice. The figure is modified from Ref. [103] and Pub. I with permission of APS.

be visualized as a tetrahedron in a specific orientation (Fig. 3.1d). For this $3Q^3$ orientation three rotational domains exist, two of them can be seen in the sample area of Fig. 3.1a.
In Pub. I similar systems were investigated, where an additional Pd or Rh adlayer has been grown on Mn/Re(0001) (see sketch in Fig. 3.1b). In Fig. 3.1b SP-STM measurements for two islands of Pd/Mn bilayers on a Re(0001) substrate are shown. The spin structure is rotated by 180° between the two islands due to a step edge, yielding effectively two tip magnetization directions in a single image. On both islands no rotational domains exist, which is a qualitative difference to Mn/Re(0001). The insets show SP-STM simulations for the $3Q^1$ state (see Fig. 3.1e+f), based on DFT calculations. A comparison to SP-STM simulations by an atomistic model reveals, that the Pd and the Mn layer contribute roughly equal to the spin-polarized current (cf. Fig. 2.27). Both simulations use the same spin texture, which is rotated by 180° to model the two islands from Fig. 3.1b. These simulations are in very good agreement with the experiment. In the $3Q^1$ orientation one spin is pointing out of the magnetic plane and the other three spins have the same z-component, which can be represented by a tetrahedron in Fig. 3.1e. This orientation is rotational symmetric around the surface normal and does not exhibit any rotational domains.

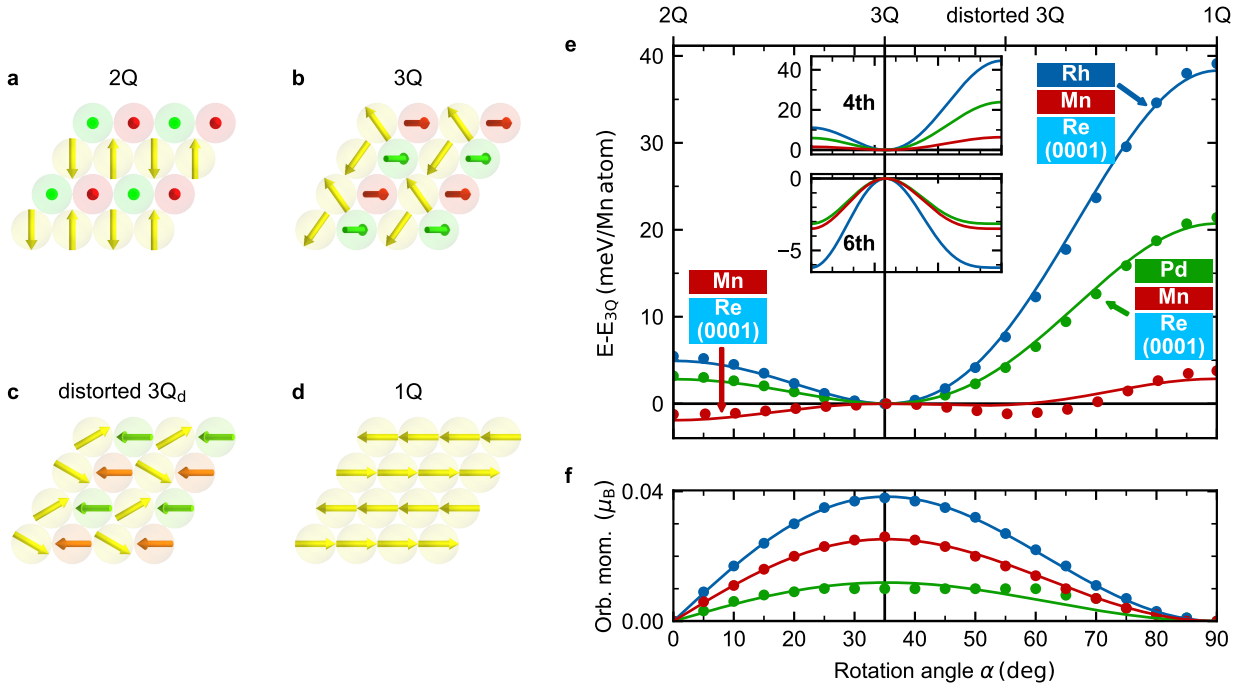

Figure 3.2: HOI and TOM along the 2Q-3Q-1Q path. a-d Four spin structures of the 2Q-3Q-1Q path are shown: the 2Q, 3Q, distorted 3Q and 1Q state, respectively. **e** The total energy along the path, calculated via DFT and neglecting SOC interactions, is marked by points for a Mn monolayer, a Pd/Mn bilayer and a Rh/Mn bilayer on the Re(0001) surface. The solid lines represent a fit to the 4^{th} and 6^{th} order HOI. The contributions are displayed separately in the insets. **f** Orbital moments, calculated via DFT. Due to the absence of SOC these can be attributed to the TOM. The figure is modified from Pub. I with permission of APS.

This leads to a qualitative difference between 3Q^1 and 3Q^3 orientation in SP-STM measurements. Both states can be transformed into each other by a global spin rotation. So far it was unclear, what leads to the different coupling of the spin texture to the atomic lattice.

In Pub. I total energy calculations by DFT and an atomistic model are used to find the magnetic ground state and orientation with respect to the atomic lattice. DFT calculations show that the 3Q state is energetically favored in contrast to the corresponding 1Q state, the RW-AFM, for Mn/Re(0001) [103, 104] as well as Pd/Mn/Re(0001) (Pub. I). However, the energy difference between 3Q and 1Q is larger for Pd/Mn/Re(0001).

In general multi-Q states can be stabilized by higher-order exchange interactions (HOI) [41, 58]. The effect of HOI can be seen for a continuous transformation from the 2Q over the 3Q to the 1Q state, which is illustrated in Fig. 3.2a-d. All states along this path are superpositions of spin spirals and are degenerate with respect to the Heisenberg exchange energy and the DMI. Total energy calculations via DFT along this path, shown in Fig. 3.2e, reveal that the ground state of Mn/Re(0001) is a distorted 3Q state [104], while it is the ideal 3Q state for Pd/Mn/Re(0001) (Pub. I). For this distorted 3Q state one of the 1Q states has a larger contribution, than the other one (cf. Ref. [104, 179]). By fitting an atomistic model on the DFT data, HOI of the 4^{th} and the 6^{th} order can be differentiated. A frustration of the 4^{th} order in combination with 6^{th} order HOI in Mn/Re(0001) leads to the distorted 3Q state

[104]. This frustration is lifted with the additional Pd or Rh layer, resulting in the ideal 3Q state as the ground state (Pub. I).

Spin-orbit coupling (SOC) effects can couple the spin structure to the atomic lattice. The distorted 3Q state in Mn/Re(0001) couples in the $3Q^3$ orientation, whereas the ideal 3Q state in Pd/Mn/Re(0001) and Rh/Mn/Re(0001) couples in a $3Q^1$ orientation. This suggests, that the orientation is linked to a possible distortion of the 3Q state.

The DMI does not prefer a specific orientation for all states along the path. Pub. I shows that, depending on the sign, the magnetocrystalline anisotropy energy (MAE) favors a specific orientation of nearly all states. The ideal 3Q state is the only exception, where all orientations are degenerate with respect to the MAE, due to the symmetry of the magnetic structure. A 3Q state, which is distorted toward the 1Q state, will orient in a $3Q^2$ orientation for an easy-axis MAE and in a $3Q^3$ orientation for an easy-plane MAE. This is consistent with the $3Q^3$ orientation of the distorted 3Q state in Mn/Re(0001) [104]. A typically even weaker interaction, the anisotropic symmetric exchange (ASE), can lift the energetic degeneracy of all orientations even for the ideal 3Q state. Independent of its sign, it favors the $3Q^1$ orientation (Pub. I).

Due to the lack of rotational domains the $3Q^1$ states looks qualitatively different than the $3Q^2$ or $3Q^3$ state in SP-STM images. Therefore, the ideal and distorted 3Q states can be differentiated by their orientation. This is especially interesting, as the ideal 3Q state has the largest topological orbital moments along the 2Q-3Q-1Q path (Fig. 3.2f).

The topological orbital moments cannot only form a ferromagnetic pattern but also an antiferromagnetic one as it could be shown in Pub. II. For a Fe monolayer on three Ir layers on a Re(0001) substrate a nearly rectangular unit cell is observed via SP-STM measurements (see Ref. [155] and Pub. II) . Due to different rotational domains a non-coplanar spin structure is suggested by the experiment. DFT calculations, performed in this thesis, reveal a strong exchange frustration and significant HOI (Pub. II). Under the constraint of a constant magnetic moment a multi-Q state can be constructed from two spin spirals [41]. A multi-Q state, consistent with the unit cell from the SP-STM measurements, is shown in Fig. 3.3a. The spin spirals, that are used for the superposition are shown in Fig. 3.3b+c. This multi-Q state has 16 atoms in the unit cell, where two substructures can be identified, which are marked by purple dashed lines. One of the structures resembles an atomic-scale skyrmion (S) and the other one an antiskyrmion (A). Although these are on an atomic scale and form no isolated spin structures, the skyrmionic and antiskyrmionic structure have an opposite topology in terms of their scalar spin chirality, which manifests in a topological orbital moment (TOM). This TOM is always perpendicular to the magnetic plane. The sign and strength of the TOM, calculated by DFT, is indicated by colored hexagons. Note that the topological charge, that is often used for the classification of isolated spin texture cannot be defined for these atomic scale lattices (cf. Sec. 2.4.8). This multi-Q state is energetically clearly preferred over the spin spirals, used for its construction.

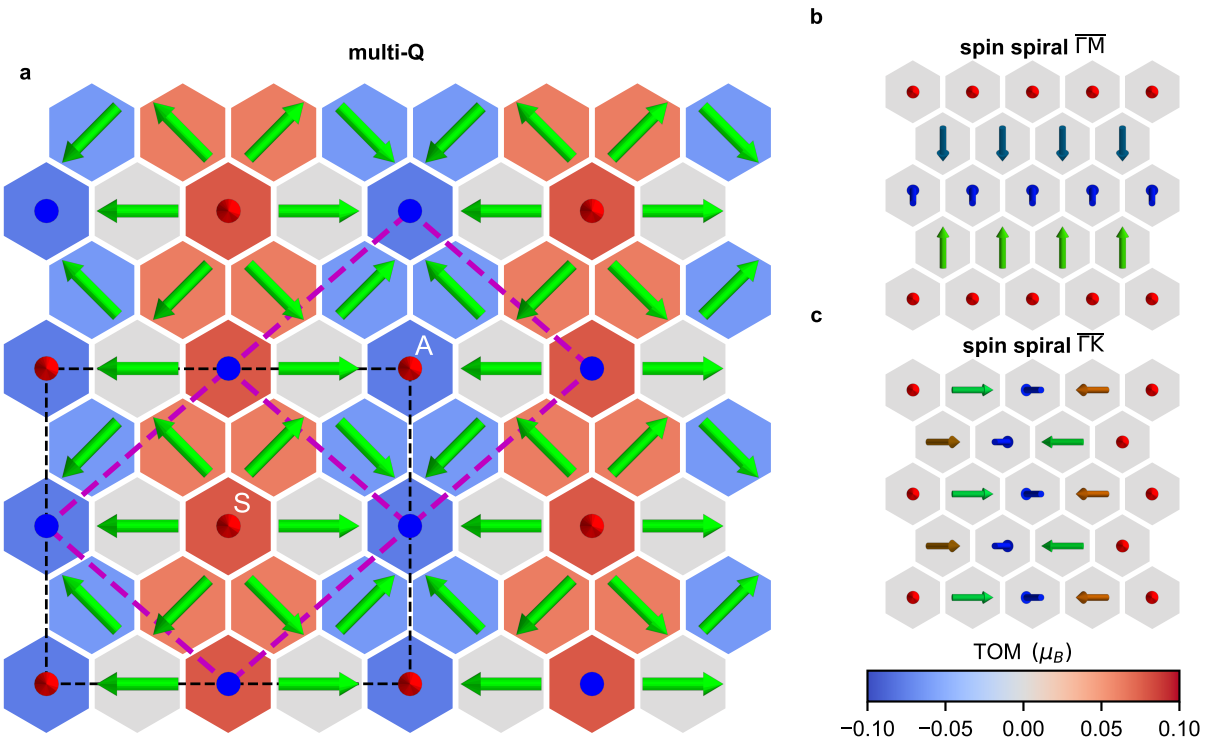

Figure 3.3: Spin structure and topological orbital moments of a multi-Q state. **a** The multi-Q state is energetically preferred over spin spirals by HOI. It can be constructed from two perpendicular spin spirals along the **b**$\overline{\Gamma M}$ and **c** $\overline{\Gamma K}$ direction. The spin spirals have a vanishing TOM and are therefore considered as a trivial topology. The multi-Q state has a non-zero TOM as calculated by DFT. Red (blue) color denotes upwards (downwards) pointing TOM with respect to the surface normal. The centers of atomic-scale substructures of the spin lattices are denoted by letters: skyrmionic (S) and antiskyrmionic (A). The figure is modified from Pub. II with permission of npj Spintronics.

While the multi-Q state is not consistent with SP-STM measurements, similar states can be obtained by small modifications of the spin structure, that can explain the experimental data. These states, constructed from the multi-Q state, also have a significant lower energy than any spin spiral state (see Pub. II).

However DFT total energy calculations clearly show, that a non-coplanar spin texture will form the ground state, which is stabilized by the 4site-4spin interaction (Pub. II). For the multi-Q state the TOM is forming a row-wise antiferromagnetic pattern. The skyrmionic and antiskyrmionic contributions are exactly compensating over the unit cell for the multi-Q state. This reflects the opposite topology of the two spin structures. The TOM calculated via DFT is in very good agreement with the atomistic model, that depends on the scalar spin chirality [56]. This system shows, that the superposition of two topological trivial spin spiral states can lead to a non-coplanar spin texture with non-trivial topology. This superposition is stabilized by HOI.

All systems investigated by DFT, Pd/Mn/Re(0001), Rd/Mn/Re(0001) and Fe/Ir-3/Re(0001), are on a Re substrate, which becomes superconducting at 1.7 K. Therefore, these systems

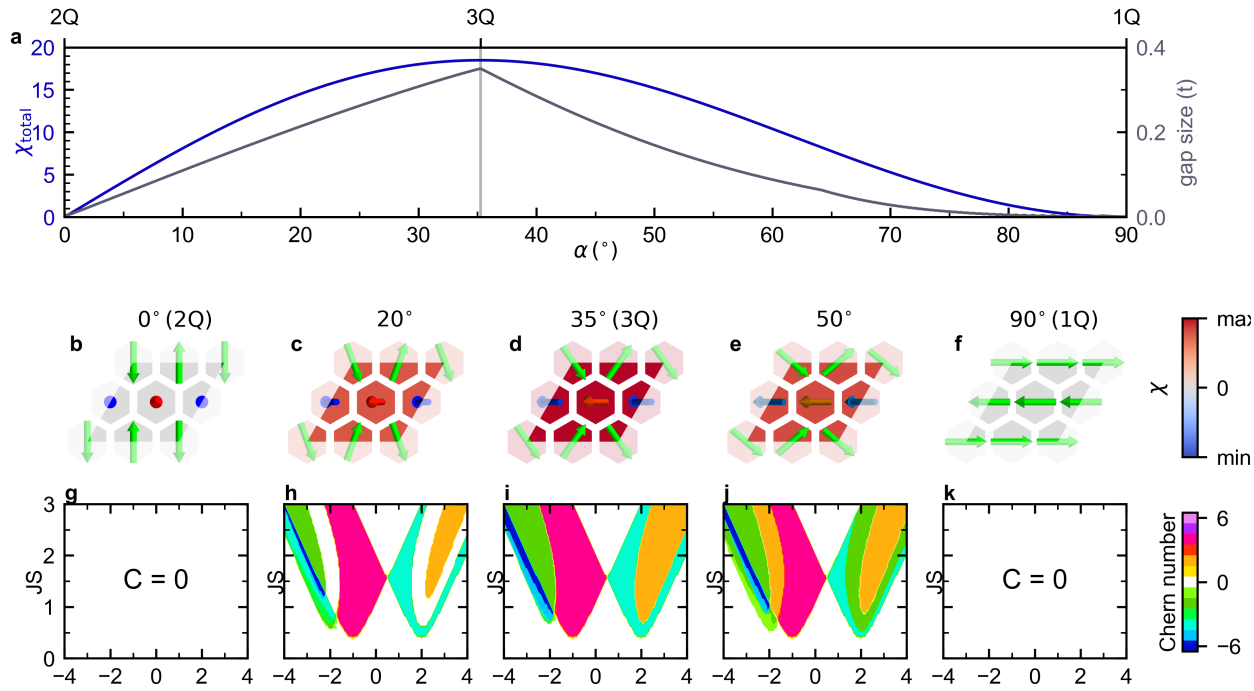

Figure 3.4: Topological superconductivity induced by states along the 2Q-3Q-1Q path. a Scalar spin chirality of the spin state and minimal size of the band gap in the adjacent superconductor. **b-f** The spin texture for five states along the path is shown. The color of the hexagons indicates the scalar spin chirality. **g-k** Chern number as calculated via a tight-binding model. Here the parameters μ and JS are varied. The parameters for the tight-binding calculations are $t = 1, \Delta = 0.4, \alpha = 0$ and $\mu = -1, JS = 1$ for **a** and $0 \leq JS \leq 3, -4 \leq \mu \leq 4$ for **g-k**. The figure is modified from Pub. III with permission of npj Spintronics.

form a promising MSH platform with non-coplanar complex spin textures in the vicinity of a superconductor. In Pub. III a tight-binding model is used to investigate which of these atomic-scale spin structures can induce topological superconductivity. The topology of the spin textures is thereby quantified by the scalar spin chirality.

A tight-binding model allows to vary the interaction parameters and the spin texture. Therefore, a general trend for the connection between the topology of the spin structure and the topological superconductivity can be estimated.

Topological superconductivity is known to emerge for a FM structure under the influence of SOC. To isolate the effect of the spin topology, SOC is neglected in Pub. III. In Fig. 3.4a the total scalar spin chirality of the unit cell for the 2Q-3Q-1Q path is shown. For five states along this path the spin structure and the lattice site resolved scalar spin chirality is depicted in Fig. 3.4b-f. The scalar spin chirality for all states is homogeneous over the lattice. It is vanishing for the coplanar 2Q state and the collinear 1Q state. For all other states it is non-zero and maximized for the 3Q state. For each of the states along the path the band structure can be calculated via the tight-binding model. The superconducting order parameter of the model defines the bandgap in the absence of a magnetic layer. When the magnetic layer is introduced, the band gap will be reduced. The minimal band gap of the 2D-BZ is shown in gray in Fig. 3.4a. The band gap is maximal for the 3Q state

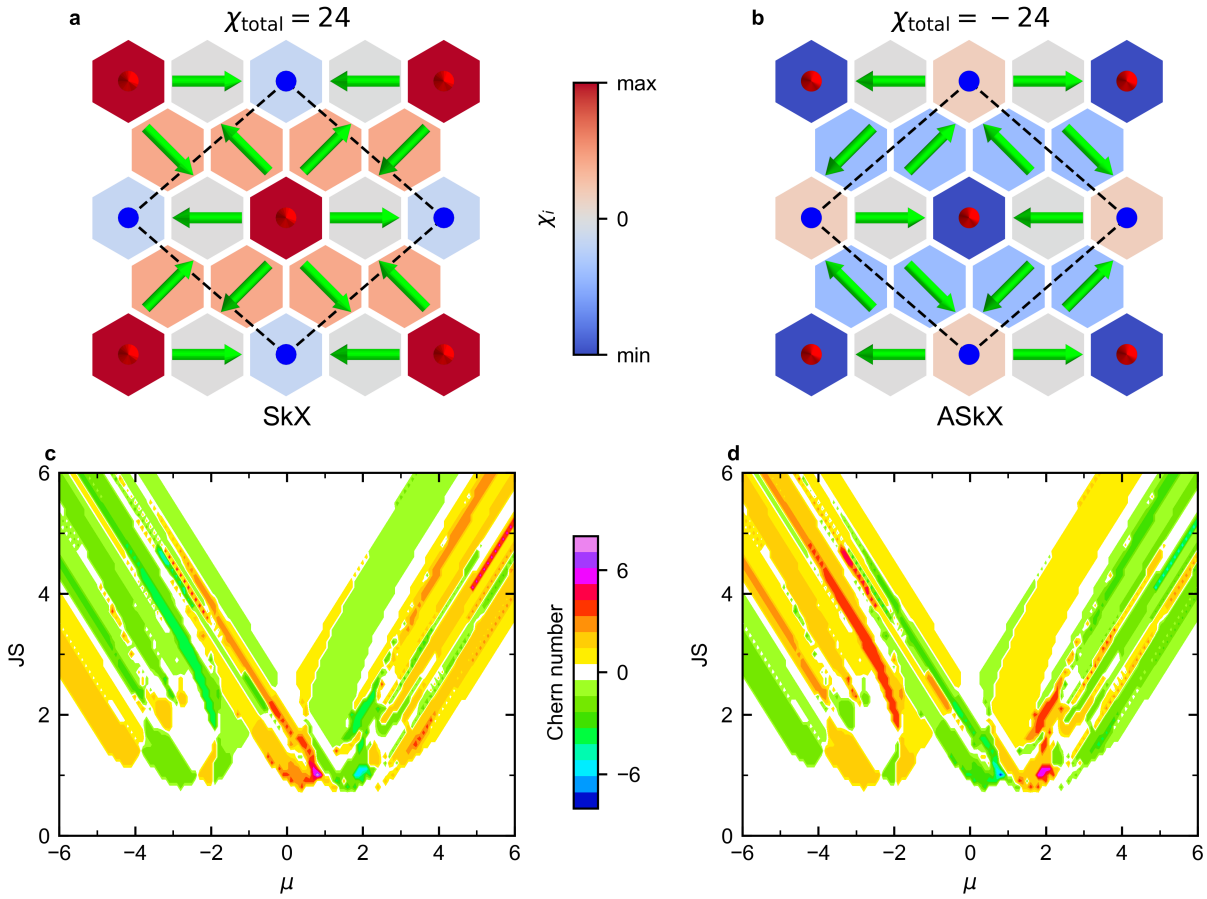

Figure 3.5: Topology of a skyrmionic and antiskyrmionic lattice. The real space topology of the spin texture is reflected by the scalar spin chirality marked by colored hexagons for the **a** SkX and **b** ASkX state, which contain a skyrmionic respectively antiskyrmionic spin texture on the atomic scale. The spin texture is indicated by colored arrows and the unit cell is marked by black dashed lines. The Chern numbers for a MSH system containing the SkX or ASkX lattice are given in **c** for the SkX and in **d** for the ASkX state as a function of the chemical potential, μ, and coupling strength, JS. The other parameters of the tight-binding calculation are $t = 1, \alpha = 0, \Delta = 0.7$. The figure is modified from Pub. III with permission of npj Spintronics.

and reducing toward the 2Q and 1Q state, where it is completely vanishing. The band gap does not follow the same function as the scalar spin chirality, but has the same trend. The states with large scalar spin chirality lead to a comparably large band gap. For a distorted 3Q state at $\alpha = 55°$, which could be the ground state in Mn/Re(0001) [104], the band gap is only around half of the band gap of the ideal 3Q state. This showcases, why the experimental distinction between the ideal and distorted 3Q state can be crucial. In Fig. 3.4g-k the Chern numbers are shown as function of the chemical potential, μ, and the coupling strength, JS.

For the 2Q and 1Q state the Chern numbers are vanishing for the whole investigated phase space. Hence, both states induce no strong topological superconductivity. For all other states along the path the Chern number is non-zero for large parts of the phase space. This holds true even for states with small scalar spin chirality, i.e. close to the 2Q or 1Q state. Strong topological superconductivity can be induced by all, even slightly,

non-coplanar states along the path. However, the band gap scales roughly with the scalar spin chirality, which makes states with a large scalar spin chirality especially interesting for an experimental realization (see Pub. III).

Besides the 3Q state also the multi-Q state, shown in Fig. 3.3a, has a significant scalar spin chirality. Surprisingly no topological superconductivity was found for this state (Pub. III). Differing from the 3Q state, the multi-Q state has a non-homogeneous scalar spin chirality. Over the magnetic unit cell the contributions of the skyrmionic and antiskyrmionic structure are compensating and the total scalar spin chirality is vanishing. By a periodic repetition of only the skyrmionic or antiskyrmionic part the so-called skyrmionic lattice (SkX) and the antiskyrmionic lattice (ASkX) can be constructed. These states are shown in Fig. 3.5a+b, with the unit cell indicated by black dashed lines. Both structures have a non-zero total scalar spin chirality, which is $\chi_{\text{total}} = 24$ for the SkX and exactly opposite for the ASkX lattice. Both spin textures can induce topological superconductivity, which is reflected by non-zero Chern numbers obtained via the tight-binding model for large parts of the phase space (Fig. 3.5c+d). Furthermore, the Chern number for the SkX lattice is exactly opposite to the Chern number of the ASkX lattice for all values of μ and JS. This suggests, that besides the scalar spin chirality also the Chern number is compensated for the multi-Q state (Fig. 3.3). Note, that both lattices have the exact opposite scalar spin chirality, but cannot be transformed into each other by inversion, instead they form independent spin textures. These findings from Pub. III suggest, that a connection between the topology in spin space and topological superconductivity exists and that the total scalar spin chirality can be a good measure to identify interesting states for topological superconductivity. Although the effect of SOC was neglected in this study, test calculations demonstrate that the results are stable against including SOC (see Supplementary Information of Pub. III).

Non-zero Chern numbers indicate strong topological superconductivity which manifests in edge states all around the boundary of a magnetic island and an open band gap on the island. But even, when the bandgap is closed at specific points of the 2D-Brillouin zone, TNPSC can exist. Here the formation of edge modes depends on the crystallographic direction of the edge. TNPSC can for example occur for an AFM spin structure, when SOC is considered [39, 91].

While for strong topological superconductors the number of edge modes coincides with the difference in the topological invariant, boundaries between two different nodal point superconductors have not been investigated so far.

In Pub. IV a Mn monolayer (ML) and bilayer (BL) on a superconducting Ta(110) substrate were investigated. Motivated by experiments of our collaborators, both are considered to be TNPSC and step edges create boundaries between both phases. In the tight-binding model the ML and BL are represented by different sets of parameters. The band structures near the Fermi energy are shown in Fig. 3.6a+b The BL has four nodal points, while the ML has six.

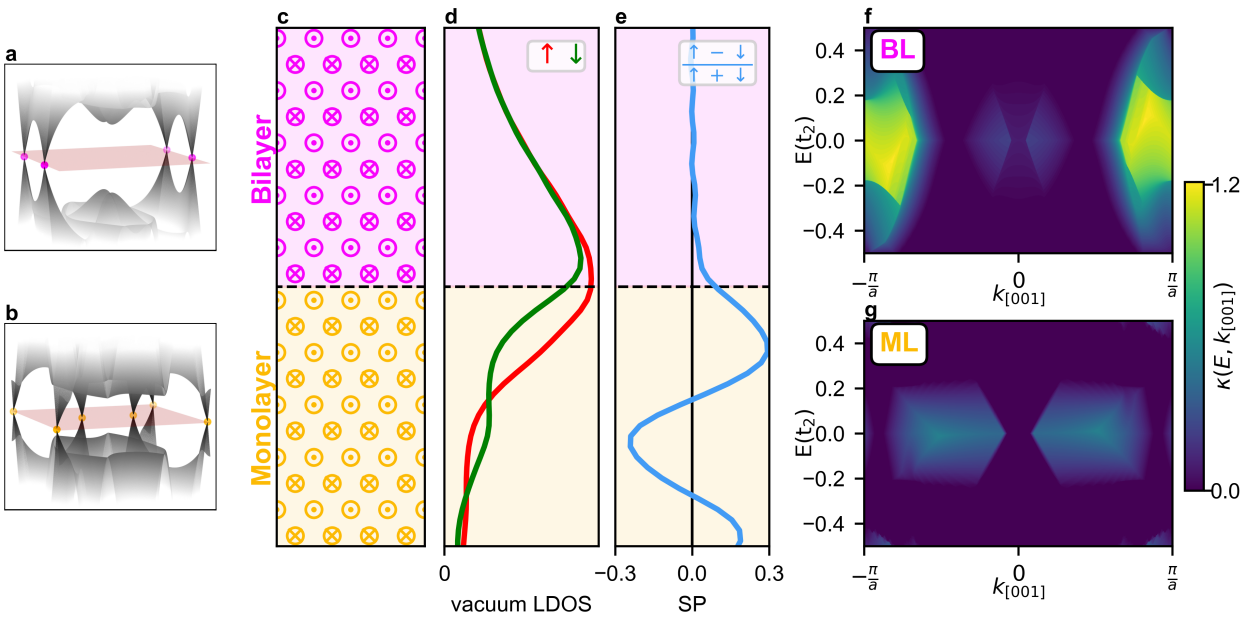

Figure 3.6: Spin-polarized edge state at the interface of two TNPSC. The band structures close to the Fermi energy (red sheet) is shown for **a** the bilayer and **b** the monolayer. The position of the nodal points is highlighted. **c** Sketch of the spin structure of an edge along the [001] direction. **d** Integrated signal form zero-bias SP-STM simulations for 100 % tip polarization, a tip height of 4 Å and a decay parameter of 1 $Å^{-1}$. **e** Spin-polarization calculated from **d**. **f, g** decay constants for surface states $\kappa(E, k_{[001]})$ for the bilayer and the monolayer , respectively. For details on the calculations and the parameters of the tight-binding calculations see Pub. IV. The figure is modified from Pub. IV.

Experimental SP-STM measurements reveal the existence of edge states for a boundary along the [001] direction between the ML and the BL (see Pub. IV). The boundary for this edge is sketched in Fig. 3.6c. Integrated zero-bias SP-STM simulations in Fig. 3.6d show a maximum for a ↑ and a ↓ polarized tip near the boundary, representing an edge mode. Both polarizations differ in their contribution, leading to a spin polarization of up to 30 % (Fig. 3.6e). This is quite a surprising result, as the ML and BL terminate at the boundary with the opposite orientation of the magnetic moments. The reason for this spin-polarization lies in the different decay lengths of the edge state into the ML and the BL, which is demonstrated in Pub. IV. The faster decay into the ML can be seen in the vacuum LDOS (Fig. 3.6d) for both spin-polarizations. Due to the comparably fast decay the contributions of the AFM spin texture cannot compensate, leading to a spin polarization of the edge state defined by the termination of the ML.

The decay length of surface states depends on the electronic structure and can be calculated via the complex band structure. In Fig. 3.6f+g the energy and $k_{[001]}$ resolved decay parameters $\kappa(E, k_{[001]})$ are given. The darkest areas with $\kappa = 0$ correspond to the bulk band structure. The comparison of κ for the ML and BL show, that the decay of surface states is quite different, due to the different electronic structure. Generally the decay is faster, the further a state is from bulk states. This makes different decay length of edge states and consequently a spin polarization for AFM structures a general phenomenon.

4 Summary

This work presents complex magnetic structures in realistic magnet-superconductor-hybrid (MSH) systems which can also be studied experimentally. Furthermore, the effects of the spin texture on the superconducting state is studied. Thereby, this thesis bridges the gap between the spin topology and the topology of the superconducting substrate.

As an example of an MSH system, Fe/Ir-3/Re(0001) is shown in Fig. 4.1. The Fe layer hosts a complex spin structure, such as the atomic-scale skyrmionic lattice (SkX), while the Re substrate can be superconducting. Despite the presence of Ir interlayers the magnetic moments can interact with the superconducting substrate, as indicated by purple springs in Fig. 4.1a. The non-trivial spin texture manifests e.g. in topological orbital moments (TOMs) or non-trivial transport properties. A topological superconducting phase leads to the emergence of topologically protected Majorana modes, which are of great interest, e.g. for topological quantum computing. A central question is whether the topology of the spin texture is connected to the topology of the superconducting phase. While several topological spin textures are known to induce topological superconductivity [88, 89, 100] a systematic investigation has not been made.

In this work various spin textures of different topology are investigated in their ability to induce topological superconductivity in conventional superconductors. To examine the connection between spin structure and superconducting phase, continuous transformations between trivial and topological spin textures are considered. The topology of the spin texture is measured by the scalar spin chirality $\chi_{ijk} = \mathbf{s}_i \cdot (\mathbf{s}_j \times \mathbf{s}_k)$, which is non-zero for non-coplanar spin textures, as sketched in Fig. 4.1a. The scalar spin chirality is a good measure of spin topology, as non-coplanar spin structures break the time-reversal symmetry even when the net magnetic moment is compensated. This leads to measurable effects like the topological Hall effect or TOMs. Both originate from a preferred chirality of electronic motion, as indicated a black circular arrow in Fig. 4.1b. For the SkX lattice the total scalar spin chirality is non-zero, which indicates a non-trivial spin topology.

The superconducting properties of the MSH system depend on the band structure, which is shown in the 2D-BZ in Fig. 4.1c. The two bands correspond to the first band under and above the Fermi energy, respectively. The distance between both bands corresponds to the superconducting bandgap. The topology of the electronic structure is reflected in the Berry-curvature, which is indicated on the sheet at the Fermi energy. Positive and negative contributions are marked in red and blue, respectively.

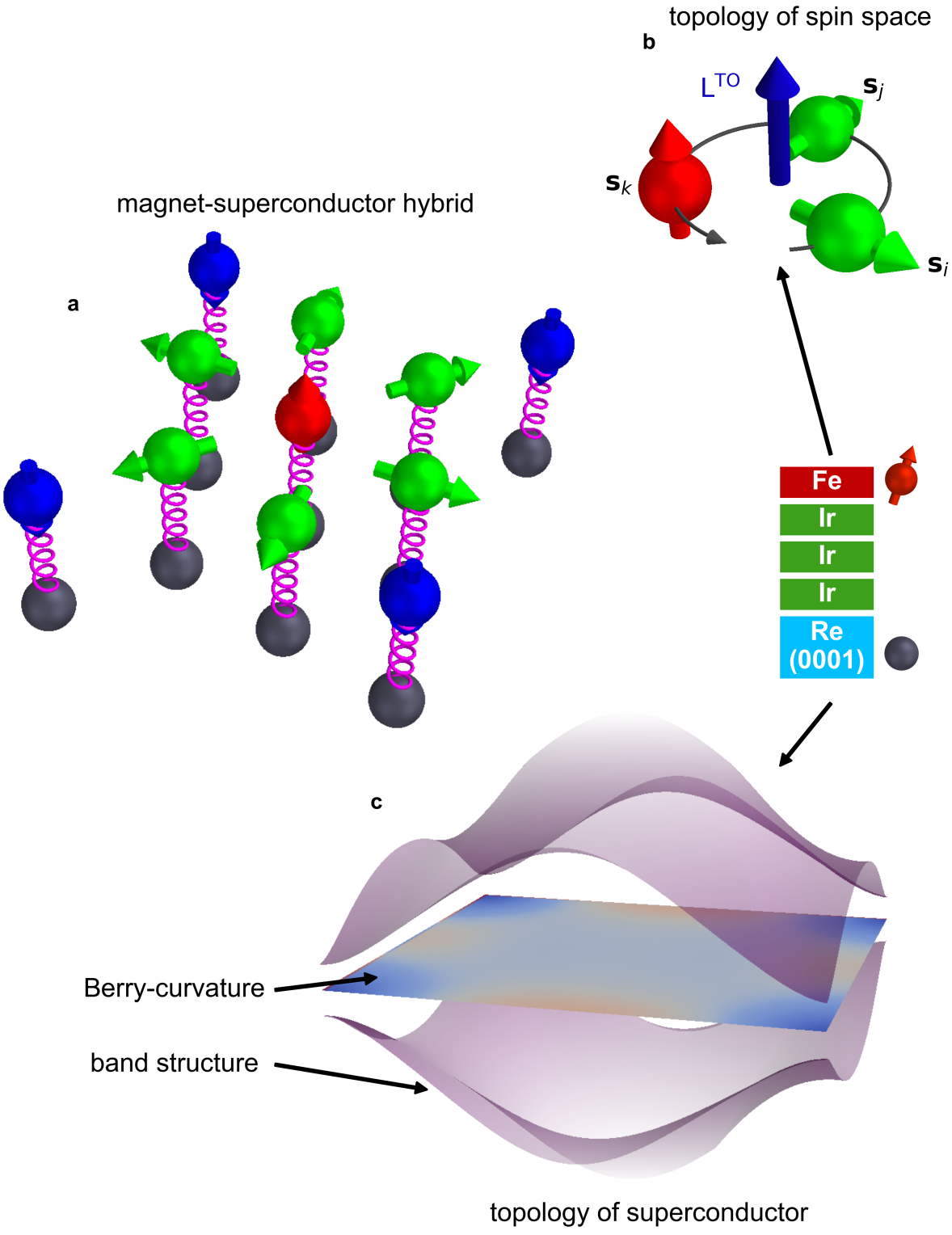

Figure 4.1: Sketch of Fe/Ir-3/Re(0001) as an exemplary MSH system. a The arrows and colored spheres represent the directions of magnetic moments and atoms in the magnetic layer. The black spheres represent atoms from the superconducting substrate and the coupling between both is indicated by springs. **b** Three lattice sites of the SkX state and an exemplary preferred chirality of electronic motion (round black arrow). The resulting TOM is indicated by a blue arrow. **c** The first bands above and below the Fermi energy are shown in purple. The distance between both bands therefore amounts to the band gap. The colored sheet is located at the Fermi energy and the red (blue) colors represent a positive (negative) Berry curvature. The Chern number is given by the 2D-BZ integral of the Berry curvature, which here amounts to $C = -1$. The tight-binding parameters for the band structure and the Berry-curvature are $t = 1, \mu = 1, \Delta = 0.7, JS = 3$.

The topological phase is determined by a topological invariant, the Chern number, calculated as the BZ-integral of the Berry-curvature. For this example the Chern number is $C = -1$, which is a topological superconducting phase. This showcases that, for the SkX state, a non-trivial spin topology coincides with topological superconductivity.
To find topological spin structures that exist in realistic MSH systems, several methods were combined in this thesis. For systems such as Pd/Mn/Re(0001) or Fe/Ir-3/Re(0001) the magnetic ground state was identified using DFT. The magnetic interactions, which stabilize the ground state are interpreted by a parametrized atomistic spin model. Via spin-polarized scanning tunneling microscopy (SP-STM) simulations, the theoretical data can be compared to experimental data of collaborators from the University of Hamburg.
In Pub. I the ideal 3Q state with homogeneous topology was found as the ground state of Pd/Mn/Re(0001) and Rh/Mn/Re(0001). Further it is shown that the orientation of the 3Q state on the atomic lattice depends on a possible distortion.
Pub. II presents atomic-scale skyrmion lattices with non-homogeneous spin topology for Fe/Ir-3/Re(0001). The TOM, reflecting the topology, forms an antiferromagnetic pattern. Higher-order exchange interactions (HOI) could be identified as crucial interactions to stabilize atomic-scale skyrmionic lattices, while the size of the unit cell is predominantly defined by the exchange interaction and Dzyaloshinskii-Moriya interaction (DMI).
In Pub. III a tight-binding model is applied to investigate the effect of various spin textures on the superconducting substrate. This includes the ground states found in Pub. I and Pub. II. STM simulations demonstrate how the signatures of topological protected edge modes would manifest in experiments. The calculations suggest a correlation between spin topology and topological superconductivity.
Mn mono- and bilayers on the Ta(110) surface form a model system for two different topological nodal point superconductors (TNSCPs). Pub. IV demonstrates that spin-polarized edge modes exist between both domains. Edge modes between two different TNSPC domains have not been reported before. The spin-polarization can be attributed to different decay length of the edge state in the mono- and the bilayer.
Overall various non-trivial spin textures in realistic MSH systems were found and their stabilizing mechanisms identified. The TOM, a measurable quantity dependent on the spin topology, is analyzed. Topological superconductivity is predicted for several atomic-scale spin structures and a connection to the spin topology is indicated.

5 Coupling of the triple-Q state to the atomic lattice by anisotropic symmetric exchange

Name: Coupling of the triple-Q state to the atomic lattice by anisotropic symmetric exchange

Published: Physical Review B **108**, L180411 (2023)

DOI: https://doi.org/10.1103/PhysRevB.108.L180411

Authors: **Felix Nickel**, André Kubetzka, Soumyajyoti Haldar, Roland Wiesendanger, Stefan Heinze, Kirsten von Bergmann

Author contributions: A.K. and K.v.B performed the experimental measurements and analyzed the data. **F.N.** performed the DFT calculations for Pd/Mn/Re(0001) and Rh/Mn/Re(0001), all atomistic spin simulations and SP-STM calculations. **F.N.** and S.He. analyzed the theoretical data. K.v.B, S.He. and **F.N.** wrote the manuscript with contributions of all authors.

Letter

Coupling of the triple-q state to the atomic lattice by anisotropic symmetric exchange

Felix Nickel,[1,*] André Kubetzka,[2] Soumyajyoti Haldar,[1] Roland Wiesendanger,[2] Stefan Heinze,[1,3] and Kirsten von Bergmann[2,†]

[1]*Institut für Theoretische Physik und Astrophysik, Christian-Albrechts-Universität zu Kiel, D-24098 Kiel, Germany*
[2]*Department of Physics, University of Hamburg, Jungiusstraße 11, 20355 Hamburg, Germany*
[3]*Kiel Nano, Surface, and Interface Science (KiNSIS), University of Kiel, 24118 Kiel, Germany*

(Received 18 July 2023; accepted 8 November 2023; published 30 November 2023)

We identify the triple-**q** (3Q) state as magnetic ground state in Pd/Mn and Rh/Mn bilayers on Re(0001) using spin-polarized scanning tunneling microscopy and density-functional theory. An atomistic model reveals that in general the 3Q state with tetrahedral magnetic order and zero net spin moment is coupled to a hexagonal atomic lattice in a highly symmetric orientation via the anisotropic symmetric exchange interaction, whereas other spin-orbit coupling terms cancel due to symmetry. Our experiments are in agreement with the predicted orientation of the 3Q state. A distortion from the ideal tetrahedral angles would lead to other orientations of the 3Q state with a reduced topological orbital magnetization compared to the ideal 3Q state.

DOI: 10.1103/PhysRevB.108.L180411

The triple-**q** (3Q) state is a three-dimensional spin structure on a two-dimensional hexagonal lattice. It can be understood as a superposition of three symmetry-equivalent spin spiral (1Q) states resulting in a noncoplanar magnetic state with tetrahedral angles between all adjacent magnetic moments and four atoms in the magnetic unit cell (Fig. 1). This fascinating magnetic state was predicted more than 20 years ago [1,2], but the first experimental observation was reported only recently for an hcp-stacked Mn monolayer on Re(0001) using spin-polarized scanning tunneling microscopy (SP-STM) [3]. The ideal 3Q state does not exhibit a net spin moment, however, theoretical investigations have shown a significant topological orbital moment (TOM) and a spontaneous topological Hall effect, without the necessity of spin-orbit coupling (SOC) [4–7]. Recently, neutron scattering experiments on the layered material $Co_{1/3}TaS_2$ were interpreted as validation of the 3Q state, and indeed, transport measurements of this bulk system are in agreement with a magnetic-field-induced switching of the TOM direction and reveal the topological Hall effect [8,9]. For magnetic 3Q states in a two-dimensional system the TOM is always perpendicular to the layer and the two different directions are related to the sign of the scalar spin chirality in an *all-in* versus *all-out* configuration (see Fig. 1). Another emergent phenomenon of the 3Q state is highlighted by a theoretical proposal that demonstrates a topological superconducting phase induced by this noncoplanar magnetic state when it is adjacent to a conventional superconductor [10].

The 3Q state can arise in frustrated antiferromagnets, for instance as a ground state in a hexagonal lattice of spins with antiferromagnetic nearest- and next-nearest-neighbor interactions ($1 < J_1/J_2 < 8$) [2,3]. To lower the energy with respect to the otherwise degenerate 1Q state higher-order interactions (HOI) are necessary. One prominent HOI term is the biquadratic interaction, which is one of the four-spin interactions which arise in fourth order in a perturbative expansion of the Hubbard model [11–13]. The aforementioned TOMs that can occur in these noncoplanar magnetic states can interact with the emergent magnetic field leading to the topological chiral magnetic interaction that constitutes a sixth-order term [7]. Due to this topological chiral magnetic interaction, large distortions from the perfect tetrahedron angle can occur as proposed for Mn/Re(0001) [14].

The possibility of a coupling of the ideal 3Q state to the crystal lattice is an intriguing question which has not been addressed so far. Figure 1 displays several 3Q states which have different orientations of the spins with respect to the magnetic lattice plane: a 3Q state with a given TOM can occur in three symmetric spin orientations with respect to the plane, denoted as $3Q^1$, $3Q^2$, and $3Q^3$ [3]. An energy variation between these states, i.e., a preferred coupling to the lattice, must originate from SOC.

Here, we use SP-STM to investigate the magnetic ground states of Pd/Mn and Rh/Mn bilayers on Re(0001) in real space. We find that both systems exhibit a hexagonal magnetic superstructure, indicative of the 3Q state with tetrahedral arrangement of the magnetic moments. Based on density-functional theory (DFT) we confirm the 3Q magnetic ground state of these two systems and calculate the resulting TOMs. We investigate the role of different SOC terms and find that neither the magnetocrystalline anisotropy energy (MAE) nor the Dzyaloshinskii-Moriya interaction (DMI) contribute to the total energy of the ideal 3Q state. Instead we show that the anisotropic symmetric exchange interaction (ASE), also referred to as pseudodipolar interaction or compass anisotropy [15,16], couples the 3Q state to the atomic lattice. The ASE has also been shown to play a role for the coupling of the spins to the lattice in a uniaxial antiferromagnetic state [3],

*nickel@physik.uni-kiel.de
†kirsten.von.bergmann@physik.uni-hamburg.de

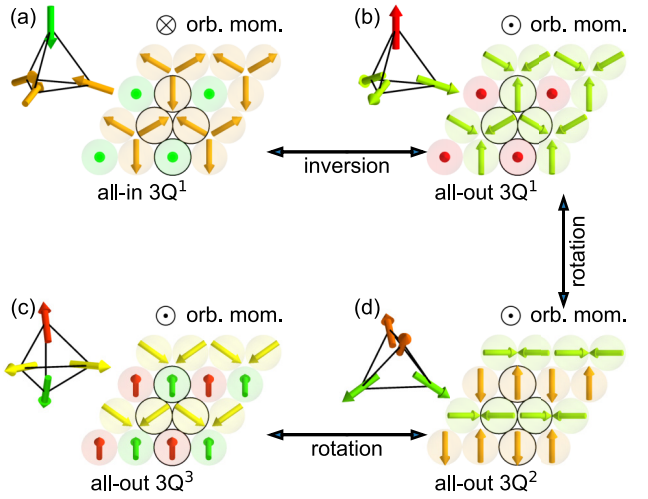

FIG. 1. Illustration of the 3Q state in different highly symmetric orientations with respect to the hexagonal atomic lattice; the respective direction of the TOM is indicated. Note that the 3Q states in (a) and (b) are connected by an inversion of all spins, whereas the states in (b)–(d) can be converted into each other by a continuous rotation of the spin structure.

and it can induce skyrmion lattices in two-dimensional van der Waals magnets [17] and in centrosymmetric crystals lacking DMI [18].

The starting point of our SP-STM investigation is the Mn monolayer on Re(0001), which preferentially grows in fcc stacking. The experimentally found magnetic ground state is the row-wise antiferromagnetic state that is the constituting 1Q state of the tetrahedral 3Q state [3], however, DFT predicts that the 1Q and the 3Q states are nearly degenerate. To drive the system into a 3Q ground state we try to tune the interactions by covering the extended fcc-Mn monolayer by nonmagnetic overlayers [20,21], namely Pd and Rh. Both Pd and Rh grow pseudomorphically as triangular-shaped islands on the fcc-stacked Mn monolayer, see perspective view of a Pd/Mn/Re(0001) sample in Fig. 2(a) and Supplemental Material [22] for Rh/Mn/Re(0001); note that due to the hcp crystal structure of Re(0001), the relative layer positions of the Pd and Mn layers are interchanged on adjacent Re terraces, cf. the two sketches of the bilayer structures, which are rotated by 180° with respect to each other.

In Fig. 2(b) the height contrast for the two Pd/Mn bilayer areas is adjusted separately to the same value for better visibility; the small white patches are Pd islands and clusters on top of the Pd/Mn bilayer. We find that the Pd/Mn exhibits an atomic-scale pattern of magnetic origin, which slightly varies over the islands but dominantly appears as vertical stripes on the left island, and like a hexagonal pattern on the right island, see enlarged insets. The length scale of the magnetic superstructure indicates that the 3Q state is the magnetic ground state. Depending on the tip magnetization direction relative to the 3Q state, different superstructure patterns are expected; indeed, in a measurement with a different tip magnetization direction, the left Pd/Mn island can also exhibit a hexagonal pattern, see Fig. 2(c). Also the Rh/Mn bilayers show the same magnetic superstructure unit cell, albeit with very small contrast amplitude [22]. Nevertheless, this is an indication

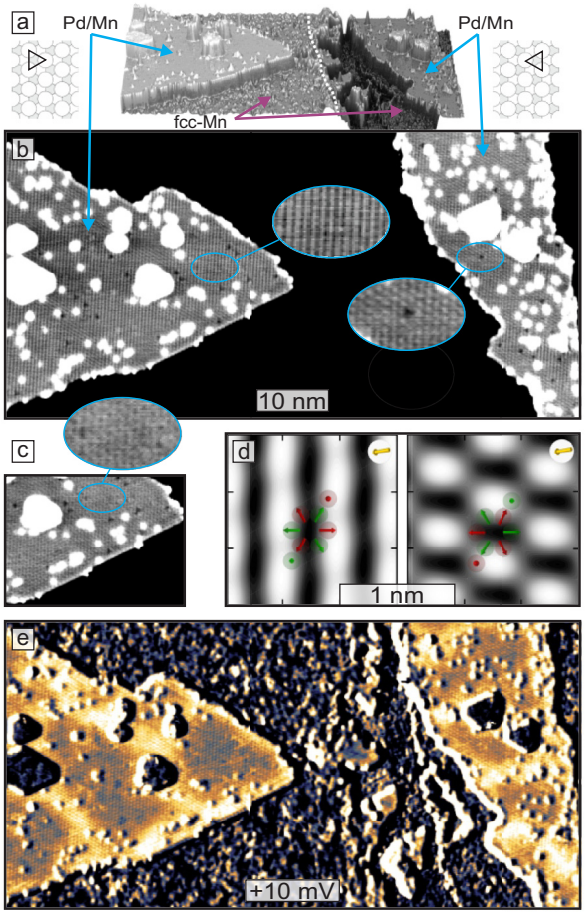

FIG. 2. (a) Perspective view of a sample of about 0.3 atomic layers of Pd on about 0.8 atomic layers of Mn on Re(0001); the dotted white line marks a buried Re(0001) step edge. (b) Spin-resolved constant-current STM image of the same area as shown in (a), with the height contrast adjusted separately for the two Pd/Mn bilayer areas to $\delta z = \pm 10$ pm ($U = +10$ mV, $I = 5$ nA, $T = 4.2$ K, Cr-bulk tip). (c) Selected area of (b) imaged with a different tip magnetization direction, exhibiting a different pattern. (d) SP-STM images of the $3Q^1$ ground state of $Pd_{fcc}/Mn_{fcc}/Re(0001)$ calculated from DFT based on the spin-polarized model of STM [19] for a bias voltage of -100 meV and at a distance of 6 Å above the surface. The tip magnetization direction is indicated by the orange arrow. Green and red spheres (arrows) denote the Pd and Mn atoms (magnetic moment directions). The two images represent the same 3Q rotated by 180°, as realized in two Pd/Mn bilayers on adjacent terraces. (e) Map of differential tunnel conductance acquired simultaneously to (b).

that also the Rh/Mn bilayer exhibits the 3Q state. With the help of SP-STM simulations we can find a combination of 3Q state and tip magnetization that reproduces the magnetic patterns observed on the two Pd/Mn areas in the measurement of Fig. 2(b). We use the constraint that the configuration of a bilayer, and thus also a given 3Q state, must be rotated by 180° on adjacent Re terraces and find a canted tip magnetization that nicely reproduces the experimentally observed magnetic contrast, see the DFT-based SP-STM simulations displayed in Fig. 2(d). Note that an inversion of all sample spins (or the tip magnetization direction) only slightly changes the observed patterns.

The dI/dU map in Fig. 2(e) is acquired simultaneously to (b). It shows a signal variation that is spatially correlated to the slight changes of the magnetic pattern on the Pd/Mn islands, suggesting a contribution of an electronic contrast mechanism due to local changes in the magnetic state [23,24]. We interpret the darker areas as magnetic domains, and the brighter areas as transition regions between them. Indeed, close analysis shows that there is a phase shift between different areas of the stripe contrast in the left island [22], indicating that they are either phase shifted or inversional domains. In contrast to the sharp domain walls previously observed by SP-STM for the $3Q^3$-like configuration in hcp-stacked Mn on Re(0001) [3], the transitions between different 3Q areas in Pd/Mn are much more extended. It is worth noting that, despite the presence of several independent domains, no rotational domains are observed. For both the $3Q^2$ and $3Q^3$ state rotational domains are expected to coexist, and with an arbitrary and unknown tip magnetization direction, as in our case, they could be easily discriminated. This suggests that we have the $3Q^1$ configuration in our Pd/Mn bilayer.

To understand the experimental observations we have performed DFT calculations for Pd/Mn and Rh/Mn bilayers on Re(0001) based on the full-potential linearized-augmented plane-wave method as implemented in the FLEUR code [25–27] and using the projector-augmented wave method as implemented in the VASP code [28,29] (see Supplemental Material [22] for computational details). We have calculated the spin spiral (1Q) dispersions for both systems and extracted the isotropic pairwise exchange constants [30]. However, if also superposition states that can be stabilized by HOIs are considered, our DFT calculations show that for both systems the 3Q state (Fig. 1) is by about 20 meV/Mn atom lower than the respective lowest 1Q state. This is in agreement with the experimentally observed $p(2 \times 2)$ magnetic unit cell and we conclude that the 3Q state is the ground state for both the Pd/Mn and the Rh/Mn bilayer on Re(0001). In order to evaluate the role of the HOIs for these systems we calculate the energy of different superposition states along the path continuously connecting the 1Q and the 2Q state via the 3Q state, see Fig. 3 [14]. The configuration of the superposition state is given by

$$\mathbf{s}_i(\alpha) = \mathbf{s}_i^{2Q}\cos(\alpha) + \mathbf{s}_i^{1Q}\sin(\alpha), \qquad (1)$$

where $\mathbf{s}_i(\alpha)$ represents a spin at lattice site i in the state characterized by α, and $\mathbf{s}_i^{2Q}$ and $\mathbf{s}_i^{1Q}$ are the spin orientations for the 2Q and 1Q state, respectively (Fig. 3(a), see also Ref. [22]). The angle α is varied between 0° (2Q state) and 90° (1Q state). The 3Q state occurs at an angle of $\arcsin(1/\sqrt{3}) \approx 35.26°$.

The energy difference between the 3Q and the 1Q state (RW-AFM) ΔE_{3Q-1Q} is on the order of 20 and 40 meV/Mn atom for the Pd/Mn and the Rh/Mn bilayer, respectively. The DFT total energy differences along the path can be fitted by HOI contributions of fourth and sixth order [Fig. 3(b) and insets]. We find that while ΔE_{3Q-1Q} for both systems is dominated by the fourth-order interaction, also the sixth-order interaction is significant with a value of about 15% compared to the fourth-order contribution. As a reference, we also show the energies for the hcp-Mn/Re(0001), which was found to exhibit a $3Q^3$-like state in SP-STM experiments [3] (note that in the bilayers studied here the Mn is in fcc stacking). We find that the energy variation along the 2Q-3Q-1Q path is significantly smaller; here the contributions of fourth- and sixth-order terms are of similar size, giving rise to a minimum at an angle of about 55°, which can be interpreted as a distorted $3Q^3$-like state, proposed as ground state for Mn/Re(0001) [14]. One can also calculate the HOI constants explicitly [13], see Supplemental Material [22] for the values. The sixth-order terms have the largest effective value for Rh/Mn/Re(0001). This is accompanied by a large TOM [Fig. 3(c)], which maximizes for the 3Q state, and decreases if the 3Q state is distorted towards the 2Q or the 1Q state. The direction of the TOM is linked to the specific spin configuration and inverts between the all-in and the all-out states; however, the continuous rotation of all spin directions does not alter the size or the sign of the TOM (cf. Fig. 1). The presence of TOMs, which occur due to the scalar spin chirality $\chi_{ijk} = \mathbf{s}_i \cdot (\mathbf{s}_j \times \mathbf{s}_k)$ even in the absence of SOC, is an indicator for topological-chiral interactions [7,14].

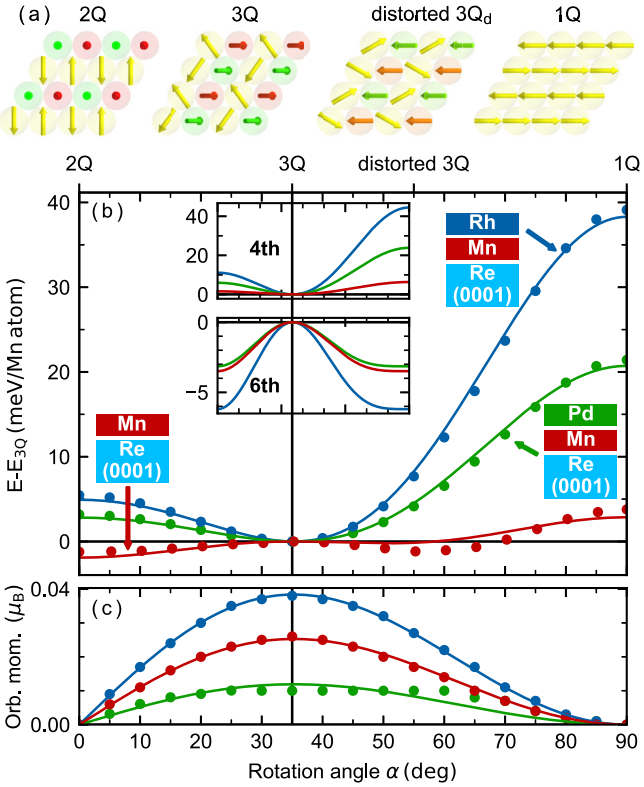

FIG. 3. (a) Sketch of the 2Q, the 3Q, a distorted 3Q, and the 1Q (RW-AFM) state. (b) Energy dispersion for spin states along the path 2Q-3Q-1Q according to Eq. (1) for Pd/Mn/Re(0001), Rh/Mn/Re(0001), and hcp-stacked Mn/Re(0001). The symbols represent DFT data, the lines show fits to the DFT values using HOI contributions of fourth and sixth order. The insets show the contributions of the fourth and sixth order separately. (c) Absolute value of the TOM of the Mn atoms in the films. Symbols show DFT values and lines a fit to the scalar spin chirality. Data for Mn/Re(0001) are taken from Ref. [14].

We have shown that the ideal undistorted 3Q state is the ground state of Pd/Mn and Rh/Mn bilayers on Re(0001). Now we want to analyze the impact of SOC onto the specific configuration of the 3Q state. In Fig. 4 we show the energy due

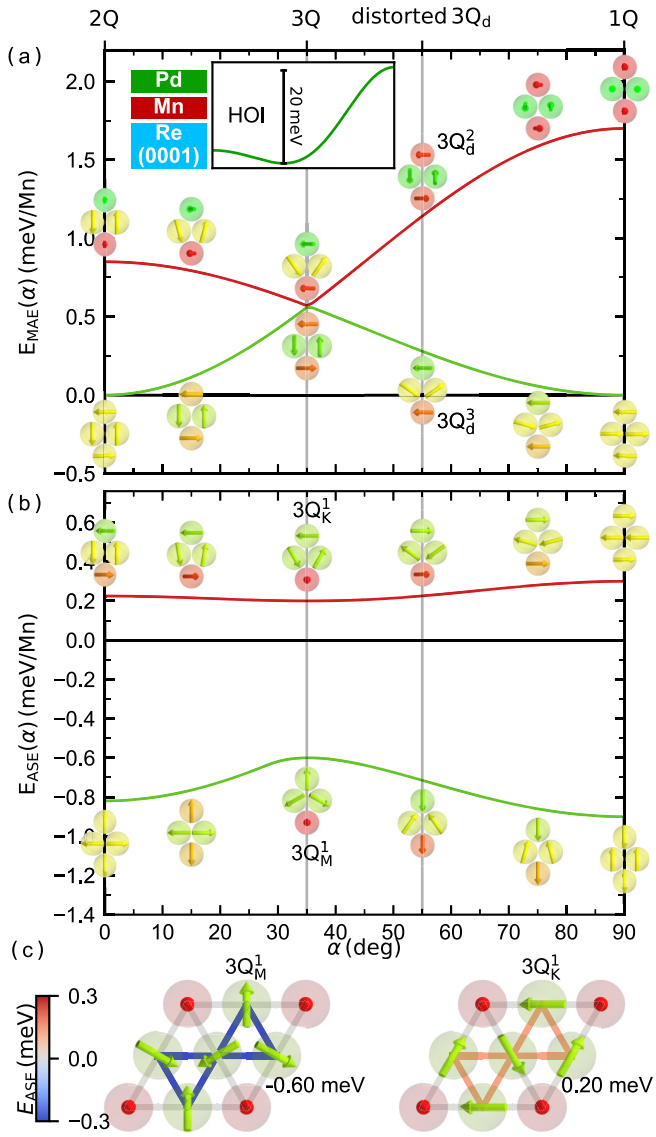

FIG. 4. Energy contributions of (a) the MAE and (b) the ASE for spin states along the path 2Q-3Q-1Q according to Eq. (1) with interaction strengths obtained via DFT for Pd/Mn/Re(0001). The line indicates the minimal (green) and maximal (red) energy contributions out of all possible global spin rotations. For selected points along the path the spin configurations that minimize or maximize the energy are displayed. (c) Sketches of the two 3Q states with minimal and maximal ASE energy, the bonds are colorized according to their individual contributions to the total ASE. In the $3Q_M^1$ state all in-plane components are along the $\overline{\Gamma M}$ direction, whereas in the $3Q_K^1$ state they are along $\overline{\Gamma K}$, i.e., the close-packed atomic rows.

to MAE and ASE along the 2Q-3Q-1Q path for the Pd/Mn bilayer [22,31]. For each state along the path, we allowed global rotations of the complete spin structure. Then we performed a global optimization to find the spin orientations of lowest (green) and highest (red) energy. We find that an undistorted 3Q state with tetrahedral angles between all nearest-neighbor moments cannot gain MAE [Fig. 4(a)], regardless of the orientation, as obvious from symmetry considerations. In contrast, the in-plane MAE of -1.70 meV/Mn atom [22] gives rise to an energy gain of 0.7 meV/Mn atom for a 2Q or 1Q state with all spins in the easy plane (cf. green line). Also in case of an out-of-plane easy axis the 3Q state would always be unfavored compared to the 2Q and 1Q states (cf. red line). However, for Pd/Mn the large HOI contribution favoring the 3Q state (see inset) more than overcompensates the MAE difference between the 3Q and the 2Q/1Q states, resulting in a vanishing effect of the MAE on our system. In contrast, when a distorted 3Q state is favored by the sixth-order HOIs, as is the case for hcp-Mn/Re(0001) with $\alpha \approx 55°$, the MAE can select between different orientations of the 3Q state.

Figure 4(b) shows the same graph for the ASE energy, which can be calculated for a given magnetic state via

$$E_{\mathrm{ASE}} = -\sum_{i,j} J_{\mathrm{ASE}}(\mathbf{s}_i \cdot \mathbf{d}_{ij})(\mathbf{s}_j \cdot \mathbf{d}_{ij}). \tag{2}$$

Here $\mathbf{d}_{ij}$ is the normalized connection vector between two lattice sites defined by i, j, and $\mathbf{s}_i$, $\mathbf{s}_j$ are the corresponding normalized spin moments. This interaction favors either a ferromagnetic or an antiferromagnetic alignment along the connection $\mathbf{d}_{ij}$ depending on the sign of J_{ASE}. If one or both magnetic moments are perpendicular to $\mathbf{d}_{ij}$ the contribution vanishes. For Pd/Mn the value of the ASE calculated by DFT is $J_{\mathrm{ASE}} = -0.30$ meV/Mn atom [22]. In contrast to the MAE, the ASE favors a specific orientation of the spin structure with respect to the lattice for every α, including the 3Q state [Fig. 4(b)]. For a given sign of the ASE, the energy difference between the different superposition states, i.e., a variation of α, is small with only up to 0.2 meV/Mn atom. In contrast, the energy difference between different spin configurations for the same α are much larger, on the order of up to 1 meV/Mn atom. We have also studied the effect of magnetic dipole-dipole interactions on the different states, however, the energy scale is much lower with a maximum energy difference of 0.25 meV/Mn atom [22]. We find that for a 3Q ground state the ASE always favors the $3Q^1$ orientation, regardless of the sign of the ASE. The sign of the ASE selects the specific orientation of the spins within the $3Q^1$ state, and the lowest energy configurations for negative and positive ASE are displayed in Fig. 4(c) left and right, respectively. For each of these $3Q^1$ states the energy is invariant under the inversion of all spins (e.g., from all-out to all-in) and under the inversion of the z components. This leads to four degenerate states, which is confirmed for Pd/Mn/Re(0001) by self-consistent DFT calculations including SOC for the four $3Q_M^1$ states and one $3Q_K^1$ state [22,32].

In conclusion, we have inspected the different energy terms that govern the detailed spin configuration of the 3Q state. We find that in general the ASE determines both the orientation and the relative spin alignments of the ideal 3Q state. In the case of Pd/Mn/Re(0001) it is the $3Q_M^1$ configuration, which exhibits threefold symmetry and consequently does not show rotational domains in the experiment. A distortion of the 3Q state can be generated by topological chiral interactions, and always leads to a $3Q^2$ or $3Q^3$ type, depending on the sign of the MAE. Experimentally such a distorted 3Q state with twofold symmetry can be identified by the presence of rotational magnetic domains, as demonstrated for hcp-Mn/Re(0001) [3], which provides strong evidence that the predicted topological chiral interactions [7,14] play a role in that system. However, for distorted states both the TOM

and the topological Hall effect will be reduced compared to the ideal 3Q state. Our work provides key microscopic insight into the detailed spin configuration of the 3Q state. The knowledge of the magnetic moment directions is important for an understanding of the response of domains and domain walls in such topological orbital ferromagnets to external magnetic fields, which in turn is crucial for their transport properties.

We thank Moritz Goerzen for valuable discussions. K.v.B. and S.H. gratefully acknowledge financial support from the Deutsche Forschungsgemeinschaft (DFG, German Research Foundation) via Projects No. 402843438, No. 418425860, and No. 462602351, and computing time provided by the North-German Supercomputing Alliance (HLRN).

[1] T. Momoi, K. Kubo, and K. Niki, Possible chiral phase transition in two-dimensional solid ^{3}He, Phys. Rev. Lett. **79**, 2081 (1997).

[2] P. Kurz, G. Bihlmayer, K. Hirai, and S. Blügel, Three-dimensional spin structure on a two-dimensional lattice: Mn/Cu(111), Phys. Rev. Lett. **86**, 1106 (2001).

[3] J. Spethmann, S. Meyer, K. von Bergmann, R. Wiesendanger, S. Heinze, and A. Kubetzka, Discovery of magnetic single- and triple-**q** states in Mn/Re(0001), Phys. Rev. Lett. **124**, 227203 (2020).

[4] I. Martin and C. D. Batista, Itinerant electron-driven chiral magnetic ordering and spontaneous quantum Hall effect in triangular lattice models, Phys. Rev. Lett. **101**, 156402 (2008).

[5] M. Hoffmann, J. Weischenberg, B. Dupé, F. Freimuth, P. Ferriani, Y. Mokrousov, and S. Heinze, Topological orbital magnetization and emergent hall effect of an atomic-scale spin lattice at a surface, Phys. Rev. B **92**, 020401(R) (2015).

[6] J.-P. Hanke, F. Freimuth, A. K. Nandy, H. Zhang, S. Blügel, and Y. Mokrousov, Role of Berry phase theory for describing orbital magnetism: From magnetic heterostructures to topological orbital ferromagnets, Phys. Rev. B **94**, 121114(R) (2016).

[7] S. Grytsiuk, J.-P. Hanke, M. Hoffmann, J. Bouaziz, O. Gomonay, G. Bihlmayer, S. Lounis, Y. Mokrousov, and S. Blügel, Topological-chiral magnetic interactions driven by emergent orbital magnetism, Nat. Commun. **11**, 511 (2020).

[8] P. Park, W. Cho, C. Kim, Y. An, Y.-G. Kang, M. Avdeev, R. Sibille, K. Iida, R. Kajimoto, K. H. Lee, W. Ju, E.-J. Cho, H.-J. Noh, M. J. Han, S.-S. Zhang, C. D. Batista, and J.-G. Park, Tetrahedral triple-Q ordering in the metallic triangular lattice antiferromagnet $Co_{1/3}TaS_2$, arXiv:2303.03760.

[9] H. Takagi, R. Takagia, S. Minami, T. Nomoto, K. Ohishi, M.-T. Suzuki, Y. Yanagi, M. Hirayama, N. D. Khanh, K. Karube, H. Saito, D. Hashizume, R. Kiyanagi, Y. Tokura, R. Arita, T. Nakajima, and S. Seki, Spontaneous topological hall effect induced by non-coplanar antiferromagnetic order in intercalated van der waals materials, Nat. Phys. **19**, 961 (2023).

[10] J. Bedow, E. Mascot, T. Posske, G. S. Uhrig, R. Wiesendanger, S. Rachel, and D. K. Morr, Topological superconductivity induced by a triple-**q** magnetic structure, Phys. Rev. B **102**, 180504(R) (2020).

[11] M. Takahashi, Half-filed Hubbard model at low temperature, J. Phys. C: Solid State Phys. **10**, 1289 (1977).

[12] A. H. MacDonald, S. M. Girvin, and D. Yoshioka, $\frac{t}{U}$ expansion for the Hubbard model, Phys. Rev. B **37**, 9753 (1988).

[13] M. Hoffmann and S. Blügel, Systematic derivation of realistic spin models for beyond-heisenberg solids, Phys. Rev. B **101**, 024418 (2020).

[14] S. Haldar, S. Meyer, A. Kubetzka, and S. Heinze, Distorted 3*q* state driven by topological-chiral magnetic interactions, Phys. Rev. B **104**, L180404 (2021).

[15] D. Smith, New mechanisms for magnetic anisotropy in localised s-state moment materials, J. Magn. Magn. Mater. **1**, 214 (1976).

[16] J. B. Staunton, B. L. Gyorffy, J. Poulter, and P. Strange, A relativistic RKKY interaction between two magnetic impurities-the origin of a magnetic anisotropic effect, J. Phys. C **21**, 1595 (1988).

[17] D. Amoroso, P. Barone, and S. Picozzi, Spontaneous skyrmionic lattice from anisotropic symmetric exchange in a Ni-halide monolayer, Nat. Commun. **11**, 5784 (2020).

[18] M. Hirschberger, S. Hayami, and Y. Tokura, Nanometric skyrmion lattice from anisotropic exchange interactions in a centrosymmetric host, New J. Phys. **23**, 023039 (2021).

[19] D. Wortmann, S. Heinze, P. Kurz, G. Bihlmayer, and S. Blügel, Resolving complex atomic-scale spin structures by spin-polarized scanning tunneling microscopy, Phys. Rev. Lett. **86**, 4132 (2001).

[20] N. Romming, C. Hanneken, M. Menzel, J. E. Bickel, B. Wolter, K. von Bergmann, A. Kubetzka, and R. Wiesendanger, Writing and deleting single magnetic skyrmions, Science **341**, 636 (2013).

[21] N. Romming, H. Pralow, A. Kubetzka, M. Hoffmann, S. von Malottki, S. Meyer, B. Dupé, R. Wiesendanger, K. von Bergmann, and S. Heinze, Competition of Dzyaloshinskii-Moriya and higher-order exchange interactions in Rh/Fe atomic bilayers on Ir(111), Phys. Rev. Lett. **120**, 207201 (2018).

[22] See Supplemental Material at http://link.aps.org/supplemental/10.1103/PhysRevB.108.L180411 for details on the experiments, DFT calculations and the atomistic model. It also contains Refs. [33–38].

[23] K. von Bergmann, M. Menzel, D. Serrate, Y. Yoshida, S. Schröder, P. Ferriani, A. Kubetzka, R. Wiesendanger, and S. Heinze, Tunneling anisotropic magnetoresistance on the atomic scale, Phys. Rev. B **86**, 134422 (2012).

[24] C. Hanneken, F. Otte, A. Kubetzka, B. Dupé, N. Romming, K. von Bergmann, R. Wiesendanger, and S. Heinze, Electrical detection of magnetic skyrmions by tunneling non-collinear magnetoresistance, Nat. Nanotechnol. **10**, 1039 (2015).

[25] See https://www.flapw.de.

[26] P. Kurz, F. Förster, L. Nordström, G. Bihlmayer, and S. Blügel, *Ab initio* treatment of noncollinear magnets with the full-potential linearized augmented plane wave method, Phys. Rev. B **69**, 024415 (2004).

[27] M. Heide, G. Bihlmayer, and S. Blügel, Describing Dzyaloshinskii-Moriya spirals from first principles, Phys. B **404**, 2678 (2009).

[28] G. Kresse and J. Furthmüller, Efficient iterative schemes for *ab initio* total-energy calculations using a plane-wave basis set, Phys. Rev. B **54**, 11169 (1996).

[29] See https://www.vasp.at.

[30] Note, that the DMI does not play a role for the magnetic ground state in these films. The contribution of SOC to the energy dispersion of spin spirals, which allows the determination of the DMI parameters, is displayed in the Supplemental Material [22].

[31] Note that the spin-chiral interaction which also arises due to SOC [7] does not play a role for the coupling of the 3Q state to the atomic lattice as can be shown analytically [22].

[32] The DFT calculations including SOC give a total energy difference of 0.75 meV between the $3Q^{1}_{\mathrm{M}}$ and $3Q^{1}_{\mathrm{K}}$ state, which is in very good agreement with the value of 0.8 meV obtained by the atomistic model.

[33] S. Ouazi, T. Pohlmann, A. Kubetzka, K. von Bergmann, and R. Wiesendanger, Scanning tunneling microscopy study of Fe, Co and Cr growth on Re(0001), Surf. Sci. **630**, 280 (2014).

[34] K. von Bergmann, A. Kubetzka, O. Pietzsch, and R. Wiesendanger, Interface-induced chiral domain walls, spin spirals and skyrmions revealed by spin-polarized scanning tunneling microscopy, J. Phys.: Condens. Matter **26**, 394002 (2014).

[35] S. H. Vosko, L. Wilk, and M. Nusair, Accurate spin-dependent electron liquid correlation energies for local spin density calculations: a critical analysis, Can. J. Phys. **58**, 1200 (1980).

[36] J. P. Perdew, K. Burke, and M. Ernzerhof, Generalized gradient approximation made simple, Phys. Rev. Lett. **77**, 3865 (1996).

[37] W. Li, S. Paul, K. von Bergmann, S. Heinze, and R. Wiesendanger, Stacking-dependent spin interactions in Pd/Fe bilayers on Re(0001), Phys. Rev. Lett. **125**, 227205 (2020).

[38] S. Paul, S. Haldar, S. Malottki, and S. Heinze, Role of higher-order exchange interactions for skyrmion stability, Nat. Commun. **11**, 4756 (2020).

Supplemental Material for "Coupling of the triple-Q state to the atomic lattice by anisotropic symmetric exchange"

Felix Nickel,[1,*] André Kubetzka,[2] Soumyajyoti Haldar,[1]
Roland Wiesendanger,[2] Stefan Heinze,[1,3] and Kirsten von Bergmann[2]

[1] *Institut für Theoretische Physik und Astrophysik, Christian-Albrechts-Universität zu Kiel, D-24098 Kiel, Germany*
[2] *Department of Physics, University of Hamburg, Jungiusstraße 9-11, 20355 Hamburg, Germany*
[3] *Kiel Nano, Surface, and Interface Science (KiNSIS), University of Kiel, Germany*

(Dated: November 9, 2023)

S1. EXPERIMENTAL DETAILS

The experiments were performed in a multi-chamber ultra-high vacuum system. Re(0001) was cleaned by flash annealing and occasional annealing in oxygen [1]. Mn was evaporated from a Knudsen cell at 690° C, whereas Pd and Rh were evaporated from rods by electron beam heating. Mn was deposited about $10-15$ min after the last flash annealing, i.e., well above room temperature, and the Pd or Rh overlayers were added about 30 min after the flash of the Re crystal; the deposition rates are on the order of $5-10$ min per monolayer. The samples were transferred in-vacuo into the low temperature STM. For the spin-resolved STM measurements a Cr bulk tip was used, which has an arbitrary tip magnetization direction. The tip magnetization direction can be changed by gentle tip-sample collisions or voltage pulses. In SP-STM the magnetic contribution to the tunnel current scales with the projection of the local sample magnetization onto the tip magnetization direction [2].

* Email: nickel@physik.uni-kiel.de

S2. COMPUTATIONAL DETAILS

We have performed density functional theory (DFT) calculations to investigate the magnetic interactions with two different codes. On the one hand, we have used the all-electron code `FLEUR` which uses the full-potential linearized augmented plane-wave (FLAPW) method [3–5]. On the other hand, we have applied the projector augmented wave (PAW) method as implemented in the `VASP` code [6, 7]. Here we provide the computational details of the calculations using both codes.

Spin spirals, 3Q state and *uudd* states. For most calculations using the `FLEUR` code the cut-off parameter for the plane waves has been set to $k_{\max} = 4.1\,\text{a.u.}^{-1}$. The radius of the muffin-tin spheres was chosen as 2.45 a.u. for Re and 2.3 a.u. for Mn, Pd and Rh. The `FLEUR` code has been used for the spin spiral calculations [4] neglecting and including SOC, the energy of the *uudd* and 3Q states, and for the calculations of SP-STM images of the 3Q state. The SOC contribution to the energy of spin spirals was calculated using perturbation theory [5]. The exchange-correlation (xc) functional for all calculations in `FLEUR` was chosen in local density ap-

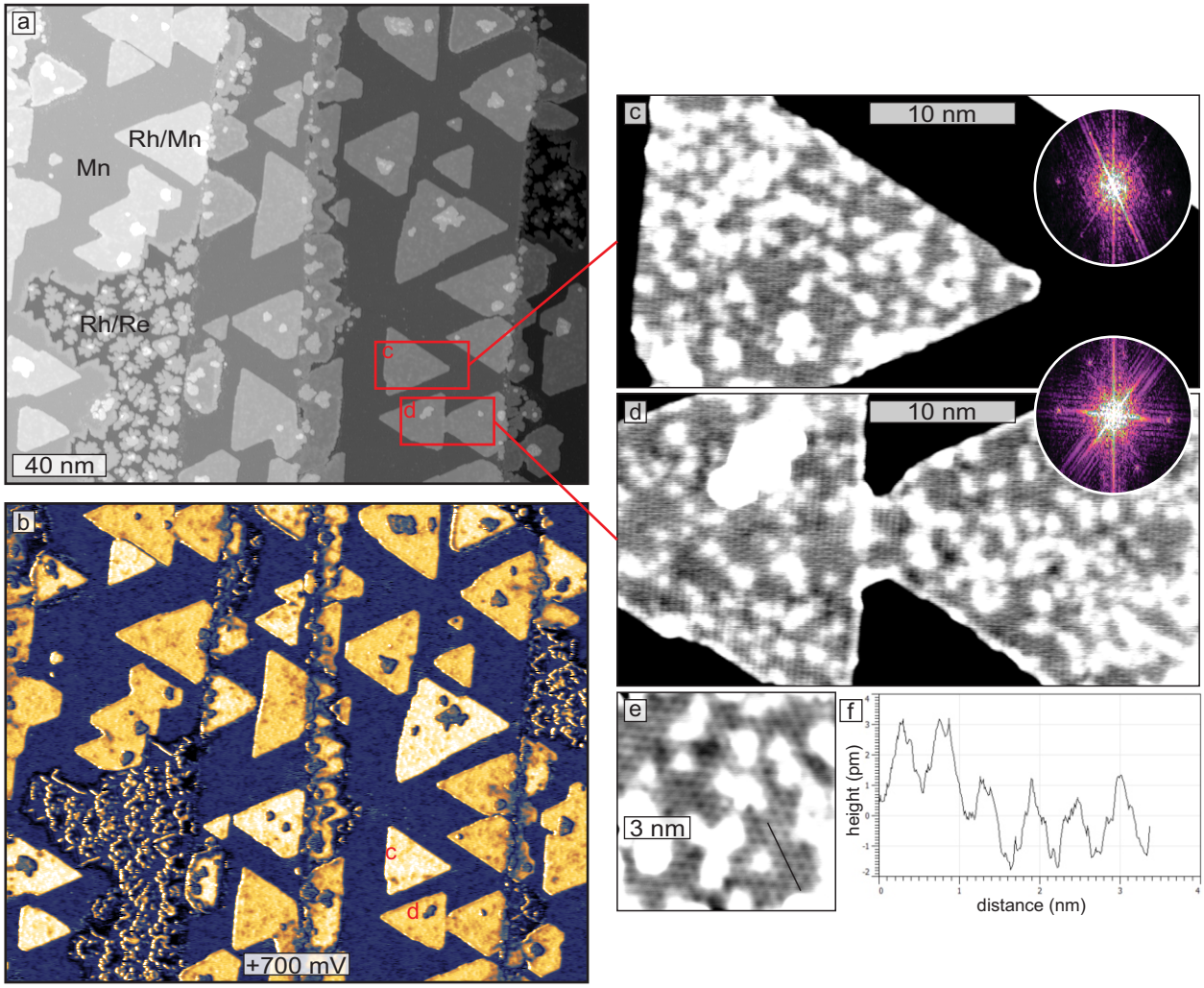

FIG. S1. (a) Constant-current STM image and (b) simultaneously acquired map of differential tunnel conductance of a sample of about 0.4 atomic layers of Rh on about 0.8 atomic layers of Mn on Re(0001), the different exposed layers are indicated ($U = +700\,\mathrm{mV}$, $I = 2\,\mathrm{nA}$, $T = 4.2\,\mathrm{K}$, Cr-bulk tip). (c),(d) Closer view spin-resolved constant-current STM images of the two areas of different Rh stacking indicated by the boxes in (a), height contrast $\Delta z = \pm 10\,\mathrm{pm}$; insets show the FFT of the respective Rh/Mn islands ($U = +10\,\mathrm{mV}$, $I = 5\,\mathrm{nA}$, $T = 4.2\,\mathrm{K}$, Cr-bulk tip). (e) High-resolution SP-STM constant-current image of a Rh/Mn bilayer area of a comparable sample ($U = +5\,\mathrm{mV}$, $I = 5\,\mathrm{nA}$, $T = 4.2\,\mathrm{K}$, Cr-bulk tip) exhibiting the hexagonal magnetic superstructure. (f) Line profile at the position indicated in (e), demonstrating that the magnetic state has a periodicity of a 3Q state with a magnetic corrugation amplitude on the order of 2 pm.

proximation (LDA) [8]. For the spin spiral calculations with and without SOC a mesh of (44×44) k-points was used in the full 2D-BZ. The calculations for the 3Q state and the *uudd* states in their respective super cells were performed on a (22×22) k-point mesh, which has the same density of k-points as that used in the spin spiral calculations. The ASE and MAE energies have been calculated with a grid of (90×90) k-points in the full 2D-BZ.

3Q states including SOC. For self-consistent calculations of the total energy of different orientations of the 3Q states including SOC the cut-off parameter were increased in order to determine even small energy differences. The calculations were performed self consistently in LDA and including SOC via the `FLEUR` code on a (44×44) k-point grid in the full 2D-BZ of the magnetic unit cell. The cut-off parameter for the basis functions was set to $k_{max} = 4.3\,\mathrm{a.u.}^{-1}$.

Path along 2Q-3Q-1Q and relaxations. The `VASP` code was used for the structural relaxation of all systems and to calculate the energy of states along the path 2Q-3Q-1Q. The energy difference between the 1Q state (RW-AFM) and the 3Q state has been calculated in both codes and a good agreement was observed. For the total energy calculations the VWN [8] xc-functional was used as in `FLEUR` with a grid of (16×16) k-points in the full 2D-

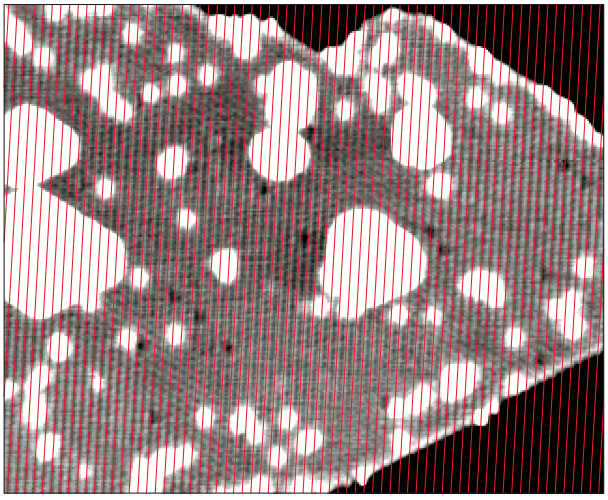

FIG. S2. (a) Same data set as Fig. 2(b) of the main text with equally spaced red lines to visualize that the vertical stripes of magnetic origin are phase-shifted between different domains.

BZ. The xc-functional has been treated in generalized gradient approximation (GGA) for structural relaxations using the PBE functional [9] and a grid of (15×15) k-points has been chosen. The relaxed interlayer distances of the adlayer, the Mn layer and the top two Re layers have been obtained in the RW-AFM state. We chose the experimental lattice constant of Re, 2.76 Å, for all atom distances within one layer and 2.23 Å, for all non-relaxed interlayer distances. Note, that these distances differ by less than 0.6% from the distances obtained by GGA calculations.

S3. SPIN SPIRAL CALCULATIONS

A spin spiral is characterized by a wave vector $\mathbf{q}$, and the spin at lattice site $\mathbf{R}_i$ is given by $\mathbf{S}_i = S(\cos(\mathbf{q}\cdot\mathbf{R}_i), \sin(\mathbf{q}\cdot\mathbf{R}_i), 0)$, with S denoting the size of the spin and $\mathbf{s}_i = \mathbf{S}_i/S$ being the normalized spin moment. The energy dispersion $E(\mathbf{q})$ is calculated via the FLEUR code using the generalized Bloch theorem [4]. Fig. S3 shows the energy dispersion $E(\mathbf{q})$ of spin spirals in $\mathrm{Pd_{fcc}/Mn_{fcc}}$ and $\mathrm{Rh_{fcc}/Mn_{fcc}}$ on Re(0001). For comparison also the data for $\mathrm{Mn_{hcp}}$/Re(0001) taken from Ref. [10] is shown. For Mn/Re(0001) the spin spiral state with the lowest energy is at the $\overline{\mathrm{M}}$-point, i.e. the row-wise antiferromagnetic (RW-AFM) state, which is by about 240 meV/Mn atom below the ferromagnetic (FM) state at the $\overline{\Gamma}$ point.

For Pd/Mn/Re(0001), the RW-AFM state ($\overline{\mathrm{M}}$ point) is also the lowest spin spiral state and the 3Q state is even lower in energy as it is also the case in Mn/Re(0001) (Fig. S3). However, the energy difference between the RW-AFM and the 3Q state, $\Delta E_{\mathrm{3Q-RWAFM}}$, is greatly enhanced. For Rh/Mn/Re(0001), a spin spiral at the $\overline{\mathrm{K}}$-point, i.e. the Néel state, is the spin spiral state of lowest energy. Since the energy gain of the 3Q state over the RW-AFM state becomes very large in Rh/Mn/Re(0001),

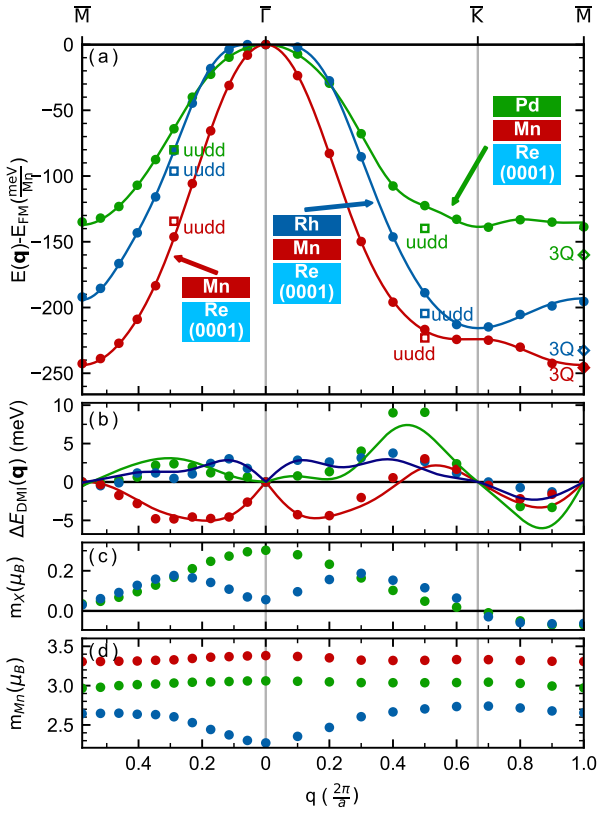

FIG. S3. (a) Energy dispersion $E(\mathbf{q})$ of spin spirals in the scalar-relativistic approximation, i.e. neglecting SOC, along the high-symmetry direction $\overline{\mathrm{M}} - \overline{\Gamma} - \overline{\mathrm{K}} - \overline{\mathrm{M}}$ for $\mathrm{Mn_{fcc}}$/Re(0001), $\mathrm{Pd_{fcc}/Mn_{fcc}}$/Re(0001) and $\mathrm{Rh_{fcc}/Mn_{fcc}}$/Re(0001) (see icons). Symbols denote DFT values and the curves show a fit to the Heisenberg model. The total energies of the two *uudd* states (open squares) and the 3Q state (open diamonds) are given at the q value of the corresponding spin spiral (1Q) state. (b) Energy contribution to spin spirals due to SOC, $\Delta E_{\mathrm{DMI}}(\mathbf{q})$. (c, d) show the magnitude of the magnetic moments of the adlayer and the Mn layer, respectively. Data for Mn/Re(0001) are taken from Ref. [10].

the 3Q state is even lower in energy than the Néel state (Fig. S3).

By fitting the energy dispersion $E(\mathbf{q})$ (Fig. S3(a)) with the Heisenberg model of pair-wise exchange interactions $-J_{ij}(\mathbf{s}_i \cdot \mathbf{s}_j)$ between normalized spin moments $\mathbf{s}_i$ and $\mathbf{s}_j$ at sites i and j we obtain the exchange constants J_{ij}. The exchange constants are given in Table S1 resolved up to seventh nearest-neighbor shells for the systems shown in Fig. S3.

The energy contribution of SOC to the dispersion of cycloidal spin spirals is calculated in first-order perturbation theory [5] and displayed in Fig. S3(b). By fitting this energy contribution, we can determine the Dzyaloshinskii-Moriya interaction (DMI) parameters (for values see Table S1). Whereas in Mn/Re(0001) the DMI favors a clockwise rotational sense of cycloidal spin spirals, indicated by the negative sign, Pd/Mn/Re(0001)

system	J_1	J_2	J_3	J_4	J_5	J_6	J_7	D_1	D_2	D_3	D_4	D_5	D_6	D_7
Mn_{hcp}/Re(0001)	−21.19	−6.72	−2.00	−0.62	0.12	−0.36	0.16	1.21	1.02	0.19	0.30	−0.05	0.13	0.01
Pd_{fcc}/Mn_{fcc}/Re(0001)	−16.32	−1.39	0.70	0.26	0.23	0.32	−0.06	−1.24	1.08	−0.24	−0.02	0.09	−0.34	0.02
Rh_{fcc}/Mn_{fcc}/Re(0001)	−26.61	0.62	1.00	0.47	0.29	0.38	0.34	−0.67	0.23	−0.36	0.03	−0.17	−0.05	−0.09

TABLE S1. Exchange (J_i) and DMI (D_i) constants for i-th nearest-neighbor shells as obtained from energy dispersions of spin spirals calculated via DFT along the high symmetry lines $\overline{\mathrm{M}}-\overline{\Gamma}-\overline{\mathrm{K}}-\overline{\mathrm{M}}$. The constants are given for seven neighbors and were obtained by a fit to the data shown in Fig. S3. Data for Mn_{hcp}/Re(0001) are taken from Ref. [10].

and Rh/Mn/Re(0001) both favor a counter-clockwise rotational sense. The absolute value of the DMI contribution is smallest for Pd/Mn/Re(0001), larger for Rh/Mn/Re(0001) and largest for Mn/Re(0001). We can conclude, that an overlayer changes the DMI in sign and magnitude.

The DMI is mediated between two magnetic atoms by an atom with a high SOC constant. With an Rh or Pd adlayer the DMI is not only mediated by the Re substrate, also interactions involving atoms from the adlayer are possible. Further the adlayer changes the distance between Mn and Re. This leads to different hybridization and a further change in the DMI. This can be examined by a decomposition of the DMI contributions of each layer (not shown).

S4. HIGHER-ORDER INTERACTION CONSTANTS

The fourth-order HOI are the biquadratic interaction, the three-site, and the four-site four spin interactions [11]:

$$\begin{aligned} H_{4\mathrm{th}} = &- \sum_{i,j} B_{ij}(\mathbf{s}_i\cdot\mathbf{s}_j)^2 - \sum_{ijk} Y_{ijk}[(\mathbf{s}_i\cdot\mathbf{s}_j)(\mathbf{s}_j\cdot\mathbf{s}_k)+(\mathbf{s}_j\cdot\mathbf{s}_i)(\mathbf{s}_i\cdot\mathbf{s}_k)+(\mathbf{s}_i\cdot\mathbf{s}_k)(\mathbf{s}_k\cdot\mathbf{s}_j)] + \\ &- \sum_{ijkl} K_{ijkl}[(\mathbf{s}_i\cdot\mathbf{s}_j)(\mathbf{s}_k\cdot\mathbf{s}_l)+(\mathbf{s}_i\cdot\mathbf{s}_l)(\mathbf{s}_j\cdot\mathbf{s}_k)-(\mathbf{s}_i\cdot\mathbf{s}_k)(\mathbf{s}_j\cdot\mathbf{s}_l)], \end{aligned} \tag{S1}$$

where B_{ij}, Y_{ijk} and K_{ijkl} are the higher-order exchange constants. The nearest-neighbor HOIs can be obtained via DFT [10–12] by calculating in addition to $\Delta E_{3\mathrm{Q}-\mathrm{RWAFM}}$ the total DFT energy differences between the two *uudd* states and the respective 90° spin spiral (1Q) states. From these energy differences the HOI in nearest neighbor approximation are:

$$Y_1 = \frac{1}{8}\left(E^{uudd}_{\frac{\overline{\mathrm{M}}}{2}} - E^{1Q}_{\frac{\overline{\mathrm{M}}}{2}}\right) - \frac{1}{8}\left(E^{uudd}_{\frac{4\overline{\mathrm{K}}}{4}} - E^{1Q}_{\frac{3\overline{\mathrm{K}}}{4}}\right) \tag{S2}$$

$$B_1 = \frac{3}{32}\left(E^{3Q}_{\overline{\mathrm{M}}} - E^{1Q}_{\overline{\mathrm{M}}}\right) - \frac{1}{8}\left(E^{uudd}_{\frac{4\overline{\mathrm{K}}}{4}} - E^{1Q}_{\frac{3\overline{\mathrm{K}}}{4}}\right) \tag{S3}$$

$$K_1 = \frac{1}{8}\left(E^{uudd}_{\frac{4\overline{\mathrm{K}}}{4}} - E^{1Q}_{\frac{3\overline{\mathrm{K}}}{4}}\right) + \frac{Y_1}{2} + \frac{B_1}{2} \tag{S4}$$

Here the lower index defines a point in the 2D-BZ and the upper index defines if the state is a spin spiral (1Q), a *uudd*, or a 3Q state.

The nearest-neighbor HOI constants B_1, Y_1, and K_1 obtained for Mn/Re(0001) are significant, however, their contributions nearly cancel with respect to the energy difference between the 3Q and RW-AFM state, $\Delta E_{3\mathrm{Q}-\mathrm{RWAFM}} = \frac{16}{3}(2K_1 + B_1 - Y_1)$ (cf. Table S2). In Pd/Mn/Re(0001) and Rh/Mn/Re(0001) this frustration of the HOI is lifted which leads to a larger energy difference between 1Q and 3Q state.

Note, that the first three pair-wise exchange constants obtained from fitting the energy dispersion of spin spirals need to be adapted if the HOI constants are included [13]. The modified exchange constants are:

$$J_1' = J_1 - Y_1 \tag{S5}$$

$$J_2' = J_2 - Y_1 \tag{S6}$$

$$J_3' = J_3 - \frac{B_1}{2} \tag{S7}$$

S5. DFT CALCULATION OF THE ASE AND MAE CONSTANTS IN PD/MN/RE(0001) AND RH/MN/RE(0001)

To obtain the strength of the ASE we considered the RW-AFM state, in which all spins are aligned within the film plane. The in-plane angle φ of all spins is then varied (Fig. S4) and for each angle the total energy including SOC is calculated self-consistently using the `FLEUR` code.

film	J_1'	J_2'	J_3'	B_1	Y_1	K_1	ΔE
Mn	−22.40	−3.40	0.88	−1.56	−2.29	−0.43	−0.7
Pd/Mn	−16.16	−1.23	0.70	0.00	−0.16	−2.08	−21.35
Rh/Mn	−26.56	0.67	1.79	−1.58	−0.05	−2.73	−37.28

TABLE S2. Pair-wise exchange (J_i') constants for i-th nearest neighbors and nearest-neighbor HOI (B_1, Y_1, K_1) constants obtained via DFT for Mn/Re(0001), Pd/Mn/Re(0001) and Rh/Mn/Re(0001). The prime denotes that the contribution of HOI has been taken into account. All constants are given in meV. The energy difference $\Delta E = E_{3Q} - E_{RW-AFM} = \frac{16}{3}(2K_1 + B_1 - Y_1)$ is given in meV/Mn atom.

For this setup the energy depends on the angle φ and the ASE constant, J_{ASE}, as

$$E_{ASE}(\varphi) - E_{ASE}(0) = 4J_{ASE}\sin^2(\varphi) \quad . \tag{S8}$$

In Fig. S4 the obtained DFT energies are shown as markers. The lines represent the fit to Eq. ((S8)). The small icons represent the spin structure for each φ used for the calculation. The strength of the ASE is $J_{ASE} = -0.30\,\text{meV}$ for Pd/Mn/Re(0001) and $J_{ASE} = -0.20\,\text{meV}$ for Rh/Mn/Re(0001). The sign indicates, that both systems prefer an alignment of the spins perpendicular to rows of spins which are parallel with respect to an alignment along these rows.

To calculate the MAE we use the RW-AFM state and perform a self-consistent calculation including SOC, in which all spins are aligned along the surface normal and one self-consistent calculation including SOC, in which all spins are within the surface. Note that the contribution of the ASE has to be subtracted, as it also has a contribution to those two states. The MAE constant is $K = -1.70\,\text{meV}$ for Pd/Mn/Re(0001) and $K = -2.03\,\text{meV}$ for Rh/Mn/Re(0001). Due to the negative signs of the MAE constants, an in-plane orientation is favoured.

We assume a uniaxial MAE. In principle different directions within the plane could lead to a different energy. This effect would be mapped into the ASE constant. To check for this effect, we calculated the energy of the FM state along different axes within the surface plane. We found a maximal energy difference of 0.005 meV. From this small energy difference we conclude, that a varying MAE in the plane is negligible and the energy of the ASE constant is truly due to the ASE.

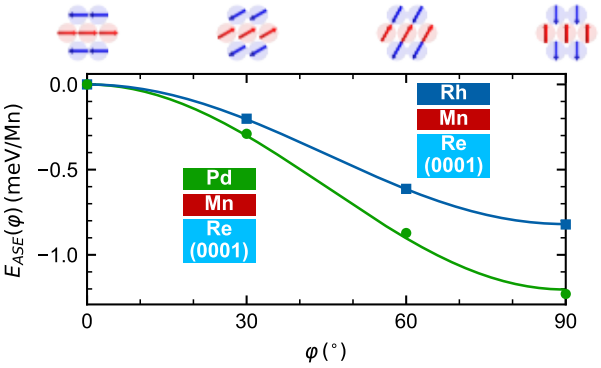

FIG. S4. DFT total energies including SOC of the RW-AFM state with all spins aligned in the surface plane. The in-plane angle φ is varied as indicated by the images on top. The total energies are given for fcc stacked Pd/Mn/Re(0001) (green) and Rh/Mn/Re(0001) (blue).

S6. ATOMISTIC MODEL FOR ASE AND MAE

To investigate the energy dependency of the ASE and MAE on a global rotation of the spin structure (Fig. 4 of the main text) we applied global rotations to each spin in the unit cell. First the spin structure is defined for a value α according to Eq. (2) from the main text. Now three rotation matrices $\underline{\mathbf{R}}_x(\phi), \underline{\mathbf{R}}_y(\theta), \underline{\mathbf{R}}_z(\psi)$ are applied to every spin in the unit cell. The angles of the rotation matrices correspond to the Euler angles and are the same for every spin in the unit cell. The rotated spin $\mathbf{S}_i^r$ at lattice site i then depends on the rotation angles according to

$$\mathbf{S}_i^r = \mathbf{S}_i^r(\phi,\theta,\psi) = \underline{\mathbf{R}}_x(\phi)\underline{\mathbf{R}}_y(\theta)\underline{\mathbf{R}}_z(\psi)\mathbf{S}_i = \underline{\mathbf{R}}(\phi,\theta,\psi)\mathbf{S}_i \quad , \tag{S9}$$

where $\mathbf{S}_i$ is the original spin at site i and $\underline{\mathbf{R}}(\phi,\theta,\psi) = \underline{\mathbf{R}}_x(\phi)\underline{\mathbf{R}}_y(\theta)\underline{\mathbf{R}}_z(\psi)$. The energy of the ASE is defined as

$$E_{ASE}(\phi,\theta,\psi) = -J_{ASE}\sum_{ij}(\mathbf{S}_i^r\cdot\mathbf{d}_{ij})(\mathbf{S}_j^r\cdot\mathbf{d}_{ij}) \quad , \tag{S10}$$

where $\mathbf{S}_i^r$ and $\mathbf{S}_j^r$ depend on the Euler angles as given by Eq. (S9). When the sum is explicitly written out for the four atom unit cell with α as a parameter and ϕ, θ, ψ as variables, the energy becomes

$$\begin{aligned} E_{ASE}^{\alpha}(\phi,\theta,\psi) = J_{ASE}(&12\sin^2(\alpha)\sin^2(\phi)\sin^2(\theta)\cos^2(\psi) + 24\sin^2(\alpha)\sin(\phi)\sin(\psi)\sin(\theta)\cos(\phi)\cos(\psi) + \\ &12\sin^2(\alpha)\sin^2(\psi)\cos^2(\phi) - 4\sin^2(\alpha)\cos^2(\psi)\cos^2(\theta) + \\ &4\sqrt{3}\sin(\phi)\sin(\psi)\sin^2(\theta)\cos^2(\alpha) - \\ &4\sqrt{3}\sin(\phi)\sin(\psi)\cos^2(\alpha)\cos^2(\theta) + 4\sin^2(\psi)\cos^2(\alpha)\cos^2(\theta) + \\ &4\sin^2(\theta)\cos^2(\alpha) - 4\sqrt{3}\sin(\theta)\cos^2(\alpha)\cos(\phi)\cos(\psi)) \, . \end{aligned} \tag{S11}$$

We used this expression for a fixed α and performed numerically a global optimization to find all local minima and maxima. For all minima we calculated the eigen-

values of the Hessian matrix, which contains the second derivatives of the energy. If one or more eigenvalues are zero a Goldstone mode exists. For the ideal 3Q state we find no Goldstone mode. From this we can conclude, that the $3Q^1$ orientation is protected by an energy barrier against global rotation. We used the same approach to examine the dependency of the MAE on a global rotation. The MAE is

$$E_{\mathrm{MAE}}(\phi,\theta,\psi) = -K\sum_i \left(\mathbf{S}_i^{\mathrm{r}}\cdot\mathbf{n}\right)^2 \quad , \tag{S12}$$

where the rotated spin depends on (ϕ,θ,ψ) as in Eq. (S9). With α as a parameter the energy of the MAE for a state on the 2Q-3Q-1Q path is given by

$$\begin{aligned} E^{\alpha}_{\mathrm{MAE}}(\phi,\theta,\psi) = 2K(&-2\sin^2(\alpha)\sin^2(\phi)\sin^2(\psi) + 4\sin^2(\alpha)\sin(\phi)\sin(\psi)\sin(\theta)\cos(\phi)\cos(\psi) - \\ &2\sin^2(\alpha)\sin^2(\theta)\cos^2(\phi)\cos^2(\psi) - \sin^2(\phi)\cos^2(\alpha)\cos^2(\psi) - \\ &2\sin(\phi)\sin(\psi)\sin(\theta)\cos^2(\alpha)\cos(\phi)\cos(\psi) - \sin^2(\psi)\sin^2(\theta)\cos^2(\alpha)\cos^2(\phi) - \\ &\cos^2(\alpha)\cos^2(\phi)\cos^2(\theta)) \ . \end{aligned} \tag{S13}$$

This energy was minimized with respect to (ϕ,θ,ψ) as previously for the ASE. The signs of J_{ASE} and K were chosen according to the values calculated by DFT for Pd/Mn/Re(0001) to obtain the energies shown in Fig. 4 of the main text. If the sign of an interaction changes, maxima of the energy landscape become minima and vice versa. The energies in Fig. 4 were also scaled with the strength of the interaction obtained by DFT.

S7. ENERGY DUE TO CHIRAL-CHIRAL AND SPIN-CHIRAL INTERACTION

The chiral-chiral interaction (CCI) and the spin-chiral interation (SCI) originate from the interaction of the topological orbital moment with the emergent magnetic field [14]. The topological orbital moment (TOM) is induced from the motion of electrons in a non-collinear spin structure. The chiral-chiral interaction has the form

$$E^{\mathrm{CCI}} = -\frac{1}{2}\sum_{ijk}\kappa_{ijk}^{\mathrm{CCI}}\left[\mathbf{S}_i\cdot(\mathbf{S}_j\times\mathbf{S}_k)\right]^2, \tag{S14}$$

where $\kappa_{ijk}^{\mathrm{CCI}}$ is the strength of the CCI on a triangle spanned by the spins (i,j,k) [14]. The SCI has the form

$$E^{\mathrm{SCI}} = -\frac{1}{2}\sum_{ijk}\kappa_{ijk}^{\mathrm{SCI}}\left(\boldsymbol{\tau}_{ijk}\cdot\mathbf{S}_i\right)\left[\mathbf{S}_i\cdot(\mathbf{S}_j\times\mathbf{S}_k)\right], \tag{S15}$$

where $\boldsymbol{\tau}\propto(\mathbf{R}_j-\mathbf{R}_i)\times(\mathbf{R}_k-\mathbf{R}_i)$ is proportional to $\mathbf{e}_z$ in the case of a 2D lattice [14]. The strength of the SCI on a triangle is $\kappa_{ijk}^{\mathrm{SCI}}$.

For both interactions a global rotation of the spins leaves the energy invariant. A global rotation can be expresssed as a rotation matrix applied on each spin as in Eq. (S9). With this rotation applied to each spin the term $[\mathbf{S}_i\cdot(\mathbf{S}_j\times\mathbf{S}_k)]$ becomes

$$\left[\mathbf{S}_i^r\cdot(\mathbf{S}_j^r\times\mathbf{S}_k^r)\right] = \underbrace{\det(\overline{\mathbf{R}}(\phi,\theta,\psi))}_{=1}\left[\mathbf{S}_i\cdot(\mathbf{S}_j\times\mathbf{S}_k)\right] \quad . \tag{S16}$$

This shows that the energies of CCI and SCI do not change upon a global rotation of the spins. Therefore, the CCI and SCI do not favor a specific orientation of the 3Q state. Further the SCI vanishes for all states along the path 2Q-3Q-1Q.

S8. COMPARISON OF PSEUDO-DIPOLAR AND DIPOLAR INTERACTIONS

Beside the pseudo-dipolar (or ASE) interaction also the dipole-dipole interaction can have an influence. The energy of the dipole-dipole interactions is given by

$$E_{\mathrm{DD}} = -\sum_{i,j}\frac{\mu_0\mu_B^2}{4\pi}\frac{3(\mathbf{m}_j\mathbf{r})\mathbf{r}-\mathbf{m}_j r^2}{r^5}\mathbf{m}_i. \tag{S17}$$

Analogously to the ASE, we have also applied a global rotation in form of three rotation matrices on each spin in the magnetic unit cell. We also performed a numerical optimization to find all minima and maxima of the energy of the dipole-dipole interaction with respect to all possible global rotations. We found the same minima as for the ASE energy, namely the $3Q^1$ state.

To compare the dipole-dipole interaction to the ASE we show in Fig. S5 the energies of the least (red) and most (green) favored orientations of all states along the path 2Q-3Q-1Q. Fig. S5(b) shows the same data as in the main text. Both interactions have a qualitatively very similar behavior. However, the sign of the ASE in Pd/Mn/Re(0001) is opposite to the (fixed) sign of the dipole-dipole term. In contrast to the dipole-dipole interaction the sign of the ASE is material dependent. Both

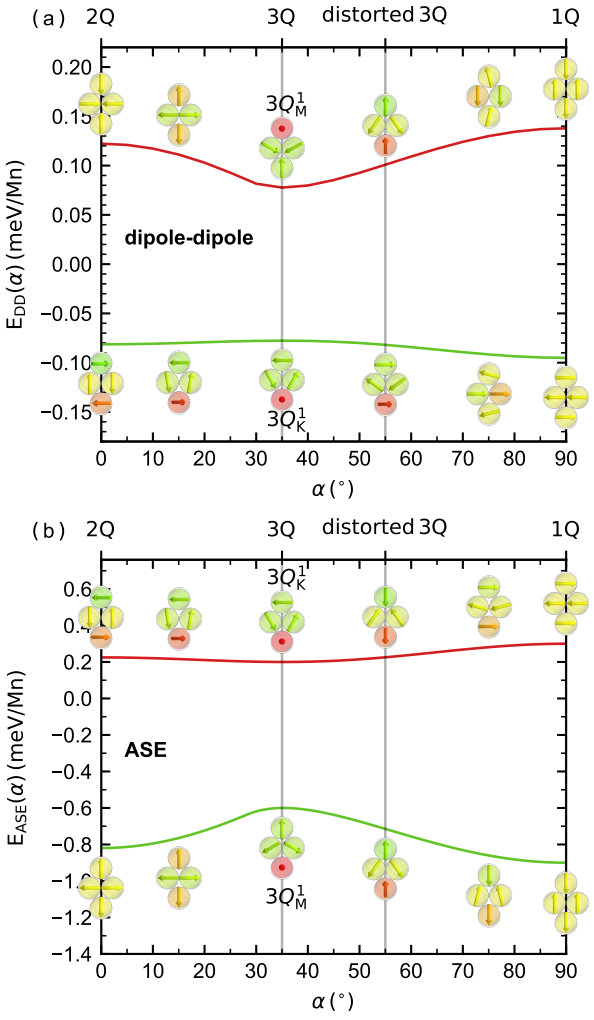

FIG. S5. Energy contribution of (a) the dipole-dipole interaction and (b) the ASE to all states along the path 2Q-3Q-1Q. The energies are given for the most (green) and least (red) favored orientations. The strength of the dipole-dipole interaction is calculated from the magnetic moment of Mn in Pd/Mn/Re(0001) obtained by DFT. The strength of the ASE is calculated by DFT as described in section S5.

interactions favor the same orientation for a positive sign of J_{ASE} but a different one for a negative sign of J_{ASE}. For the ideal 3Q state both interactions favor the $3Q^1$ state over the $3Q^2$ and the $3Q^3$ state.

The favored state of the dipole-dipole interaction is the $3Q^1_{\mathrm{K}}$ state, which is linked to the $3Q^1_{\mathrm{M}}$ state by a rotation around the z-axis. Although both interactions are competing in Pd/Mn/Re(0001), the energy of the ASE is roughly five time as large as the energy of the dipole-dipole interaction. To calculate the dipole-dipole interaction we used the magnetic moment from Mn of $3.02\,\mu_{\mathrm{B}}$ obtained by DFT calculations of the 3Q state. As the dipole-dipole interaction is long ranged, the energy depends on the size of the considered system. We set up a grid of (500×500) unit cells to calculate the dipole-dipole interaction. We also checked for the convergence with respect to the grid size. The ASE strength is calculated by DFT as described in section S5 for Pd/Mn/Re(0001).

S9. STACKING OF THE ADLAYER

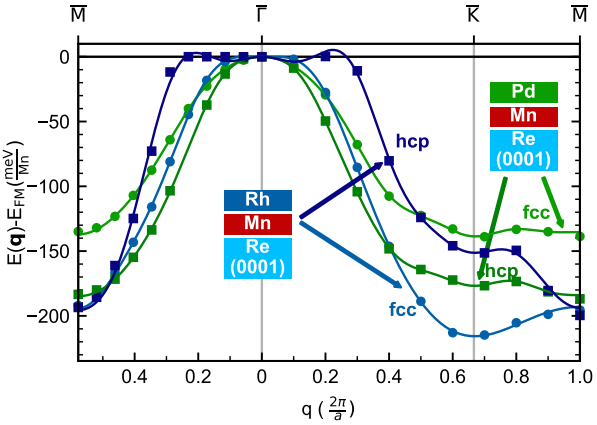

FIG. S6. Energy dispersion of spin spirals along the high-symmetry line $\overline{\mathrm{M}}-\overline{\Gamma}-\overline{\mathrm{K}}-\overline{\mathrm{M}}$ for fcc and hcp stacking of the adlayer in Pd/Mn/Re(0001) and Rh/Mn/Re(0001). Symbols denote values obtained by DFT and lines a fit to the atomistic spin model.

In the main text we present results for an fcc stacking of the Pd or Rh adlayer on Mn/Re(0001). We also assumed an fcc stacking of the Mn layer on Re(0001) as it grows preferably in this stacking. For Rh/Mn/Re(0001) both stackings of the adlayer can be observed in an experiment. For Pd/Mn/Re(0001) only one stacking is observed, but it is unknown, if it is fcc or hcp stacking. In the main text we focused on the fcc stacking.

Here we want to show that an hcp stacking of the adlayer leads to qualitatively the same results. In Fig. S6 the spin spiral energy dispersions of $\mathrm{Pd_{hcp}}$/Mn/Re(0001) and $\mathrm{Rh_{hcp}}$/Mn/Re(0001) are shown together with the energy dispersions of $\mathrm{Pd_{fcc}}$/Mn/Re(0001) and $\mathrm{Rh_{fcc}}$/Mn/Re(0001), which were discussed in the main text. Although there are quantitative energy differences, the RW-AFM is the spin spiral state of lowest energy for both stackings of Pd/Mn/Re(0001). For the hcp stacking of Rh/Mn/Re(0001) also the RW-AFM state is the spin spiral state of lowest energy, whereas for the fcc stacking the Néel state is the state of lowest energy. Due to the high contribution of the HOI the 3Q state is lower in energy than all spin spiral states in all four systems.

The higher order interactions differ even less with stacking than the exchange interactions. This can be verified by the energies along the path 2Q-3Q-1Q as shown in Fig. S7, where the energies are shown for each stacking of the adlayer. The energies for both stackings show a very similar dependency on α. Contributions to the $4th$ and $6th$ order obtained by fitting are very similar.

As the ground state is mostly defined by the HOI in Pd/Mn/Re(0001) and Rh/Mn/Re(0001) and the HOI are very similar for both stackings, the ground state and the qualitative behavior will not change with the stacking of the adlayer.

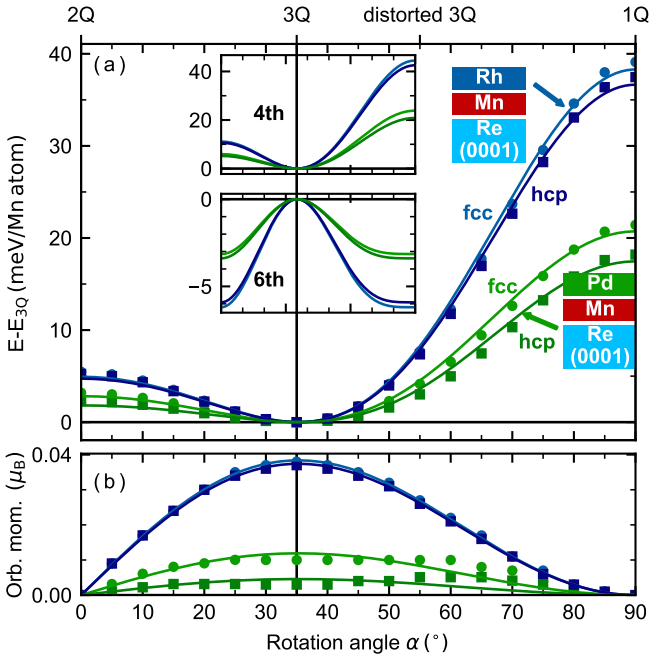

FIG. S7. (a) Energy dispersion for spin states along the path 2Q-3Q-1Q for a fcc and hcp stacking of the adlayer in Pd/Mn/Re(0001) and Rh/Mn/Re(0001). The data for fcc stacking are the same as in the main text. The points represent data from DFT calculations and the lines a fit to the HOI of 4th and 6th order. (b) Absolute value of the topological orbital moment of the Mn atoms. Symbols show DFT values and lines a fit to the scalar spin chirality.

S10. THE 3Q SPIN STRUCTURE

In Tab. S3 the (x, y, z) magnetization components of the $3Q^1$, $3Q^2$, $3Q^3$ state as well as the 1Q and 2Q state are displayed. Here the lattice vectors of the two-dimensional surface unit cell

$$\mathbf{a}_1 = a \begin{pmatrix} 0.5 \\ -\sqrt{(3)}/2 \\ 0 \end{pmatrix} , \tag{S18}$$

$$\mathbf{a}_2 = a \begin{pmatrix} 0.5 \\ \sqrt{(3)}/2 \\ 0 \end{pmatrix} \quad \text{and} \tag{S19}$$

were used, with a the bulk lattice constant.

state	position	mx	my	mz
$3Q^1$	$0\mathbf{a}_1 + 0\mathbf{a}_2$	0	0	1
	$1\mathbf{a}_1 + 0\mathbf{a}_2$	$\sqrt{(2)}/3$	$-\sqrt{(6)}/3$	$-1/3$
	$1\mathbf{a}_1 + 1\mathbf{a}_2$	$-\sqrt{(8)}/3$	0	$-1/3$
	$0\mathbf{a}_1 + 1\mathbf{a}_2$	$\sqrt{(2)}/3$	$\sqrt{(6)}/3$	$-1/3$
$3Q^2$	$0\mathbf{a}_1 + 0\mathbf{a}_2$	$\sqrt{(6)}/3$	0	$1/3$
	$1\mathbf{a}_1 + 0\mathbf{a}_2$	0	$-\sqrt{(6)}/3$	$-1/3$
	$1\mathbf{a}_1 + 1\mathbf{a}_2$	$-\sqrt{(6)}/3$	0	$1/3$
	$0\mathbf{a}_1 + 1\mathbf{a}_2$	0	$\sqrt{(6)}/3$	$-1/3$
$3Q^3$	$0\mathbf{a}_1 + 0\mathbf{a}_2$	$-1/\sqrt{(3)}$	0	$\sqrt{(6)}/3$
	$1\mathbf{a}_1 + 0\mathbf{a}_2$	$1/\sqrt{(3)}$	$-\sqrt{(6)}/3$	0
	$1\mathbf{a}_1 + 1\mathbf{a}_2$	$-1/\sqrt{(3)}$	0	$-\sqrt{(6)}/3$
	$0\mathbf{a}_1 + 1\mathbf{a}_2$	$1/\sqrt{(3)}$	$\sqrt{(6)}/3$	0
2Q	$0\mathbf{a}_1 + 0\mathbf{a}_2$	0	0	-1
	$1\mathbf{a}_1 + 0\mathbf{a}_2$	0	1	0
	$1\mathbf{a}_1 + 1\mathbf{a}_2$	0	0	1
	$0\mathbf{a}_1 + 1\mathbf{a}_2$	0	-1	0
1Q	$0\mathbf{a}_1 + 0\mathbf{a}_2$	-1	0	0
	$1\mathbf{a}_1 + 0\mathbf{a}_2$	1	0	0
	$1\mathbf{a}_1 + 1\mathbf{a}_2$	-1	0	0
	$0\mathbf{a}_1 + 1\mathbf{a}_2$	1	0	0

TABLE S3. Orientations of the magnetic moments in the unit cell for the $3Q^1$, $3Q^2$and $3Q^3$state. The positions are given in units of the lattice vectors (cf. Eq. (S18) and (S19)). The states are given in the all-out configuration as shown in Fig. 1 of the main text.

S11. ENERGETICALLY DEGENERATE $3Q^1$ STATES

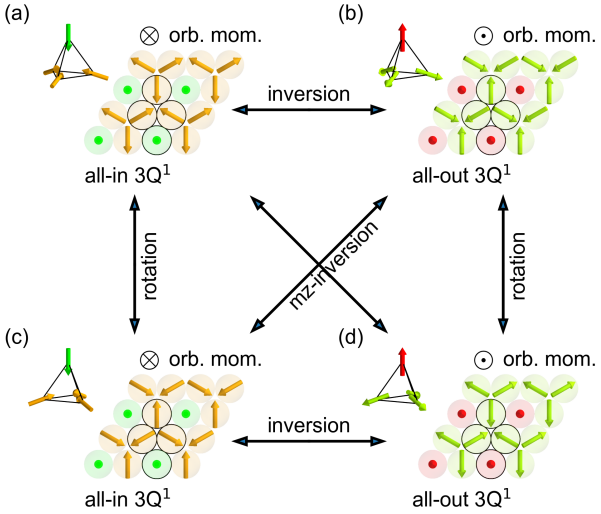

FIG. S8. Illustration of the $3Q^1$ state on the hexagonal lattice in a magnetic monolayer. All shown $3Q^1$ states are degenerate in energy. (a,c) are all-in $3Q^1$ states, whereas (b,d) are all-out $3Q^1$ states. Between the states the operation, which transforms them into each other, is indicated.

The ASE always favors the $3Q^1_M$ or $3Q^1_K$ state depending on the sign. For each $3Q^1$ state four energetically degenerate states exist. These four states are sketched for the $3Q^1_M$ state in Fig. S8. The transformations, which leave the energy invariant, are a 180° rotation around the z-axis, an inversion of all spins or a combination of both, which results in an inversion of the z-component of each spin. To verify that these states are degenerate in energy, we calculated the energy of each state in our atomistic spin model including exchange interactions, higher-order exchange interactions, DMI, MAE, ASE, spin-chiral-interactions and chiral-chiral interactions. We also tested for an interlayer contribution of ASE for magnetic bilayers. With these contribution all four states are energetically degenerate. To verify that we are not missing an energy contribution in our model, which could lift the degeneracy, we calculated the total energy for all four states in Pd/Mn/Re(0001) with DFT. We found no energy difference between all four states within the numerical accuracy of our calculations.

S12. CONTRIBUTIONS TO TOTAL ASE

Fig. S9 shows the bond-resolved contribution of the ASE for the $3Q^2$ and $3Q^3$ states of lowest energy; a value of $J_{\mathrm{ASE}} = -0.3\,\mathrm{meV}$ was assumed as obtained for Pd/Mn/Re(0001). The energies per bond for the $3Q^1$ state which minimizes the energy and the $3Q^1$ state which maximizes the energy are shown in Fig. 5(c) of the main text.

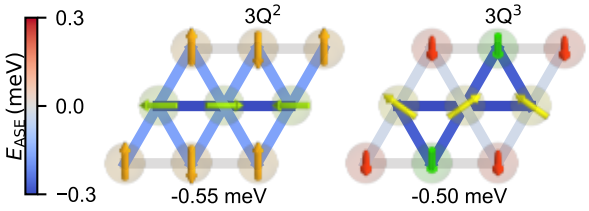

FIG. S9. Contribution to each pair of spins due to the ASE. A blue (red) line represents a negative (positive) contribution in this specific bond. The J_{ASE} parameter was set to $J_{\mathrm{ASE}} = -0.3\,\mathrm{meV}$.

[1] S. Ouazi, T. Pohlmann, A. Kubetzka, K. von Bergmann, and R. Wiesendanger, Scanning tunneling microscopy study of Fe, Co and Cr growth on Re(0001), Surf. Sci. **630**, 280 (2014).

[2] K. von Bergmann, A. Kubetzka, O. Pietzsch, and R. Wiesendanger, Interface-induced chiral domain walls, spin spirals and skyrmions revealed by spin-polarized scanning tunneling microscopy, J. Phys.: Condens. Matter **26**, 394002 (2014).

[3] See `https://www.flapw.de`.

[4] P. Kurz, F. Förster, L. Nordström, G. Bihlmayer, and S. Blügel, *Ab initio* treatment of noncollinear magnets with the full-potential linearized augmented plane wave method, Phys. Rev. B **69**, 024415 (2004).

[5] M. Heide, G. Bihlmayer, and S. Blügel, Describing Dzyaloshinskii-Moriya spirals from first principles, Phys. B **404**, 2678 (2009).

[6] G. Kresse and J. Furthmüller, Efficient iterative schemes for *ab initio* total-energy calculations using a plane-wave basis set, Phys. Rev. B **54**, 11169 (1996).

[7] See `https://www.vasp.at`.

[8] S. H. Vosko, L. Wilk, and M. Nusair, Accurate spin-dependent electron liquid correlation energies for local spin density calculations: a critical analysis, Can. J. Phys. **58**, 1200 (1980).

[9] J. P. Perdew, K. Burke, and M. Ernzerhof, Generalized gradient approximation made simple, Phys. Rev. Lett. **77**, 3865 (1996).

[10] J. Spethmann, S. Meyer, K. von Bergmann, R. Wiesendanger, S. Heinze, and A. Kubetzka, Discovery of magnetic single- and triple-**q** states in Mn/Re(0001), Phys. Rev. Lett. **124**, 227203 (2020).

[11] M. Hoffmann and S. Blügel, Systematic derivation of realistic spin models for beyond-heisenberg solids, Phys. Rev. B **101**, 024418 (2020).

[12] W. Li, S. Paul, K. von Bergmann, S. Heinze, and R. Wiesendanger, Stacking-Dependent Spin Interactions in Pd/Fe Bilayers on Re(0001), Phys. Rev. Lett. **125**, 227205 (2020).

[13] S. Paul, S. Haldar, S. Malottki, and S. Heinze, Role of higher-order exchange interactions for skyrmion stability, Nat. Commun. **11**, 4756 (2020).

[14] S. Grytsiuk, J.-P. Hanke, M. Hoffmann, J. Bouaziz, O. Gomonay, G. Bihlmayer, S. Lounis, Y. Mokrousov, and S. Blügel, Topological–chiral magnetic interactions driven by emergent orbital magnetism, Nat. Commun. **11**, 511 (2020).

6 Antiferromagnetic order of topological orbital moments in atomic-scale skyrmion lattices

Name: Antiferromagnetic order of topological orbital moments in atomic-scale skyrmion lattices

Published: npj Spintronics **3**, 7 (2025)

DOI: https://doi.org/10.1038/s44306-025-00074-3

Authors: Felix Nickel, André Kubetzka, Mara Gutzeit, Roland Wiesendanger, Kirsten von Bergmann, Stefan Heinze

Author contributions: K.v.B. and A.K. performed the experimental measurements and analyzed the data. **F.N.** performed the DFT calculations on Fe/Ir-3/Re(0001) and all atomistic spin simulations. M.G. performed the DFT calculations on Fe/ Ir(111). S.H. and **F.N.** analyzed the theoretical data. K.v.B., S.H. and **F.N.** wrote the manuscript with contributions from all authors.

npj | spintronics

Article

https://doi.org/10.1038/s44306-025-00074-3

Antiferromagnetic order of topological orbital moments in atomic-scale skyrmion lattices

Check for updates

Felix Nickel[1] ✉, André Kubetzka[2], Mara Gutzeit[1], Roland Wiesendanger[2], Kirsten von Bergmann[2] ✉ & Stefan Heinze[1,3] ✉

Topological orbital moments can arise in non-coplanar spin structures even in the absence of spin-orbit coupling and a net topological orbital magnetization occurs for the triple-Q state and for isolated skyrmions. For atomic-scale skyrmion lattices, a significant effect can also be expected, however, no studies have been reported yet. Here, we observe via spin-polarized scanning tunneling microscopy (SP-STM) a non-coplanar atomic-scale spin structure with a roughly square magnetic unit cell for a pseudomorphic Fe monolayer on three atomic Ir layers on the Re(0001) surface. Employing density functional theory (DFT) calculations we consider different skyrmionic lattices as potential magnetic ground states which are found to be energetically favored with respect to any spin spiral state. Comparison of simulated and experimental SP-STM images provides strong evidence for an atomic-scale skyrmion lattice. By mapping the DFT total energies to an atomistic spin model we demonstrate that these spin textures are stabilized by the interplay of the Dzyaloshinskii-Moriya and four-spin interactions. We evaluate the emerging phenomena of the different non-coplanar magnetic states and find significant local topological orbital moments oriented perpendicular to the surface, which order in an antiferromagnetic fashion.

Magnetic skyrmions have raised widespread attention because of their fascinating topological and dynamical properties[1,2]. Due to the spin topology of a skyrmion an emergent magnetic field arises which causes the topological Hall effect[3] allowing electrical detection of single skyrmions[4]. Another key consequence of electron motion in the fictitious magnetic field is the topological orbital moment. It can occur in non-coplanar spin structures even in the absence of spin-orbit coupling and depends on the local scalar spin chirality[3,5–7]. The scalar spin chirality is proportional to the topological charge density and can serve as a measure of topological transport properties[3,5,6,8].

Topological orbital moments have been predicted for several types of spin structures such as multi-Q states[5,9], atomic-scale spin lattices[8], and isolated skyrmions[6,10]. In the triple-Q state[11–13]—exhibiting tetrahedron angles between adjacent spins on a hexagonal lattice and a net vanishing spin moment—the topological orbital moments align such that a net orbital magnetization remains[5]. Such topological orbital ferromagnetism has also been proposed for the bulk antiferromagnet γ-FeMn[14]. A net topological orbital moment remains as well for single skyrmions in a ferromagnetic background and it has been suggested that these are observable via XMCD[6]. The orbital magnetization can be manipulated by an external magnetic field which has been shown via the spontaneous topological Hall effect in the triple-Q state[15,16]. Other prime candidates for the investigation of topological orbital moments are zero-field non-coplanar magnetic states that have been experimentally found in Fe monolayers in contact with a hexagonal Ir film[17,18]. Due to the large tilting angles between adjacent spin moments such spin textures could result in significant topological orbital moments. Designing appropriate nano-scale non-collinear spin structures and harnessing their orbital moment may be of great benefit in spintronic applications[19,20].

Here, we investigate the non-coplanar spin structure of Fe/Ir-3/Re(0001) using SP-STM experiments with different tip magnetization directions as well as DFT calculations and an atomistic spin model. We show via DFT that multi-Q states and atomic-scale skyrmionic lattices constructed based on the experimentally determined magnetic unit cell are energetically significantly favored with respect to all single-Q (spin spiral) states due to higher order interactions. Indeed, comparison of measured and simulated SP-STM images indicate the presence of an atomic-scale

[1]Institut für Theoretische Physik und Astrophysik, Christian-Albrechts-Universität zu Kiel, D-24098 Kiel, Germany. [2]Department of Physics, University of Hamburg, Jungiusstraße 11, 20355 Hamburg, Germany. [3]Kiel Nano, Surface, and Interface Science (KiNSIS), University of Kiel, Kiel, Germany.
✉e-mail: nickel@physik.uni-kiel.de; kirsten.von.bergmann@physik.uni-hamburg.de; heinze@physik.uni-kiel.de

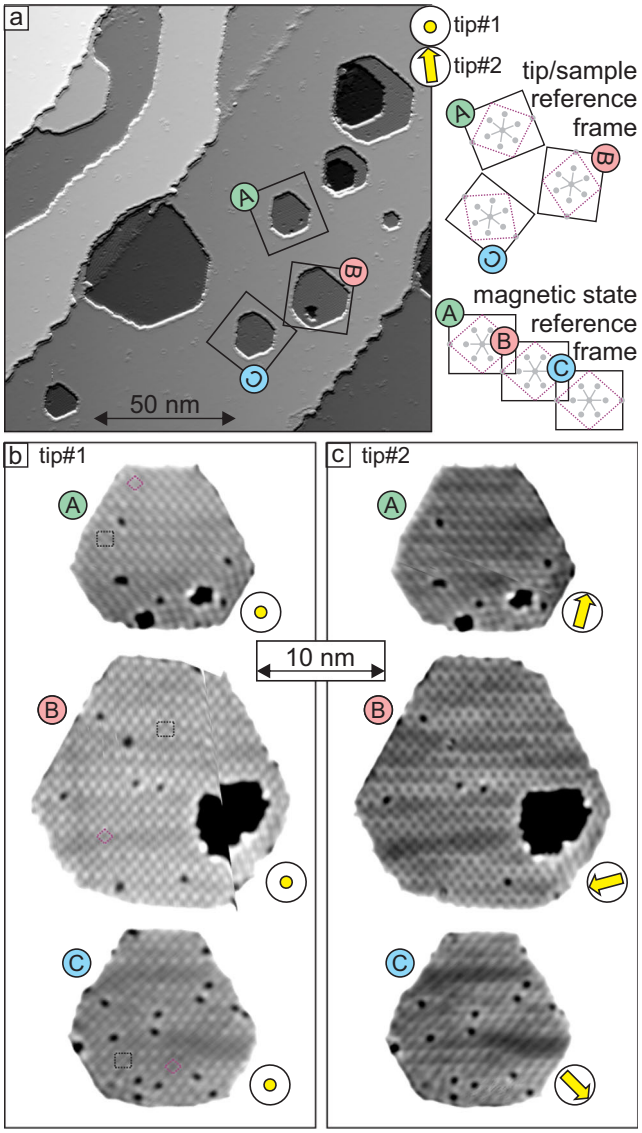

Fig. 1 | SP-STM measurements of Fe/Ir-3/Re(0001). a Overview partially differentiated constant-current SP-STM measurement. **b**, **c** SP-STM measurements of the three Fe/Ir3 areas indicated by squares in (**a**), measured with two slightly different tips as indicated; the gray scale spans 40 pm; the yellow arrows refer to tentative tip magnetization directions and their relative orientation for the rotational magnetic domains. Sketches at the top right explain the connection between the SP-STM image in (**a**), and the zoomed and rotated areas in (**b**, **c**); the two derived possible magnetic unit cells are purple and black, and gray dots indicate the hexagonally arranged Fe atoms. Measurement parameters: **a** $U = +100$ mV, $I = 1$ nA; **b** $U = +40$ mV, $I = 1$ nA; **c** $U = +5$ mV, $I = 4$ nA; all: $T = 4$ K, Cr bulk tip; the glitch in island B of **b** stems from a briefly retracted tip and subsequent creep; the fast scan direction of the islands in **b** and **c** is along the horizontal axis of the overview image in (**a**).

skyrmion lattice. The superposition states are stabilized by the four-site four spin interaction as shown via mapping DFT total energies to an atomistic spin model. Due to their non-coplanar spin textures significant local topological orbital moments arise in these multi-Q states and atomic-scale skyrmionic lattices. Intriguingly, these considered spin structures exhibit antiferromagnetic order of the arising topological orbital moments.

Results

SP-STM experiments

Pseudomorphic Fe monolayers on Ir ultra-thin films on Re(0001) have been investigated experimentally before[18] and in the case of an Ir film with a thickness of three atomic layers an atomic-scale two-dimensional magnetic unit cell has been found. An overview SP-STM image is shown in Fig. 1a and three Fe monolayer patches are labeled A,B,C. These three Fe islands are embedded in an additional Ir layer and the observed modulations are of magnetic origin. We find that these three areas represent rotational domains of the same magnetic state. Due to the incompatibility of the symmetry of the magnetic state and the hexagonal atomic arrangement three rotational domains of the magnetic state can occur, and the areas labeled by A,B,C correspond to those rotations. In Fig. 1b, c the three Fe islands are shown in the magnetic unit cell reference frame, i.e., their relative 120° rotations on the sample have been accommodated for (cf. sketches to the right of Fig. 1a). Each set of these SP-STM images has been measured with one magnetic tip, but the tip changed between the data displayed in Fig. 1b, c. In the images measured with tip#1 (Fig. 1b) a roughly square magnetic unit cell can be seen clearly in some parts of the islands, see purple boxes. However, in other parts of the island a larger superstructure dominates, as indicated by black boxes. We attribute this ambiguity of the size of the magnetic unit cell to either boundary effects that lead to an incommensurability, or to an intrinsic incommensurability of magnetic and structural periodicities (in the vertical direction of Fig. 1b).

Close inspection of the magnetic contrast shows that it is qualitatively similar in all three images of Fig. 1b, whereas the observed magnetic pattern changes for the rotational domains displayed in Fig. 1c. This is characteristic for a non-collinear magnetic state imaged with an out-of-plane magnetized tip in the first case (Fig. 1b), and a magnetic tip that also has an in-plane magnetization component in the latter case (Fig. 1c)[17]. Tentative tip magnetization directions are indicated in yellow to visualize the origin: the sample's out-of-plane components always show the same pattern, regardless of the orientation of the magnetic unit cell; however, an in-plane magnetized tip will pick up different sample magnetization components depending on how the magnetic unit cell is rotated relative to the tip magnetization direction. For tip#2 a two-dimensionally periodic pattern is observed in islands A and B, whereas for island C a stripe pattern is found, which is reminiscent of the SP-STM measurements of the Fe monolayer on Ir(111), which exhibits a square nanoskyrmion lattice[17].

First-principles calculations

To understand the origin of the magnetic ground state of Fe/Ir-3/Re(0001), we have performed first-principles calculations based on DFT (for computational details see "Methods"). We calculate the total energy of various collinear and non-collinear magnetic states with and without including spin-orbit coupling (SOC). We start with spin spiral states since these represent the general solution of the classical Heisenberg model on a periodic lattice and therefore allow to scan a large part of the magnetic phase space.

The energy dispersion $E(\mathbf{q})$ of spin spirals in Fe/Ir-3/Re(0001) neglecting the effect of SOC (gray curve in Fig. 2) displays two minima along the high-symmetry directions $\overline{\Gamma}$-$\overline{M}$ and $\overline{\Gamma}$-$\overline{K}$ with an energy of about 5 meV/Fe atom below the ferromagnetic (FM) state ($\overline{\Gamma}$ point) exhibiting a similar length of the spin spiral vector $\mathbf{q}$. This indicates the stabilization of spin spirals by frustrated exchange interactions. Note, that the total energy scale of the dispersion is below 25 meV/Fe atom which is an extremely small value. This is due to a small FM nearest-neighbor (NN) exchange interaction which competes with antiferromagnetic beyond-NN exchange (values are given in Supplementary Table 1).

The influence of higher-order interactions (HOI) can be revealed by calculating the total energy of superposition states of spin spirals, so-called multi-Q states: the collinear up-up-down-down (*uudd* or double row-wise antiferromagnetic) states along both high-symmetry directions[21–24] and the non-collinear 3Q state[9,11–13]. Within the Heisenberg model of pair-wise exchange these states are degenerate with the spin spiral (single-Q) states from which they are constructed. This degeneracy can be lifted by HOI. Therefore, a total DFT energy difference between single-Q and multi-Q states—obtained neglecting SOC in the calculation—is an indication of HOI. Note, that within DFT all magnetic interactions are implicitly contained within the exchange-correlation functional.

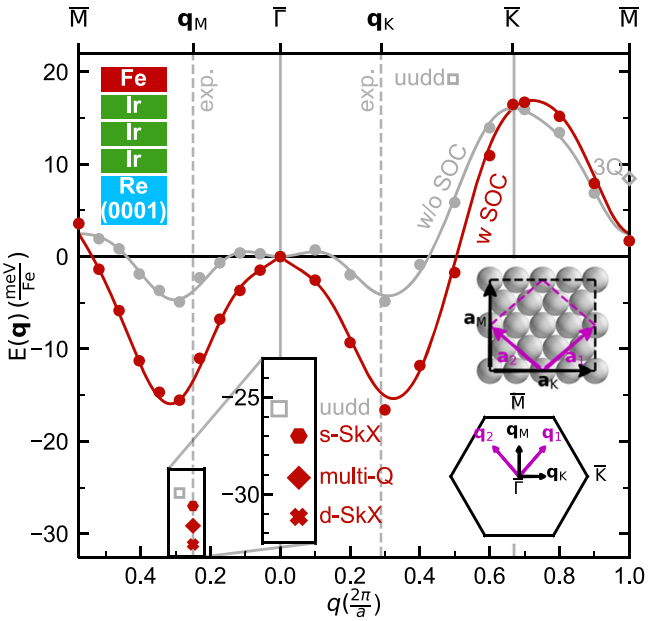

Fig. 2 | DFT total energies of spin states in Fe/Ir-3/Re(0001). Energy dispersion of spin spirals obtained via DFT along the high-symmetry lines $\overline{\text{M}}$-$\overline{\Gamma}$-$\overline{\text{K}}$-$\overline{\text{M}}$ with and without including SOC displayed by filled red and gray circles, respectively. The solid line represents a fit of the atomistic model to the DFT values. The total energies of the two *uudd* states and the 3Q state calculated via DFT are marked. The self-consistently calculated DFT total energies including SOC for the three spin lattices (Fig. 3) are also marked. All energies are given with respect to the FM state. In the inset the unit cells of the magnetic contrast is shown with the magnetic unit cell vectors $\mathbf{a}_1$ and $\mathbf{a}_2$ and $\mathbf{a}_\text{M}$ and $\mathbf{a}_\text{K}$ in purple and black, respectively obtained based on the experimental SP-STM images (cf. Fig. 1). The Brillouin zone is also sketched as an inset and the spin spiral vectors $\mathbf{q}_1$, $\mathbf{q}_2$, $\mathbf{q}_\text{K}$ and $\mathbf{q}_\text{M}$ are indicated. Dashed gray lines indicate the experimentally determined absolute values of $\mathbf{q}_\text{K}$ and $\mathbf{q}_\text{M}$.

In Fig. 2 a clear deviation of the energies of the *uudd* and the 3Q states from the corresponding 1Q states is evident, which means that HOI exhibit a significant strength in this system. Out of the spin spiral states and the mentioned model-type multi-Q states the *uudd* state in $\overline{\Gamma M}$ direction has the lowest energy by $\Delta E \approx 20$ meV/Fe atom lower than the minima of the single-Q state dispersion neglecting SOC (gray curve in Fig. 2). ΔE indicates the energy scale of the HOI.

The energy dispersion of spin spirals including the contribution of SOC, i.e., Dzyaloshinskii-Moriya interaction (DMI), is displayed in the red curve in Fig. 2 (for separate contributions see Supplementary Note 1 and Supplementary Fig. 1). Due to the DMI the minima in the spin spiral dispersion gain even more energy compared to the FM state, so that the energy difference is about 15 meV/Fe atom. As the DMI has no contribution to the collinear *uudd* state, the energy difference between the *uudd* state and the spin spiral of minimal energy is reduced by SOC.

To construct a superposition state with the experimentally observed magnetic unit cell (cf. Fig. 1), we convert the real space magnetic lattice vectors of the roughly square commensurate unit cell $\mathbf{a}_1$ and $\mathbf{a}_2$ into spin spiral vectors $\mathbf{q}_1$ and $\mathbf{q}_2$ in reciprocal space (see inset of Fig. 2). From $\mathbf{q}_1$ and $\mathbf{q}_2$ we can obtain spin spiral vectors $\mathbf{q}_\text{M}$ and $\mathbf{q}_\text{K}$ in the high symmetry directions (see inset in Fig. 2). These are given by $\mathbf{q}_\text{M} = \frac{1}{2}(\mathbf{q}_1 + \mathbf{q}_2) = \frac{\pi}{2a}\hat{e}_y$ and $\mathbf{q}_\text{K} = \frac{1}{2}(\mathbf{q}_1 - \mathbf{q}_2) = \frac{\pi}{\sqrt{3}a}\hat{e}_x$, respectively, and they are related to the larger magnetic unit cell with lattice vectors $\mathbf{a}_\text{M}$ and $\mathbf{a}_\text{K}$ also observed in the experimental data. These $\mathbf{q}$ vectors are close to the energy minima of $E(\mathbf{q})$ obtained from DFT calculations (Fig. 2). The size of the magnetic unit cell is defined by the interactions with the largest energy contribution, which are the exchange interaction and the DMI. Compared to the multi-Q state in Fe/Ir(111)[17,25] the minima of the spin spiral calculations are at larger values of $|\mathbf{q}|$ for Fe/Ir-3/Re(0001) (Fig. 2). This leads to a reduction of the size of the unit cell.

The multi-Q state is constructed from these spin spirals using the analytical expression given in ref. 17 (see also "Methods" section) and its spin texture is displayed in Fig. 3a. Within DFT it is energetically significantly lower in total energy than the spin spiral minimum and a few meV/Fe atom lower than the *uudd* state along $\overline{\Gamma\text{M}}$ (Fig. 2). The two-dimensional magnetic unit cell of the multi-Q state contains 16 atoms (Fig. 3a) and two spins point upwards with respect to the surface (red) and two spins point downwards (blue). All other spins are oriented in the film plane (green arrows). From the unit cell of the multi-Q state we can identify two substructures which show a spin configuration on an atomic scale reminiscent of an individual skyrmion or antiskyrmion (purple boxes in Fig. 3a).

While these atomic-scale spin structures cannot be defined as skyrmions within a continuum description, they still share key properties of skyrmions such as vorticity and chirality of the spins surrounding the center. As a measure of their topological properties, we use the scalar spin chirality which is non-vanishing for these atomic-scale spin structures and is linked to topological orbital moments as discussed below and the topological Hall effect[3,5,7,8]. The two different upward pointing spins of the multi-Q state in Fig. 3a can be viewed as the center of an atomic-scale skyrmionic (S) or antiskyrmionic (A) building block of the lattice, respectively, compare purple boxes in Fig. 3a with Fig. 3d, e (In the same manner the downward pointing spins could be seen as the centers of equivalent substructures).

Topological orbital moments

In order to gain further insight into the properties of the multi-Q state we have calculated the topological orbital moment (TOM) per atom via DFT. In Fig. 3a, the TOM of every Fe atom is displayed by the color of the hexagon at the corresponding lattice site (for values see Supplementary Fig. 2). Note, that the skyrmionic spin structure possesses a positive TOM, while the antiskyrmionic spin structure exhibits a negative TOM, with the largest contribution at the positions of out-of-plane spins. Therefore, we observe rows of positive and negative TOM in the multi-Q state. The absolute value of the TOM, calculated by DFT, per skyrmionic or antiskyrmionic plaquette amounts to about 0.32 μ_B, while the sum of all TOMs in the black magnetic unit cell vanishes (For the contribution of a plaquette, we sum the contributions of all spins in the substructure, where the contributions from the corners are considered with an factor of $\frac{1}{4}$).

Starting from the multi-Q state, one can obtain other spin configurations consistent with the experimentally determined magnetic unit cell and we consider two other likely non-coplanar candidates. By inverting the two in-plane oriented spins in the antiskyrmionic substructure pointing along the *x*-direction (Fig. 3a), the magnetic state obtains the rotational sense favored by the DMI (Fig. 3b). This operation transforms the antiskyrmionic structure (Fig. 3e) into a new type of substructure which we refer to as pseudo-skyrmionic (labeled by p-S, see Fig. 3f). The resulting spin structure contains an atomic-scale skyrmionic and a pseudo-skyrmionic plaquette in the unit cell (Fig. 3b) and is denoted as double-skyrmionic lattice (d-SkX). The d-SkX state is even lower in total energy within DFT than the multi-Q state (Fig. 2).

In the d-SkX the TOM of the skyrmionic plaquette is 0.19 μ_B and thus similar to that in the multi-Q state. For the pseudo-skyrmionic substructure the TOM is smaller and inverted with respect to the corresponding antiskyrmionic plaquette in the multi-Q state (cf. Fig. 3a, b), leading to a checkerboard antiferromagnetic TOM order. The total TOM is still compensated.

Finally, we consider a spin texture which comprises only one type of skyrmionic substructure per unit cell (Fig. 3c), reminiscent of the nanoskyrmion lattice in the Fe monolayer on Ir(111)[17]. This single-skyrmionic lattice (s-SkX) is obtained from the multi-Q state by replacing the antiskyrmionic by a skyrmionic substructure. The s-SkX contains one skyrmionic plaquette and the resulting TOMs at the out-of-plane spins form a checkerboard pattern. In contrast to the previous two spin textures (multi-Q and d-SkX) the s-SkX exhibits a net TOM of about 0.17 μ_B per sykrmionic plaquette. If all spins of the displayed s-SkX are inverted an energetically degenerate state is obtained with a total TOM in the opposite direction, similar to the case of the triple-Q state[13]. However, in our DFT calculations

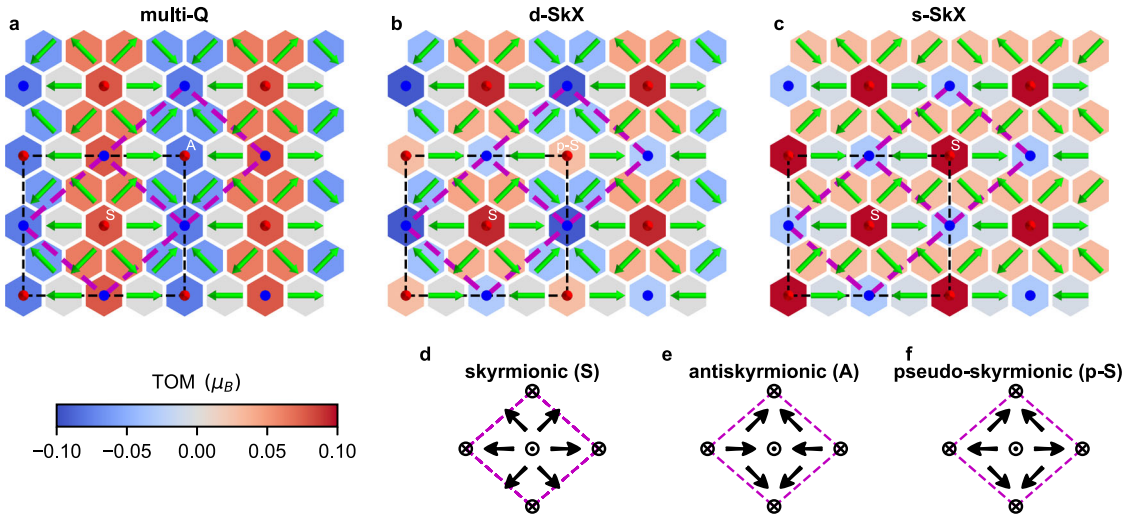

Fig. 3 | Spin structure and topological orbital moments of atomic-scale spin lattices. a multi-Q state, **b** double-skyrmionic lattice (d-SkX), and **c** single-skyrmionic lattice (s-SkX). The multi-Q state is constructed from a superposition of spin spirals with **q** vectors corresponding to the magnetic unit cell obtained in experiment (see text for details). The d-SkX lattice has been obtained from the multi-Q state by flipping two spins in the antiskyrmionic substructure to optimize the DMI energy. For the s-SkX lattice the antiskyrmionic substructures in the multi-Q state have been replaced by skyrmionic substructures to reduce the size of the magnetic unit cell. The dashed black (purple) box marks the magnetic unit cell of the multi-Q and d-SkX (s-SkX). The color of the hexagons display the topological orbital moment (TOM) for each atom calculated by DFT (see color bar at bottom). Red (blue) color denotes upwards (downwards) pointing TOM with respect to the surface normal. For the ease of discussion in the text, the centers of atomic-scale substructures of the spin lattices are denoted by letters: skyrmionic (S), antiskyrmionic (A), and pseudo-skyrmionic (p-S) which are also shown by the sketches in (**d**)–(**f**).

Table 1 | DFT energies vs. atomistic spin model

	DFT		Spin model	
	w/o SOC	w/SOC	w/o SOC	w/SOC
multi-Q state	−26.7	−29.2	−22.6	−23.0
d-SkX lattice	−27.2	−31.2	−24.4	−26.2
s-SkX lattice	−23.4	−27.0	−20.5	−22.0

Total energies of the three atomic-scale spin lattices considered for Fe/Ir-3/Re(0001) (cf. Fig. 3) with respect to the FM state with and without (w/o) SOC. The total energies are given as calculated by DFT and obtained using the atomistic spin model. All energies are given in meV/Fe atom.

the s-SkX is energetically unfavorable with respect to both the multi-Q state and the d-SkX (Fig. 2).

To understand the origin of these orbital moments emerging even without SOC, we compare the TOM calculated via DFT with an atomistic model. Within this atomistic model, the TOM at site i, $\mathbf{L}_i^{\mathrm{TO}}$, can be related to the scalar spin chirality[7]:

$$\mathbf{L}_i^{\mathrm{TO}} = \sum_{(jk)} \kappa_{ijk}^{\mathrm{TO}} \chi_{ijk} \tau_{ijk} \tag{1}$$

where i, j, k denote neighboring lattice sites and the sum (jk) is over all pairs of neighboring lattice sites of site i. For the investigated lattices $\tau_{ijk} = \hat{\mathbf{z}}$ is the unit vector along the direction perpendicular to the surface.

The scalar spin chirality is defined as $\chi_{ijk} = \mathbf{s}_i \cdot (\mathbf{s}_j \times \mathbf{s}_k)$ and only the spin structure is needed for its calculation. This makes Eq. (1) appealing to determine the TOM. Note, that the scalar spin chirality has also a profound effect on the transport properties of a magnetic material and can lead to a topological Hall conductivity in the absence of spin-orbit coupling[5,8].

However, the topological orbital susceptibility $\kappa_{ijk}^{\mathrm{TO}}$ depends on the electronic structure and can vary for each triangle (ijk). To obtain $\kappa_{ijk}^{\mathrm{TO}}$ from our DFT calculations of the $\mathbf{L}_i^{\mathrm{TO}}$, we assume it to be independent of the chosen triangle (ijk), i.e., $\kappa_i^{\mathrm{TO}} = \kappa_{ijk}^{\mathrm{TO}}$. Indeed, for all three investigated lattices, we find that κ_i^{TO} is nearly independent of the site i of the Fe atom, which is consistent with a nearly constant Fe spin moment on all lattice sites (see Supplementary Fig. 2 and Supplementary Note 2).

The values obtained for the three different skyrmionic lattices show only a very small variation among them with $\kappa_i^{\mathrm{TO}} = 0.019 \pm 0.002\,\mu_B$ (see Supplementary Table 2 for all values). The calculated TOMs at the individual sites obtained within the atomistic model considering a constant orbital susceptibility agree very well with the ones calculated by DFT. This demonstrates that the spatial variation of the TOM originates mostly from the change of the spin structure, rather than from the change in the electronic structure, and that the atomistic model already gives a good approximation of the TOM. The nanoskyrmion lattice in Fe/Ir(111)[17] shows a similar behavior, as the TOM is vanishing for the multi-Q state and non-vanishing if the skyrmionic structures are isolated by a scissor operation (for these data see Supplementary Note 3 and Supplementary Figs. 3 and 4).

Atomistic spin model

An atomistic spin model (see "Methods") has been parameterized by the DFT data shown in Fig. 2, which includes pair-wise and higher-order exchange (HOI), DMI, magnetocrystalline anisotropy energy (MAE) and anisotropic symmetric exchange (ASE) (for details about the parameterization see Supplementary Note 1). The DFT total energies calculated with and without SOC for the multi-Q state, the d-SkX and s-SkX lattice are given in Table 1. The order among the three states is the same with and without SOC, but the values show that the s-SkX and the d-SkX states gain more energy due to SOC than the multi-Q state. The total energies of the spin model show the same trend as the DFT calculations.

The exchange, DMI, and four-site-four-spin interaction have the largest contribution to the total energy (for all values see Supplementary Table 1 and for the other interactions see Supplementary Note 4 and Supplementary Fig. 5) and we present their energy contributions per Fe atom in Fig. 4. Among the three spin structures, the multi-Q state exhibits the lowest exchange energy (Fig. 4a) which is due to the construction as a superposition of spin spirals close to the energy minima of the dispersion (cf. Fig. 2). Therefore, a flip of some spins increases the exchange energy as seen for the d-SkX (Fig. 4b). The s-SkX is the least favored lattice concerning the exchange interaction (Fig. 4c). Regarding the DMI the multi-Q state shows two rows with an opposite rotational sense with positive and negative contributions (Fig. 4d). By flipping two spins in the unfavorable row (bottom and top row in Fig. 4d) the rotational sense is switched and the DMI

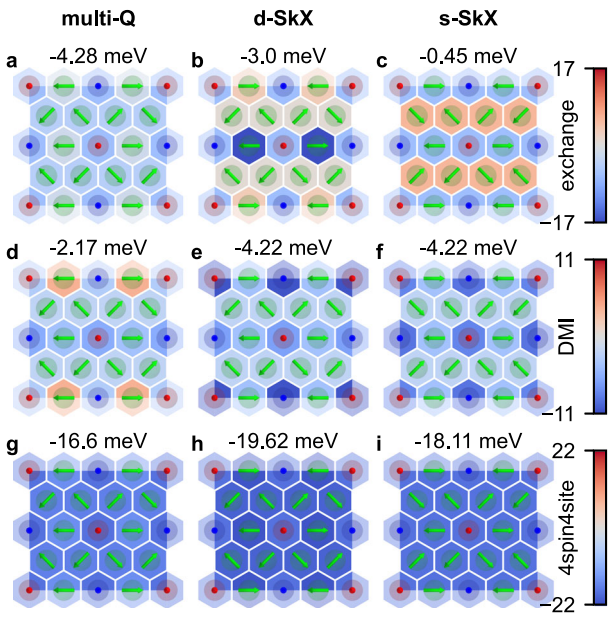

Fig. 4 | Energy decomposition of magnetic interactions. Energy contributions of **a**–**c** the exchange interaction, **d**–**f** the DMI, and **g**–**i** the four-site-four-spin interaction obtained in the atomistic spin model for the multi-Q state (left row), the d-SkX lattice (middle row), and the s-SkX lattice (right row). All energies are displayed with respect to the FM state. The interactions of all contributing shells of neighbors have been added. A scale bar is given for each interaction and above each plot the sum over all atoms in the unit cell is given. All energies are given in meV per atom.

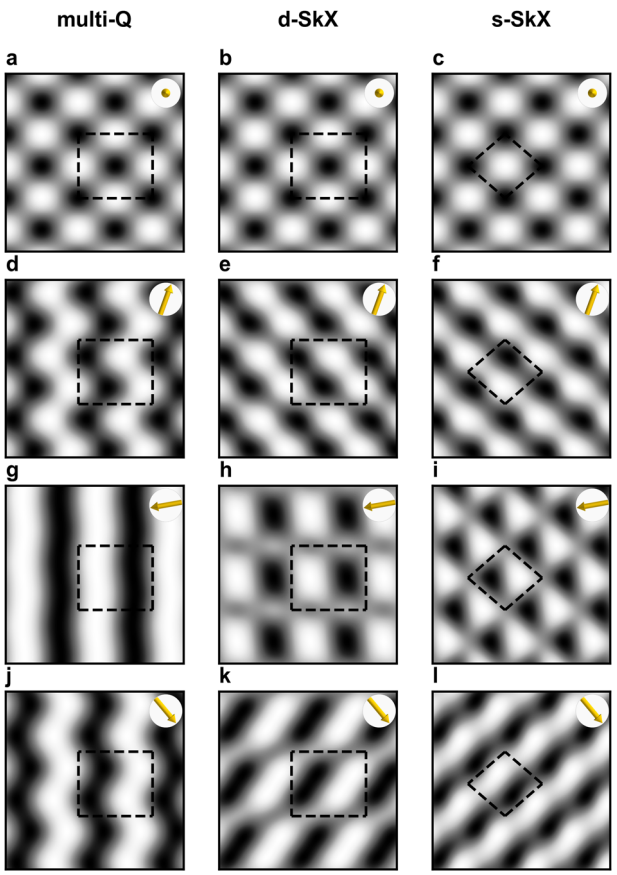

Fig. 5 | SP-STM simulations. Simulated images are shown for **a**, **d**, **g**, **j** the multi-Q state, **b**, **e**, **h**, **k** the d-SkX, and **c**, **f**, **i**, **l** the s-SkX. For each spin lattice the simulated SP-STM image is displayed for an out-of-plane orientation of the tip magnetization (top row) and for three in-plane orientations of the tip with an angle of 120° between the different orientations (three lower rows). The tip magnetization direction is indicated in the top right corner of each panel by a yellow arrow and the dashed lines mark the magnetic unit cell as shown in Fig. 3.

energy can be reduced. Therefore, compared to the multi-Q state, the d-SkX and the s-SkX optimize the DMI energy (Fig. 4e, f) with the same rotational sense in each row.

All three spin lattices gain significant energy compared to the FM state due to the four-site-four-spin interaction (Fig. 4g–i). Regarding the four-site-four-spin interaction the flip of two spins in the bottom row reduces the energy of the d-SkX with respect to the multi-Q state. The reduction of the size of the unit cell from the d-SkX to the s-SkX is slightly unfavorable in terms of the four-site-four-spin interaction. The role played by the four-site-four-spin interaction is very similar to that in the nanoskyrmion lattice of Fe/Ir(111)[17]. Note, that the three-site-four-spin or the biquadratic interaction can also favor multi-Q states or nanoskyrmion lattices. However, in the system considered here these terms have only a minor strength (see values in Supplementary Table 1). The d-SkX is energetically most favorable among all considered spin lattices. It gains energy due to DMI and four-site-four-spin interaction with respect to the multi-Q state and due to exchange and four-site-four-spin interaction with respect to the s-SkX.

SP-STM simulations

For a direct comparison of the three spin lattices (Fig. 3) with the experimental data (Fig. 1), we simulated SP-STM images using the spin-polarized generalization of the Tersoff-Hamann model[26–28]. For an out-of-plane tip magnetization as shown in Fig. 5a–c all three lattices have the same roughly square contrast. These SP-STM simulations are in good agreement with the experimental magnetic contrast observed with tip#1 on all three islands in Fig. 1b. At the same time it becomes evident, that an out-of-plane tip is not suitable to distinguish between the three different proposed spin lattices. In contrast, different patterns are observed for the three different magnetic states when an in-plane magnetized tip is used, as evident from the SP-STM simulation in Fig. 5d–l. For each spin lattice a set of three different in-plane orientations of the tip magnetization has been used that are linked by 120° angles with respect to each other, such that they correspond to a fixed tip magnetization on three different rotational domains of the spin structure as observed in the SP-STM measurements for islands A, B, and C (Fig. 1c).

One characteristic feature observed in the experimental SP-STM images are the stripes visible on island C. We find a similar pattern in our SP-STM simulations for the d-SkX and the s-SkX for an in-plane tip magnetization that is roughly perpendicular to the stripes, see Fig. 5k, l. However, such stripes are never observed for the multi-Q state, regardless of the tip magnetization direction. In contrast, for the multi-Q the simulations show wavy or straight stripes along the vertical direction for all in-plane tip magnetization directions, see Fig. 5d, g, j. Because this kind of pattern is not in agreement with the experimental results we rule out the presence of this multi-Q state in our system. The patterns for the d-SkX and the s-SkX resulting from the rotated tip magnetization directions in Fig. 5e-i can all be recognized in the experimental images of Fig. 1c, which makes a distinction between those two states challenging.

Discussion

We propose a spontaneous atomic-scale skyrmionic lattice as the magnetic ground state of an Fe monolayer on three atomic Ir layers on the Re(0001) surface. Our first-principles calculations reveal sizeable topological orbital magnetic moments with antiferromagnetic alignment for the different proposed spin textures which can be explained by the local scalar spin chirality due to the non-coplanar spin order in the skyrmionic lattices. The topological orbital susceptibility obtained via DFT is nearly constant for all

Fe atoms in the lattice and is nearly independent of the considered spin lattice. This makes the atomistic model a very good approximation for the topological orbital moments. We find that Fe-based film systems have a significantly larger orbital susceptibility than Mn-based film systems[13] (see Supplementary Table 2) which can lead to a larger topological orbital magnetization. This might make Fe-based thin-film systems interesting candidates for the emerging field of orbitronics and the observation of transport phenomena such as the topological Hall effect[5,8].

Based on the comparison with the experiment, the multi-Q state can be ruled out as the magnetic ground state of Fe/Ir-3/Re(0001) in agreement with the DFT calculation. While in DFT the d-SkX is slightly lower in total energy compared to the s-SkX, in our experiments we cannot identify whether the d-SkX or the s-SkX is realized in our system due to the lateral variation of the apparent magnetic unit cell. Because Re becomes superconducting below 1.7 K such a zero magnetic field spin lattice is a promising candidate for future studies of emerging phenomena in atomic-scale non-coplanar magnet-superconductor hybrid systems[29–31], including the role of topological orbital moments in proximity to a superconductor.

Methods

SP-STM experiments

The samples were prepared in a multi-chamber ultra-high vacuum system. The Re(0001) surface was cleaned by high-temperature flashes[32] and Ir and Fe were evaporated from rods by electron beam heating[18]. Samples were then transferred *in-vacuo* into an STM that is operated at 4 K. The tip is made of Cr bulk material. The tip magnetization direction can be changed in-situ by gentle modifications of the tip apex. The spin-polarized contribution to the tunnel current scales with the projection of tip and sample magnetization directions, and the nano-scale magnetic order can be detected directly in constant-current imaging mode[33].

DFT calculations

We have performed density functional theory (DFT) calculations to investigate the magnetic ground state and the magnetic interactions in Fe monolayers on three atomic layers of Ir on the Re(0001) surface. DFT calculations have been carried out using two different methods. We have used the all-electron code FLEUR based on the full-potential linearized augmented plane-wave (FLAPW) method (see https://www.flapw.de)[34,35]. In addition, we have applied the projector augmented wave (PAW) method as implemented in the VASP code[36] (see https://www.vasp.at). Here we provide computational details of the calculations using both codes.

The FLEUR code has been used for spin spiral calculations[34] neglecting and including spin-orbit coupling (SOC), and to obtain the total energies of the *uudd* states and the 3Q state. The SOC contribution to the energy of spin spirals was calculated using first order perturbation theory[35]. The magnetocrystalline anisotropy energy (MAE), defined as the total energy difference between the energy for a magnetization oriented along the in-plane and the out-of-plane direction, has been calculated self-consistently including SOC for the FM state[37].

For all calculations using the FLEUR code the cut-off parameter for the basis functions has been set to $k_{\max} = 4.1\,\text{a.u.}^{-1}$. The radius of the muffin-tin spheres was chosen as 2.45 a.u. for Re and 2.3 a.u. for Ir and Fe. The exchange-correlation (xc) functional for all calculations in FLEUR was chosen in local density approximation (LDA)[38]. For the spin spiral calculations with and without SOC a mesh of (44×44) k-points was used in the full 2D-BZ. The calculations for the 3Q state and the *uudd* states in their respective super-cells were performed on a (22×22) k-point mesh, which has the same density of k-points as that used in the spin spiral calculations. For the calculations of the MAE in the FM state a mesh of (223×223) k-points was used. For all calculations with the FLEUR code asymmetric films with one Fe layer, three Ir layers, and six layers of Re have been used. The Fe and Ir layers have been chosen in fcc stacking on the Re(0001) surface.

Structural relaxations of Fe/Ir-3/Re(0001) have been performed using the VASP code in the RW-AFM state. For the relaxations the GGA xc-functional PBE[39] and a (15×15) grid of k-points was used. The multi-Q state, the d-SkX, and the s-SkX have been calculated in a supercell with 16 atoms per layer and the same number of substrate layers as in the spin spiral calculations. The cut-off of the wavefunctions was set to 268 eV and a grid of (15×15) k-points was used for these supercell calculations. The LDA xc-functional by Vosko, Wilk and Nusair[38] has been applied. Topological orbital moments have been calculated using the VASP code. For fcc-Fe/Ir(111) they have been obtained based on the computational setup given in ref. 25.

Construction of the multi-Q state

The superposition of spin spirals defined by $\mathbf{q}_\mathrm{M}$ and $\mathbf{q}_\mathrm{K}$ under the constraint of a constant magnitude of the magnetization is given by the construction presented in ref. 17:

$$\mathbf{S}_i = S \begin{pmatrix} \sin(\mathbf{q}_\mathrm{M} \cdot \mathbf{R}_i) \\ \cos(\mathbf{q}_\mathrm{M} \cdot \mathbf{R}_i)\sin(\mathbf{q}_\mathrm{K} \cdot \mathbf{R}_i) \\ \cos(\mathbf{q}_\mathrm{M} \cdot \mathbf{R}_i)\cos(\mathbf{q}_\mathrm{K} \cdot \mathbf{R}_i) \end{pmatrix} \tag{2}$$

where $\mathbf{R}_i$ denotes the atomic site i and $\mathbf{S}_i$ is the spin moment at this site. From Eq. (2) it is apparent that the spin exhibits a constant value of S at every lattice site. Note that $\mathbf{q}_\mathrm{M}$ and $\mathbf{q}_\mathrm{K}$ are obtained from the experimentally determined reciprocal lattice vectors $\mathbf{q}_1$ and $\mathbf{q}_2$ by $\mathbf{q}_\mathrm{M} = \frac{1}{2}(\mathbf{q}_1 + \mathbf{q}_2)$ and $\mathbf{q}_\mathrm{K} = \frac{1}{2}(\mathbf{q}_1 - \mathbf{q}_2)$, respectively.

Atomistic spin model

The atomistic spin model applied in our work contains exchange interaction, DMI, higher-order interaction (HOI), MAE and anisotropic symmetric exchange (ASE). The corresponding Hamiltonian is given by:

$$\begin{aligned} H = & \underbrace{-\sum_{i,j} J_{ij}(\mathbf{s}_i \cdot \mathbf{s}_j)}_{\text{exchange}} \underbrace{-\sum_{i,j} \mathbf{D}_{ij}(\mathbf{s}_i \times \mathbf{s}_j)}_{\text{DMI}} \underbrace{-\sum_{i,j} B_{ij}(\mathbf{s}_i \cdot \mathbf{s}_j)^2}_{\text{biquadratic}} \\ & \underbrace{-\sum_{ijk} Y_{ijk}[(\mathbf{s}_i \cdot \mathbf{s}_j)(\mathbf{s}_j \cdot \mathbf{s}_k) + (\mathbf{s}_j \cdot \mathbf{s}_i)(\mathbf{s}_i \cdot \mathbf{s}_k) + (\mathbf{s}_i \cdot \mathbf{s}_k)(\mathbf{s}_k \cdot \mathbf{s}_j)]}_{\text{3site-4spin}} \\ & \underbrace{-\sum_{ijkl} K_{ijkl}[(\mathbf{s}_i \cdot \mathbf{s}_j)(\mathbf{s}_k \cdot \mathbf{s}_l) + (\mathbf{s}_i \cdot \mathbf{s}_l)(\mathbf{s}_j \cdot \mathbf{s}_k) - (\mathbf{s}_i \cdot \mathbf{s}_k)(\mathbf{s}_j \cdot \mathbf{s}_l)]}_{\text{4site-4spin}} \\ & \underbrace{-\sum_{i} K_u(\mathbf{s}_i \cdot \hat{\mathbf{z}})^2}_{\text{MAE}} \underbrace{-J_{\text{ASE}} \sum_{ij} (\mathbf{s}_i \cdot \mathbf{d}_{ij})(\mathbf{s}_j \cdot \mathbf{d}_{ij})}_{\text{ASE}}, \end{aligned} \tag{3}$$

where $\mathbf{s}_i = \mathbf{S}_i/|\mathbf{S}_i|$ denotes a normalized spin moment at a lattice site specified by i, $\hat{\mathbf{z}}$ is the unit vector perpendicular to the surface and $\mathbf{d}_{ij}$ is the normalized connection vector between the lattice sites i and j. The interactions are sorted in shells according to the distance of the lattice sites. For all atoms of each shell the same interaction constants are assumed. For the exchange and the DMI the interaction parameters for the first ten shells have been calculated. For all other interactions only the interaction parameter of the first shell has been calculated.

SP-STM simulations

The simulations of SP-STM images are based on the spin-polarized generalization of the Tersoff-Hamann model[26,27]. We used a simplified SP-STM model in which the independent orbital approximation is applied[28]. In this model only the orientation of the magnetic moments with respect to the tip magnetization and the tip-sample distance are needed.

Data availability

All relevant data are available from the corresponding authors upon reasonable request.

Code availability

All relevant code is available from the corresponding authors upon reasonable request.

Received: 23 July 2024; Accepted: 25 January 2025;
Published online: 14 March 2025

References

1. Nagaosa, N. & Tokura, Y. Topological properties and dynamics of magnetic skyrmions. *Nat. Nanotechnol.* **8**, 899–911 (2013).
2. Fert, A., Cros, V. & Sampaio, J. Skyrmions on the track. *Nat. Nano.* **8**, 152–156 (2013).
3. Taguchi, Y., Oohara, Y., Yoshizawa, H., Nagaosa, N. & Tokura, Y. Spin chirality, Berry phase, and anomalous Hall effect in a frustrated ferromagnet. *Science* **291**, 2573 (2001).
4. Maccariello, D. et al. Electrical detection of single magnetic skyrmions in metallic multilayers at room temperature. *Nat. Nanotechnol.* **13**, 233 (2018).
5. Hanke, J.-P. et al. Role of Berry phase theory for describing orbital magnetism: from magnetic heterostructures to topological orbital ferromagnets. *Phys. Rev. B* **94**, 121114(R) (2016).
6. dos Santos Dias, M., Bouaziz, J., Bouhassoune, M., Blügel, S. & Lounis, S. Chirality-driven orbital magnetic moments as a new probe for topological magnetic structures. *Nat. Commun.* **7**, 13613 (2016).
7. Grytsiuk, S. et al. Topological-chiral magnetic interactions driven by emergent orbital magnetism. *Nat. Commun.* **11**, 511 (2020).
8. Hoffmann, M. et al. Topological orbital magnetization and emergent Hall effect of an atomic-scale spin lattice at a surface. *Phys. Rev. B* **92**, 020401 (2015).
9. Haldar, S., Meyer, S., Kubetzka, A. & Heinze, S. Distorted 3*q* state driven by topological-chiral magnetic interactions. *Phys. Rev. B* **104**, L180404 (2021).
10. Lux, F., Freimuth, F., Blügel, S. & Mokrousov, Y. Engineering chiral and topological orbital magnetism of domain walls and skyrmions. *Commun. Phys.* **1**, 60 (2018).
11. Kurz, P., Bihlmayer, G., Hirai, K. & Blügel, S. Three-dimensional spin structure on a two-dimensional lattice: Mn/Cu(111). *Phys. Rev. Lett.* **86**, 1106–1109 (2001).
12. Spethmann, J. et al. Discovery of magnetic single- and triple-**q** states in $\mathrm{Mn}/\mathrm{Re}(0001)$. *Phys. Rev. Lett.* **124**, 227203 (2020).
13. Nickel, F. et al. Coupling of the triple-q state to the atomic lattice by anisotropic symmetric exchange. *Phys. Rev. B* **108**, L180411 (2023).
14. Hanke, J.-P., Freimuth, F., Blügel, S. & Mokrousov, Y. Prototypical topological orbital ferromagnet *γ*-FeMn. *Sci. Rep.* **7**, 41078 (2017).
15. Park, P. et al. Tetrahedral triple-q ordering in the metallic triangular lattice antiferromagnet $Co_{1/3}TaS_2$. *Nat. Commun.* **14**, 8346 (2023).
16. Takagi, H. et al. Spontaneous topological Hall effect induced by non-coplanar antiferromagnetic order in intercalated van der Waals materials. *Nat. Phys.* **19**, 961 (2023).
17. Heinze, S. et al. Spontaneous atomic-scale magnetic skyrmion lattice in two dimensions. *Nat. Phys.* **7**, 713–718 (2011).
18. Kubetzka, A., Bürger, J. M., Wiesendanger, R. & von Bergmann, K. Towards skyrmion-superconductor hybrid systems. *Phys. Rev. Mater.* **4**, 081401 (2020).
19. Jo, D., Go, D., Choi, G.-M. & Lee, H.-W. Spintronics meets orbitronics: emergence of orbital angular momentum in solids. *npj Spintronics* **2**, 19 (2024).
20. Dal Din, A., Amin, O. J., Wadley, P. & Edmonds, K. W. Antiferromagnetic spintronics and beyond. *npj Spintronics* **2**, 25 (2024).
21. Hardrat, B. et al. Complex magnetism of fe monolayers on hexagonal transition-metal surfaces from first principles. *Phys. Rev. B* **79**, 094411 (2009).
22. Krönlein, A. et al. Magnetic ground state stabilized by three-site interactions: Fe/Rh(111). *Phys. Rev. Lett.* **120**, 207202 (2018).
23. Hoffmann, M. & Blügel, S. Systematic derivation of realistic spin models for beyond-Heisenberg solids. *Phys. Rev. B* **101**, 024418 (2020).
24. Gutzeit, M., Haldar, S., Meyer, S. & Heinze, S. Trends of higher-order exchange interactions in transition metal trilayers. *Phys. Rev. B* **104**, 024420 (2021).
25. Gutzeit, M., Drevelow, T., Goerzen, M. A., Haldar, S. & Heinze, S. Spontaneous square versus hexagonal nanoscale skyrmion lattices in Fe/Ir(111). *Phys. Rev. B* **108**, L060405 (2023).
26. Tersoff, J. & Hamann, D. R. Theory of the scanning tunneling microscope. *Phys. Rev. B* **31**, 805–813 (1985).
27. Wortmann, D., Heinze, S., Kurz, P., Bihlmayer, G. & Blügel, S. Resolving complex atomic-scale spin structures by spin-polarized scanning tunneling microscopy. *Phys. Rev. Lett.* **86**, 4132–4135 (2001).
28. Heinze, S. Simulation of spin-polarized scanning tunneling microscopy images of nanoscale non-collinear magnetic structures. *Appl. Phys. A* **85**, 407–414 (2006).
29. Bedow, J. et al. Topological superconductivity induced by a triple-q magnetic structure. *Phys. Rev. B* **102**, 180504(R) (2020).
30. Mæland, K. & Sudbø, A. Quantum topological phase transitions in skyrmion crystals. *Phys. Rev. Res.* **4**, L032025 (2022).
31. Mæland, K. & Sudbø, A. Topological superconductivity mediated by skyrmionic magnons. *Phys. Rev. Lett.* **130**, 156002 (2023).
32. Ouazi, S., Pohlmann, T., Kubetzka, A., von Bergmann, K. & Wiesendanger, R. Scanning tunneling microscopy study of Fe, Co and Cr growth on Re(0001). *Surf. Sci.* **630**, 280–285 (2014).
33. von Bergmann, K., Kubetzka, A., Pietzsch, O. & Wiesendanger, R. Interface-induced chiral domain walls, spin spirals and skyrmions revealed by spin-polarized scanning tunneling microscopy. *J. Phys. Condens. Matter* **26**, 394002 (2014).
34. Kurz, P., Förster, F., Nordström, L., Bihlmayer, G. & Blügel, S. Ab initio treatment of noncollinear magnets with the full-potential linearized augmented plane wave method. *Phys. Rev. B* **69**, 024415 (2004).
35. Heide, M., Bihlmayer, G. & Blügel, S. Describing Dzyaloshinskii-Moriya spirals from first principles. *Phys. B Condens. Matter* **404**, 2678–2683 (2009).
36. Kresse, G. & Furthmüller, J. Efficient iterative schemes for ab initio total-energy calculations using a plane-wave basis set. *Phys. Rev. B* **54**, 11169–11186 (1996).
37. Li, C., Freeman, A. J., Jansen, H. J. & Fu, C. L. Magnetic anisotropy in low-dimensional ferromagnetic systems: Fe monolayers on Ag(001), Au(001), and Pd(001) substrates. *Phys. Rev. B* **42**, 5433 (1990).
38. Vosko, S. H., Wilk, L. & Nusair, M. Accurate spin-dependent electron liquid correlation energies for local spin density calculations: a critical analysis. *Can. J. Phys.* **58**, 1200–1211 (1980).
39. Perdew, J. P., Burke, K. & Ernzerhof, M. Generalized gradient approximation made simple. *Phys. Rev. Lett.* **77**, 3865–3868 (1996).

Acknowledgements

It is our pleasure to thank Yuriy Mokrousov for valuable discussions. We gratefully acknowledge financial support from the Deutsche Forschungsgemeinschaft (DFG, German Research Foundation) via projects no. 402843438, no. 418425860, and no. 462602351, and computing time provided by the North-German Supercomputing Alliance (HLRN).

Author contributions

K.v.B. and A.K. performed the experimental measurements and analyzed the data. F.N. performed the DFT calculations on Fe/Ir-3/Re(0001) and all atomistic spin simulations. M.G. performed the DFT calculations on Fe/Ir(111). S.H. and F.N. analyzed the theoretical data. K.v.B., S.H. and F.N. wrote the manuscript with contributions from all authors.

Funding
Open Access funding enabled and organized by Projekt DEAL.

Competing interests
The authors declare no competing interests.

Additional information
Supplementary information The online version contains supplementary material available at https://doi.org/10.1038/s44306-025-00074-3.

Correspondence and requests for materials should be addressed to Felix Nickel, Kirsten von Bergmann or Stefan Heinze.

Supplementary Information for "Antiferromagnetic order of topological orbital moments in atomic-scale skyrmion lattices"

Felix Nickel,[1,*] André Kubetzka,[2] Mara Gutzeit,[1]
Roland Wiesendanger,[2] Kirsten von Bergmann,[2,†] and Stefan Heinze[1,3,‡]

[1] *Institut für Theoretische Physik und Astrophysik, Christian-Albrechts-Universität zu Kiel, D-24098 Kiel, Germany*
[2] *Department of Physics, University of Hamburg, Jungiusstraße 9-11, 20355 Hamburg, Germany*
[3] *Kiel Nano, Surface, and Interface Science (KiNSIS), University of Kiel, Germany*

(Dated: October 23, 2024)

S1. SPIN SPIRAL ENERGY DISPERSIONS AND INTERACTION CONSTANTS

A spin spiral is characterized by a wave vector $\mathbf{q}$, and the spin at lattice site $\mathbf{R}_i$ is given by $\mathbf{S}_i = S(\cos(\mathbf{q}\cdot\mathbf{R}_i), \sin(\mathbf{q}\cdot\mathbf{R}_i), 0)$, with S denoting the size of the spin and $\mathbf{s}_i = \mathbf{S}_i/S$ being the normalized spin moment. The energy dispersion $E(\mathbf{q})$ is calculated via the FLEUR code using the generalized Bloch theorem [1].

In Fig. 2 in the main text the total energy dispersion of spin spirals is given for an fcc stacking of the Fe layer on Ir-3/Re(0001), which consists of the result from a scalar-relativistic calculation and the contributions due to SOC obtained by first order perturbation theory [2]. In Fig. S1(a) the data from Fig. 2 of the main text is reproduced. The individual contributions from the scalar-relativistic spin spiral calculation and the calculation of the contributions due to SOC, i.e. the energy due to Dzyaloshinskii-Moriya interaction (DMI), are shown in Fig. S1(b,c), respectively.

In Fig. S1, we present for comparison the results obtained for an hcp stacking of the Fe monolayer on Ir-3/Re(0001). For hcp-Fe/Ir-3/Re(0001) the total dispersion also exhibits two spin spiral energy minima. However, these are located at slightly larger $\mathbf{q}$ than for fcc stacking and they are asymmetric since the depth of the minima is very different. This means the periodicity of the spin structure in the hcp system is smaller than in fcc. As a result the energy minima for the hcp stacking fit less well to the observed unit cell in the SP-STM measurements (cf. Fig. 1 from the main text).

For both stackings the DMI (cf. Fig. S1(c)) has a significant contribution to the spin spiral energy minima. Note, that the DMI contributions for the hcp and the fcc system are very similar. In the scalar-relativistic approximation (Fig. S1(b)) hcp-Fe/Ir-3/Re(0001) exhibits only a small energy minimum along $\overline{\Gamma}$-$\overline{\mathrm{K}}$ and no minimum along $\overline{\Gamma}$-$\overline{\mathrm{M}}$. For fcc stacking, on the other hand, the energy minima are located very close to those in the total energy dispersion in panel (a). Therefore, we conclude that the nearly quadratic magnetic unit cell is observed in a fcc stacking of the Fe monolayer.

From the energy dispersion of spin spirals obtained via DFT the exchange and DMI constants can be determined by a fit. However, the energies of the scalar-relativistic spin spiral calculations contain also contribution from higher-order interactions (HOI). To differentiate between higher-order exchange and Heisenberg pair-wise exchange the energy of further multi-Q states

* Email: nickel@physik.uni-kiel.de
† Email: kirsten.von.bergmann@physik.uni-hamburg.de
‡ Email: heinze@physik.uni-kiel.de

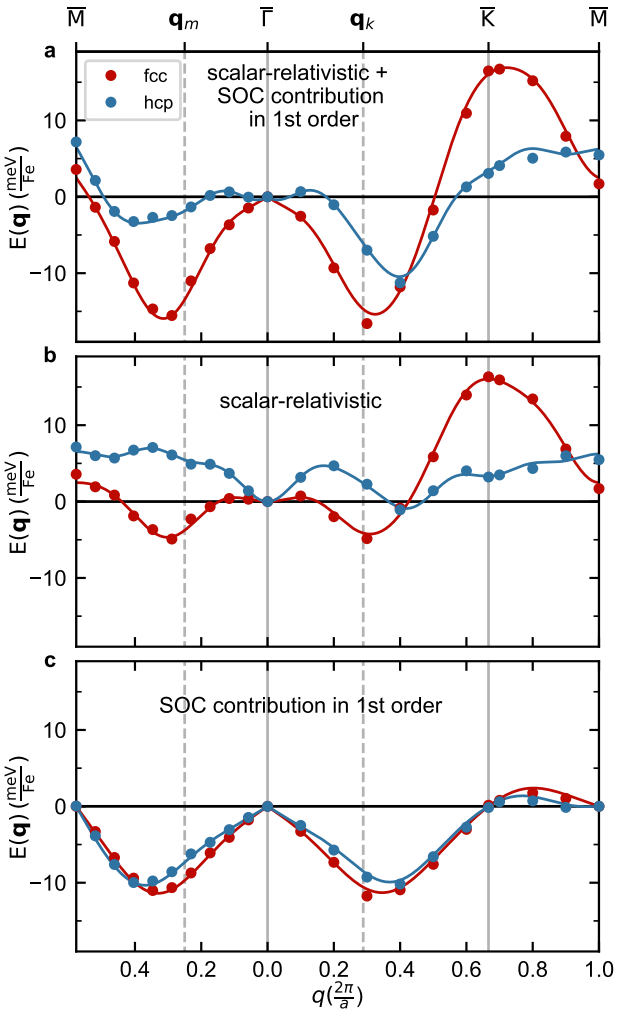

FIG. S1. Energy dispersion of spin spirals in hcp-Fe/Ir-3/Re(0001) and fcc-Fe/Ir-3/Re(0001) along the high symmetry lines $\overline{\text{M}}$-$\overline{\Gamma}$-$\overline{\text{K}}$-$\overline{\text{M}}$ obtained via DFT (a) in scalar-relativistic approximation plus the contribution due to SOC in first order perturbation theory (b) in scalar-relativistic approximation and (c) SOC contribution calculated in first order perturbation theory. Symbols denote DFT data and lines represent the energy of the atomistic spin model with parameters obtained by a fit to the DFT data. For the fit only the displayed DFT energies of spin spirals were mapped to the atomistic spin model and no other interaction constants were obtained.

is needed, such as the *uudd* states and the 3Q state. One can determine the HOI by the additional states and perform a correction of the Heisenberg exchange constants obtained from the fit to the spin spiral dispersion [3–5].

To treat all magnetic interactions on equal footing, we have chosen a different approach here, in which we fit all parameters simultaneously. In addition to the energies of the *uudd* states and the 3Q state we also calculate the total energies of the multi-Q lattice, the d-SkX, and s-SkX state in scalar-relativistic approximation, i.e. neglecting SOC. The MAE and ASE cannot be derived from the SOC contributions of the spin spirals because MAE and ASE are not included in the first-order perturbation theory. To determine these interactions self-consistent calculation with SOC have been performed. Here we used the ferromagnetic state in two orientations along the x and y direction and DFT calculations for the multi-Q, the d-SkX, and s-SkX state including SOC. In these self-consistent calculations the DMI as well as the MAE and ASE contributions are contained. For each of the states calculated by DFT we calculate the theoretical contribution by the atomistic spin model (Eq. (2) in the Methods section of the manuscript) and fitted the parameters to the energies from DFT. Thereby, we perform a single fit for all calculated DFT energies to the spin model.

The parameters obtained by this fit give a good agreement between the total energies from DFT and the atomistic spin model as shown in Tab. 1 in the main text. In principle also other higher-order interactions such as topological chiral interactions, next-nearest neighbor HOI, or anisotropic HOI could contribute to the energy of the spin structures. Based on the sufficiently good description by our spin model we consider those interactions to play a minor role in the investigated system.

S2. TOPOLOGICAL ORBITAL MOMENTS

The topological orbital moment (TOM) can be calculated via DFT from a scalar-relativistic calculation in which the effects of SOC are neglected. Thus there is no orbital moment contribution due to SOC in such calculations and the only remaining contribution is the TOM. The values of the TOM obtained by DFT are presented in Fig. 3 of the main text. The same data is shown in Fig. S2, where the values of the TOM are given explicitly at the individual lattice sites. In the atomistic model the TOM can be written as

$$\mathbf{L}_i^{\text{TO}} = \sum_{(jk)} \kappa_{ijk}^{\text{TO}} \chi_{ijk} \boldsymbol{\tau}_{ijk} \tag{S1}$$

where i, j, k denote neighboring lattice sites and the sum (jk) is over all pairs of neighboring lattice sites from lattice site i. The direction of the TOM is given by the vector $\boldsymbol{\tau}_{ijk} \propto (\mathbf{R}_j - \mathbf{R}_i) \times (\mathbf{R}_k - \mathbf{R}_i)$, where $\mathbf{R}_i$, $\mathbf{R}_j$, and $\mathbf{R}_k$ are the position vectors of lattice sites i, j, and k, respectively. For a magnetic monolayer $\boldsymbol{\tau}_{ijk}$ is perpendicular to the surface. In the present case $\boldsymbol{\tau}_{ijk} = \hat{\mathbf{z}}$, which is the unit vector along the z-direction. The scalar spin chirality is defined as $\chi_{ijk} = \mathbf{s}_i \cdot (\mathbf{s}_j \times \mathbf{s}_k)$ and κ_{ijk}^{TO} is the topological orbital susceptibility, which depends on the three contributing lattice sites. The TOM at one specific lattice site is the sum of the contributions of all surrounding triangles. For each surrounding triangle (ijk) we assume for simplicity the same topological orbital susceptibility $\kappa_i^{\text{TO}} = \kappa_{ijk}^{\text{TO}}$ which only depends on the lattice site i.

In Fig. S2(a-c) the topological orbital moments are given based on this model. The topological orbital susceptibility has been chosen spatially constant ($\kappa_i^{\text{TO}} =$

J_1	J_2	J_3	J_4	J_5	J_6	J_7	J_8	J_9	J_{10}	B_1	Y_1	K_1
1.96	−2.36	−0.51	0.46	0.29	−0.34	0.32	−0.87	−0.26	0.61	0.04	−0.17	−1.51
D_1	D_2	D_3	D_4	D_5	D_6	D_7	D_8	D_9	D_{10}	K_u	J_{ASE}	
0.63	−0.08	0.83	−0.76	−0.81	0.59	0.77	−0.69	−0.17	0.01	2.73	0.62	

TABLE S1. Interaction constants for $\mathrm{Fe_{fcc}}$/Ir-3/Re(0001). The terms are defined in Eq. (S2). The higher-order exchange interactions are treated in the nearest-neighbor approximation (B_1, Y_1, K_1). All values are given in meV.

system	state	κ^{TO} (μ_B)
Fe/Ir-3/Re(0001)	multi-Q	0.017
Fe/Ir-3/Re(0001)	d-SkX	0.019
Fe/Ir-3/Re(0001)	s-SkX	0.021
Fe/Ir(111)	nano-SkX	0.025
Pd/Mn/Re(0001)	3Q	0.005
Mn/Re(0001)	3Q	0.006
Rh/Mn/Re(0001)	3Q	0.008

TABLE S2. Topological orbital susceptibility κ^{TO} obtained for Fe monolayers from DFT calculations of the TOM by a comparison with the atomistic spin model (see text for details).

κ^{TO}) for each magnetic state according to the values given in Tab. S2. These values were obtained by fitting the maximal values of the model to the maximal values obtained by DFT. The assumption of a constant κ^{TO} allows to see the influence of the spin structure on the TOM. When comparing the TOM of the model (a-c) to the TOM obtained by DFT (d-f) one can see a very good agreement. This agreement for an assumed constant $\kappa_i^{\mathrm{TO}} = \kappa^{\mathrm{TO}}$ shows, that the spatial variation of the TOM mostly originates from the spin structure rather than from a variation in κ_i^{TO}.

The approximation of a constant topological orbital susceptibility should hold if the electronic structure varies only slightly between the different Fe atoms. As a rough measure of the variation, the magnetic spin moments are displayed in Fig. S2(g-i). The maximal difference of the magnetic moments is $0.04\,\mu_B$, i.e. only about 1.5% of the average moment. This small variation in the magnetic moments indicates only a small change in the electronic structure. In Tab. S2 are also the topological orbital susceptibilities for Pd/Mn/Re/(0001), Mn/Re(0001) and Rh/Mn/Re(0001) shown, calculated for 3Q state as shown in [6]. The topological orbital susceptibility in the Mn based systems is roughly a quarter from that one in the investigated Fe based systems.

S3. NANOSKYRMION LATTICE IN FE/IR(111)

In Fig. S3 the nanoskyrmion lattice (nano-SkX) of fcc-Fe/Ir(111) [7] is displayed. The color of the hexagons denotes the magnitude of the z-component of the topological orbital moment in panels (a,b) and the magnitude of the magnetic moment in panel (c). In Fig. S3(a) the topological orbital moments are shown as obtained by the atomistic spin model (cf. Eq. (S3)). The topological orbital susceptibility has been calculated as $0.025\,\mu_B$ for all sites. In Fig. S3(b) the z-components of the orbital moments are shown as calculated via DFT in the scalar-relativistic approximation. Although some deviations exist between the model and the DFT values, the overall trend fits quite well between both. The magnetic moments also vary only very little for the different Fe atoms (Fig. S3(c)). The topological orbital susceptibility in Fe/Ir(111) is slightly larger, but on the same order of magnitude as in Fe/Ir-3/Re(0001) (see values in Tab. S2).

To understand the pattern, which the TOM forms on the lattice, Fig. S4 shows the TOM calculated by the atomistic model for the multi-Q state (Fig. S4(a)) and the nano-SkX (Fig. S4(b)).

The TOM in the multi-Q state forms horizontal rows of positive and negative contributions. All these contributions are canceling each other, so that the total TOM of the unit cell is compensated. Similar to the 2D spin structures in Fe/Ir-3/Re(0001) (cf. Fig. 3 of the main text), one could define skyrmionic or antiskyrmionic substructures, which have an opposite contribution to the TOM.

In the nano-SkX (Fig. S4(b)), which has a smaller 2D unit cell, the TOM forms a checkerboard pattern. The TOM of the plaquettes of positive and negative contributions have a different magnitude, which results in a non-vanishing TOM over the whole unit cell. The net orbital moment of the nano-SkX amounts to 0.11 μ_{B}. Analogous to the multi-Q lattice and the s-SkX lattice in Fig. 3 of the main text, a reduction of the unit cell size leads to a net TOM.

S4. SITE-RESOLVED ENERGY CONTRIBUTIONS

In Fig. S5 the energy contributions of the individual Fe spins are given based on the atomistic spin model with DFT interaction parameters. The plot is analogous to Fig. 4 in the main text and shows the contributions due to the biquadratic interaction (a-c), the 3-site-4-spin interaction (d-f), the MAE (g-i) and the ASE (j-l) for the multi-Q state, the d-SkX, and the s-SkX. Note, that for all these interactions the three spin lattices show only minor energy differences below 1 meV.

The biquadratic interaction disfavors these spin lattices with respect to the FM state by about 0.2 meV, whereas the 3-site-4-spin interaction favors these states

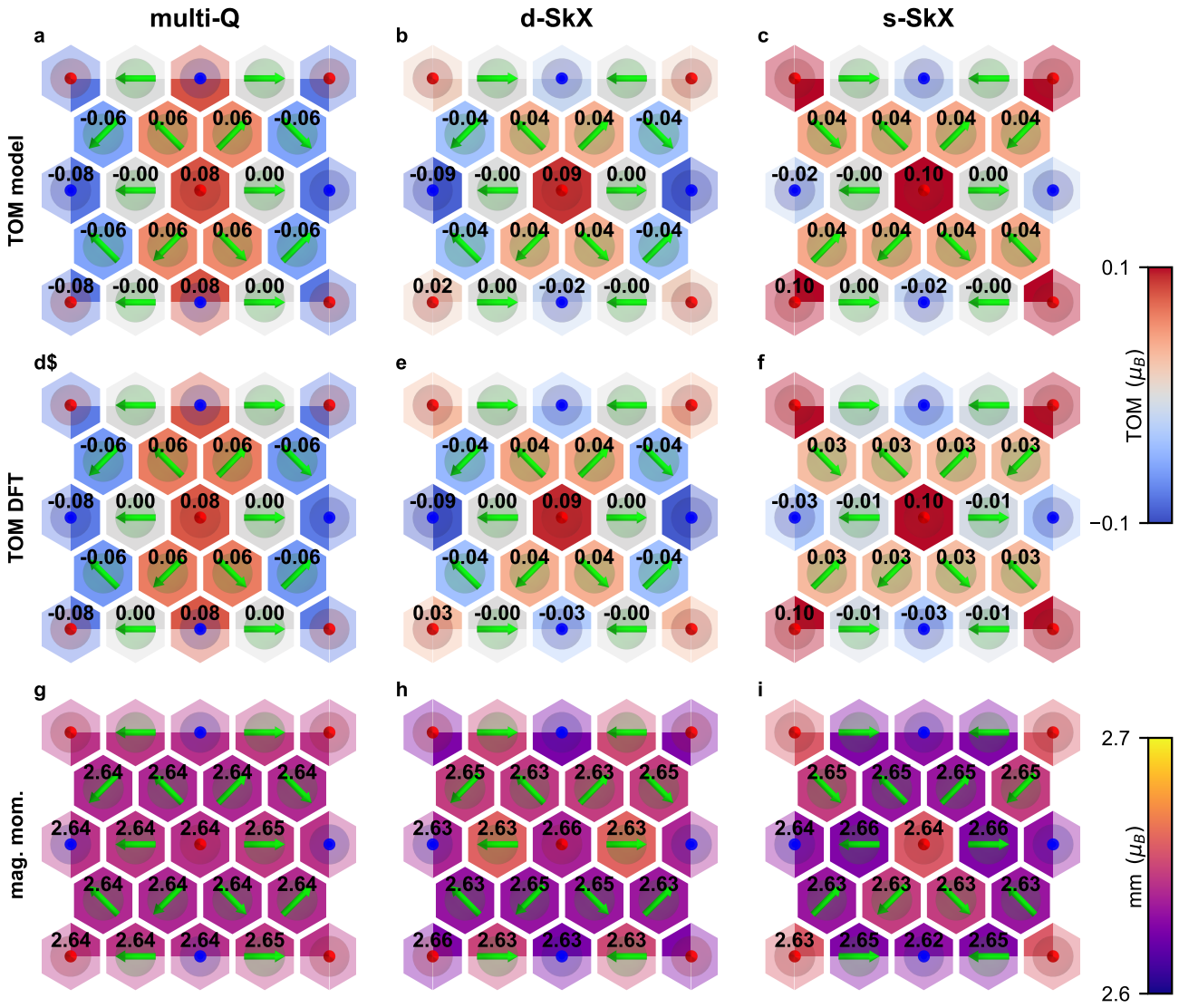

FIG. S2. (a-c) Topological orbital moments calculated in the atomistic model using the topological orbital susceptibility given in Tab. S2. (d-f) Topological orbital moments calculated via DFT. (g-i) Magnetic moments obtained by the same DFT calculation. Values are shown for (a, d, g) the multi-Q state, (b, e, h) the d-SkX, and (c, f, i) the s-SkX.

by about 2 meV with respect to the FM state. The MAE favors an orientation of all spins perpendicular to the surface, which is why all three spin lattices are less favoured than the FM state due to MAE. The ASE provides the lowest energy contribution for a FM alignment along the connection vector. This is mostly satisfied for the multi-Q state and the least for the s-SkX lattice. As all these interactions have only minor energy contributions, the interactions shown in the main text are the decisive ones for stabilizing the nanoscale spin lattices.

[1] P. Kurz, F. Förster, L. Nordström, G. Bihlmayer, and S. Blügel, *Ab initio* treatment of noncollinear magnets with the full-potential linearized augmented plane wave method, Phys. Rev. B **69**, 024415 (2004).

[2] M. Heide, G. Bihlmayer, and S. Blügel, Describing Dzyaloshinskii–Moriya spirals from first principles, Physica B Condens. Matter **404**, 2678 (2009).

[3] M. Hoffmann and S. Blügel, Systematic derivation of realistic spin models for beyond-heisenberg solids, Phys. Rev. B **101**, 024418 (2020).

[4] S. Paul, S. Haldar, S. Malottki, and S. Heinze, Role of higher-order exchange interactions for skyrmion stability,

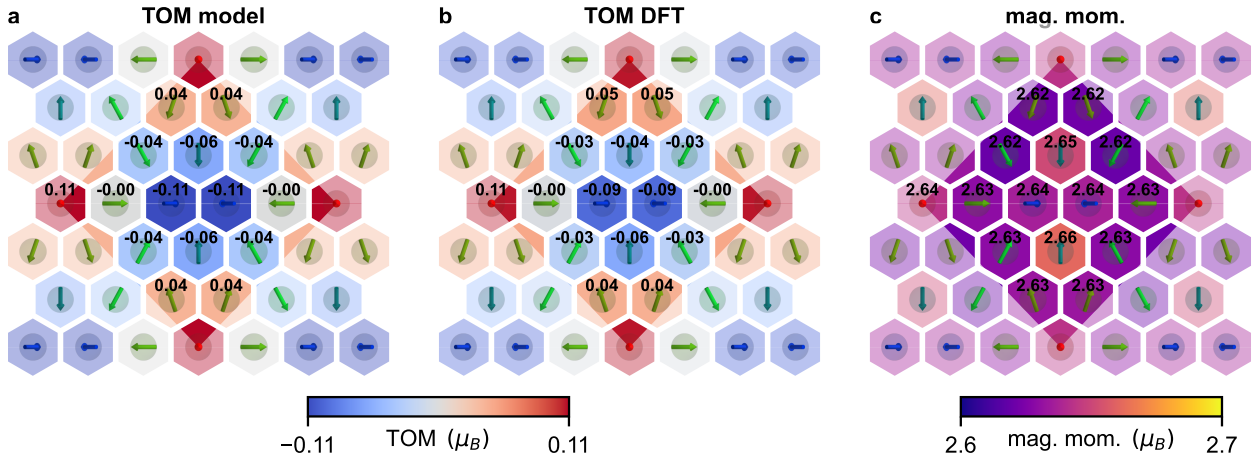

FIG. S3. Topological orbital moments and magnetic moments for the nanoskyrmion lattice of Fe/Ir(111). (a) TOM calculated by the atomistic model, scaled with the topological orbital susceptibility given in Tab. S2. (b) TOM calculated by DFT. (c) Magnetic moments calculated by DFT.

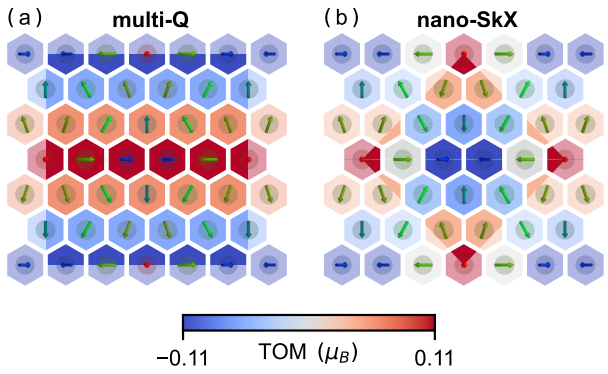

FIG. S4. Topological orbital moments calculated based on the atomistic model for Fe/Ir(111) using the topological orbital susceptibility given in Tab. S2 for (a) the multi-Q_M state and (b) the nanoskyrmion lattice.

Nat. Commun. **11**, 4756 (2020).
[5] M. Gutzeit, T. Drevelow, M. A. Goerzen, S. Haldar, and S. Heinze, Spontaneous square versus hexagonal nanoscale skyrmion lattices in Fe/Ir(111), Phys. Rev. B **108**, L060405 (2023).
[6] F. Nickel, A. Kubetzka, S. Haldar, R. Wiesendanger, S. Heinze, and K. von Bergmann, Coupling of the triple-q state to the atomic lattice by anisotropic symmetric exchange, Phys. Rev. B **108**, L180411 (2023).
[7] S. Heinze, K. von Bergmann, M. Menzel, J. Brede, A. Kubetzka, R. Wiesendanger, G. Bihlmayer, and S. Blügel, Spontaneous atomic-scale magnetic skyrmion lattice in two dimensions, Nature Physics **7**, 713 (2011).

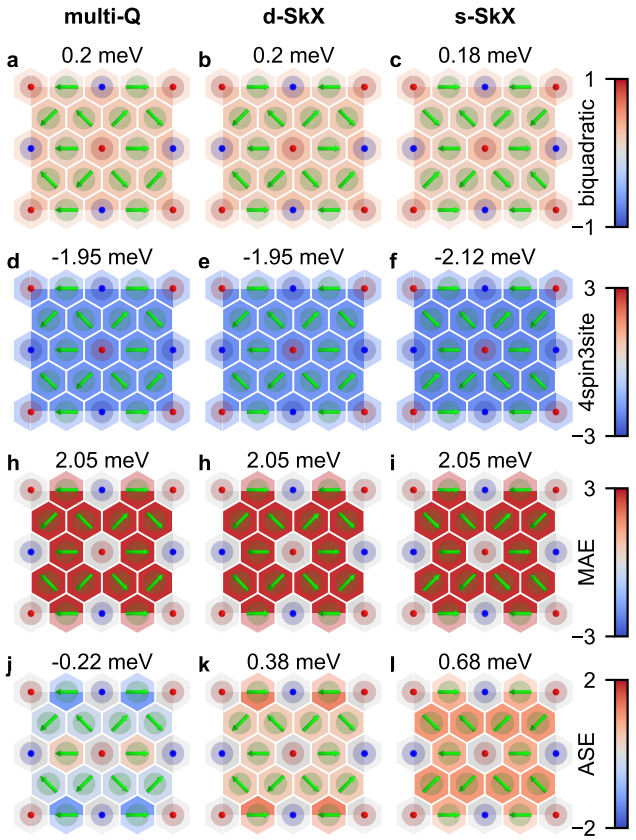

FIG. S5. Energy contributions of each atom from the (left) multi-Q lattice, the (middle) d-SkX lattice and (right) s-SkX lattice. The total energy gain calculated by the atomistic model is (a) −23.0 meV (b) −26.2 meV and (c) −22.0 meV

7 Topological properties of magnet-superconductor hybrid systems due to atomic-scale non-coplanar spin textures

Name: Topological properties of magnet-superconductor hybrid systems due to atomic-scale non-coplanar spin textures

Published: npj Spintronics **3**, 13 (2025)

DOI: https://doi.org/10.1038/s44306-025-00076-1

Authors: **Felix Nickel**, Stefan Heinze

Author contributions: **F.N.** developed the tight-binding code and performed the calculations. **F.N.** and S.H. analyzed the data and wrote the manuscript.

npj | spintronics

Article

https://doi.org/10.1038/s44306-025-00076-1

Topological properties of magnet-superconductor hybrid systems due to atomic-scale non-coplanar spin textures

Felix Nickel[1] ✉ & Stefan Heinze[1,2] ✉

Topological superconductivity can be induced in an s-wave superconductor by an adjacent magnetic layer with a non-collinear spin structure. Good candidates are atomic-scale spin textures with large tilting angles between neighboring spins which exhibit intriguing properties such as topological orbital moments and topological Hall conductivity. Here we investigate the coupling of such non-coplanar spin structures to an adjacent superconducting layer based on a tight-binding model. We consider spin structures recently observed in ultrathin Fe and Mn-based films on the Re(0001) surface such as the triple-Q state, atomic- and nano-scale skyrmion lattices, and study the effect of a continuous distortion of the spin state. We characterize the topology of the spin texture via the scalar spin chirality and the topology of the superconductor by its Chern number. We find that a non-zero total scalar spin chirality, leads to a gapped topological superconducting phase while only trivial superconducting phases can appear for a vanishing value. Our study shows that the size of the superconducting gap in the topological phase rises with the total scalar spin chirality. For an atomic-scale skyrmion lattice, we predict the existence of chiral edge modes on a realistic island structure detectable by the local density of states or supercurrents.

An intriguing property of superconducting materials is the possible occurrence of various phases that are topologically protected by the superconducting band gap[1]. This topological superconductivity is highly desirable as it allows the formation of localized zero energy modes such as Majorana bound states (MBS)[2]. These localized modes occur on the boundaries of topological superconductors with different topological phases or between a topological and a trivial superconductor[3,4]. MBS are of great interest for quantum computing as they obey non-Abelian statistics[5–7]. To utilize these topological bound states a possibility of their manipulation is required. A promising approach is to use topological superconductivity induced by a magnetic spin structure in the vicinity of a conventional s-wave superconductor[8–15]. This approach has two advantages: (i) such magnet-superconductor hybrid systems represent an experimentally feasible approach for topological superconductivity allowing an exploration down to the atomic scale and (ii) magnetic structures can be manipulated by external means such as fields or currents, which may result in a control of the superconducting phase. Rashba-type spin-orbit coupling can also induce topological superconductivity[16,17]. However, manipulation is not straightforward.

In the past, it has been predicted that various spin structures can induce topological superconductivity including the magnetic triple-Q (3Q) state[18], a lattice of skyrmions[19], and an atomic-scale non-coplanar spin lattice[9]. Emergent topological superconductivity due to magnon excitations has also been proposed for a nanoskyrmion lattice[20]. Recently, a number of atomic-scale non-collinear magnetic structures have been revealed based on spin-polarized scanning tunneling microscopy (SP-STM) and explained via density functional theory (DFT) in ultrathin magnetic films on the Re(0001) surface[21–25]. These spin structures have been proposed to exhibit intriguing magnetic properties such as topological orbital moments, spontaneous topological Hall effect, and topological chiral interactions[22,25–27]. Since Re becomes superconducting below 1.7 K, it is of great interest to study the possibility of topological superconductivity in these magnet-superconductor-hybrid (MSH) systems and the role of the topological properties of the spin state. An experimental verification seems feasible in the proposed systems as well, since topological superconductivity in an MSH system with a Re substrate was reported before[4].

Here, we investigate whether the atomic-scale non-coplanar spin structures recently discovered in magnetic films on the Re(0001) surface can induce topological superconductivity. We consider the ideal and the distorted triple-Q state[21,22,24] as well as atomic-scale skyrmion lattices[25] and nano-scale hexagonal skyrmion lattices. We apply a tight-binding model in order to calculate the coupling of the magnetic structure to the electronic states of the superconductor (Fig. 1a). From the calculated band structure we obtain the Chern number as a measure of the topological phase of the

[1]Institut für Theoretische Physik und Astrophysik, Christian-Albrechts-Universität zu Kiel, Kiel, Germany. [2]Kiel Nano, Surface, and Interface Science (KiNSIS), University of Kiel, Kiel, Germany. ✉e-mail: nickel@physik.uni-kiel.de; heinze@physik.uni-kiel.de

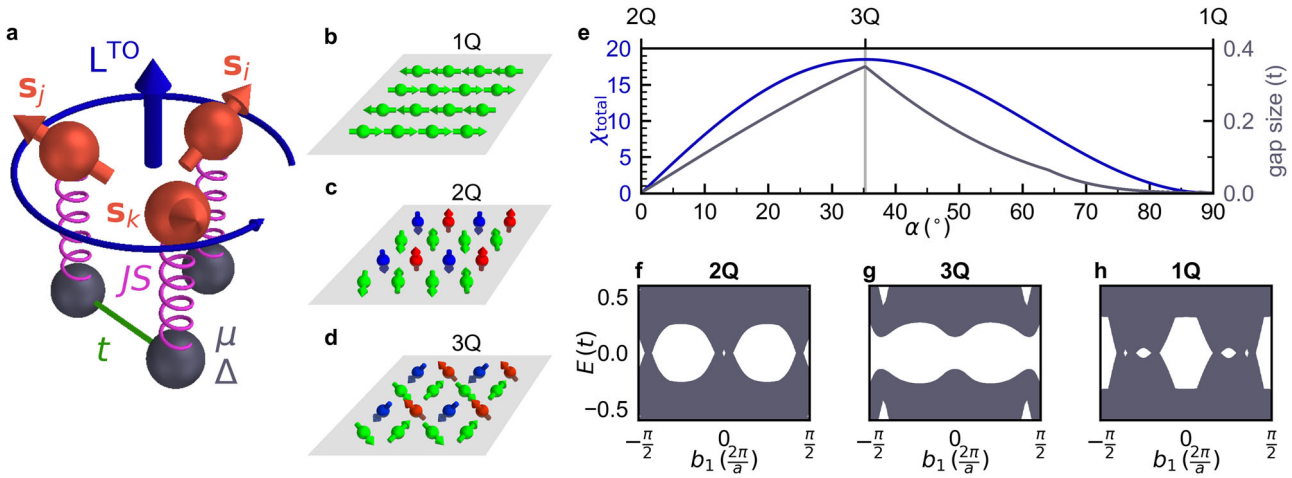

Fig. 1 | Setup and topological properties of a magnet-superconductor-hybrid system. a Schematic drawing of a magnet-superconductor-hybrid (MSH) system. Red spheres represent the atom sites in the magnetic layer and the arrows the local direction of the magnetic spin moments $\mathbf{s}_i$, $\mathbf{s}_j$, and $\mathbf{s}_k$. The topological orbital moment, $\mathbf{L}^{\mathrm{TO}}$, which can occur for a non-coplanar spin structure, is marked by a blue arrow. The blue circle shows the preferred chirality of electron motion. Black spheres denote the atom sites of the superconducting substrate. The coupling between the magnetic and the superconducting layer is marked by purple spirals. The parameter in the tight-binding calculations representing this coupling is given by *JS*. The hopping parameter between two superconducting lattice sites, *t*, the chemical potential, μ, and the superconducting order parameter, Δ, are displayed as well. **b**–**d** Visualization of the spin structures of the 1Q, 2Q, and 3Q states. The color encodes the direction of each spin. An in-plane orientation is represented by a green color. An orientation along the $+z$ ($-z$) direction is represented in red (blue). **e** Scalar spin chirality and gap size of states along the 2Q–3Q–1Q path. The scalar spin chirality is summed over the unit cell. The gap size is calculated as the minimal size of the superconducting gap in the 2D-BZ considering each state along the path. **f**–**h** Projected band structures of the superconducting layer in a magnet-superconductor-hybrid with the 2Q state, the 3Q state, and the 1Q state, respectively, as calculated in the two-dimensional Brillouin zone (2D-BZ) via the tight-binding model. The band structure is projected onto the reciprocal lattice vector $\mathbf{b}_1$. All parameters of the tight binding calculation are the same for each state (t, μ, Δ, JS) = (1, − 1, 0.4, 1), and only the adjacent spin structure changes.

superconductor. The scalar spin chirality is used as a measure of the topology of the spin structure[28]. It is directly linked to the emergent magnetic field and the topological orbital moments obtained based on DFT[25,26].

For the atomic-scale spin structures studied here, we observe that a non-vanishing total scalar spin chirality in the magnetic layer allows an induced topological phase in the adjacent superconductor. However, a trivial gapped superconducting phase occurs for non-coplanar spin structures which exhibit only locally a non-zero scalar spin chirality that compensates over the unit cell. We find that the topological superconductivity is robust with respect to continuous distortions of the spin lattices as long as the total scalar spin chirality is non-zero. Therefore, one can use the scalar spin chirality, which is straightforward to calculate for a given spin structure, in these MSH systems to check for the possibility of a topological superconducting phase and does not need to obtain the Chern number from the electronic structure which is computationally much more demanding. Further, we test the correlation of the total scalar spin chirality and topological superconductivity for various other spin textures. We underline the topological superconductivity predicted here for a Fe monolayer on the Ir-3/Re(0001) surface[25] by demonstrating the existence of chiral edge states for islands of the atomic-scale skyrmion lattice based on the calculated local density of states and supercurrents.

Results

Ideal and distorted triple-Q state

The 3Q state—predicted more than 20 years ago[29,30]—is a non-coplanar spin structure with four spins in the magnetic unit cell pointing into the directions of a tetrahedron. This intriguing three-dimensional spin structure on a two-dimensional lattice is stabilized by higher-order exchange interactions. The 3Q state (Fig. 1d) is constructed from the superposition of three symmetry equivalent spin spiral (1Q) states which correspond to the row-wise antiferromagnetic (RW-AFM) states (Fig. 1b). A superposition of two of the three 1Q states with a different propagation direction results in the 2Q state (Fig. 1c). This state is non-collinear but still coplanar.

The 3Q state has been discovered only recently in a Mn monolayer on the Re(0001) surface using spin-polarized scanning tunneling microscopy[21]. Later a distortion of the 3Q state in this ultrathin film system was proposed due to topological chiral interactions[22]. An ideal 3Q state with perfect tetrahedral angles between adjacent spins was observed if the Mn monolayer is covered by an atomic Pd or Rh adlayer, i.e., in Pd/Mn/Re(0001) and Rh/Mn/Re(0001)[24]. In the layered bulk material $Co_{1/3}TaS_2$, the 3Q state was very recently discovered using neutron scattering and the spontaneous topological Hall effect was measured[31,32].

In the following, we study the topological properties of a magnet-superconductor-hybrid (MSH) system that exhibits the 1Q, 2Q, or 3Q state in the magnetic layer. Note that the influence of the ideal 3Q state on a superconducting state has already been extensively studied[18]. Here we build on this previous work and investigate how a continuous transformation of the spin state affects the adjacent superconductor. Figure 1a shows a sketch of the MSH structure considered in our work. Due to a non-coplanar spin structure of the spin moments in the magnetic layer (red spheres and arrows), a specific chirality for electrons moving around the magnetic moments can be favored (see blue circle). A topological orbital moment (TOM) results from the preferred chirality[27] which is oriented perpendicular to the magnetic plane (see blue arrow). The TOM can be related to the scalar spin chirality χ_{ijk} given by $\chi_{ijk} = \mathbf{s}_i \cdot (\mathbf{s}_j \times \mathbf{s}_k)$ for three spins $\mathbf{s}_i$, $\mathbf{s}_j$, $\mathbf{s}_k$ at sites *i*, *j*, and *k* (see Fig. 1a). This quantity vanishes if the three spins are aligned collinear or coplanar. The spin chirality of a spin $\mathbf{s}_i$ is given as the sum over the spin chiralities of all triangles containing the spin *i* and the neighboring pair of spins *j*, *k* as

$$\chi_i = \sum_{(jk)} \mathbf{s}_i \cdot (\mathbf{s}_j \times \mathbf{s}_k) \tag{1}$$

We further define the total scalar spin chirality of a spin structure as the sum over all scalar spin chiralities of the magnetic unit cell, i.e., $\chi_{\mathrm{total}} = \sum_i \chi_i$. A non-zero scalar spin chirality, representing a non-coplanar magnetic structure, results in topological orbitals moments[27] (see "Methods") and a topological Hall effect[26,33].

Below the magnetic layer, there is a superconducting substrate (dark gray spheres in Fig. 1a). In our tight-binding model, the

superconductor is parameterized by the onsite terms: chemical potential, μ, and superconducting order parameter, Δ, and the hopping term t (see "Methods" for details). The magnetic layer is coupled to the superconductor via the coupling constant JS (indicated by purple spirals in Fig. 1a). Due to the non-uniform magnetic structure, a different magnetization direction can be induced in each atom of the superconducting layer.

The total scalar spin chirality χ_{total} is shown in Fig. 1e for the geodesic path in spin space from the 2Q state via the 3Q state to the 1Q state[22]. The spin at site i is then given by

$$\mathbf{s}_i(\alpha) = \mathbf{s}_i^{2Q}\cos(\alpha) + \mathbf{s}_i^{1Q}\sin(\alpha), \tag{2}$$

where the spin state is characterized by the angle α and $\mathbf{s}_i^{2Q}$ and $\mathbf{s}_i^{1Q}$ denotes the spin at site i in the 2Q and 1Q state, respectively. Along this path, we find the ideal 3Q state ($\alpha \approx 35^\circ$) realized in Pd/Mn/Re(0001)[24], as well as the distorted 3Q state ($\alpha \approx 55^\circ$) proposed as the ground state in Mn/Re(0001)[22]. The scalar spin chirality χ_i on this path is the same at every lattice site, where χ_{total} varies as $\chi_{\text{total}} \propto \cos^2\alpha \sin\alpha$ and vanishes for the coplanar 2Q state and for the collinear 1Q state. As expected the 3Q state has the largest scalar spin chirality along the path and it is decreasing toward the 2Q or 1Q state. Since transport properties such as the topological Hall effect[34] depend on the scalar spin chirality[26,33], these are maximized for the 3Q state.

In Fig. 1f–h we display the projected band structures calculated via the tight-binding model for the superconducting layer that is coupled to the magnetic layer with the 2Q state, the 3Q state, and the 1Q state, respectively. For each state, the band structure has been calculated in the whole two-dimensional Brillouin zone (2D-BZ) and is projected onto the reciprocal lattice vector $\mathbf{b}_1$. The band structure for the 3Q state shows a band gap at the Fermi energy. For the 2Q and 1Q states, this band gap is closed. This fundamentally different state in the superconductor reveals already a major influence of the spin structure on the superconductor.

On the continuous path in spin space from the 2Q to the 3Q and 1Q state the band gap rises nearly linearly towards the 3Q state and decreases again towards the 1Q state (Fig. 1e). The coplanar 2Q state and the collinear 1Q state both lead to a vanishing scalar spin chirality and a suppressed band gap. The 3Q state, on the other hand, has a non-vanishing scalar spin chirality and also does not suppress the superconducting gap. The size of the band gap is slightly lower than half the value of the unperturbed superconductor given by 2Δ. However, for the distorted 3Q state at $\alpha \approx 55^\circ$, the gap is reduced significantly which makes experimental studies more challenging. As shown in Fig. 1e the superconducting gap increases with rising scalar spin chirality, however, the dependence on the angle α is different. The correlation of the band gap and the scalar spin chirality seems to be universal also for other sets of parameters (see Supplementary Fig. 1). While the maximal band gap at the 3Q state varies with the chemical potential μ and the coupling strength JS, the general dependence does not change (see Supplementary Note 1 and Supplementary Fig. 1).

The dependence of the band gap on the scalar spin chirality can be understood in a hand-waving fashion, because the formation of Cooper pairs requires spin-up and spin-down electrons in the vicinity of the Fermi energy. The band gap will be suppressed for strictly separated spin-up and spin-down states due to an effective uniform magnetic field created e.g., by a ferromagnet with exchange split bands. In contrast, a non-coplanar spin structure leads to a spin mixing of the orbitals and allows for a non-vanishing band gap. While the band gap also scales with the superconducting order parameter, no qualitative changes occur for a different value of Δ (see Supplementary Figs. 2 and 3 and Supplementary Note 2).

From the band structure, we can conclude that the 3Q state induces a significant band gap in the superconductor, however, we cannot conclude whether it is in a topological trivial or non-trivial state. To classify the superconducting phase the Chern number of the system can be calculated from the wave functions. The Chern number is calculated as the 2D-BZ integral of the Berry curvature given by (see refs. 35,36)

$$C = \frac{1}{2\pi i}\int_{BZ} \mathrm{d}^2k \,\mathrm{Tr}\left(P_{\mathbf{k}}[\partial_{k_x}P_{\mathbf{k}}, \partial_{k_y}P_{\mathbf{k}}]\right) \tag{3}$$

where

$$P_{\mathbf{k}} = \sum_{E_k<E_F} |\Psi_{\mathbf{k}}\rangle\langle\Psi_{\mathbf{k}}| \tag{4}$$

is the projector of all occupied eigenstates of the Hamiltonian (see Eq. (7) in the "Methods" section). The Chern number is an integer and a Chern number of zero represents a trivial phase while a non-zero value corresponds to a non-trivial superconducting phase.

While the scalar spin chirality is fixed by the spin structure of the magnetic layer, the band structure of the superconductor depends on the parameters used in the tight-binding calculation and a specific set has been chosen for the results displayed in Fig. 1. In the following the tight-binding parameters are varied in order to reveal in general the dependence between band structure of the superconductor and spin structure of the magnetic layer. In Fig. 2a five spin structures are chosen for the magnetic layer along the spin path presented in Fig. 1e including the 1Q, 2Q, and 3Q state. The total scalar spin chirality from Fig. 1e is given above each panel in Fig. 2b, which shows the atomically resolved scalar spin chirality in the magnetic unit cell. For each of these states, the scalar spin chirality is constant over the four-atom magnetic unit cell as seen from the uniform color on each lattice site.

Figure 2 c, d show the properties of the adjacent superconducting layer obtained via the tight-binding model considering the spin structures from Fig. 2a. The hopping parameter and the superconducting order parameter are set to $(t, \Delta) = (1, 0.4)$. The chemical potential and the coupling to the magnetic structure are varied between $-4 \le \mu \le 4$ and $0 \le JS \le 3$. Figure 2c shows the Chern number and Fig. 2d the size of the superconducting gap. Parameters in this range were suggested from ab initio calculations[37] and previously used in other tight-binding investigations[18]. The parameters used in Fig. 1 are marked in Fig. 2c, d with red stars for the 2Q, 3Q, and 1Q states. For the 3Q state, we can conclude that the system from Fig. 1d is in fact in a non-trivial phase with a Chern number of $C = 4$, while the 2Q and 1Q state are in a trivial phase (for a closed gap the Chern number is not defined. However, this is not marked specially in the plot since the areas with a closed gap cannot be in a topological superconductor phase). For the ideal 3Q state the Chern numbers and phases match with those shown in ref. 18.

When comparing the 3Q state to distorted 3Q states with $\alpha = 20^\circ$ or $\alpha = 50^\circ$ new phase transitions occur in the superconducting layer (Fig. 2c). For $\alpha = 20^\circ$ some of the areas that were in a non-trivial phase for the 3Q state now display a vanishing Chern number. Note, that a zero Chern number marks a phase with no strong topological superconductivity, however, weak- or higher-order topological superconductivity[38,39] could still arise (see Supplementary Fig. 4 and Supplementary Note 3). However, topological superconductivity is still expected for a large region of the phase space and the phase diagram is slowly varying with the transformation of the spin structure. A distortion of the spin structure leads to no qualitative changes in the superconducting phases, although the size of the band gap can be altered. A fundamentally different phase diagram occurs for the 2Q ($\alpha = 0^\circ$) and the 1Q state ($\alpha = 90^\circ$). In these cases, the Chern number is zero for the whole sampled phase space. Therefore, these spin structures do not induce gapped topological superconductivity.

Transitions between different superconducting phases can only occur, if the band gap closes. Therefore, the size of the superconducting gap is displayed in Fig. 2d. The color bar is limited to 0.1 since the regions with a small or vanishing gap are especially interesting. For $\alpha = 0^\circ$ and $\alpha = 90^\circ$ the band gap is fully closed for a large part of the phase space. Especially for parts, where the 3Q state is in a topological phase, the 1Q and 2Q state show a closed band gap, which was already observed in Fig. 1f, h. This goes along with a vanishing scalar spin chirality at each lattice site. When the spin

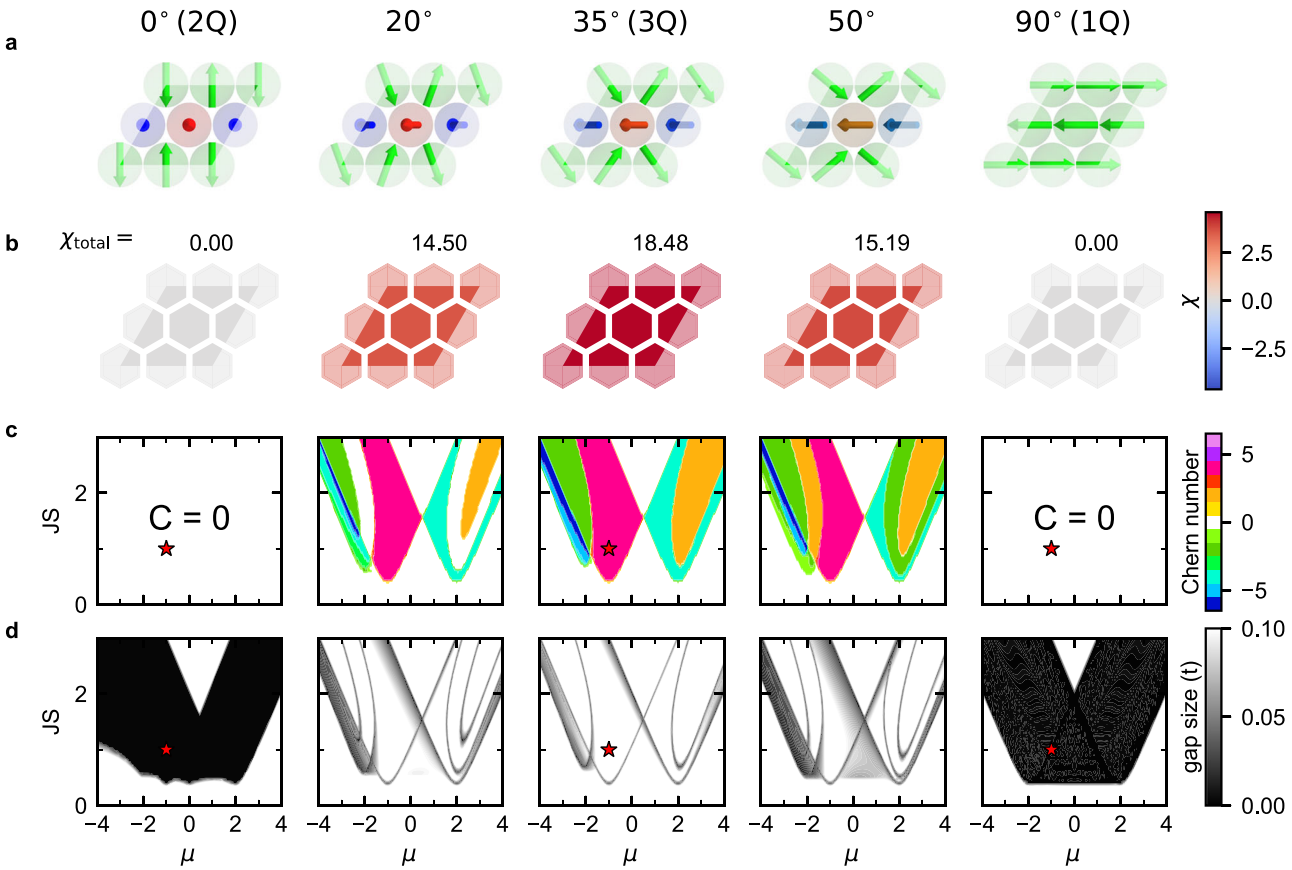

Fig. 2 | Topological properties of an MSH system with various spin states along the 2Q–3Q–1Q path. a Five selected spin structures along the path, including the 2Q, 3Q, and 1Q states, are displayed. **b** The atom-resolved scalar spin chirality is displayed for each spin structure and the total value χ_{total} is given above each panel. The magnetic unit cell is highlighted by a parallelogram for all spin structures in (**a**, **b**). **c** Chern numbers calculated with the tight-binding model for the spin structures shown in (**a**) for parameters $t = 1$, $\Delta = 0.4$. The chemical potential μ and the coupling to the magnetic state JS are varied between $-4 \leq \mu \leq 4$ and $0 \leq JS \leq 3$ in order to sample a large part of the phase space. The color represents the Chern number for a specific set of parameters. White areas represent a trivial state, which has a Chern number of 0. **d** Size of the band gap around the Fermi energy E_F for the calculation presented in panel **c**. The size of the band gap is evaluated over the whole Brillouin zone.

structure is transformed to an angle of $\alpha < 0°$ or $\alpha > 90°$, non-coplanar spin structures form, which have a non-vanishing Chern number (see Supplementary Fig. 5 and Supplementary Note 4). Therefore, the values of $\alpha = 0°$ and $\alpha = 90°$ mark phase transitions along the path.

The results for various spin structures along the 2Q–3Q–1Q path and tight-binding parameters demonstrate that the 3Q state has the largest scalar spin chirality and topological non-trivial phases with comparably large band gaps. As the spins are tilted in a fashion to decrease the scalar spin chirality, either towards the 2Q or the 1Q state, the size of the superconducting gap is also decreasing (cf. Fig. 1e). Here topological superconductivity still exists, but these phases might be less interesting for an experimental realization due to the small band gap. Some changes and additional phases can occur in the superconducting phase diagram of the Chern number. If the scalar spin chirality finally vanishes at the 1Q or 2Q state, only trivial phases can be found but also the superconductivity is suppressed for parameters which formerly were representing non-trivial phases. These distortions of the 3Q state can occur due to higher-order exchange interactions and their competition with magnetocrystalline anisotropy[22,24]. Other, less-ordered, distortions could arise due to thermal spin fluctuations. For random fluctuations of the 3Q state, the band gap is also reduced. For small fluctuations, as expected at low temperatures, the effect is also relatively small (see Supplementary Fig. 6 and Supplementary Note 5).

Atomic-scale skyrmion lattices

The spin structures studied in the previous section exhibit a spatially homogeneous scalar spin chirality and a topological phase occurred in the adjacent superconductor for a non-vanishing value. Now we turn to spin lattices in which the scalar spin chirality varies within the magnetic unit cell. There are two fundamentally different types of spin lattices: (i) spin states for which the total scalar spin chirality over the entire magnetic unit cell vanishes due to a compensation of individual non-zero contributions and (ii) spin states for which the local, as well as the total scalar spin chirality, are finite. As representatives of both groups, we investigate in this section a multi-Q state and an atomic-scale skyrmion lattice (SkX) constructed based on experimental observations in a monoatomic Fe layer on three Ir layers on a Re(0001) substrate (cf. ref. 25).

As shown previously, a spin spiral state can induce nodal point superconductivity[9]. Perpendicular to the propagation direction $\mathbf{q}$ of a spin spiral all magnetic moments form ferromagnetic rows making this state coplanar. A superposition of two or more such spin spirals, coined a multi-Q state, can be non-coplanar. An example is the triple-Q state discussed in the previous section. A more complex multi-Q state is displayed in Fig. 3a. It is a superposition of two perpendicular spin spirals propagating along the wave vectors $\mathbf{q}_M$ and $\mathbf{q}_K$. These reciprocal vectors $\mathbf{q}_M$ and $\mathbf{q}_K$ were constructed from the experimentally observed real space lattice vectors $\mathbf{a}_M$ and $\mathbf{a}_K$ as sketched in Fig. 3a. The construction ensures a constant magnitude of the magnetic moments[40] and a vanishing total spin moment of the spin structure.

Two substructures can be identified within the magnetic unit cell of the multi-Q state which resemble an atomic-scale skyrmion and an anti-skyrmion (see black dashed diamonds in Fig. 3a). The scalar spin chirality obtained at each lattice site is marked in Fig. 3a by the color of the hexagons.

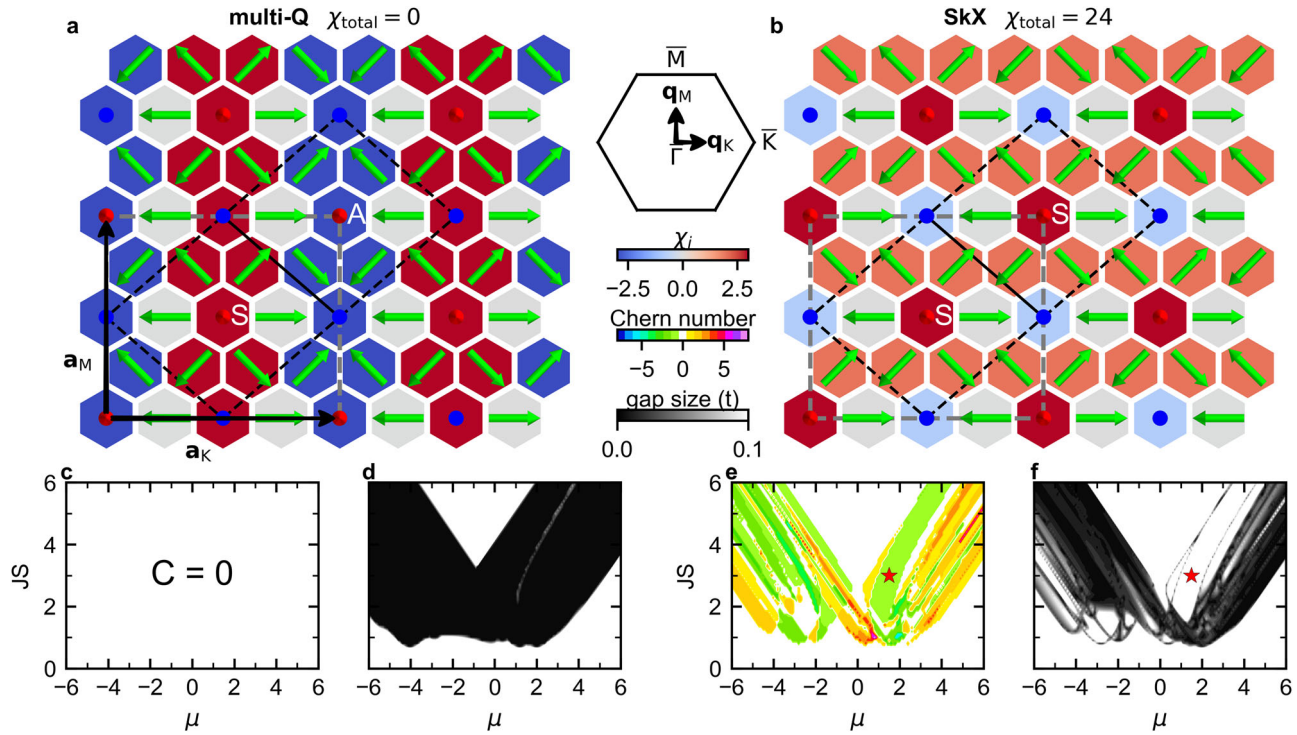

Fig. 3 | Topological properties of an MSH system with a multi-Q vs skyrmion lattice state. a Multi-Q state constructed from two perpendicular spin spiral vectors $\mathbf{q}_M$ and $\mathbf{q}_K$ as displayed in the inset showing the 2D-BZ. A skyrmionic and an anti-skyrmionic substructure have been marked by black dashed lines and an S or an A at the central spin, respectively. The scalar spin chirality is given by the color of hexagons in the background (see color scale bar on the side). **b** Atomic-scale skyrmion lattice (SkX) constructed from the skyrmionic substructure of the multi-Q state. Scalar spin chirality and the skyrmionic substructures have been marked as in (**a**). **c**, **e** Chern number and **d**, **f** gap size obtained from the tight-binding model using the multi-Q state (**c**, **d**) and the SkX state (**e**, **f**). The calculations were performed for the parameters $(t, \Delta) = (1, 0.7)$, $-6 \le \mu \le 6$, and $0 \le JS \le 6$. The parameter set $\mu = 1.5$ and $JS = 3$ used in further calculations using the SkX state is marked by a red star in (**e**, **f**).

The total scalar spin chirality χ_{total} of a substructure is the sum of χ_i from all lattice sites within a plaquette. The skyrmionic plaquette has a positive net χ_{Sk} and the antiskyrmionic structure exhibits a negative net χ_{ASk}. As the scalar spin chirality can be used to characterize topological properties[28], the atomic scale spin structures with opposite net χ_{total} behave similarly to isolated skyrmions and antiskyrmions, which have an opposite topological charge. Summed over the unit cell the scalar spin chirality $\chi_{Sk} + \chi_{ASk}$ of the multi-Q states vanishes as skyrmionic and antiskyrmionic contributions cancel each other.

The Chern number obtained for the adjacent superconductor vanishes for the entire large range of tight-binding parameters (Fig. 3c) and the band gap (Fig. 3d) is closed for a larger part of the phase space which indicates suppressed superconductivity. Therefore, the multi-Q state does not induce topological superconductivity although it represents a non-coplanar spin structure. This is a qualitatively different behavior than that observed for the 3Q state, which is also a superposition of spin spirals, and demonstrates that a non-coplanar spin structure alone is not sufficient to induce topological superconductivity. Note, that in contrast to the multi-Q state studied here, the 3Q state displays a non-vanishing total scalar spin chirality (cf. Fig. 2b). Note that the investigated phase space here is larger than for the 2Q–3Q–1Q path in order to include the phases investigated for the skyrmion lattice in ref. 19. Also the superconducting order parameter has been increased to $\Delta = 0.7$ to ensure a faster convergence of the Chern number. As demonstrated in Supplementary Figs. 2 and 3 and Supplementary Note 2 the change of the superconducting order parameter does not lead to a qualitative difference in the results.

Since the contributions of the scalar spin chirality of the skyrmionic and antiskyrmionic structures cancel and no topological superconductivity is found, we now consider a spin-lattice that contains only one of the substructures and has been proposed as the magnetic ground state of Fe/Ir-3/Re(0001)[25]. Figure 3b shows the atomic-scale skyrmion lattice, where the antiskyrmionic structures were replaced by skyrmionic structures, which reduces the size of the unit cell by one-half. The scalar spin chirality of the skyrmionic structure is slightly reduced, as the neighboring spins have changed, but it still has a significant positive contribution and the net scalar spin chirality amounts to $\chi_{total} = 24$ for the 16-atom cell.

The calculated Chern number in the adjacent superconductor (Fig. 3e) is non-zero for large parts of the phase space. Similar to the case of the 3Q state regions with different values of the Chern number exist. The band gap (Fig. 3f) closes at the phase transitions. For some phases the band gap is very small, however, there are also phases with a sufficiently large band gap and a non-zero Chern number. Note, that replacing all skyrmionic by anti-skyrmionic spin structures, i.e., constructing an antiskyrmion lattice (ASkX), leads to a spin state with $\chi_{total} = -24$. The exact opposite topological phases occur in the superconducting layer, i.e., the sign of the Chern number is flipped for all parameter sets when compared to the SkX state (see Supplementary Note 6 and Supplementary Fig. 7).

While the SkX and ASkX induce topological superconductivity, the multi-Q state, as a combination of both does not. Intuitively this can be understood as the Chern number arises from a non-zero Berry-curvature, here induced by the non-coplanar spin structure. The time reversal of the system would change the sign of the Berry curvature and of the scalar spin chirality. This implies, that two substructures with opposite scalar spin chirality induce opposite Berry curvature, which subsequently leads to a vanishing Chern number as observed for the multi-Q state.

To check the generality of our result, we consider another non-coplanar skyrmion lattice with locally non-zero scalar spin chirality and vanishing χ_{total} which has been proposed in ref. 25. In this so-called double-skyrmion lattice (d-SkX) the antiskyrmionic spin structure of the multi-Q state is slightly modified. Similar to the 2Q–3Q–1Q path in spin space discussed in the previous section, we can construct a continuous transformation from the double-skyrmion lattice to the skyrmion lattice (see

Supplementary Note 7 and Supplementary Figs. 8 and 9). Based on the tight-binding model, we find a similar behavior of the adjacent superconductor (Supplementary Fig. 9). For the d-SkX, the total scalar spin chirality vanishes and a trivial topological phase occurs. Along the path in spin space towards the SkX, one obtains $\chi_{\text{total}} \neq 0$, and topological superconducting phases are observed. Similar to the trend of the 2Q–3Q–1Q path, the size of the band gap generally increases for a larger χ_{total}. This suggests, that also the size of the band gap depends on the total scalar spin chirality (see Supplementary Fig. 1 and Supplementary Note 1).

For comparison, we studied the connection between the topology of the spin space and the superconductor for MSH systems with the multi-Q state and the nanoskyrmion lattice reported for Fe/Ir(111)[40]. These spin structures exhibit similar topological properties as the multi-Q state and SkX in Fe/Ir-3/Re(0001). Our tight-binding calculations show that the same behavior occurs regarding the effect on the adjacent superconductor, i.e., no topological phase for the multi-Q state and topological superconductivity in a large part of the phase space for the nanoskyrmion lattice (Supplementary Note 8 and Supplementary Fig. 10).

The studied non-coplanar atomic-scale spin textures can induce topological superconductivity even in the absence of SOC. In real materials, SOC is often present. To test the robustness against contributions of SOC we calculated the Chern number for the SkX and multi-Q state for three different strengths of SOC (see Supplementary Fig. 11 and Supplementary Note 9). We find small changes in the phase space of the Chern number for the SkX state for weak to moderate SOC strength but still a zero Chern number for the multi-Q state. Qualitatively, the results do not change upon including SOC.

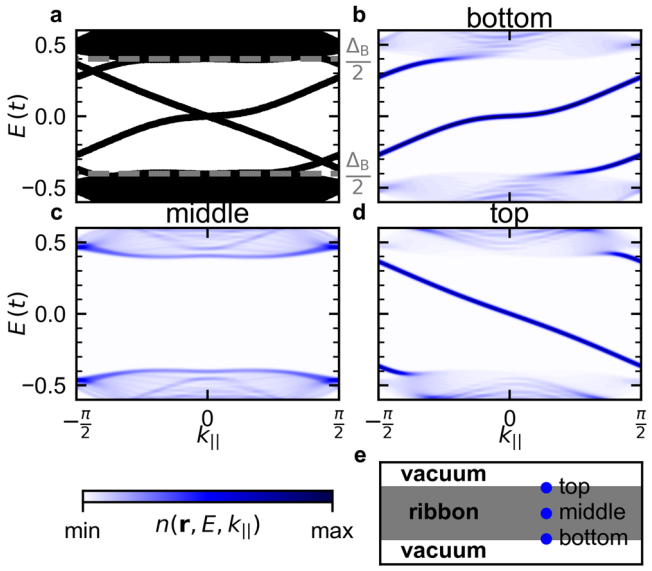

Fig. 4 | Band structure of a ribbon with the SkX state adjacent to vacuum. Band structure and spectral function are displayed for a ribbon geometry with a periodic direction along $\mathbf{a}_1$. **a** Band structures for a ribbon along the $\mathbf{a}_1$ direction. **b**–**d** Spectral functions for all orbitals of two adjacent atomic rows at the bottom, middle, and top of the ribbon (see sketch in (**e**). For each spectral function, the contributions of two rows of atoms in the periodic direction are summed. The tight-binding parameters were chosen as $(t, \mu, JS, \Delta) = (1, 1.5, 3, 0.7)$ marked by a red star in Fig. 3e, f.

Chiral edge states of an atomic-scale skyrmion lattice

In the previous section, we discovered, that an atomic-scale skyrmion lattice can induce topological superconductivity due to its spin topology. Here we investigate the boundary between a topological superconducting phase induced by the SkX state and a trivial state in order to check for the fingerprints of the topological phase. At the boundary between areas with different Chern numbers edge states should occur, where the number of edge states coincides with the difference in the Chern numbers of the adjacent superconducting phases. For the SkX lattice, we first study an ideal ribbon geometry of an infinite stripe in one direction and a finite size in the perpendicular direction. We choose a fixed set of tight-binding parameters such that the Chern number is $C = -1$ (see red star in Fig. 3f, g). For this phase, we create a ribbon with a width of 40 unit cells in one direction and an infinite length in the other direction. In the non-periodic direction, the ribbon adjoins the vacuum, which is in a trivial state. Qualitatively, the results should be the same for a boundary towards any other trivial state.

In Fig. 4a the band structure is shown for the periodic direction along $\mathbf{a}_1$. Only two modes are located within the energy interval of $[-0.4, 0.4]$ around the Fermi energy, while the majority of eigenstates are below or above the band gap with a value of $\Delta_B = 0.8$. To check whether these modes are located at the edges of the ribbon, we analyze the spectral function (Fig. 4b–d) which shows the localization of a state at a specific lattice site (see sketch in Fig. 4e). Note that the contributions from all orbitals of two rows in the periodic direction are added up. Therefore, the spectral function shows the localization in these two rows.

Clearly, neither of the two in-gap modes appears in the center of the ribbon and bulk-like behavior occurs indicated by the superconducting band gap (Fig. 4c). The mode with a positive slope ($\frac{\partial E}{\partial k_{||}} > 0$) is found at the bottom edge of the ribbon since the spectral function is large for this mode (Fig. 4b). On the top edge (Fig. 4d) the other mode is located which exhibits a negative slope ($\frac{\partial E}{\partial k_{||}} < 0$). The opposite direction of modes on the top and bottom edges demonstrates the chirality of the edge mode. On each edge, one mode crosses the band gap consistent with a change of the Chern number by 1 from the SkX state ($C = -1$) to the vacuum ($C = 0$). This clearly shows the topological superconducting state. Note, that one also obtains chiral edge states for ribbons along the other lattice vector (Supplementary Note 10 and Supplementary Fig. 12).

The infinite ribbon structure resembles an idealized geometry allowing us to see the edge modes in reciprocal space. To investigate a more realistic geometry that is accessible by experiments we choose the shape and size of a Fe island observed by scanning tunneling microscopy on an Ir-3/Re(0001) substrate[23]. For this film system, the SkX state has been proposed as the magnetic ground state[25]. We used the same tight-binding parameters as for the ribbon geometry. The coupling of the magnetic state to the superconductor JS is assumed to vary spatially. On the magnetic island, the coupling is chosen as $JS = 3$, and on the superconducting surface, it is $JS = 0$, which reflects the absence of magnetic atoms. Due to the non-uniform shape of the boundary, the termination of the spin structure varies along the edge of the island. For the parameters used on the magnetic island, the Chern number amounts to $C = -1$ and on the superconducting surface, it is $C = 0$ (cf. Fig. 3c).

Figure 5a, b shows the energy and spatially resolved local density of states (LDOS) obtained via tight-binding calculations for this configuration. All lattice sites in Fig. 5b within the black line are considered as the magnetic island. The energy-resolved LDOS (Fig. 5a) is given for three points on the island: on the superconducting surface, at the edge of the island, and on a lattice site of the magnetic island. The LDOS on the superconducting surface shows a very clear band gap around the Fermi energy, created by the superconducting order parameter of $\Delta = 0.7$ leading to a band gap of $\Delta_S = 1.4$. States within the interval $E \in [-0.7, 0.7]$ exist only due to a thermal broadening. The LDOS on the magnetic island (purple curve) also displays a band gap, however, reduced in size with respect to the free superconducting surface. This band gap corresponds to the bulk band gap obtained due to the coupling of the superconducting layer to the SkX state $\Delta_B = 0.8$ (cf. Fig. 4a). On lattice sites at the island edge (blue curve) a clear peak is seen at the LDOS at zero energy ($E = 0$). This shows that in-gap states exist only on the edge of the magnetic island.

To visualize these in-gap states the LDOS is displayed for $E = 0$ on the island and superconducting surface (Fig. 5b). The largest contributions are located at the edge of the island. At further distances to the edge, no states can be observed at zero energy. The LDOS varies around the boundary, but at each point of the boundary, some states are located at zero energy. This shows that zero energy states are located on the boundary of the island and

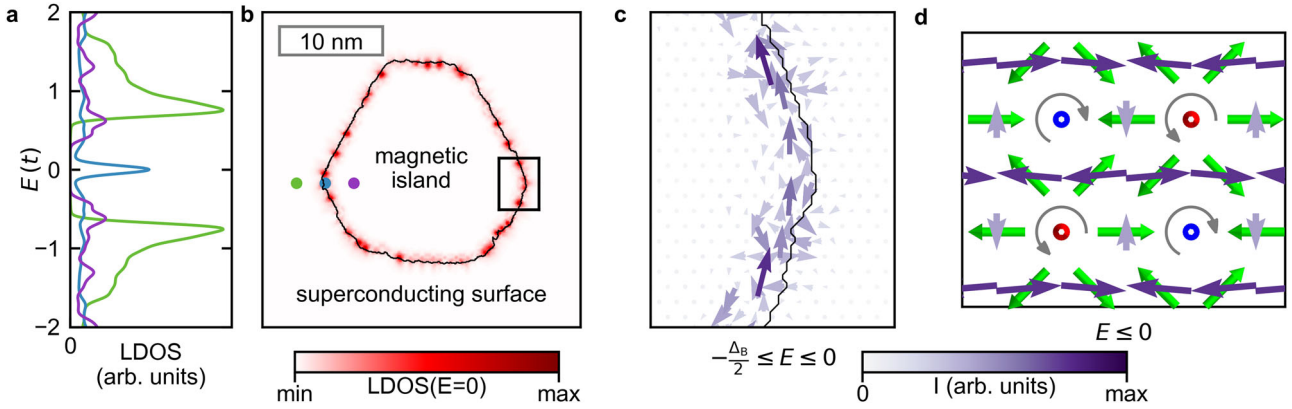

Fig. 5 | LDOS and supercurrent of a magnetic island with the SkX state on a superconducting surface. The island is constructed based on an experimentally observed island in Fe/Ir-3/Re(0001)[23,25]. **a** LDOS on the superconducting surface (green), at the island edge (blue), and on the magnetic island (purple). **b** Magnetic island and LDOS at zero energy ($E = 0$). The border of the magnetic island is indicated by a black line. The positions of the three lattice sites used for the LDOS in (**a**) are marked. The green and the purple points have a distance of ten lattice sites from the edge. **c** Supercurrent for an energy interval inside of the superconducting gap $E \in [-\frac{\Delta_B}{2}, 0]$. The displayed area of the island is marked by a black box in (**b**). **d** Supercurrent for an infinitely large sample of the SkX state. The current has been calculated for all states below the Fermi energy. The tight-binding parameters are $(t, \mu, \Delta) = (1, 1.5, 0.7)$. The magnetic island is represented by a coupling constant of $JS = 3$ and the superconducting surface by $JS = 0$.

form edge modes. Such edge modes can be experimentally measured by scanning tunneling microscopy (STM) or scanning tunneling spectroscopy (STS)[41–43].

For the ribbon geometry, we found chiral edge modes using the spectral function. To investigate a possible chirality of the edge modes observed on the realistic island geometry (Fig. 5a, b) we have calculated supercurrents (see "Methods" for details). In Fig. 5c the supercurrent is shown for an area on the right side of the island from Fig. 5b, which is marked by a black box. The supercurrent is only calculated for states with an energy of $-\frac{\Delta_B}{2} \le E \le 0$. The obtained current is therefore only generated by edge states, since the energies are within the bulk band gap of the superconducting layer coupled to the SkX state. A counter-clockwise rotation of the supercurrent around the border of the island can be seen. This shows the chirality of the edge modes even on this experimentally motivated island. A rectangular island with straight edges shows the same result (see Supplementary Fig. 13 and Supplementary Note 11). The net current on the edges, indicating the chirality of the edge states, could be measured for example by scanning superconducting quantum interference device (SQUID)[44] or scanning electron microscope[45].

Besides the counter-clockwise current generated by the edge states, there is also a current from the bulk states $E \le 0$ of the island. This is shown in Fig. 5d, where the currents of all states below the Fermi energy on an infinite large SkX state are displayed. Note that the range $-\frac{\Delta_B}{2} \le E \le 0$ is unoccupied for the bulk states. These currents are also circular around the upward (red) and downward (blue) pointing spins. The rotation around the upward spin is counter-clockwise and the rotation around the downward pointing spin is clockwise. The upward-pointing spin is the center of a skyrmionic substructure. For nanometer-size skyrmions, it is known that a supercurrent around the skyrmion center will form[19,46]. This property seems to exist even in the atomic limit of the skyrmionic structure. Averaged over the unit cell the current of the bulk states is compensated. Interestingly, the central spin of the skyrmionic structure has a positive scalar spin chirality, leading to a counter-clockwise rotation. The net scalar spin chirality of the whole island is also positive and exhibits a counter-clockwise rotation of the edge states.

Discussion

We have studied a variety of non-coplanar spin structures, which can induce topological superconductivity due to their spin topology even in the absence of spin-orbit coupling. In our work we continuously transform the atomic scale spin structures and compare the topology of the spin structures—measured via the scalar spin chirality—with possible induced topological superconductivity. The scalar spin chirality depends purely on the spin structure and is therefore independent of the electronic structure of the specific material. Higher-order exchange interactions have been shown to stabilize non-coplanar spin textures such as the 3Q state at interfaces[25,40,47,48] and in intercalated van der Waals materials[31,32]. The induced topological superconductivity is robust against small distortions of the considered spin structures. In general, large tilting angles lead to an increased band gap which should facilitate the experimental observation of the superconducting phase. Many of the investigated spin structures such as the ideal 3Q state, the distorted 3Q state, or atomic-scale skyrmion lattices have been revealed in experimentally realized MSH systems[21,22,24,25], which might make an observation of topological superconductivity in these systems possible. Key properties of topological superconductivity such as chiral edge modes, which can be observed experimentally and are known for nanometer-size skyrmions, can also be induced by atomic-scale skyrmion lattices.

The scalar spin chirality has been used in our study as a measure of the spin topology[28]. For all investigated spin lattices we found that gapped topological superconducting phases characterized by a non-zero Chern number can only occur if the total scalar spin chirality is non-zero as well. Even non-coplanar spin structures such as the multi-Q and the d-SkX lattice, which have a locally non-zero scalar spin chirality but a vanishing net scalar spin chirality, do not induce gapped topological superconductivity. We have confirmed this connection between spin topology and topological superconductivity for the square nanoskyrmion lattice of fcc-Fe/Ir(111)[40] (Supplementary Fig. 10), a hexagonal atomic-scale skyrmion lattice proposed as the ground state of hcp-Fe/Ir(111)[47,49], and an antiferromagnetic atomic-scale spin-lattice predicted as the magnetic ground state of Fe/Ir(001)[33] (see Supplementary Notes 12 and 13 and Supplementary Figs. 14, 15, and 16).

We have further investigated the collapse of a hexagonal ordered lattice of skyrmions with a radius of around 4.4 lattice sites adjacent to a superconducting layer to highlight the difference between the total scalar spin chirality and the topological charge (Supplementary Note 14 and Supplementary Figs. 17 and 18). Such a nanoscale skyrmion lattice has been observed for a Pd adlayer on Fe/Ir-3/Re(0001)[23]. On a Re(0001) surface the skyrmions have a diameter of 2.4 nm. Along the minimum energy path from the skyrmion state to the ferromagnetic state, we find that topological superconductivity is possible as long as the total scalar spin chirality is finite. In contrast, a topological charge of zero is not an indicator of the absence of topological superconductivity. For a lattice of antiferromagnetic skyrmions, we do not find a topological superconducting phase consistent with their vanishing total scalar spin chirality (see Supplementary Note 15 and Supplementary Fig. 19).

For all non-coplanar spin structures considered in our work gapped topological superconductivity can only be induced in an adjacent superconducting layer if the net scalar spin chirality is non-zero, i.e., for a non-trivial spin topology. The connection between the easy-to-calculate scalar spin chirality and the possibility of topological superconductivity simplifies the identification of potentially interesting spin structures and may be valuable for future explorations of magnet-superconductor-hybrid systems.

Methods

Lattice geometry

The spin structures discussed in the main text are defined on a hexagonal lattice with lattice vectors

$$\mathbf{a}_1 = a_0\left(0.5, -\frac{\sqrt{(3)}}{2}, 0\right)^{\mathrm{T}} \quad \mathbf{a}_2 = a_0\left(0.5, \frac{\sqrt{(3)}}{2}, 0\right)^{\mathrm{T}} \tag{5}$$

and the reciprocal vectors

$$\mathbf{b}_1 = \frac{2\pi}{a_0}\left(1, -\frac{1}{\sqrt{(3)}}, 0\right)^{\mathrm{T}} \quad \mathbf{b}_2 = \frac{2\pi}{a_0}\left(1, \frac{1}{\sqrt{(3)}}, 0\right)^{\mathrm{T}}. \tag{6}$$

All states of the transformation path 2Q–3Q–1Q exhibit a magnetic supercell with lattice vectors $\mathbf{a}_1^{3\mathrm{Q}} = \mathbf{a}_1 + \mathbf{a}_2$ and $\mathbf{a}_2^{3\mathrm{Q}} = 2\mathbf{a}_2$. The lattice vectors for the multi-Q and SkX state are given by $\mathbf{a}_1^{\mathrm{SkX}} = 4\mathbf{a}_1 + 4\mathbf{a}_2$ and $\mathbf{a}_2^{\mathrm{SkX}} = -2\mathbf{a}_1 + 2\mathbf{a}_2$.

Tight-binding Hamiltonian

To calculate the topological phase of an MSH, we use a tight-binding model for a single superconducting layer which is subject to an induced magnetic field by an adjacent magnetic layer (Fig. 1a). The coupling strength between the superconductor and the magnetic layer is described by a parameter JS. This coupling strength is constant over the whole layer, but the spin structure itself is spatially varying, described by the spins $\mathbf{s}_i$ at each lattice site $\mathbf{r}_i$. The spin can be divided into the magnetic moment S_i and the spin direction as a unity vector $\hat{\mathbf{s}}_i$, so that $\mathbf{s}_i = S_i * \hat{\mathbf{s}}_i$. We assume the magnetic moment to be constant over the lattice leading to $S_i = S$ for all lattice sites i. Further, the Hamiltonian contains the chemical potential μ, the hopping parameter t between neighboring lattice sites i, j, and the superconducting order parameter Δ. The Hamiltonian is then given by:

$$\begin{aligned} H \;=\; & -\mu\sum_{i,\alpha} c_{i,\alpha}^{\dagger}c_{i,\alpha} + \Delta\sum_{i}\left(c_{i,\uparrow}^{\dagger}c_{i,\downarrow}^{\dagger} + c_{i,\downarrow}c_{i,\uparrow}\right) \\ & + t\sum_{i,j,\alpha} c_{i,\alpha}^{\dagger}c_{j,\alpha} + JS\sum_{i,\alpha,\beta} c_{i,\alpha}^{\dagger}(\hat{\mathbf{s}}_i\cdot\boldsymbol{\sigma})c_{i,\beta} \end{aligned} \tag{7}$$

where $c_{i,\alpha}$ and $c_{i,\alpha}^{\dagger}$ are the electronic creation and annihilation operators at the position $\mathbf{r}_i$ with spin α and $\boldsymbol{\sigma}$ is the vector of the Pauli spin matrices. The setup for these MSH systems and the calculation parameters are sketched in Fig. 1a. We are interested in classifying spin structures that can induce topological superconductivity even in the absence of spin-orbit coupling (SOC). Therefore, we do not include SOC in our model.

One can show, that a non-uniform spin structure can induce an effective Rashba-type SOC[18,19]. However, not every induced SOC leads to a topological non-trivial superconducting phase. The tight binding model allows us to calculate the electronic structure for a model MSH system. From the electronic structure properties such as the Chern number, the local density of states, and the supercurrent can be calculated (see below). As real materials often exhibit SOC, we tested the robustness of our results for non-coplanar spin structures against including SOC. We found non-trivial superconductivity also upon including SOC and no qualitative changes with respect to the calculations neglecting SOC (see Supplementary Fig. 11 and Supplementary Note 9).

Chern number

To classify the superconducting phase the Chern number of the system can be calculated from the wave functions obtained by solving the tight-binding model defined by Eq. (7). The Chern number is calculated as the two-dimensional Brillouin zone (2D-BZ) integral of the Berry curvature as given by Eqs. (4 and 5). A uniform mesh of (1000×1000) k-points was used for the calculation of the Chern numbers, as well as the band gaps for most of the systems. Only for the nano-scale skyrmion lattice and the AFM skyrmions on a square lattice each represented on a 10×10 spin-lattice we used a (100×100) grid of k-points as the Brillouin zone is smaller than in the other systems due to the increased unit cell in the real space.

Local density of states

When the eigenenergies ϵ_n and wavefunctions $|\Psi_n\rangle$ of the tight binding Hamiltonian are calculated one can use these to obtain the local density of states (LDOS) at each lattice site. Here n is the band index which also contains both spin channels, as well as electronic and hole states. The local density of states as a function of the binding energy E is then given by:

$$\eta_i(E) = \sum_n \delta(E - \epsilon_n)\langle i|\Psi_n\rangle\langle\Psi_n|i\rangle \tag{8}$$

Supercurrents

Similar to the LDOS the eigenvectors can be used to obtain a current between lattice site $\mathbf{r}_i$ and $\mathbf{r}_j$. This current can be evaluated in an energy interval $[E_{\min}, E_{\max}]$ via[50,51]

$$\mathbf{I}_{\mathbf{r}_i-\mathbf{r}_j} = \frac{2et}{\hbar}\Re\left[\sum_{E_{\min}\le\epsilon_n\le E_{\max}}\langle i|\Psi_n\rangle\langle\Psi_n|j\rangle\frac{\mathbf{r}_i-\mathbf{r}_j}{|\mathbf{r}_i-\mathbf{r}_j|}\right] \tag{9}$$

Here t is the hopping parameter, e is the electronic charge and $\Re$ marks the real part. The contributions of each spin channel are added, as the band index n included both spin channels. To obtain a current for each lattice site the contributions between one lattice site and all neighboring lattice sites are multiplied by the respective normalized connection vector and summed. This gives a vectorial current at each lattice site for a given energy window.

Topological orbital moments

The topological properties of the spin structure can be described by the scalar spin chirality[28] as discussed in the main text. Compared to the topological charge[52] the scalar spin chirality is also well-defined for atomic-scale spin structures. The scalar spin chirality χ_{ijk} is related to the topological orbital moment at site i by ref. 27

$$\mathbf{L}_i = \sum_{jk}\kappa_{ijk}\chi_{ijk}\boldsymbol{\tau}_{ijk} \tag{10}$$

where κ_{ijk} is the material-specific topological orbital susceptibility and $\boldsymbol{\tau}_{ijk} \propto (\mathbf{r}_j - \mathbf{r}_i)\times(\mathbf{r}_k - \mathbf{r}_i)$ is a vector dependent on the positions of the spins. For a 2D lattice $\boldsymbol{\tau}_{ijk}$ is a unity vector along the surface normal $\boldsymbol{\tau}_{ijk} = \hat{z}$[27]. When one assumes a spatially constant topological orbital susceptibility, the TOM is proportional to the scalar spin chirality. For some of the shown lattices, the susceptibility has shown to be approximately constant in space[24,25], which makes this a qualified assumption for the investigated lattices.

Continuous transformation of spin states

To investigate the change in the spin chirality or the Chern number and its dependence on the spin structure we create a continuous

transformation between two spin structures. A spin $\mathbf{s}_i$ at lattice site i along the path of the transformation can be written as

$$\mathbf{s}_i(\alpha) = \mathbf{s}_i^{\mathrm{ini}} \cos(\alpha) + \mathbf{s}_i^{\mathrm{fin}} \sin(\alpha), \tag{11}$$

where $\mathbf{s}_i^{\mathrm{ini}}$ is the spin at site i in the initial state, $\mathbf{s}_i^{\mathrm{fin}}$ is the spin at site i in the final state, and $\alpha \in [0, \frac{\pi}{2}]$ a parameter. Such a path in spin space is discussed in Fig. 1 for the 1Q, 2Q, and 3Q state and in the Supplemental Material for the path from the skyrmion lattice to the d-SkX (Supplementary Fig. 9) and for the antiferromagnetic square spin-lattice proposed for Fe/Ir(001) (Supplementary Fig. 15).

Data availability

All relevant data are available from the corresponding authors upon reasonable request.

Code availability

All relevant code is available from the corresponding authors upon reasonable request.

Received: 13 December 2024; Accepted: 26 February 2025;
Published online: 01 April 2025

References

1. Sato, M. & Ando, Y. Topological superconductors: a review. *Rep. Prog. Phys.* **80**, 076501 (2017).
2. Wilczek, F. Majorana returns. *Nat. Phys.* **5**, 614–618 (2009).
3. Chen, W. & Schnyder, A. P. Majorana edge states in superconductor-noncollinear magnet interfaces. *Phys. Rev. B* **92**, 214502 (2015).
4. Palacio-Morales, A. et al. Atomic-scale interface engineering of Majorana edge modes in a 2d magnet-superconductor hybrid system. *Sci. Adv.* **5**, eaav6600 (2019).
5. Kitaev, A. Y. Unpaired Majorana fermions in quantum wires. *Phys. Uspekhi* **44**, 131 (2001).
6. Sengupta, K., Žutić, I., Kwon, H.-J., Yakovenko, V. M. & Das Sarma, S. Midgap edge states and pairing symmetry of quasi-one-dimensional organic superconductors. *Phys. Rev. B* **63**, 144531 (2001).
7. Ivanov, D. A. Non-abelian statistics of half-quantum vortices in *p*-wave superconductors. *Phys. Rev. Lett.* **86**, 268–271 (2001).
8. Nadj-Perge, S., Drozdov, I. K., Bernevig, B. A. & Yazdani, A. Proposal for realizing Majorana fermions in chains of magnetic atoms on a superconductor. *Phys. Rev. B* **88**, 020407 (2013).
9. Nakosai, S., Tanaka, Y. & Nagaosa, N. Two-dimensional *p*-wave superconducting states with magnetic moments on a conventional *s*-wave superconductor. *Phys. Rev. B* **88**, 180503 (2013).
10. Crawford, D., Mascot, E., Morr, D. K. & Rachel, S. High-temperature Majorana fermions in magnet-superconductor hybrid systems. *Phys. Rev. B* **101**, 174510 (2020).
11. Crawford, D. et al. Majorana modes with side features in magnet-superconductor hybrid systems. *npj Quantum Mater.* **7**, 117 (2022).
12. Conte, R. L., Wiebe, J., Rachel, S., Morr, D. K. & Wiesendanger, R. Magnet-superconductor hybrid quantum systems: a materials platform for topological superconductivity. *Riv. Nuovo Cim*. https://doi.org/10.1007/s40766-024-00060-1 (2025).
13. Yang, G., Stano, P., Klinovaja, J. & Loss, D. Majorana bound states in magnetic skyrmions. *Phys. Rev. B* **93**, 224505 (2016).
14. Garnier, M., Mesaros, A. & Simon, P. Topological superconductivity with deformable magnetic skyrmions. *Commun. Phys.* **2**, 126 (2019).
15. Brüning, R. et al. The non-collinear path to topological superconductivity. Preprint at https://doi.org/10.48550/arXiv.2405.14673 (2024).
16. Sato, M., Takahashi, Y. & Fujimoto, S. Non-abelian topological order in *s*-wave superfluids of ultracold fermionic atoms. *Phys. Rev. Lett.* **103**, 020401 (2009).
17. Loder, F., Kampf, A. P. & Kopp, T. Route to topological superconductivity via magnetic field rotation. *Sci. Rep.* **5**, 15302 (2015).
18. Bedow, J. et al. Topological superconductivity induced by a triple-q magnetic structure. *Phys. Rev. B* **102**, 180504 (2020).
19. Mascot, E., Bedow, J., Graham, M., Rachel, S. & Morr, D. K. Topological superconductivity in skyrmion lattices. *npj Quantum Mater.* **6**, 6 (2021).
20. Mæland, K. & Sudbø, A. Topological superconductivity mediated by skyrmionic magnons. *Phys. Rev. Lett.* **130**, 156002 (2023).
21. Spethmann, J. et al. Discovery of magnetic single- and triple-**q** states in $\mathrm{Mn/Re(0001)}$. *Phys. Rev. Lett.* **124**, 227203 (2020).
22. Haldar, S., Meyer, S., Kubetzka, A. & Heinze, S. Distorted 3*q* state driven by topological-chiral magnetic interactions. *Phys. Rev. B* **104**, L180404 (2021).
23. Kubetzka, A., Bürger, J. M., Wiesendanger, R. & von Bergmann, K. Towards skyrmion-superconductor hybrid systems. *Phys. Rev. Mater.* **4**, 081401 (2020).
24. Nickel, F. et al. Coupling of the triple-q state to the atomic lattice by anisotropic symmetric exchange. *Phys. Rev. B* **108**, L180411 (2023).
25. Nickel, F. et al. Antiferromagnetic order of topological orbital moments in atomic-scale skyrmion lattices. *npj Spintronics* **3**, 7 (2025).
26. Hanke, J.-P. et al. Role of Berry phase theory for describing orbital magnetism: from magnetic heterostructures to topological orbital ferromagnets. *Phys. Rev. B* **94**, 121114(R) (2016).
27. Grytsiuk, S. et al. Topological–chiral magnetic interactions driven by emergent orbital magnetism. *Nat. Commun.* **11**, 511 (2020).
28. Dos Santos Dias, M., Bouaziz, J., Bouhassoune, M., Blügel, S. & Lounis, S. Chirality-driven orbital magnetic moments as a new probe for topological magnetic structures. *Nat. Commun.* **7**, 13613 (2016).
29. Kurz, P., Bihlmayer, G., Hirai, K. & Blügel, S. Three-dimensional spin structure on a two-dimensional lattice: Mn /Cu(111). *Phys. Rev. Lett.* **86**, 1106–1109 (2001).
30. Momoi, T., Kubo, K. & Niki, K. Possible chiral phase transition in two-dimensional solid ^{3}He. *Phys. Rev. Lett.* **79**, 2081–2084 (1997).
31. Takagi, H. et al. Spontaneous topological hall effect induced by non-coplanar antiferromagnetic order in intercalated van der Waals materials. *Nat. Phys.* **19**, 961 (2023).
32. Park, P. et al. Tetrahedral triple-q ordering in the metallic triangular lattice antiferromagnet $Co_{1/3}TaS_2$. *Nat. Commun.* **14**, 8346 (2023).
33. Hoffmann, M. et al. Topological orbital magnetization and emergent hall effect of an atomic-scale spin lattice at a surface. *Phys. Rev. B* **92**, 020401 (2015).
34. Martin, I. & Batista, C. D. Itinerant electron-driven chiral magnetic ordering and spontaneous quantum hall effect in triangular lattice models. *Phys. Rev. Lett.* **101**, 156402 (2008).
35. Avron, J. E., Seiler, R. & Simon, B. Homotopy and quantization in condensed matter physics. *Phys. Rev. Lett.* **51**, 51–53 (1983).
36. Bianco, R. & Resta, R. Mapping topological order in coordinate space. *Phys. Rev. B* **84**, 241106 (2011).
37. Kim, H. et al. Toward tailoring Majorana bound states in artificially constructed magnetic atom chains on elemental superconductors. *Sci. Adv.* **4**, eaar5251 (2018).
38. Wong, K. H. et al. Higher order topological superconductivity in magnet-superconductor hybrid systems. *npj Quantum Mater.* **8**, 31 (2023).
39. Wong, K. H. et al. Competing higher order topological superconducting phases in triangular lattice magnet-superconductor hybrid systems. *Phys. Rev. B* **109**, 144521 (2024).
40. Heinze, S. et al. Spontaneous atomic-scale magnetic skyrmion lattice in two dimensions. *Nat. Phys.* **7**, 713–718 (2011).
41. Lo Conte, R. et al. Coexistence of antiferromagnetism and superconductivity in mn/nb(110). *Phys. Rev. B* **105**, L100406 (2022).

42. Bazarnik, M. et al. Antiferromagnetism-driven two-dimensional topological nodal-point superconductivity. *Nat. Commun.* **14**, 614 (2023).
43. Soldini, M. O. et al. Two-dimensional Shiba lattices as a possible platform for crystalline topological superconductivity. *Nat. Phys.* **19**, 1848–1854 (2023).
44. Spanton, E. M. et al. Images of edge current in InAs/GaSb quantum wells. *Phys. Rev. Lett.* **113**, 026804 (2014).
45. Tetienne, J.-P. et al. Quantum imaging of current flow in graphene. *Sci. Adv.* **3**, e1602429 (2017).
46. Baumard, J., Cayssol, J., Bergeret, F. S. & Buzdin, A. Generation of a superconducting vortex via néel skyrmions. *Phys. Rev. B* **99**, 014511 (2019).
47. Gutzeit, M., Drevelow, T., Goerzen, M. A., Haldar, S. & Heinze, S. Spontaneous square versus hexagonal nanoscale skyrmion lattices in Fe/Ir(111). *Phys. Rev. B* **108**, L060405 (2023).
48. Saxena, V. et al. Strain-driven domain wall network with chiral junctions in an antiferromagnet. Preprint at https://doi.org/10.48550/arxiv.2408.12580 (2024).
49. von Bergmann, K., Menzel, M., Kubetzka, A. & Wiesendanger, R. Influence of the local atom configuration on a hexagonal skyrmion lattice. *Nano Lett.* **15**, 3280–3285 (2015).
50. Caroli, C., Combescot, R., Nozieres, P. & Saint-James, D. Direct calculation of the tunneling current. *J. Phys. C Solid State Phys.* **4**, 916 (1971).
51. Rachel, S., Mascot, E., Cocklin, S., Vojta, M. & Morr, D. K. Quantized charge transport in chiral majorana edge modes. *Phys. Rev. B* **96**, 205131 (2017).
52. Prass, P., Lux, F. R., Prodan, E., van Straten, D. & Mokrousov, Y. A c*-algebraic view on the interaction of real- and reciprocal space topology in skyrmion crystals. *SciPost. Phys. Core* **7**, 080 (2024).

Acknowledgements

It is our pleasure to thank Thore Posske for many insightful discussions about topological superconductivity and for help with technical aspects of the calculation of the Chern number. We further thank Jannis Neuhaus-Steinmetz, Jasmin Bedow, and Kirsten von Bergmann for valuable discussions. Many thanks also to Moritz Goerzen for numerous discussions about topology and the Chern number and to Hendrik Schrautzer for assistance with spin dynamics simulations and GNEB calculations. We gratefully acknowledge financial support from the Deutsche Forschungsgemeinschaft (DFG) via project no. 555842692.

Author contributions

F.N. developed the tight-binding code and performed the calculations. F.N. and S.H. analyzed the data and wrote the manuscript.

Funding

Open Access funding enabled and organized by Projekt DEAL.

Competing interests

The authors declare no competing interests.

Additional information

Supplementary information The online version contains supplementary material available at https://doi.org/10.1038/s44306-025-00076-1.

Correspondence and requests for materials should be addressed to Felix Nickel or Stefan Heinze.

Supplementary Information for "Topological properties of magnet-superconductor hybrid systems due to atomic-scale non-coplanar spin textures"

Felix Nickel[1,*] and Stefan Heinze[1,2,†]

[1] *Institut für Theoretische Physik und Astrophysik, Christian-Albrechts-Universität zu Kiel, D-24098 Kiel, Germany*
[2] *Kiel Nano, Surface, and Interface Science (KiNSIS), University of Kiel, Germany*

(Dated: February 20, 2025)

* Email: nickel@physik.uni-kiel.de

† Email: heinze@physik.uni-kiel.de

S1. SIZE OF THE BAND GAP

For the transformation between the d-SkX state and the SkX state (cf. Fig. S3), one can find topological superconducting phases even for very small distortions of the d-SkX, whereas the d-SkX can only induce trivial phases in the superconducting layer. For an experimental observation not only the existence of a topological phase is important, but also a sufficiently large band gap. For the 2Q-3Q-1Q path we showed the dependence of the band gap on the scalar spin chirality for a specific set of parameters (Fig. 1 of the main text).

In Fig. S1, we present the band gap along the 2Q-3Q-1Q transformation (Fig. S1a) and along the d-SkX to SkX transformation (Fig. S1b). We chose different values of the chemical potential μ and of the coupling strength JS in order to get an impression about the general trend. For the 2Q-3Q-1Q path the maximal bandg ap varies with the parameter set. With increasing coupling strength JS, the maximal band gap decreases. For all five selected sets of parameters chosen such that the Chern number does not change the 3Q state leads to the maximal band gap along the path. All sets show a similar dependence on the scalar spin chirality. For the distorted $3Q_\mathrm{d}$ state, which has been proposed as the ground state of Mn/Re(0001) [1], the band gap is already reduced by a factor of 2.8 with respect to the ideal 3Q state observed for Pd/Mn/Re(0001) and for Rh/Mn/Re(0001) [2].

A more complex dependence can be seen for the path from the d-SkX to the SkX state (Fig. S1b). This may be due to the fact that the scalar spin chirality is locally not uniform as it is for the 2Q-3Q-1Q path. However, even here generally a larger χ_total is connected with a larger band gap. As for the 3Q state, the maximal band gap depends on the set of parameters. Concluding from this data, one can expect a larger band gap for a larger net scalar spin chirality, which makes an experimental realization more likely.

S2. INFLUENCE OF THE SUPERCONDUCTING ORDER PARAMETER

In the main text we investigated topological properties for varying parameters of the chemical potential, μ, and the coupling strength, JS. The hopping term t and the superconducting order parameter Δ were kept fixed for each system. Here we show in an example the influence of the superconducting order parameter Δ. In Fig. 1e in the main text the band gaps are shown for the transformation of the spin structure along the 2Q-3Q-1Q path. The superconducting order parameter was set to 0.4. In Fig. S2 we used the same set of parameters, except for the superconducting order parameter which was set to $\Delta = 0.2$. The data from Fig. 1e of the main text is also shown as a reference. For both systems the Chern numbers are the same along the path. The size of the band gap scales with the superconducting order parameter. Both systems show a very similar trend along the transformation. In Fig. S3 we calculated the Chern numbers and band gaps for the 3Q state and varying JS and μ. All parameters are the same as in Fig. S2. The Chern numbers are very similar to the Chern numbers in Fig. 2c, where only the superconducting order parameter is varied between both calculations. Based on this we assume the superconducting order parameter to have no qualitative influence on the results.

S3. POTENTIALLY WEAK TOPOLOGICAL SUPERCONDUCTING PHASE

The focus of this work is the occurrence of strong topological superconductivity which can be measured by the Chern number. On any boundary between a region with non-zero Chern number and a trivial region, an edge state will occur. Consequently, the edge state is present all around a topological island on a trivial surface. However, even when no strong topological superconductivity is present, weak topological superconductivity may arise which results in edge states that occur only for certain orientations of the edge [3, 4].

While a rigorous study of weak topological superconductivity is not in the scope of this work, we investigated one set of parameters with a vanishing Chern number for the $\alpha = 20°$ state along the 2Q-3Q-1Q path. We chose the parameters $(t, \mu, JS, \Delta) = (1, 2.05, 1.85, 0.4)$, which correspond to $C = 0$ in a region, which is encapsulated by non-zero Chern numbers (cf. Fig. 2 of the main text). For this specific set of parameters, we created an island by 50 repetitions of the magnetic unit cell (cf. methods section of the main text) in each periodic direction.

The LDOS at zero energy for this island is shown in Fig. S4a. On two of the four edges there are edge modes located, whereas the other two edges exhibit an open band gap. A logarithmic color map has been chosen, as modes with a large zero-energy LDOS are located at the sharp corners. Fig. S4b,c show the spectral function for a ribbon along the $\mathbf{a}_1$ and $\mathbf{a}_2$ direction, respectively. In the non-periodic direction the ribbon has a width of 50 unit cells, which is the same width as for the island in

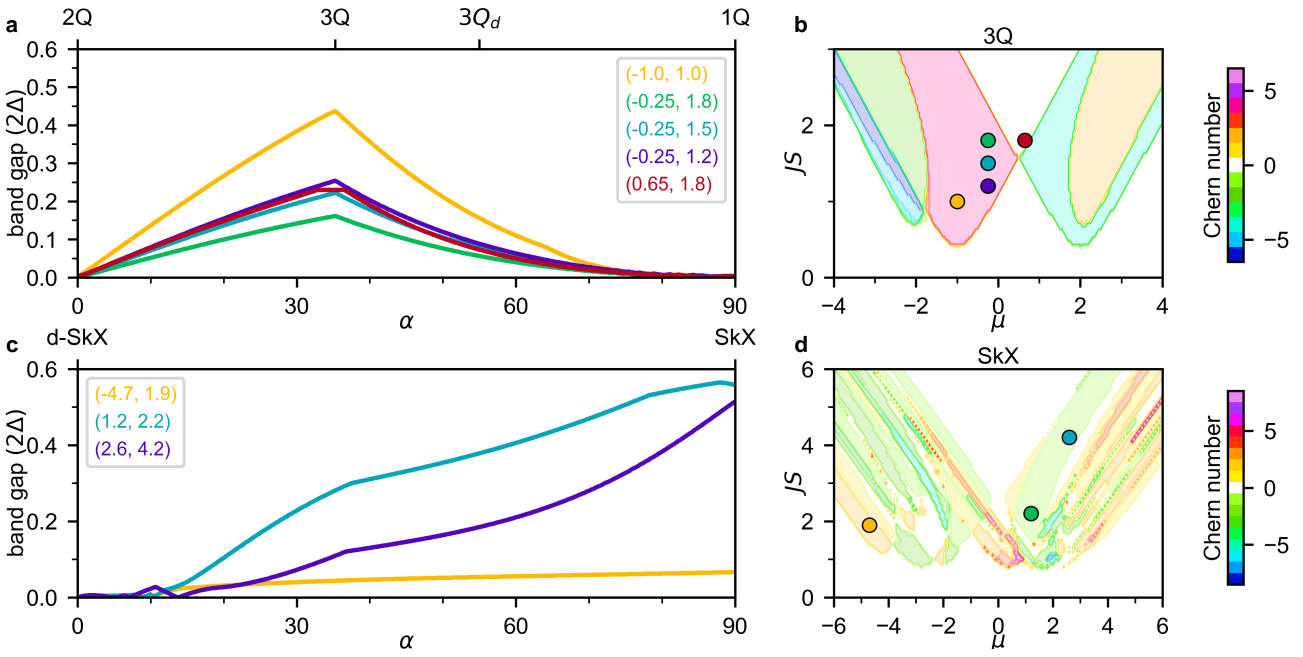

FIG. S1. **Band gap size for a MSH system along the 2Q-3Q-1Q and d-SKX to SkX path.** The minimal band size of the band gap in the 2D-BZ is dislpayed for a fixed set of parameters, while the spin structure is continuously transformed. **a** The spin structures are transformed along the 2Q-3Q-1Q path, with parameters $(t, \Delta) = (1, 0.4)$ and five different sets of μ, JS, which are shown in the legend. **b** The Chern numbers for the 3Q state for a large variety of values of the chemical potential μ and coupling strength JS as shown in Fig. 2c of the main text. The parameters used in **a** are marked by colored circles. **c** Spin structures along the transformation between the d-SkX and the SkX state with $(t, \Delta) = (1, 0.7)$ and three sets of μ, JS. **d** Chern numbers for the SkX state as shown in Fig. 3e of the main text with round markers indicating the parameters used in **c**.

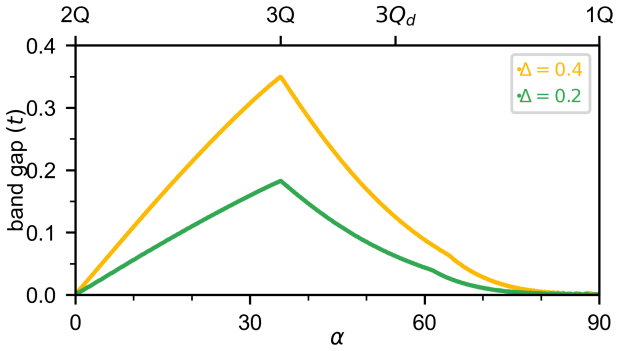

FIG. S2. **Band gap along the 2Q-3Q-1Q transformation path.** The band gap is calculated for the parameters $(t, \mu, JS) = (1, -1, 1)$. The superconducting order parameter Δ is chosen as 0.2 and 0.4, where the later represents the data from Fig. 1e of the main text.

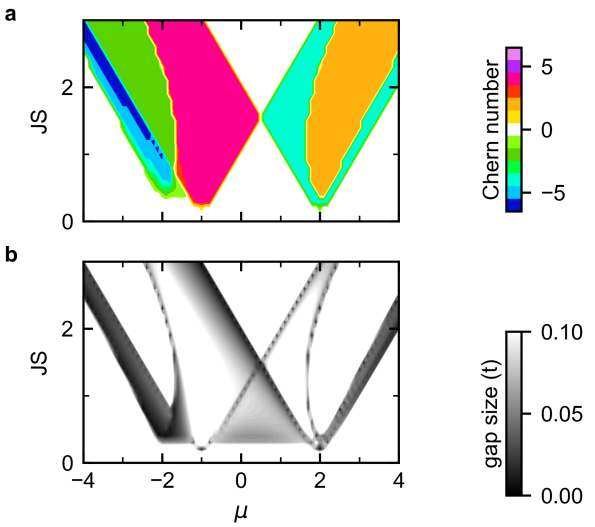

FIG. S3. **Chern number and band gap for the 3Q state.** All parameters are the same as in Fig. 2 of the main text, except for the superconducting order parameter which has been reduced by one half to $\Delta = 0.2$.

Fig. S4a. The spectral function is summed over all four lattice sites in the unit cell, which is directly at the edge. In Fig. S4b the spectral function has a band gap, which fits to the vanishing LDOS at this edge in Fig. S4a. In Fig. S4c the band gap is closed, which fits to the edge states at zero energy in Fig. S4a. For this specific set of parameters the edge modes on the edges along the $\mathbf{a}_2$ direction suggest, that weak topological superconductivity might be present here. A more thorough investigation of this phase concerning weak topological superconductivity

might be interesting for future investigations.

S4. EXTENDED 2Q-3Q-1Q PATH

In the main text spin structures were presented along a transformation path between the 2Q and the 1Q state, where the 3Q and distorted 3Q state are along this path. The transformation follows Eq. (2) from the main text, where values of $\alpha \in [0°, 90°]$ were considered. For the 2Q state ($\alpha = 0°$) and the 1Q state (($\alpha = 0°$)) a closed band gap for a large part of the phase space was observed.

To check, if the closing points at $\alpha = 0°$ and $\alpha = 90°$ mark a phase transition, we calculated the Chern number and band gaps for values of $\alpha = -20°$ and $\alpha = 110°$. The data is shown in Fig. S5. For both spin structures (Fig. S5a) which exhibit a non-zero scalar spin chirality (Fig. S5b) we observe non-zero Chern numbers and non-vanishing band gaps (Fig. S5c,d), which implies the existence of topological superconductivity. This shows that the points $\alpha = 0°$ and $\alpha = 90°$ indeed represent phase transitions along the transformation described in the main text.

S5. RANDOM FLUCTUATIONS OF SPINS

Besides the continuous distortion of the spin structure also other distortions, e.g. due to thermal excitations, can occur. To estimate the influence of arbitrary distortions on the superconducting substrate we used the 3Q state and added random distortions to the spins. A similar approch was used in Ref. [5], where no qualitative difference due to spin fluctuations were observed. For each of the four spins in the unit cell two random angles were created. These angles were added to the φ_i and ϑ_i components of the spin $\mathbf{s}_i$ in spherical coordinates. The angles were created based on a normal distribution with a given standard derivation σ. The standard derivation is the same for all spins in the unit cell. For one standard derivation 1000 randomly distorted spin structures were created. For each of the spin structures the band gap has been calculated with the same parameters as for the ideal 3Q state in the main text. The mean band gap was determined from all 1000 calculations and the distribution via the 80% percentile, meaning 80% of the band gaps are within this region.

This procedure was performed for standard derivations in the interval $[0.1°, 20°]$ and the data is shown in Fig. S6. The yellow points mark the mean value and the blue area gives the 80% region. The mean value is decreasing with increasing distortion, but even for $\sigma = 20°$ it is not vanishing. With a larger σ also the variation of the band gap becomes larger. A black line marks the band gap of the ideal 3Q state. While a distortion will always decrease the size of the band gap, a small distortion will not drastically change the size. As experiments on magnet-superconductor-hybrid systems have to be performed at temperatures below the critical temperature (e.g. 1.7 K for Re), thermal fluctuations can be expected to have no large influence on the measured properties.

S6. ANTISKYRMION LATTICE

In the main text, we have discussed how the atomic-scale skyrmion lattice (SkX) state is constructed from the multi-Q state by replacing the antiskyrmionic substructure with a skyrmionic one. In the same manner, the skyrmionic spin structure can be replaced with an antiskyrmionic one. The resulting spin state is shown in Fig. S7a along with the spatially resolved scalar spin chirality. One can see a mostly negative contribution in line with the expectations from the multi-Q state, in which the antiskyrmionic structure has a negative contribution (Fig. 3a of the main text). Fig. S7b shows the Chern number obtained from the tight-binding model for the adjacent superconducting layer in the magnet-superconductor-hybrid (MSH) system for a large range of parameters. As for the SkX state (cf. Fig. 3e of the main text), non-zero values of the Chern number can be observed for a large part of the phase space. In fact, the phases are exactly as for the SkX, however, with opposite signs of the Chern number. This strengthens the impression, that while each of the substructures of the multi-Q state can induce topological superconductivity their contributions cancel in the multi-Q state since both substructures are present. Fig. S7 c displays the size of the band gap for the same parameters as in Fig. S7 b.

S7. CONTINUOUS TRANSFORMATION OF THE D-SKX STATE INTO THE SKX STATE

In the main text we have discussed the multi-Q and the SkX state and their coupling to an adjacent superconductor. Based on DFT calculations [6] a so-called double skyrmionic lattice (d-SkX) been proposed as another potential ground state of Fe/Ir-3/Re(0001). One can create a continuous transformation between the d-SkX and the SkX state using Eq. (9) of the main text. Similar as for the 2Q-3Q-1Q path, we can use this continuous transformation to approximate how much the topological properties change for a deformation of the spin structure. Similar to the multi-Q state, the d-SkX state is a non-coplanar spin state with a locally non-zero scalar spin chirality. However, the total scalar spin chirality vanishes.

Along the path in spin space the net scalar spin chirality is increasing towards the SkX state (Fig. S8). Five states along the transformation have been selected in Fig. S9a, where the result for the SkX state is known from the main text (cf. Fig. 3 of the main text). The lattice site resolved scalar spin chirality is displayed in Fig. S9b. For the d-SkX lattice two areas with the same magnitude but opposite sign are canceling each other. Along the path

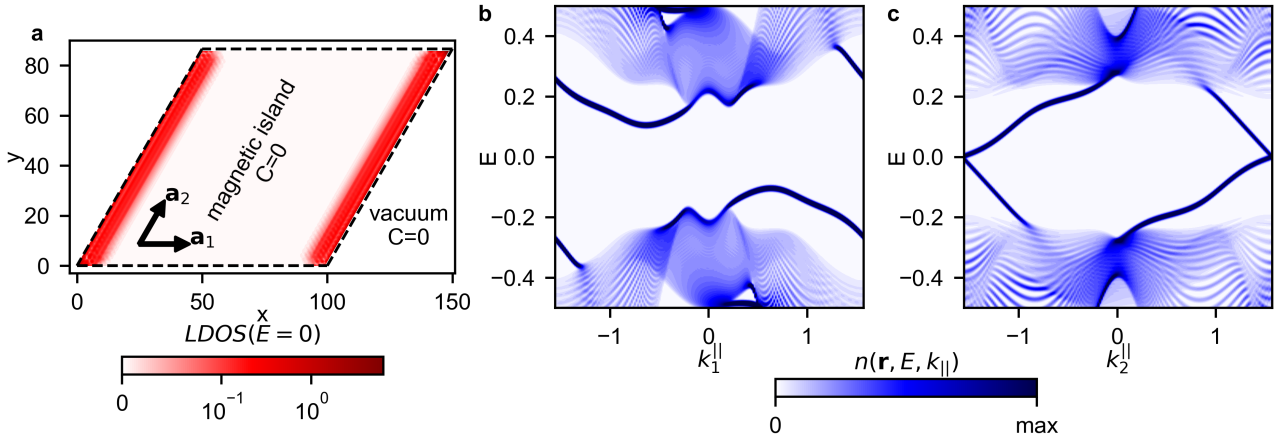

FIG. S4. **Island and ribbon for the $\alpha = 20°$ state along the 2Q-3Q-1Q path. a** Spatially resolved LDOS for magnetic island constructed from (50×50) unit cells (unit cell vectors are given in the methods section of the main text). The perimeter of the island is marked by a black dashed line. Outside of the island is vacuum, which is a trivial state. The tight-binding parameters are $(t, \mu, JS, \Delta) = (1, 2.05, 1.85, 0.4)$. These parameters correspond to a phase with vanishing Chern number. On the sharp corners, modes with large LDOS are localized. Therefore, the color bar is logarithmic, where the region $[0, 0.1]$ is linearized, which allows to better visualize the modes on the edge. **b,c** Spectral function at the boundary of a ribbon along the $\mathbf{a}_1$ (**b**) and the $\mathbf{a}_2$ (**c**) directions. The contribution of all four atoms of the unit cell directly at the edge are summed.

the positive contributions become larger than the negative contributions resulting in a finite χ_{total}. Fig. S9c,d show the Chern numbers and band gap, respectively, of the superconducting layer obtained via the tight-binding model for $t = 1, \Delta = 0.7$, $0 \leq JS \leq 6$ and $-6 \leq \mu \leq 6$. For all spin structures except the d-SkX state regions exist in which the Chern number is non-zero. A lot of phase transitions occur in many areas of the phase space resulting in small band gaps. Towards the SkX state larger band gaps occur for non-trivial phases. Even for a small distortions of the d-SkX state topological phases can be found. However, the superconducting gap is very small which makes an experimental detection difficult. As for all states presented in the main text the existence of a topological superconducting phase correlates with a non-vanishing total scalar spin chirality.

S8. NANOSKYRMION LATTICE IN FE/IR(111)

In the main text, we focused on atomic-scale skyrmion lattices in Fe/Ir-3/Re(0001). In this film system, Re plays the role of the adjacent superconductor with a transition temperature of 1.7 K. Nanoskyrmion lattices have previously been found in a monoatomic Fe layer on the Ir(111) surface [7]. Although the critical temperature is very low with $T_c = 0.1\,\text{K}$, Ir can be superconducting. Even if an experimental realization is unlikely, the effect of the discovered spin structures on a superconducting substrate in such a model system is quite interesting. Emergent topological superconductivity due to magnon excitations of such a nanoskyrmion lattice has been already studied in Ref. [8]. Here we want to investigate the effect on the same setup as in the main text and compare the lattices in Fe/Ir(111) to those in Fe/Ir-3/Re(0001).

Fig. S10a shows a multi-Q state and the corresponding nanoskyrmion lattice as described in Ref. [7]. The multi-Q state was constructed as a superposition of two spin spirals with perpendicular propagation direction. In this state four different substructures can be identified, two of which are reminiscent of a skyrmion and two reminiscent of an antiskyrmion. By a scissor operation the antiskyrmionic structures have been removed and the size of the unit cell reduced by one half for the nanoskymrion lattice, which has also been observed to be the ground state in Fe/Ir(111) [7].

In Fig. S10b the spatial resolved scalar spin chirality is displayed. For the multi-Q state χ_i forms rows with positive and negative contributions. On the nanoskyrmion lattice χ_i resembles a checkerboard pattern, where the negative (blue) contributions are slightly larger than the positive (red) contributions. This leads to a non-vanishing net scalar spin chirality of $\chi_{\text{total}} = -8.29$ for the nanoskyrmion, whereas it is zero for the multi-Q state. For the multi-Q lattice each skyrmionic structure has an antiskyrmionic counterpart, which are canceling in the scalar spin chirality. This counterpart is missing in the nanoskyrmion, lifting the compensation.

The Chern number for the tight-binding parameters $(t, \Delta) = (1,\ 0.7)$, $-6 \leq \mu \leq 6$ and $0 \leq JS \leq 6$ are plotted in Fig. S10c. As for the multi-Q state in Fe/Ir-3/Re(0001) (cf. Fig. 3 of the main paper) the Chern number is vanishing in the whole investigated phase space for the multi-Q state. For the nanoskymrion lattice non-trivial superconductivity exists for a variety of parameters.

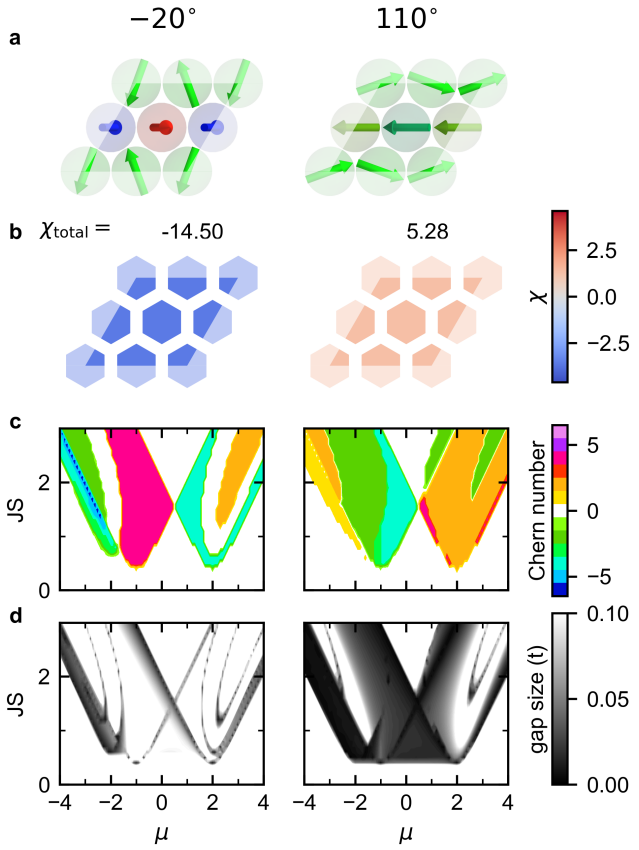

FIG. S5. **Topological properties of states on the extended 2Q-3Q-1Q path.** **a** Two spin structures for $\alpha = -20°$ and $\alpha = 110°$ are shown. **b** The atom resolved scalar spin chirality is displayed for each spin structure and the total value χ_{total} is given above each panel. The magnetic unit cell is highlighted by a parallelogram for all spin structures in **a** and **b**. **c** Chern numbers calculated with the tight-binding model for the spin structures shown in panel **a** for parameters $t = 1, \Delta = 0.4$. The chemical potential μ and the coupling to the magnetic state JS are varied between $-4 < \mu < 4$ and $0 < JS < 3$ in order to sample a large part of the phase space. The color represents the Chern number for a specific set of parameters. White areas represent a trivial state, which has a Chern number of 0. **d** Size of the band gap around the Fermi energy E_F for the calculation presented in panel **c**. The size of the band gap is evaluated over the whole Brillouin zone.

S9. EFFECT OF SPIN-ORBIT COUPLING

The Hamiltonian from the main text can also be extended to include Rashba-type spin-orbit coupling (Rashba-SOC). The Hamiltonian for this contribution has the form

$$H_{\text{SOC}} = -i \sum_{\mathbf{r}_i, \mathbf{r}_j, \sigma, \sigma'} \lambda_{\mathbf{r}_i, \mathbf{r}_j} c^\dagger_{\mathbf{r},\sigma} (\hat{e}_{\mathbf{r}_i - \mathbf{r}_j} \times \boldsymbol{\sigma}) c_{\mathbf{r}_j, \sigma'}, \quad \text{(S1)}$$

where λ is the interaction strength, $\boldsymbol{\sigma}$ is a vector containing the Pauli spin-matrices, $\hat{e}_{\mathbf{r}_i - \mathbf{r}_j}$ is the normalized connection vector between the lattice sites i and j and c ($c^\dagger$)

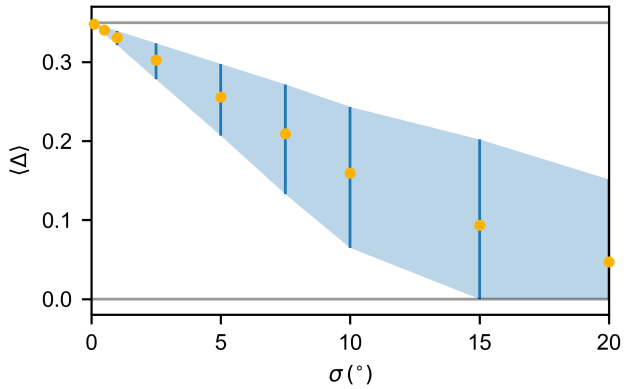

FIG. S6. **Band gap for random fluctuations of the 3Q state.** Each spin i of the ideal 3Q state has been rotated by two angles $\Delta\varphi_i$ and $\Delta\vartheta_i$. Theses angles were chosen randomly from a normal distribution for a given standard derivation. The angles are chosen individually for each lattice site. For a given standard derivation 1000 spin structures have been constructed. For each of the spin structures was the band gap calculated. The mean band gap for each standard derivation is shown here along with the 80%-percentiles.

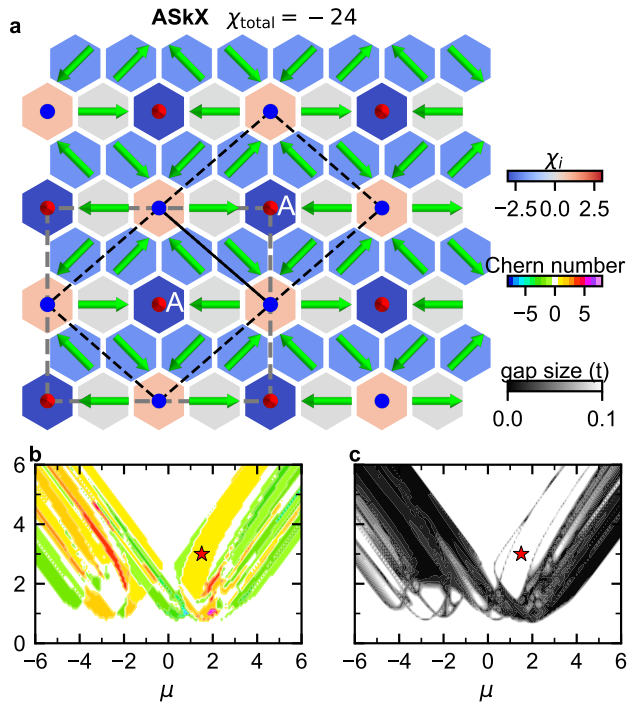

FIG. S7. **Topological properties of a MSH system with an antiskyrmion lattice.** **a** Atomic-scale antiskyrmion lattice (ASkX) state, constructed from the multi-Q state for Fe/Ir-3/Re(0001). The scalar spin chirality is marked as hexagons for each lattice site. **b** Chern number induced by the ASkX state in a superconductor for a wide range of chemical potential μ and coupling strength to the superconductor JS. **c** Band gap for the phase space as in **c**. The parameters for the tight-binding calculations are $(t, \Delta) = (1, 0.7)$, $-6 \leq \mu \leq 6$ and $0 \leq JS \leq 6$.

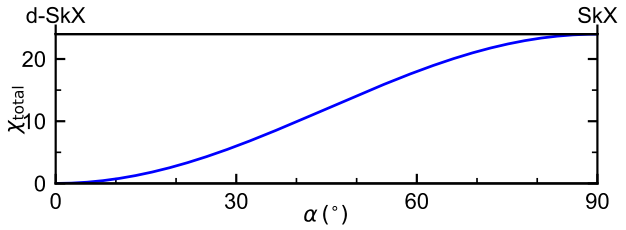

FIG. S8. **Total scalar spin chirality for spin structures along the path from the d-SkX to the SkX state.** Net scalar spin chirality for spin structures along the path in spin space obtained using Eq. (9) from the main text from the double skyrmion lattice state to the skyrmion lattice state (for spin structures see Fig. S3a).

is the creation (annihilation) operator as described in the methods section of the main text. With SOC topological nodal point superconductivity can be induced even in collinear spin states [9, 10]. With including SOC topological nodal point superconductivity might be found even for states with a zero Chern number presented in the main text. While this is not the focus of this work, we want to test how phases with non-zero Chern number are influenced by SOC.

Fig. S11 displays calculated Chern numbers and band gaps for the SkX state (cf. Fig. 3b,e,f from the main text) and the multi-Q state (cf. Fig. 3c,d,e from the main text). The strength of the Rashba-SOC has been set to $\lambda = 0.1$, $\lambda = 0.5$ and $\lambda = 1.0$ in units of the hopping parameter t. All other parameters were kept the same as in the main text. The data for $\lambda = 0$ from the main text are also shown as a reference. Upon including SOC in the calculations, the phases change a bit for the SkX state (c-f). Some formerly trivial areas can now have a non-zero Chern number as well as the other way around as shown in Fig. S11. However, qualitatively the phase diagram is similar for all values of λ. Even, when $\lambda = 1.0$ is as large as the hopping parameter, which marks a very strong contribution of SOC, the phase diagram does not drastically change.

The Chern numbers for the multi-Q state under the influence of SOC are shown in Fig. S11k-n. For all four SOC parameters $\lambda = 0.0$, $\lambda = 0.1$, $\lambda = 0.5$ and $\lambda = 1.0$, only zero Chern numbers can be observed in the entire range of the chemical potential and coupling strength. The sizes of the band gap are changing slightly with varying λ. This shows, that strong topological superconductivity can not be expected for the multi-Q state even under the influence of SOC. Quantitative occur some changes in the phase diagram for the SkX state, but qualitative are the results stable under the influence of SOC for the SkX and multi-Q state. this holds true even if the SOC in increased to the same value as the hopping parameter.

S10. RIBBON GEOMETRY FOR THE SKX STATE

In the main text, the ribbon geometry was discussed for an infinite stripe of the SkX state along the $\mathbf{a}_1$ direction. In Fig. S12, we show the band structure and the spectral functions for a ribbon in $\mathbf{a}_2$ direction. Similar to the ribbon along $\mathbf{a}_1$ most states are located outside of the bulk band gap Δ_B. The spectral function for the middle of the ribbon (cf. Fig. S12c) reveals that no states are located in the bulk band gap. On the left (Fig. S12b) and right (Fig. S12d) edge of the ribbon, on the other hand, edge modes are crossing the band gap. On the left edge, one mode is crossing the band gap and one other mode is dispersing within the band gap. The edge modes are chiral as observed also for the ribbon along the $\mathbf{a}_1$ direction (see main text).

S11. SKX LATTICE ON A RECTANGULAR ISLAND

In the main text the LDOS and supercurrents are shown for the SkX state on a realistic island as obtained from experimental STM data of Ref. [6]. In that case the edges of the island are not smooth and the termination of the spin structure is varying along the edges. The termination of the spin structure can have a large effect on the dispersion of the edge mode [11]. For comparison we show here a rectangular island made by a repetition of six unit cells in the $\mathbf{a}_1^{\mathrm{SkX}}$ and $\mathbf{a}_2^{\mathrm{SkX}}$ directions. Analogously to Fig. 5 of the main text the magnetic island is represented by a coupling strength of $JS = 3.0$ and the superconducting surface by $JS = 0$. The island has four different terminations of the spin structure. These possible edges are sketched for a (2×2) unit cell in Fig. S13(a). The local scalar spin chirality along the edges is different. The edge D has a constant scalar spin chirality, were all other edges have a spatial variation. The largest contributions of the scalar spin chirality can be found on the edges A and B. The LDOS for the (6×6) magnetic island at zero energy is shown in Fig. S13 (b). Edge modes with zero energy can be found all around the island. The LDOS coincides thereby with the local scalar spin chirality. For example has the edge B a fluctuation between large and small LDOS, where also the scalar spin chirality is varying along the edge. For edge D is the LDOS nearly constant and also the scalar spin chirality is constant. The magnitude of the zero energy LDOS therefore depends on the termination of the spin structure. Foe the region marked by dashed black lines is the supercurrent shown in Fig. S13(c). Here a net current in a counter clockwise direction located on the edge can be observed. This supercurrent exists also in the other, not shown, edges of the island, leading a to a net current around the island with the same rotational sense as in Fig. 5(c) of the main text, showing the irregular shaped island.

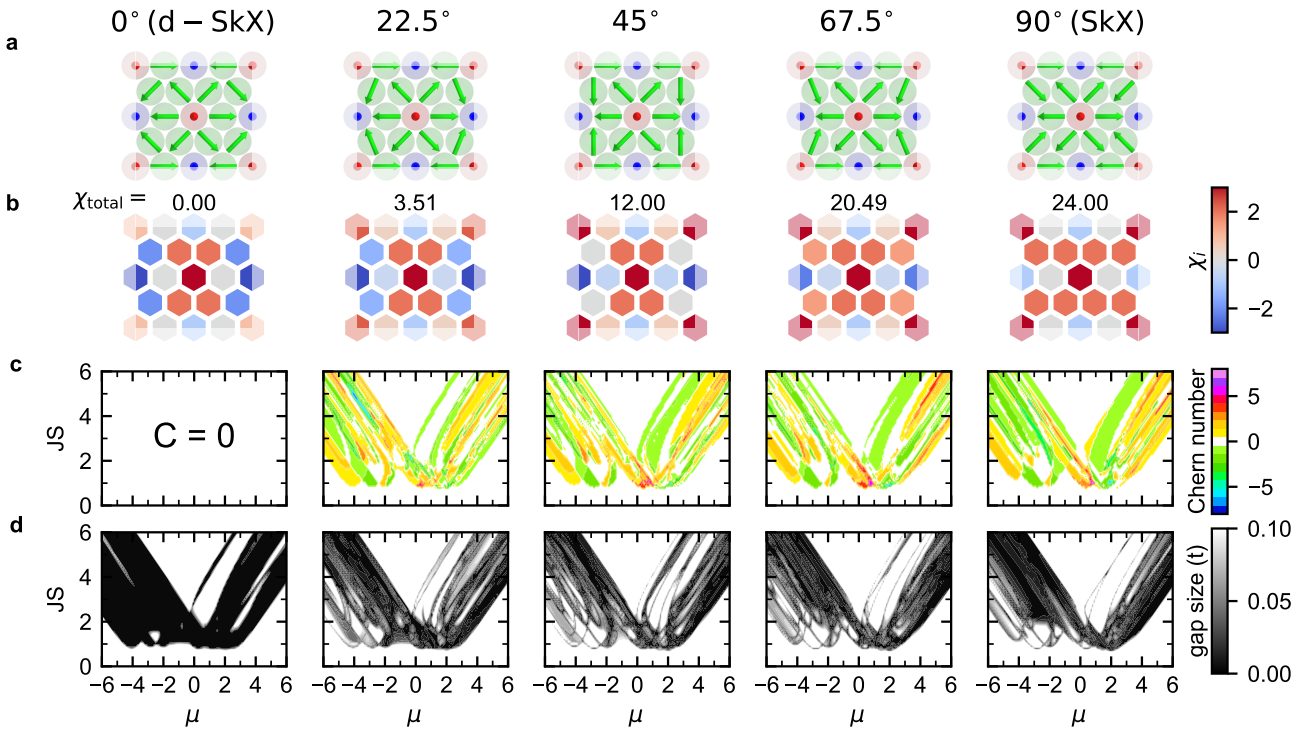

FIG. S9. **Topological properties of a MSH system with spin states along the geodesic path in spin space from the d-SkX to the SkX state.** **a** Five selected spin structures along the path including the d-SkX ($\alpha = 0°$) and SkX state ($\alpha = 90°$) constructed using Eq. (9) from the main text. **b** Atom resolved scalar spin chirality of each spin structure. Above each panel the net scalar spin chirality of the unit cell is given. **c** Chern numbers of the adjacent superconducting layer obtained from a tight-binding binding model with the spin structure from panel **a** for tight-binding parameters of $t = 1, \Delta = 0.7$ and varying chemical potential μ and coupling strength JS. **d** Size of the band gap around E_F for the calculations of panel **c**.

S12. HEXAGONAL NANOSKYRMION LATTICE

The multi-Q states for Fe/Ir(111) and Fe/Ir-3/Re(0001) were constructed as a superposition from two perpendicular spin spirals. The applied construction scheme ensures a constant magnitude of the magnetic moment at every lattice site [7]. However, also other superpositions of spin spirals have been suggested, which in general do not leave the magnitude of the magnetic moment constant. A constant magnitude can be achieved by a subsequent normalization of all moments [12, 13].

A superposition state constructed in such a way from three spin spirals, characterized by $\mathbf{q}_1$, $\mathbf{q}_2$ and $\mathbf{q}_3$, is displayed in Fig. S14a. The vectors $\mathbf{q}_1$, $\mathbf{q}_2$ and $\mathbf{q}_3$ have an angle of 120° between each other. The resulting spin texture constitutes a hexagonal skyrmion lattice and has been discussed as the magnetic ground state of an Fe monolayer in hcp stacking on the Ir(111) surface [12]. Due to the normalization of the magnetic moments the net magnetic moment does not vanish for this structure. Similar to the 3Q state all lattice sites have the same sign of the scalar spin chirality. In contrast to the 3Q state, the magnitude of χ_i is varying over the unit cell. However, due to the same sign at each lattice site the total χ_i is finite.

The Chern numbers calculated for the adjacent superconducting layer based on the tight-binding model are shown in Fig. S14b. For a large part of the sampled hase space we find non-zero Chern numbers as expected from the non-vanishing total value of the scalar spin chirality.

S13. ANTIFERROMAGNETIC SPIN LATTICE

To test whether our conclusions apply also beyond hexagonal lattices, we created an atomic-scale non-coplanar spin structure on a square lattice. We used the spin structure proposed as the ground state of Fe/Ir(001) [14], which has a square unit cell with nine atoms (Fig. S15a). This spin structure is proposed to induce an anomalous Hall effect due to its non-coplanar alignment [14] and exhibits a non-vanishing net scalar spin chirality. For comparison we set up a collinear state in the same unit cell and create a continuous transformation between both states (Fig. S15a). The collinear state has a vanishing scalar spin chirality at each lattice site, resulting also in a zero net scalar spin chirality (Fig. S15b).

Five selected spin states along this path are shown in Fig. S15a. The rotation angle of the transformation in

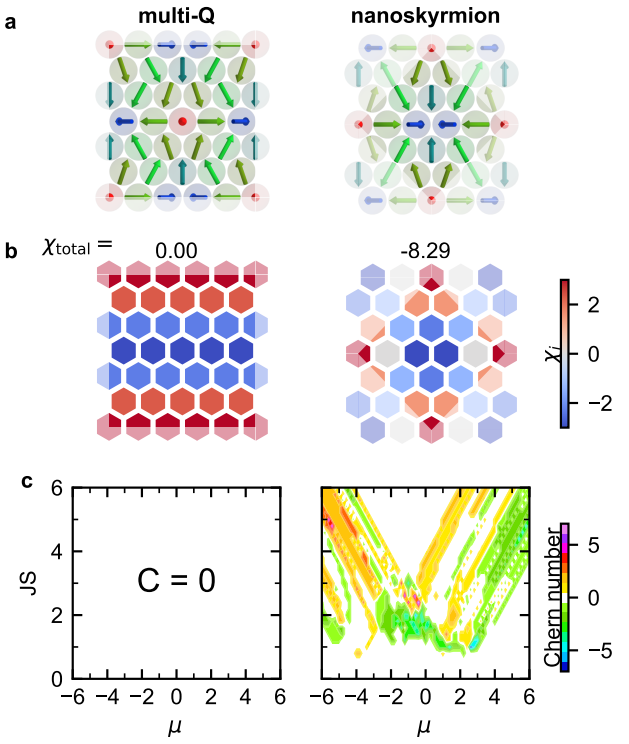

FIG. S10. **Topological properties of a MSH system with the multi-Q state and nanoskyrmion lattice of Fe/Ir(111). a** Real space spin structures of the multi-Q and nanoskyrmion lattice from Ref. [7]. **b** Scalar spin chirality χ_i on every lattice site i. The total value is given above the panels. **c** Chern number of the adjacent superconductor obtained by the tight-binding model for varying chemical potential μ and coupling to the magnetic structure JS. Fixed values for the tight binding calculations: $(t, \Delta) = (1, 0.7)$

spin space following Eq. (9) is denoted above each panel. Initially, the net scalar spin chirality increases along the path (Fig. S16), reaches a maximum at an angle of $\alpha \approx 20$ and then decreases until it is zero for the collinear state. Fig. S15b shows the atomically resolved contributions of the scalar spin chirality. At each lattice site the contributions are decreasing along the path. The sum over the unit cell is displayed above each panel.

The Chern numbers are obtained for the adjacent superconducting layer from the tight-binding model (Fig. S15c). For all spin structures along the path except for the collinear state ($\alpha = 90°$) regions with non-zero Chern numbers exist. These are the spin textures which also have a non-vanishing net spin chirality. For the collinear state the Chern number is zero for the entire investigated phase space. This is consistent with the findings of the other investigated systems.

The band gap (Fig. S15d) closes at a phase transition between different Chern numbers for the first four displayed spin structures. In the collinear case ($\alpha = 90°$) the band gap vanishes in regions in which non-zero Chern numbers were found for the other spin structures. This is the same behavior found before for spin structures on hexagonal lattices. This demonstrates that the connection between net scalar spin chirality and topological superconductivity is not limited to hexagonal lattices.

S14. SKYRMION COLLAPSE

For atomic-scale spin structures the scalar spin chirality can be used to describe its topological properties. However, for nanometer-scale or larger structures such as isolated skyrmions in a ferromagnetic background, usually the topological charge is used. Here, the area spanned by three spins $\mathbf{s}_i$, $\mathbf{s}_j$, $\mathbf{s}_k$ is projected onto a sphere. To investigate whether the scalar spin chirality or the topological charge is a better measure for possible topological superconductivity in an adjacent superconducting layer, we compare both quantities along the minimum energy path of the radial collapse of a skyrmion. The Chern numbers and other effects of a periodic lattice of isolated skyrmions have previously been investigated for different radii of skyrmions [15]. Similar to the 3Q state we want to follow up on these previous investigations by investigating the physical collapse path of these skyrmions.

In order to find a continuous transformation from the skyrmion to the ferromagnetic state we used the geodesic nudged elastic band (GNEB) method [16]. We used a 10×10 hexagonal lattice with periodic boundary conditions. This leads to the formation of a lattice of skyrmions. Differing from the atomic-scale skyrmion lattices discussed in the main text, each skyrmion is surrounded by a ferromagnetic background. We consider only nearest neighbor interactions such that the interaction between the individual skyrmions is minimized. For the magnetic interaction parameters a toy model of exchange ($J = 1\,\mathrm{meV}$) and Dzyaloshinskii-Moriya interaction ($D = 1\,\mathrm{meV}$) has been used and a magnetic field of $B = 14\,\mathrm{T}$ was chosen. The saddle point has been obtained by the climbing image method. The energy along the minimum energy path is displayed in Fig. S17a over the so-called images, which represent spin configurations on discrete points along the path. Image 1 represents the initial skyrmion (Sk) state, which has been relaxed prior to the GNEB calculation. Image 8 has the highest energy along the path and is therefore the saddle point (SP). Image 15 is the ferromagnetic (FM) final state.

In Fig. S17b the topological charge is shown for each individual image. The topological charge is -1 for the skyrmion and stays constant up to the saddle point. In the image after the saddle point (SP+1) the topological charge changes to 0 and stays zero for all further images. In contrast, the net scalar spin chirality, shown in Fig. S17c, does not change in an abrupt way. It is gradually decreasing between the skyrmion and the FM state. To investigate possible induced topological superconductivity, we calculated the Chern numbers and band gaps for images 1 (Sk), 7 (SP-1), 8 (SP), 9 (SP+1), and 15 (FM). For the images Sk, SP-1, and SP the topological

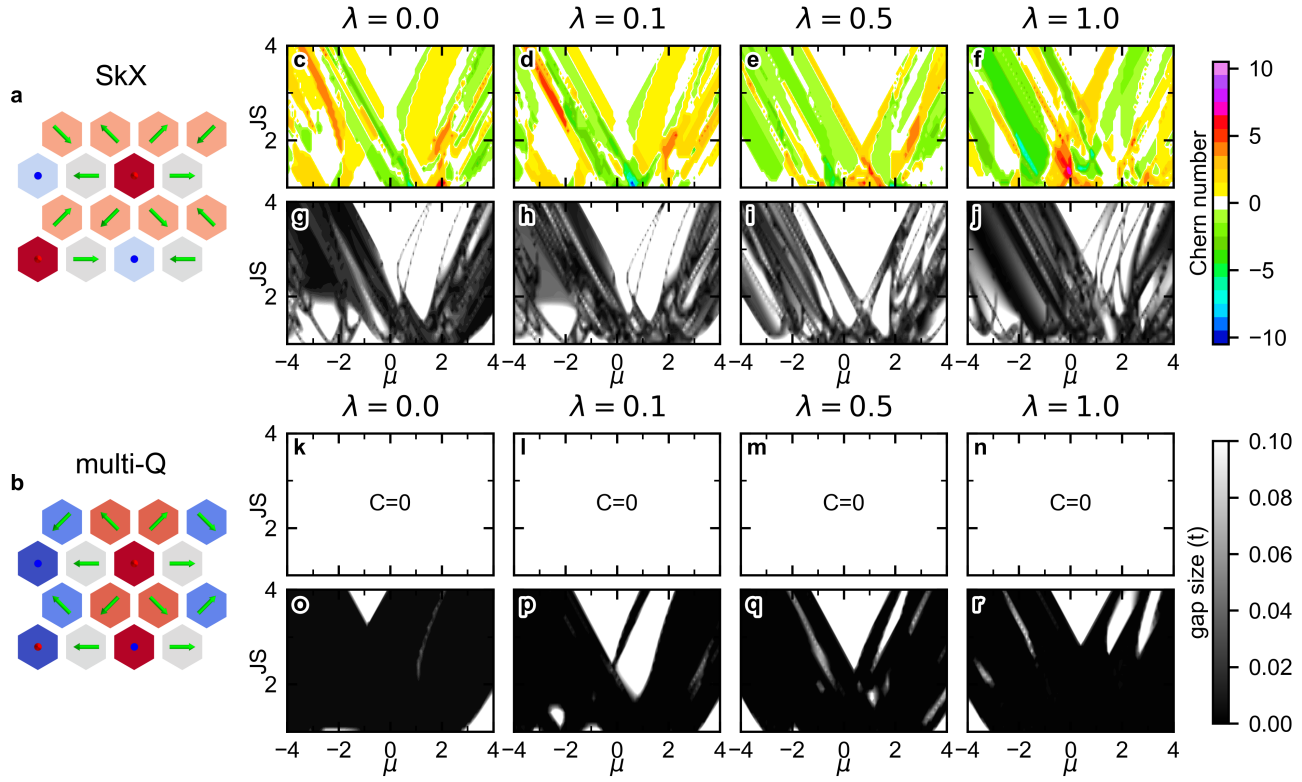

FIG. S11. **Chern numbers and band gaps for the SkX lattice and the multi-Q state including Rashba-SOC. a, b** Spin structure of the SkX and multi-Q state, respectively. **c-f** Phase diagram of the Chern number in the SkX state for an increasing value of the SOC-parameter λ. **g-j** Minimal band gap for the same parameters as in **c-f**. **k-n** Chern numbers for the multi-Q state with increasing value of λ. **o-r** Corresponding band gaps. The data for $\lambda = 0$ (**c, g, k, o**) corresponds to the data from the main text. The chemical potential and coupling to the magnetic layer are varied in a range of $-4 \leq \mu \leq 4$ and $1 \leq JS \leq 4$. The other parameters of the calculation are $(t, \Delta) = (1, 0.7)$, which are the same as used in Fig. 3 of the main text.

charge and the scalar spin chirality are non-vanishing. For the FM state both quantities are zero. However, for SP+1 the topological charge is vanishing, while the scalar spin chirality is still finite.

The spin structures for the five selected images are shown in Fig. S18a and the spatially resolved spin chirality is displayed in Fig. S18b. The scalar spin chirality is located in the areas of the largest tilting angles. The scalar spin chirality vanishes only for the FM state. In Fig. S18c the contributions to the topological density are shown. For the image SP+1 is the density of the topological charge not vanishing everywhere, but the contributions are canceling each other over the unit cell. This is a major difference to the scalar spin chirality (cf. Fig. S18 (b)), where the contributions are not canceling each other. For all other images both quantities behave similar. The Chern numbers are shown in Fig. S18d. For image 1 we find a large variety of topological phases, which is in accordance with the findings of Ref. [15]. Similar to the two previous sections the phases of the Chern numbers shift slightly, as we follow the minimum energy path between the skyrmion and the FM state. As we reach the FM state, only zero Chern numbers are found, i.e. only a trivial superconducting phase occurs. Very interestingly for the SP+1 the Chern numbers do not vanish. Here the total scalar spin chirality is non-vanishing, but the topological charge is zero. We conclude that the topological superconductivity is not linked to the topological charge of the spin structure. However, it seems to be linked to the net scalar spin chirality.

S15. ANTIFERROMAGNETIC SKYRMIONS

In the previous section, we have investigated isolated skyrmions and different types of atomic-scale spin lattices. Besides an atomic-scale skyrmion and antiskyrmion lattice, we also considered multi-Q states in which both skyrmionic and antiskyrmionic spin structures appeared. These spin structures are spatially separated and exhibit opposite scalar spin chirality which results in a vanishing total value of χ_{total} and the Chern number in the adjacent superconductor was also zero.

Skyrmions can also be stabilized in an antiferromag-

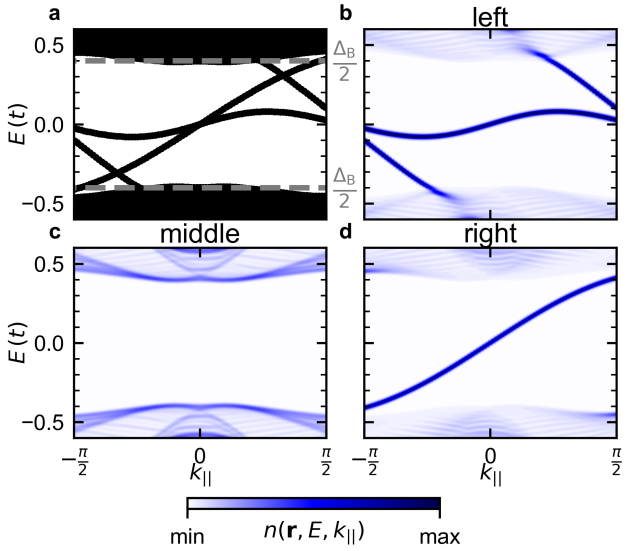

FIG. S12. **Band structure and spectral function of a ribbon with the SkX state adjacent to a vacuum.** The ribbon is infinite along the $\mathbf{a}_2$ crystallographic direction and exhibits a width of 40 unit cells in the perpendicular direction. **a** Band structure obtained via the tight-binding model for a ribbon along $\mathbf{a}_2$. **b-d** Spectral functions for two atomic rows at the left edge, in the center of the ribbon, and at the right edge, respectively. For each spectral function the contributions of two rows of atoms in the periodic direction is summed.

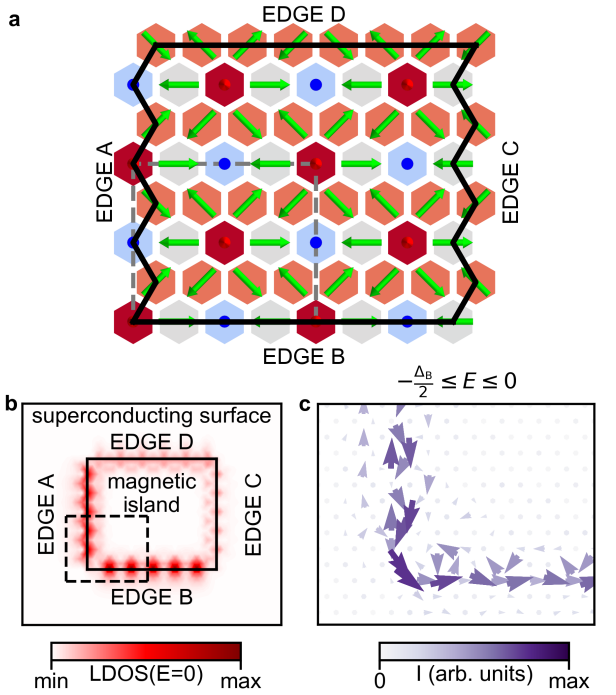

FIG. S13. **LDOS and supercurrent of a rectangular magnetic island with the SkX state.** The island is constructed from six repetitions of the magnetic unit cell in the $\mathbf{a}_1^{\mathrm{SkX}}$ and $\mathbf{a}_2^{\mathrm{SkX}}$ directions. **a** Schematic drawing of a (2×2) island with the four different edges marked by black solid lines. The edges differ in the termination of the spinstructuture and are labeled A-D. These are the same edges, that occur at the (6×6) island used in **(b, c)**. **b** LDOS at zero energy. The position of the island is indicated by a black line and the type of edge is indicated. **c** supercurrent for states in the energy interval $E \in [-\frac{\Delta_B}{2}, 0]$ for the region marked by a dashed line in **a**. All parameters of the calculations are the same as in Fig. 5 of the main text.

netic (AFM) material. Such an AFM skyrmion is built from two skyrmions with opposite polarisation on the two sublattices of the antiferromagnet which have the same center and are therefore entangled. Such an AFM skyrmion on a quadratic lattice is shown in Fig. S19a. The background of the spin structure is a checkerboard AFM state on a square lattice. This lattice can be viewed as two sublattices, one with spins pointing in the $+z$ direction and one with spins pointing in the $-z$ direction. In each of these sublattices a skyrmion is inserted with the respective polarization.

The spin structure in Fig. S19a has been relaxed using spin dynamics in order to minimize the energy using the nearest-neighbor interaction parameters of exchange $J_1 = -1\,\mathrm{meV}$, DMI $D_1 = 0.68\,\mathrm{meV}$, and magnetocrystalline anisotropy energy $K = 0.6\,\mathrm{meV}$. The parameters have been chosen in a way, that the AFM skyrmion is sufficiently large, but that the border of the simulation box is formed by the AFM background and the interactions are short ranged, to avoid interactions due to periodic boundary conditions. Periodic boundary conditions were applied for the spindynamics simulations as well as for the tight-binding calculations, which leads to a lattice of AFM skyrmions.

In Fig. S19b the scalar spin chirality of the AFM skyrmion is shown. The scalar spin chirality has the largest contributions in the wall of the two skyrmions. Towards the borders of the unit cell it is vanishing as the spins align collinear in these regions. Further, the scalar spin chirality forms a checkerboard pattern of positive and negative contributions. Averaged over the unit cell, the scalar spin chirality is vanishing. The Chern number has been calculated for the adjacent superconducting layer using the tight-binding model with parameters of $(t, \Delta) = (1, 0.7)$, $-6 \leq \mu \leq 6$ and $0 \leq JS \leq 6$. For each of these calculations the Chern number is zero, which represents only trivial superconductivity. This shows that even for spatially non-separated spin structures the sum of the scalar spin chirality over the unit cell is connected to the existence of topological non-trivial phases.

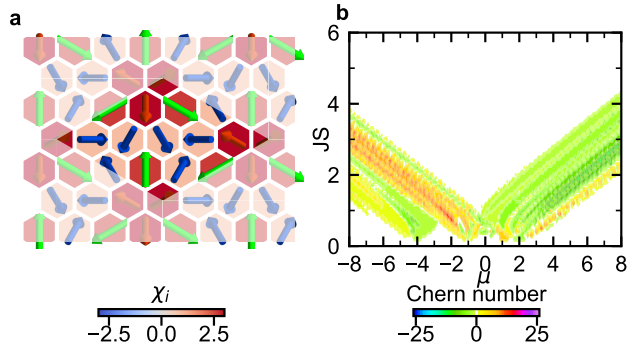

FIG. S14. **Topological properties of a MSH system with a hexagonal atomic-scale skyrmion lattice.** **a** hexagonal atomic-scale skymrion lattice, constructed from three spin spirals with 120° between the propagation directions and narmalization of the magnetic moment. The scalar spin chirality is marked as hexagons for each lattice site. **b** Chern number obtained using the tight-binding model for the lattice shown in panel **a** with parameters of $(t, \Delta) = (1, 0.7)$, $-8 \leq \mu \leq 8$ and $0 \leq JS \leq 6$.

[1] S. Haldar, S. Meyer, A. Kubetzka, and S. Heinze, Distorted 3q state driven by topological-chiral magnetic interactions, Phys. Rev. B **104**, L180404 (2021).

[2] F. Nickel, A. Kubetzka, S. Haldar, R. Wiesendanger, S. Heinze, and K. von Bergmann, Coupling of the triple-q state to the atomic lattice by anisotropic symmetric exchange, Phys. Rev. B **108**, L180411 (2023).

[3] K. H. Wong, M. R. Hirsbrunner, J. Gliozzi, A. Malik, B. Bradlyn, T. L. Hughes, and D. K. Morr, Higher order topological superconductivity in magnet-superconductor hybrid systems, npj Quantum Materials **8**, 31 (2023).

[4] K. H. Wong, J. Gliozzi, M. R. Hirsbrunner, A. Malik, B. Bradlyn, T. L. Hughes, and D. K. Morr, Competing higher order topological superconducting phases in triangular lattice magnet-superconductor hybrid systems, Phys. Rev. B **109**, 144521 (2024).

[5] S. Nakosai, Y. Tanaka, and N. Nagaosa, Two-dimensional p-wave superconducting states with magnetic moments on a conventional s-wave superconductor, Phys. Rev. B **88**, 180503 (2013).

[6] F. Nickel, A. Kubetzka, M. Gutzeit, R. Wiesendanger, K. von Bergmann, and S. Heinze, Antiferromagnetic order of topological orbital moments in atomic-scale skyrmion lattices (2024), arXiv:2405.18088 [cond-mat.mtrl-sci].

[7] S. Heinze, K. von Bergmann, M. Menzel, J. Brede, A. Kubetzka, R. Wiesendanger, G. Bihlmayer, and S. Blügel, Spontaneous atomic-scale magnetic skyrmion lattice in two dimensions, Nature Physics **7**, 713 (2011).

[8] K. Mæland and A. Sudbø, Topological superconductivity mediated by skyrmionic magnons, Phys. Rev. Lett. **130**, 156002 (2023).

[9] M. Bazarnik, R. Lo Conte, E. Mascot, K. von Bergmann, D. K. Morr, and R. Wiesendanger, Antiferromagnetism-driven two-dimensional topological nodal-point superconductivity, Nature Communications **14**, 614 (2023).

[10] T. Kieu, E. Mascot, J. Bedow, R. Wiesendanger, and D. K. Morr, Topological nodal point superconductivity in checkerboard magnet-superconductor hybrid systems, Phys. Rev. B **108**, L060509 (2023).

[11] R. Brüning, J. Bedow, R. L. Conte, K. von Bergmann, D. K. Morr, and R. Wiesendanger, The non-collinear path to topological superconductivity (2024), arXiv:2405.14673 [cond-mat.supr-con].

[12] K. von Bergmann, M. Menzel, A. Kubetzka, and R. Wiesendanger, Influence of the local atom configuration on a hexagonal skyrmion lattice, Nano Lett. **15**, 3280 (2015).

[13] M. Gutzeit, T. Drevelow, M. A. Goerzen, S. Haldar, and S. Heinze, Spontaneous square versus hexagonal nanoscale skyrmion lattices in Fe/Ir(111), Phys. Rev. B **108**, L060405 (2023).

[14] M. Hoffmann, J. Weischenberg, B. Dupé, F. Freimuth, P. Ferriani, Y. Mokrousov, and S. Heinze, Topological orbital magnetization and emergent hall effect of an atomic-scale spin lattice at a surface, Phys. Rev. B **92**, 020401 (2015).

[15] E. Mascot, J. Bedow, M. Graham, S. Rachel, and D. K. Morr, Topological superconductivity in skyrmion lattices, npj Quantum Materials **6**, 6 (2021).

[16] P. F. Bessarab, V. M. Uzdin, and H. Jónsson, Method for finding mechanism and activation energy of magnetic transitions, applied to skyrmion and antivortex annihilation, Computer Physics Communications **196**, 335 (2015).

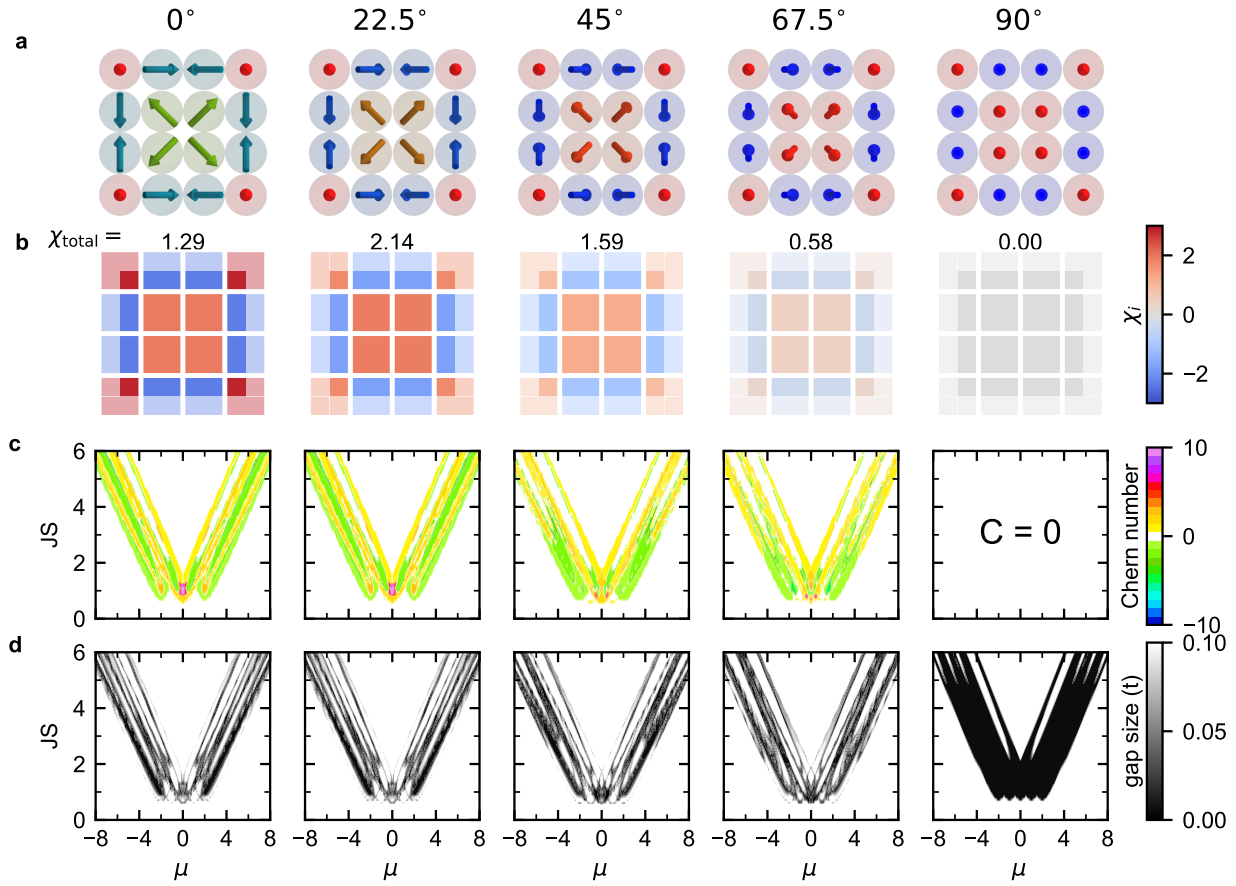

FIG. S15. **Topological properties of a MSH system with antiferromagnetic atomic-scale spin lattices.** Properties of five images along the geodesic path between a (3×3) non-coplanar spin structure on a square lattice, proposed as the ground state of Fe/Ir(001) [14], and a collinear state. **a** Real space spin structures. **b** Scalar spin chirality for every lattice site of the spin structures. **c** Chern number and **d** band gap of the adjacent superconducting layer obtained via the tight-binding model for varying chemical potential μ and coupling to the magnetic structure JS. Fixed values for the tight binding calculations: $(t, \Delta) = (1, 0.7)$.

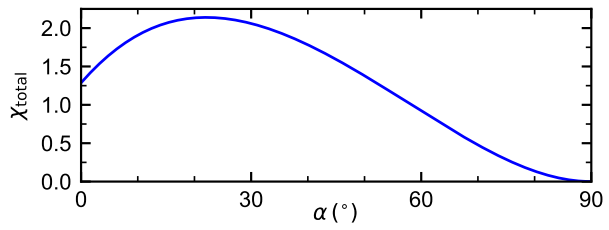

FIG. S16. **Total scalar spin chirality of antiferromagnetic spin lattices.** Net scalar spin chirality along the path in spin space from the non-coplanar (3×3) spin structure to the collinear state shown in Fig. S7a.

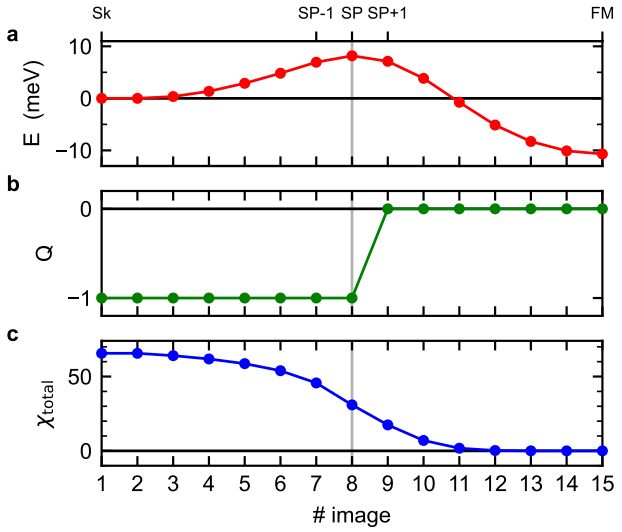

FIG. S17. **Minimum energy path of the skyrmion collapse into the ferromagnet. a** Energy of every image along the minimum energy path as obtained by the GNEB method from the initial skyrmion (Sk) state to the final ferromagnetic (FM) state on a (10×10) lattice. **b** Topological charge for each image along the path. **c** Total scalar spin chirality for each image. The position of the saddle point (SP, image with the highest energy) is marked with a vertical line. The five images which are used for further investigations (cf. Fig. S6) are shown with a larger marker size.

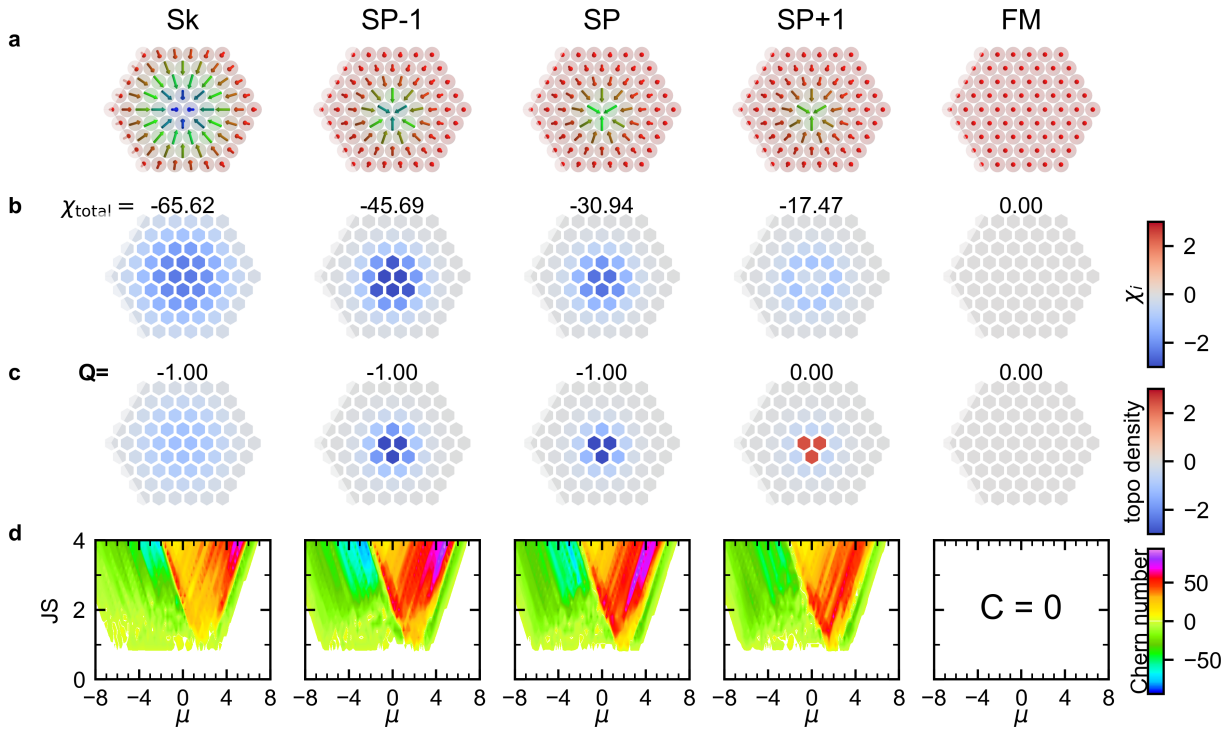

FIG. S18. **Topological properties of a MSH system along the transition path of an isolated skyrmion.** Different properties for five images of the GNEB path of the collapse of a skyrmion from Fig. S17. The first image shows the skyrmion state. Image 7 is the image before the saddle point, image 8 represents the saddle point and image 9 is the image directly after the saddle point. Image 15 shows the ferromagnetic state after the complete collapse of the skyrmion. In (a) are the spin structures of the individual images shown. In (b) is the scalar spin chirality for each lattice site of each image shown. In (c) the topological density is displayed at each lattice site. (d) shows the chern number calculated by a tight binding model with the parameters of $(t, \Delta) = (1, 0.8)$, a varying chemical potential $-8 < \mu < 8$ and coupling to the magnetic structure $JS < 4$. The chern number has been calculated on a grid of 100×100 k-points in the whole Brillouin zone.

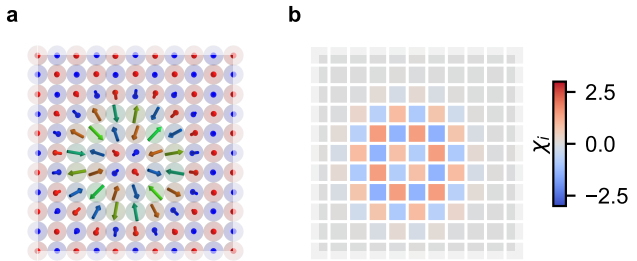

FIG. S19. **Isolated antiferromagnetic skyrmion. a** Spin structure of an AFM skyrmion on a 10×10 square lattice. **b** Scalar spin chirality χ_i for each lattice site i of the AFM skyrmion shown in panel **a**.

8 Spin-polarized edge modes between different magnet-superconductor-hybrids

Name: Spin-polarized edge modes between different magnet-superconductor-hybrids

Published: Submitted for peer-review. Preprint available: arXiv:2506.16869 (2025)

DOI: https://doi.org/10.48550/arXiv.2506.16869

Authors: Felix Zahner, **Felix Nickel**, Roberto Lo Conte, Tim Drevelow, Roland Wiesendanger, Stefan Heinze, Kirsten von Bergmann

Author contributions: F.Z. prepared the samples, performed the experiments, and together with K.v.B. and R.L.C. analyzed the data. **F.N.** developed the tight-binding model, performed the tight-binding calculations and STM simulations and analyzed the data together with S.H. T.D. performed the DFT calculations. F.Z., **F.N.**, R.L.C., S.H., and K.v.B. wrote the manuscript. All authors discussed the data and contributed to the final manuscript.
F.Z. and **F.N.** contributed equally.

Spin-polarized edge modes between different magnet-superconductor-hybrids

Felix Zahner,[1,2,*] Felix Nickel,[3,2,†] Roberto Lo Conte,[4] Tim Drevelow,[3]
Roland Wiesendanger,[1] Stefan Heinze,[3,5] and Kirsten von Bergmann[1]

[1]*Department of Physics, University of Hamburg, Jungiusstraße 11, 20355 Hamburg, Germany*
[2]*These authors contributed equally: Felix Zahner, Felix Nickel.*
[3]*Institut für Theoretische Physik und Astrophysik, Christian-Albrechts-Universität zu Kiel, D-24098 Kiel, Germany*
[4]*Zernike Institute for Advanced Materials, University of Groningen, 9747 AG, Groningen, The Netherlands*
[5]*Kiel Nano, Surface, and Interface Science (KiNSIS), University of Kiel, Germany*

The interplay of magnetism and superconductivity can lead to intriguing emergent phenomena. Here we combine two different two-dimensional antiferromagnetic magnet-superconductor hybrids (MSH) and study their properties using spin-polarized scanning tunneling microscopy. Both MSHs show the characteristics of a topological nodal point superconducting phase with edge modes to the trivial substrate superconductor. At the boundary between the two MSHs we find low-energy modes which are spin-polarized. Based on a tight-binding model we can explain the experimental observations by considering two different topological nodal point superconductors. This gives rise to spin-polarized chiral edge modes that connect topological nodal points of the two different MSH. We demonstrate via the complex band structure that due to an asymmetric lateral decay these edge modes are spin-polarized, regardless of the details of the spin structure at the boundary. The presence of spin-polarized edge states between different topological superconductors enables advanced functional design for the exploitation of MSHs as a platform for topology-based applications.

INTRODUCTION

Topological superconductivity has become of great interest, as it allows the formation of topologically protected states, such as Majorana bound states (MBS) and edge modes [1]. These modes can occur at the boundaries between trivial and topological superconductors [2, 3] or between two different topological superconducting phases. A promising platform to establish topological superconductivity are magnet-superconductor hybrid (MSH) systems, where magnetic chains or thin layers are grown on a conventional s-wave superconductor [4]. In particular, two-dimensional (2D) magnets can host a plethora of different spin textures [5, 6] which can be placed in direct proximity to a superconductor, emerging as an ideal material class for the search for topological superconductivity. This is confirmed by several theoretical predictions of the emergence of intriguing phenomena in such hybrid systems [7–13].

In the last decade, a variety of 2D magnet-superconductor hybrids have been investigated both experimentally and theoretically. For a ferromagnetic state [3, 8, 14, 15] or non-coplanar spin textures [9, 10, 13, 16, 17] gapped topological superconductivity has been found or predicted. Antiferromagnetic [12, 18–20] or spin spiral [16, 21] states can induce topological nodal point superconductivity (TNPSC). In those previous studies the boundary between a topological and a trivial superconducting phase was investigated, as it is the case for magnetic islands on the surface of a conventional superconductor. Here, the topological phase arising due to the magnetic island is surrounded by the trivial phase of the superconducting substrate.

Antiferromagnetism-based MSHs are of particular interest for applications, because in addition to their intriguing topological superconductivity they exhibit a zero net moment and ultrafast dynamics. In contrast to gapped superconductors, such TNPSCs have at least one pair of nodal points (NP), where the band gap is closed [22–24]. Such topological NPs are protected against spontaneous annihilation and can only be detached from the Fermi energy when they are merged. At boundaries with a trivial superconducting phase, these NPs are connected via low-energy modes. The occurrence of the edge mode therefore depends on the projection of the NPs on the crystallographic direction of the boundary [12, 18, 20], resulting in the emergence of edge modes only on certain edges of the MSH system.

In a recent experimental work where a magnetic spin spiral was proximitized to an s-wave superconductor, it was shown that the dispersion of the edge mode depends on the actual magnetization state at the boundary of the MSH system [21]. This observation shows a possible avenue towards the tuning of the properties of edge modes in 2D topological superconductors. However, in view of potential applications, a higher degree of controllability over the topological edge modes in MSH-systems is desirable. This could potentially be achieved by interfacing two different topological superconducting phases, whose properties could be tuned ideally via electrical means. The observation of such edge modes at the boundary between two different topological superconducting phases has so far not been reported.

Here we report on the combined experimental and theoretical investigation of the magnetic and superconducting properties of hybrid MSH systems consisting of a Mn-monolayer (ML) and a Mn-bilayer (BL) on a superconducting Ta(110) surface. Low-temperature spin-polarized scanning tunneling microscopy (SP-STM) investigations reveal the presence of local antiferromagnetic states in both Mn layers. Furthermore, highly spin-polarized low-energy edge modes are observed between the two different magnetic regions. Tight-binding model calculations allow us to explain the observed edge modes at the Mn-ML/Mn-BL boundaries as the result of

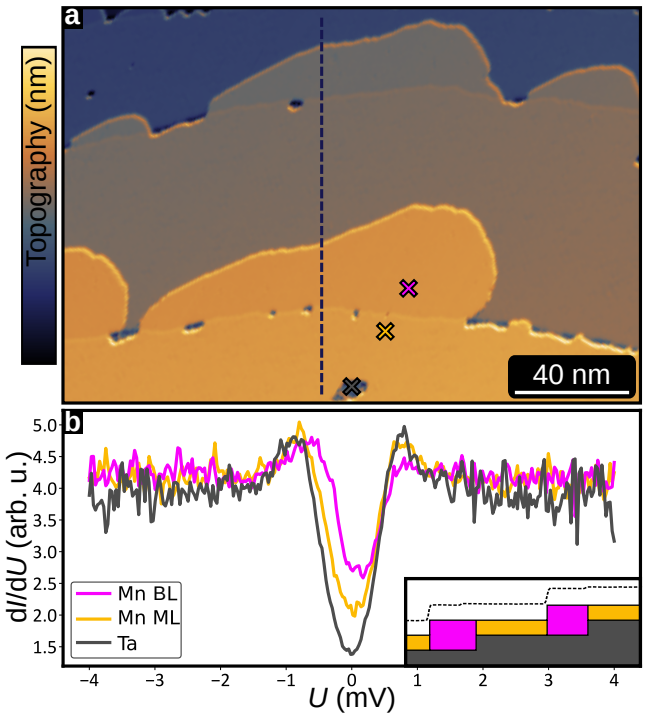

Figure 1. **Superconducting properties of Mn/Ta(110). a,** Partially differentiated constant-current STM image of a sample of 1.25 atomic layers of Mn on Ta(110). **b,** Tunnel spectra acquired at 1.3 K on the bare Ta, the Mn ML and the Mn BL, at the positions indicated by colored crosses in a. Inset shows line profile and side view sketch of the sample along the dashed black line in a. Measurement parameters: a: $U = +60$ mV, $I = 1$ nA.; b: stabilization bias $U_s = +4$ mV, stabilization current $I_s = 1$ nA, modulation bias $U_{mod} = 50\,\mu$V, $T = 1.3$ K; all: Cr-bulk tip

the presence of two different TNPSC phases in the two magnetic regions. Using the complex band structure we show that the spin-polarization of the edge mode at the boundary between slightly different antiferromagnets is a general effect originating from a different decay of the edge mode into the bulk electronic structure of the adjacent TNPSCs.

RESULTS

Experimental results on the Mn ML and Mn BL system

We have prepared ultra-thin films of Mn on Ta(110), see methods, and find that both the Mn ML as well as the Mn BL grow pseudomorphically. For a coverage of approx. 1.25 atomic layers grown at elevated temperatures we observe an almost fully closed ML with BL regions attached to the step edges, see constant-current STM image and side view sketch in Fig. 1a and b, respectively. Tunnel spectroscopy was performed at different positions of this sample as indicated by crosses in Fig. 1a, including the bare Ta substrate (i.e. a hole in the Mn ML), the Mn ML and the Mn BL, see Fig. 1b. Due to thermal broadening at the measurement temperature of 1.3 K, the density of states in the superconducting gap of the Ta does not go down to zero but is seen as a dip in the differential conductance ($\mathrm{d}I/\mathrm{d}U$) signal around zero energy. We observe similar spectra for the two different Mn layers with a slight increase of the $\mathrm{d}I/\mathrm{d}U$ signal around zero-bias compared to the Ta substrate, demonstrating that due to the proximity to the substrate also the Mn layers are superconducting. The less pronounced superconducting gap is a manifestation of additional states inside the gap, which is a hallmark of magnetic moments in proximity to a superconductor [4].

First, we focus on the characterization of the Mn ML and prepare Mn ML islands by depositing sub-monolayer amounts at room temperature, see constant-current STM image in Fig. 2a. The islands are elongated along $[001]$ and several straight edges along that direction, together with some well-developed edges along $\langle 111 \rangle$, can be seen. We have investigated the magnetic state of these Mn ML islands at low temperature using SP-STM, see current map in Fig. 2b. The lines along $[001]$ visible on the Mn ML island are separated by a distance equivalent to two atomic rows, demonstrating that the magnetic state is antiferromagnetic [25], see inset. (For further information on the magnetic state see Supplementary Notes 1 and 2).

Zero-bias $\mathrm{d}I/\mathrm{d}U$ maps of the antiferromagnetic Mn ML islands show an increased signal along their edges, see Fig. 2c. This demonstrates an increased density of states in the center of the superconducting gap at the edges compared to the interior of the island. The intensity of this edge mode varies depending on the direction of the edges, as seen in a series of spectra taken across two different edges of this island: Figures 2d,e show the $\mathrm{d}I/\mathrm{d}U$ signal (color-coded) as a function of the bias voltage and the path across the $[1\bar{1}1]$ and $[001]$ edges indicated in Fig. 2a, respectively. While we do observe an increase of the intensity within the gap for both edges, the spectra at the $[001]$ edge (Fig. 2e) clearly feature a peak close to zero bias. Such distinct edge mode properties at different edges are typical for TNPSC phases of this surface symmetry, as also seen for a similar system, the antiferromagnetic Mn ML on Nb(110)[18]. Indeed, TNPSC was predicted to occur for various antiferromagnets [12]. (For additional data with a different tip comparing the three high-symmetry edges, see Supplementary Note 4).

Next, we investigate the properties of the Mn BL, and the boundary between the ML and BL, using a sample with a nearly closed ML and BL islands. We find that the BL islands exhibit rather long straight edges along $[001]$, see current map in Fig. 3a (and corresponding constant-current STM image in Supplementary Fig. S5). SP-STM reveals that the BL is also antiferromagnetic, see Figs. 3a,b, and here both the ML and the BL have all spins aligned out-of-plane with a strict phase relation between them due to antiferromagnetic interlayer coupling, see sketch in Fig. 3c (and also Fig. S1, and S2). The termination of the antiferromagnetic state of the BL at the $[001]$ edges results in an edge with parallel spins. The two opposite magnetization directions at the edge can be identified

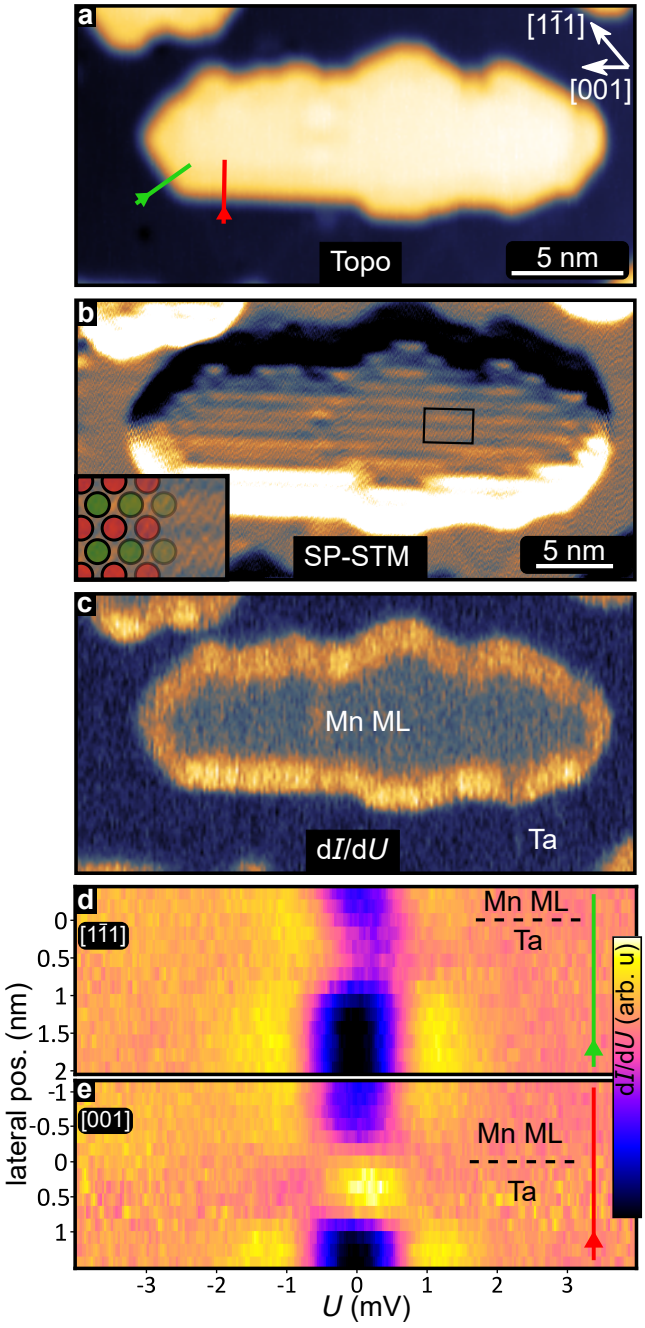

Figure 2. **Magnetic State and Edge Mode of the Mn ML on Ta(110). a,** STM constant-current image showing an island of the Mn ML with several straight edges. **b,** SP-STM current map of the same island using a spin-polarized tip, inset shows the row-wise antiferromagnetic order; fast scan direction is vertical. **c,** Zero-bias $\mathrm{d}I/\mathrm{d}U$ map of the same island (multi-pass mode). **d,e,** Spatially- and energy-resolved $\mathrm{d}I/\mathrm{d}U$ signal across a $[1\bar{1}1]/[001]$ edge along the green/red line marked in **a**, respectively. Each spectrum was normalized. Raw data in Fig. S4. Measurement parameters: a: $U = +4\,\mathrm{mV}$, $I = 1\,\mathrm{nA}$; b: $U = +5\,\mathrm{mV}$, $I = 1\,\mathrm{nA}$; c: $U = 0\,\mathrm{mV}$, $U_{\mathrm{mod}} = 50\,\mu\mathrm{V}$, measured at the tip-sample distance obtained in a; d,e: spectra with stabilization bias $U_{\mathrm{s}} = +4\,\mathrm{mV}$, stabilization current $I_{\mathrm{s}} = 1\,\mathrm{nA}$, modulation bias $U_{\mathrm{mod}} = 50\,\mu\mathrm{V}$; all: Cr-bulk tip, $T = 1.3\,\mathrm{K}$.

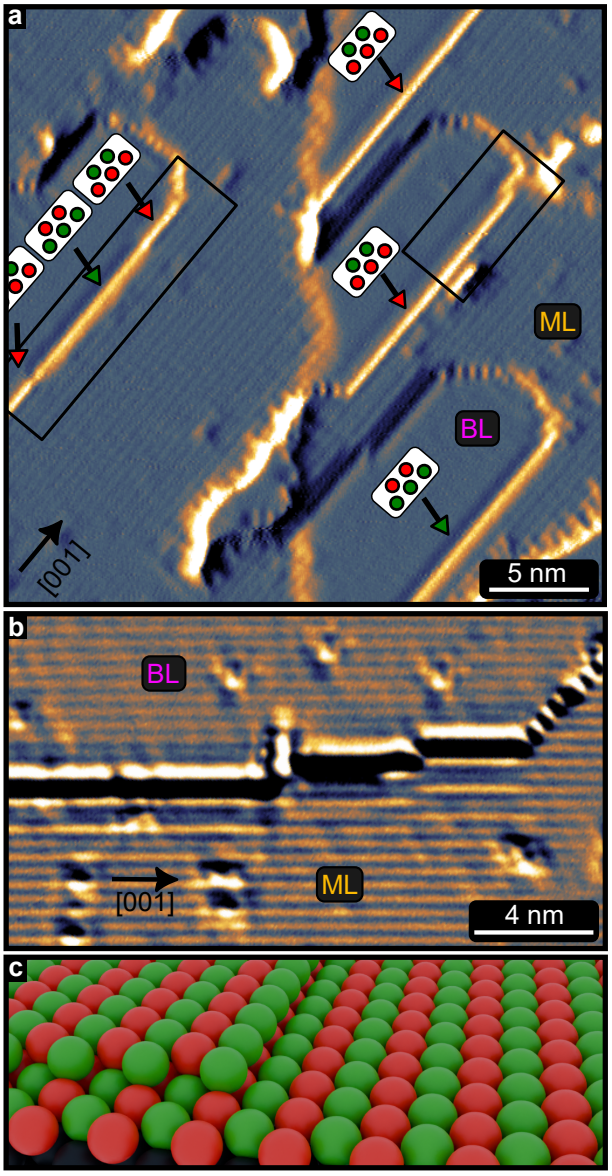

Figure 3. **Magnetic State of the Mn ML and BL on Ta(110). a,** SP-STM current map of Mn BL islands on a nearly closed Mn ML (note the buried Ta step edge in the center of the image); red/green markers indicate the two different contrast levels. **b,** SP-STM current map of a Mn BL island (top), next to an area of Mn ML (bottom). Both areas show the same magnetic stripe contrast indicative of antiferromagnetic order. **c,** Sketch of a region of Mn BL and ML. The top layer atoms sit in the fourfold hollow site positions. Measurement parameters: a: $U = +5\,\mathrm{mV}$, $I = 1\,\mathrm{nA}$, $T = 1.3\,\mathrm{K}$; b: $U = -15\,\mathrm{mV}$, $I = 2\,\mathrm{nA}$, $T = 4.2\,\mathrm{K}$; all: Cr-bulk tip.

in the SP-STM current image in Fig. 3a by two distinct signal intensities, see green and red markers. The edge indicated by the left rectangle exhibits two single atomic kinks resulting in opposite magnetization directions for adjacent segments of this island edge. Similar to the case of the Mn ML we observe edge states between the Mn BL and the trivial Ta substrate, see Fig. S8. However, due to the sample morphology only the

[001] edges of the elongated BL islands to the Ta substrate could be characterized.

The boundary between Mn ML and Mn BL

We have seen that both antiferromagnetic layers, the Mn ML and the Mn BL, show a superconducting gap and develop edge modes at the boundary to the trivial superconducting phase of the Ta substrate. This presents an opportunity to investigate the transition between the two different antiferromagnetic MSH systems. For the sample area indicated by the left rectangle in Fig. 3a we have measured the zero-bias $\mathrm{d}I/\mathrm{d}U$ intensity see Fig. 4a. We observe an increased zero-bias signal at the [001] edges between the Mn BL and the Mn ML, indicating that there is an edge mode between the two regions. We find that this edge state vanishes when the superconductivity is quenched by an external magnetic field (see Supplementary Note 6), verifying that it originates from the superconducting state. The occurrence of an edge mode at the boundary between these two MSHs suggests, that they are in different superconducting phases. Moreover, we observe two distinct intensities for this BL/ML edge mode: as seen in Fig. 4a the middle segment of the edge has a lower intensity than the ones on the left and right, which in turn have the same intensity as the edge shown in Fig. 4b (see right rectangle in Fig. 3a for its position and edge magnetization). This two stage contrast at zero-bias is correlated to the magnetization direction of the respective edges, compare Fig. 3a and Fig. 4a,b. We therefore conclude that our antiferromagnetic Mn film exhibits an edge mode at the BL/ML boundary, which shows a spin-polarization that is governed by the magnetization direction at the specific edge.

In order to characterize this spin-polarized low-energy edge mode between Mn ML and Mn BL we perform spatially-, spin-, and energy-resolved $\mathrm{d}I/\mathrm{d}U$ spectroscopy across two [001] edges with opposite spin orientations. Spectra taken on the two magnetically distinct [001] edges are shown in Fig. 4c, together with the spectra on the adjacent Mn ML and Mn BL, see inset. The spectra of both edges exhibit a peak-dip structure in the superconducting gap, but their intensity differs due to their different spin orientations. These spectra are part of a series of equidistant spectra across each edge, and the full datasets are displayed in Fig. 4d,e. Indeed, when moving from the BL (top) to the ML (bottom) we find that the $\mathrm{d}I/\mathrm{d}U$ intensity in the superconducting gap is significantly increased at the edges, with a clear maximum just below zero-bias and different signal strengths for the two oppositely magnetized edges. The difference due to the spin-polarization can more easily be seen in the asymmetry map displayed in Fig. 4f, where the difference of $\uparrow$ (Fig. 4d) and $\downarrow$ (Fig. 4e) divided by their sum is plotted as a function of position and energy. Whereas edge states have been observed before in two-dimensional MSH systems, they were located at the boundary between the magnetic TNPSC and the non-magnetic SC substrate [18, 21]. The existence of an edge mode at the boundary between what ap-

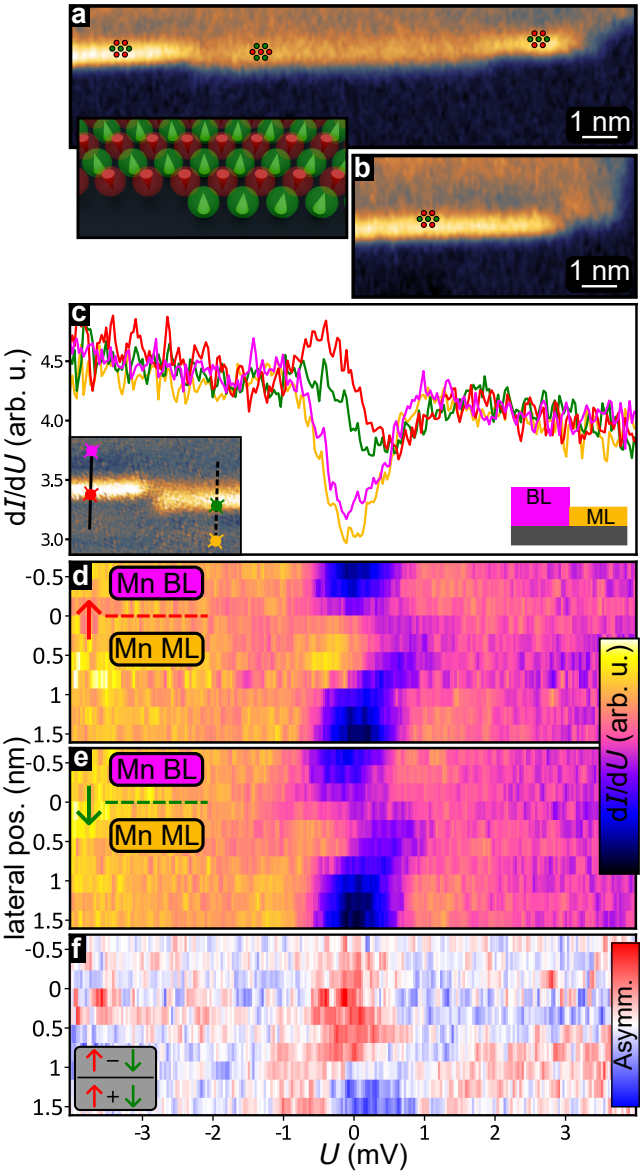

Figure 4. **Spin-polarized edge mode between ML and BL. a,b** Zero-bias $\mathrm{d}I/\mathrm{d}U$ maps at the sample areas indicated by black rectangles in Fig 3a (constant-height mode); red/green markers show the magnetization of the different segments of the [001] edge between ML and BL (to scale); inset sketches the edge magnetization across an atomic kink. **c,** Spectra of the ML, the BL, and the oppositely magnetized [001] edges; right inset shows a side view sketch of the sample, left insets shows the positions of the spectra in an SP-STM current map. **d,e,** Spatially-, spin-, and energy-resolved $\mathrm{d}I/\mathrm{d}U$ signal across [001] edges with opposite magnetization directions, see lines in inset to c; Each spectrum was normalized. Raw data in Fig S6. **f,** Calculated asymmetry of the data shown in d,e. Measurement parameters: a,b: $U = 0\,\mathrm{mV}$, $U_{\mathrm{mod}} = 50\,\mu\mathrm{V}$, $T = 1.3\,\mathrm{K}$, measured with the tip moving on a plane parallel to (110); c-e: stabilization bias $U_{\mathrm{s}} = +4\,\mathrm{mV}$, stabilization current $I_{\mathrm{s}} = 1\,\mathrm{nA}$, modulation bias $U_{\mathrm{mod}} = 50\,\mu\mathrm{V}$. Left inset in a: $U = +5\,\mathrm{mV}$, $I = 1\,\mathrm{nA}$; all: Cr-bulk tip, $\mathrm{T} = 1.3\,\mathrm{K}$.

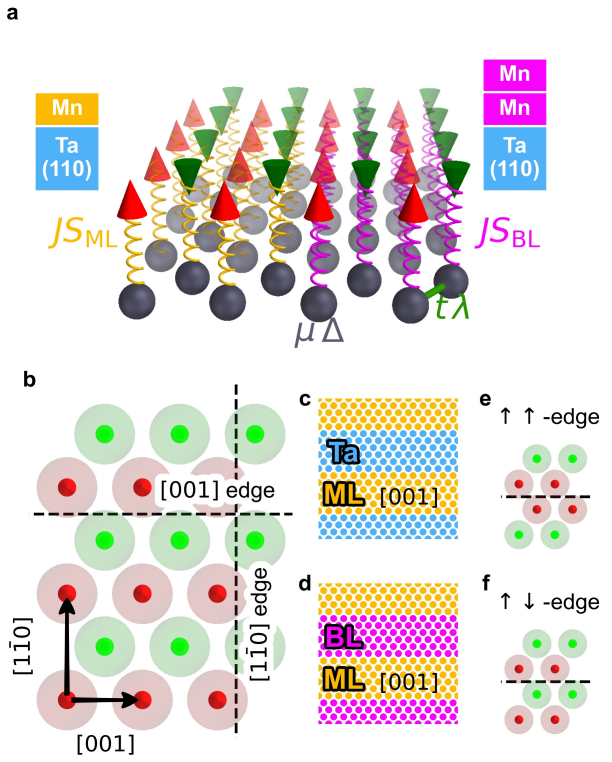

Figure 5. **Computational setup for the tight-binding model. a** Sketch of a magnetic layer containing an AFM state (cones) and a superconducting layer (spheres). Red and green cones represent the directions of the magnetic moments. The onsite parameters μ, Δ, which reflect the chemical potential and the superconducting order parameter, and the hopping parameter t as well as the Rashba-type SOC parameter λ are marked. The coupling between the magnetic and the superconducting layer is indicated by springs between the respective lattice sites. The coupling strength is denoted as JS_{ML} for the Mn/Ta(110) system and as JS_{BL} for Mn/Mn/Ta(110). The spatial transition from a ML system to a BL system is represented by a change in the local coupling, as marked by the springs of different colors. **b** Unit cell of the AFM state in the magnetic layer. Edges in two crystallographic directions are marked. **c** Stripe geometry for a ML stripe interfacing a trivial Ta domain. The stripes are periodic in $[001]$ direction and alternating in $[1\bar{1}0]$ direction. Each ML or Ta stripe has a width of 200 unit cells in the tight-binding calculation. **d** Sketch of a similar setup as in panel **c**, but here ML and BL stripes are alternating in the $[1\bar{1}0]$-direction. **e** ↑↑-edge in $[001]$ direction. **f** ↑↓-edge in $[001]$ direction.

pears to be two different magnetic TNPSCs –the antiferromagnetic Mn ML and BL in our case– raises questions about how the formation of such edge modes can be understood.

Tight binding model

The experiments demonstrate a low-energy spin-polarized edge mode between two different antiferromagnetic MHSs, represented by a Mn ML and a Mn BL on a Ta(110) surface. To understand the origin of this edge mode and its spin-dependent properties we use a tight-binding model. In the model we map all properties onto a single superconducting layer, which is influenced by the magnetization of the ML or BL via a coupling J to the spins S (Fig. 5a). Further model parameters are the chemical potential μ, the superconducting order parameter Δ, the hopping term t, and the Rashba-type SOC term λ. The Hamiltonian is given by

$$H = -\mu \sum_{i,\sigma} c^\dagger_{i,\sigma} c_{i,\sigma} + \Delta \sum_i (c^\dagger_{i,\uparrow} c^\dagger_{i,\downarrow} + c_{i,\downarrow} c_{i,\uparrow}) + t \sum_{i,j,\sigma} c^\dagger_{i,\sigma} c_{j,\sigma} - i \sum_{\mathbf{r}_i,\mathbf{r}_j,\sigma,\sigma'} \lambda_{\mathbf{r}_i,\mathbf{r}_j} c^\dagger_{\mathbf{r},\sigma} (\hat{e}_{\mathbf{r}_i - \mathbf{r}_j} \times \boldsymbol{\sigma}) c_{\mathbf{r}_j,\sigma'} + JS \sum_{i,\sigma,\sigma'} c^\dagger_{i,\sigma} (\hat{\mathbf{s}}_i \cdot \boldsymbol{\sigma}) c_{i,\sigma'} \quad (1)$$

where $c^\dagger_{i,\sigma}$ and $c_{i,\sigma}$ are the electronic creation and annihilation operators at the position $\mathbf{r}_i$ with spin σ, and $\boldsymbol{\sigma}$ is the vector of the Pauli spin matrices. The values for JS are motivated by the magnitude of the induced magnetic moments in the Ta layer as calculated by density functional theory for the Mn ML and Mn BL on Ta(110) (for details see Supplementary Note 7 and methods section), and a ratio of $JS_{\mathrm{ML}}/JS_{\mathrm{BL}} = 1.6$ is used while for the uncovered Ta surface we use $JS_{\mathrm{Ta}} = 0$. A sample with a boundary between different systems is modeled by a spatially varying coupling parameter JS (cf. Fig. 5a for an example of a boundary between Mn ML and Mn BL).

The geometry of the bcc(110) surface and the antiferromagnetic ground state of the Mn ML and BL are displayed in Fig. 5b. Based on the experimental findings together with previous theoretical investigations [18, 21] we have chosen a parameter set that ensures they are in a TNPSC phase (see methods section for a detailed discussion of the values). To model boundaries along the high-symmetry crystallographic directions between different surfaces we use a stripe geometry, where each stripe represents one material and is infinite in one direction, whereas the properties of the stripes alternate in the other direction. This ribbon geometry is sketched in Fig. 5c for an edge along the $[001]$ direction (cf. Fig. 5b) between the Mn ML and Ta. In the calculations each stripe has a width of 200 unit cells. For boundaries along $[1\bar{1}0]$ the stripes are oriented accordingly. To model a ML/BL boundary we use a stripe geometry with alternating BL and ML domains (Fig. 5d). In this case two different spin configurations at the boundary are possible: either the two layers terminate with the same spin direction (Fig. 5e), which leads to an ↑↑ edge at the boundary as in the case where the top layer of the BL is considered (see sketch in Fig. 3c); or the boundary continues the antiferromagnetic order resulting in a ↑↓ edge (Fig. 5f), which is realized in the lower Mn layer of the BL (see sketch in Fig. 3c).

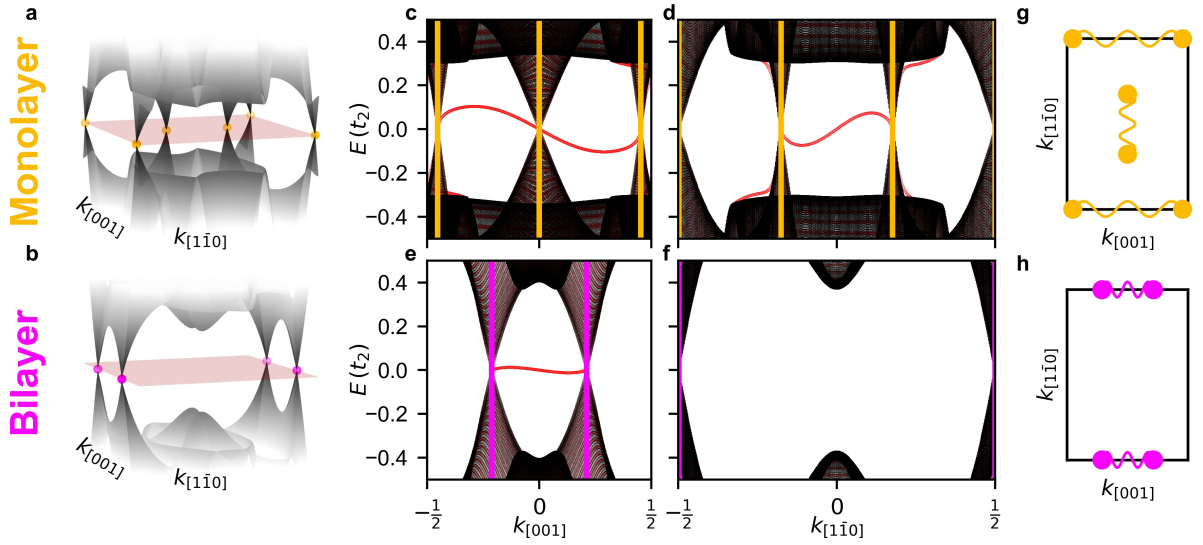

Figure 6. **Band structure calculations for monolayer and bilayer. a,b** Energy dispersion of the 2D-BZ around the Fermi energy for a Mn monolayer **a** and a Mn bilayer **b**. The red surface represents the Fermi energy and the colored round markers highlight the positions of the nodal points. **c-f** Projected band structures from an infinite sized sample (black) and the dispersion along the periodic direction of a stripe geometry (red). The dispersions are shown for the ML (**c,d**) and the BL (**e,f**). In both cases the magnetic domains are adjacent to Ta domains as sketched in Fig. 5c. **c, e** Band structure projected onto the $[001]$ direction of the 2D-BZ. The ribbon has an infinite length in the $[001]$ direction and a width of 200 magnetic unit cells in the $[1\bar{1}0]$ direction. **d, f** Band structure projected onto the $[1\bar{1}0]$ direction in which the ribbon is periodic in the same direction. The positions of the bulk nodal points from panels **a, b** are marked with vertical yellow (ML) and purple (BL) lines. **g, h** 2D-BZ with the positions of the nodal points marked. Nodal points, which are connected by edge states in the ribbon geometry are connected by curved lines.

Band structures and edge modes of MSH systems

First, we characterize the bulk properties of the ML and the BL by calculating their respective band structures (Fig. 6a,b). The ML exhibits six nodal points at the Fermi energy (red sheet) which are highlighted by yellow points. Two pairs of nodal points are located on the boundary of the two-dimensional Brillouin zone (2D-BZ) and one pair is located in the center (Fig. 6a). The BL has only two pairs of nodal points located on the boundary of the BZ (Fig. 6b). To identify whether these nodal points are topological we investigate boundaries from these TNPSC to the trivial Ta surface, where the occurrence of edge modes is a hallmark of topologically distinct properties. The bulk band structures of ML and BL, projected along the high symmetry direction of the 2D-BZ denoted by $k_{[001]}$, are shown in black in Figs. 6c,e. The red points mark the additional states arising for a stripe geometry along $[001]$ with a boundary of the ML or BL, respectively, to the trivial Ta surface (cf. Fig. 5c). For both systems, the ML and the BL, an edge state (red line) connects the two nodal points located on the boundary of the BZ, in agreement with the experimental observation of low energy modes at the boundaries between each layer and the Ta substrate. Similar stripe geometry calculations have been performed for the $[1\bar{1}0]$-direction and the corresponding projected band structures for the ML and BL are shown in Fig. 6d,f, respectively. In this crystallographic direction only the ML has an edge mode, which connects the two nodal points located in the middle of the 2D-BZ. The pairwise connection of nodal points by edge modes seen in Fig. 6c-f is summarized in Fig. 6g,h for the ML and BL, respectively. As all nodal points form pairs, connected by edge modes, we conclude that all nodal points are topological.

To investigate the boundary between the two different TNPSCs we create a pattern of alternating stripes of the ML and the BL with the stripes infinitely extended in the $[001]$-direction (Fig. 5d). To model the antiferromagnetically coupled Mn layers (cf. Fig. 3c), we assume the $\uparrow\uparrow$-edge (cf. Fig. 5e); note that similar results are found for a $\uparrow\downarrow$-edge (see Supplementary Figure S9). In the band structure along the $[001]$ direction (Fig. 7a) the positions of the nodal points obtained from the ML and BL bulk calculations (cf. Fig. 6) are marked by vertical yellow (ML) and purple (BL) lines. Due to the bulk-like properties in the wide stripes the same nodal points are also present in the stripe geometry. Two modes emerge around zero energy between nodal points (Fig. 7a). In contrast to the edge modes at an interface with a trivial phase (Fig. 6) these edge modes connect nodal points of the two different TNPSC systems, i.e. a ML nodal point is connected to a BL nodal point. This is qualitatively different to previous work on edge modes between TNPSC and trivial states [12, 18, 21]. Here we find edge states emerging between two different TNPSCs, which differ only in the coupling strength to the magnetic layer.

The spectral functions obtained in our tight-binding calcu-

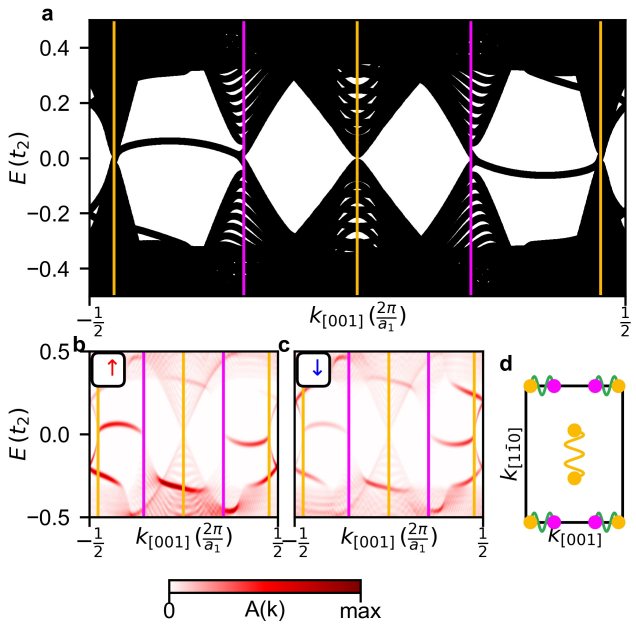

Figure 7. **Band structure for the ML/BL stripe geometry with an ↑↑ edge. a** Band structure along $k_{[001]}$ for ribbons, which are periodic in this direction. The positions of the nodal points from the ML bulk and the BL bulk are marked by vertical lines (cf. Fig- 6). **b,c** Spectral functions of the first two rows of the ML and the first two rows of the BL counting from the boundary. The spectral function is shown for the electron spin-up orbitals (**b**) and the electron spin-down orbitals (**c**). **d** Sketches of the 2D-BZ with the positions of the bulk nodal points of the ML and BL. Nodal points which are connected by edge modes for the $[001]$ or $[1\bar{1}0]$ geometry are indicated by wavy lines. For a ML/BL interface with an ↑↓ edge and a stripe geometry in the $[1\bar{1}0]$-direction see Supplementary Figures S9 and S10.

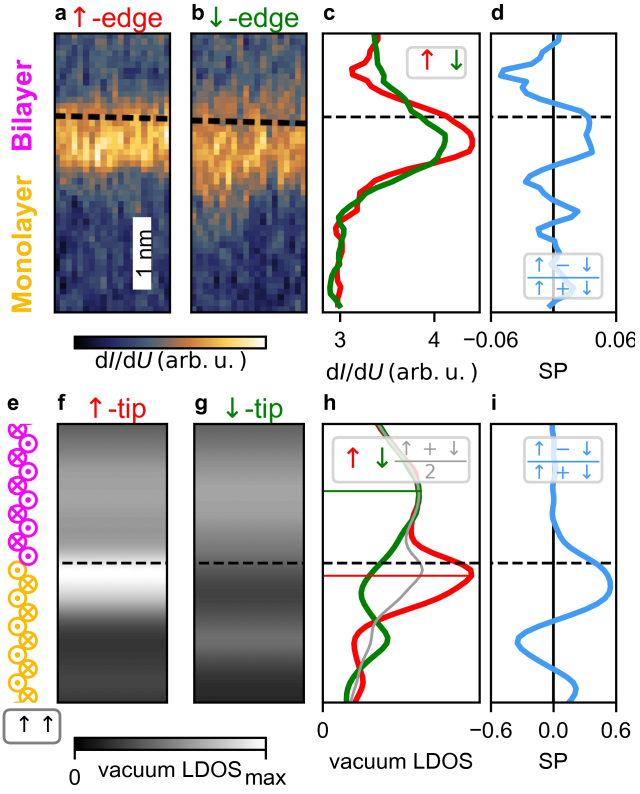

Figure 8. **Measured and simulated zero-bias SP-STM images for the ML/BL boundary with an ↑↑ edge. a,b** Zero bias $\mathrm{d}I/\mathrm{d}U$ maps of an ↑-edge and a ↓-edge between the BL(top) and ML(bottom) measured by retracing the topography measured at 4 mV. The black dashed lines shows the estimated edge position, see Fig. S6c for more information. **c** $\mathrm{d}I/\mathrm{d}U$ line profiles across the two edges in a,b created by averaging ten scan lines. **d** Calculated asymmetry between the two plots in c. **e** Sketch of the magnetic moment for a ↑↑ edge in the $[001]$-direction between the ML and BL. **f, g** Simulated zero-bias SP-STM contrast for a 100% spin polarized tip, which is ↑ polarized (**f**) or ↓ polarized (**g**).The boundary between both domains is displayed as a black dashed line. The tip height is 4 Å and the averaged voltage interval is $[-0.02, 0.02]$. **h** Integrated SP-STM signal along $[001]$ for spin-up (red), spin-down (green) and spin-averaged (gray). The position of the maximum intensity is marked by a thin solid line. **i** Spin polarization of the SP-STM signal calculated from the values shown in **h**.

lation for the four rows of atoms (two in the ML and two in the BL) located closest to the boundary are displayed in Fig. 7b,c for the spin-up (↑) and spin-down (↓) states, respectively. First, these graphs demonstrate that indeed these modes connecting NPs are located at the ML/BL boundary, and second, it can be seen that the ↑ and ↓ channels differ in their contribution to the edge mode (Fig. 7b,c), resulting in a finite spin-polarization. Some states outside of the superconducting gap also show a spin polarization. A spin polarization can also be seen for an edge along $[1\bar{1}0]$ (see Supplementary Figure S10).

In the experiments the BL/ML edge mode manifests as an increased $\mathrm{d}I/\mathrm{d}U$ signal at zero-bias compared to the bulk of the MSHs (Fig. 8a,b). The ↑-edge and the ↓-edge terminate with an opposite magnetic moment, and using the same magnetic tip the two edges have a different signal intensity, demonstrating that the edge mode is spin-polarized. In the line profiles across the edges in Fig. 8c it can be seen that the maximum intensity for each edge is located in the ML. The energy-dependent spin polarization $\mathrm{SP} = \frac{\uparrow-\downarrow}{\uparrow+\downarrow}$ is shown in Fig. 8d. To compare the experimental findings with the calculated edge states (cf. Fig. 7a) we have performed SP-STM simulations (Fig. 8f,g) based on the spin-polarized generalization of the Tersoff-Hamann model [26, 27]. In this model, the tunneling current is proportional to the spin-dependent local density of states (LDOS) at the position of the STM tip, i.e. in the vacuum (see methods for details on the STM simulation).

Using an ↑↑-edge (Fig. 5e and Fig. 7) we perform simulations for two opposite tip magnetization directions, which is equivalent to the case of two opposite edges measured with the same magnetic tip as in the experimental setup (Fig. 8a,b). For simplicity, we assume an ideal tip with a 100% spin polarization. In this case, the simulated SP-STM images for the two tip magnetizations (Fig. 8f,g) correspond to the vacuum

LDOS of the spin-up (↑) and spin-down (↓) channel (for simulations with a 50% tip spin-polarization see Supplementary Figure 11 and Supplementary Note 8). Comparison shows that the signal near the boundary is strongly spin-polarized, with the maximum intensity in the ↑ channel.

The line profiles of the two spin channels (Fig. 8h) show that the spin-up and the spin-averaged signal have their maximum intensity on the ML side, in agreement with the experimentally observed peak positions (Fig. 8c). The obtained spin polarization (Fig. 8i) also exhibits its maximum value on the ML side of the interface. When moving further into the ML the spin polarization is oscillating, while it is going to zero comparably fast in the BL. This indicates a different decay of the edge state into both MSH systems. Given the much smaller spin polarization of the experimental tip we find good qualitative agreement between the experimental and theoretical data, with an increased signal at the boundary shifted into the ML and a sizable spin polarization of this edge mode.

Spin-polarization of MSH edge modes

Based on the tight-binding model we can explain the existence of an edge state between two different TNPSC and its spin-polarization, and found good qualitative agreement with the experimental observations. However, two questions immediately arise: (i) why is the spin-polarized edge state shifted towards the ML side as seen in both experiment and theory (cf. Fig. 8) and (ii) how general is the result of the spin-polarized edge state, i.e. does it occur also for different boundary terminations and other model parameters. In correspondence with the experiment, we have so far discussed a boundary with an ↑↑-edge (Fig. 5e). However, in general an ↑↓-edge can also occur (Fig. 5f), e.g. for a buried step edge in the Ta; note that in the samples studied here the directions of the buried Ta step edges do not coincide with the [001] direction, preventing an experimental study of this boundary type. While the spin polarization at an ↑↑-edge seems rather intuitive, it is not obvious whether an edge mode at the ↑↓-edge can be spin-polarized as well (For a boundary between ML or BL and the Ta surface see Supplementary Figure 12).

To resolve this issue, we have performed tight-binding calculations for a ML/BL boundary with an ↑↓-edge (Fig. 9a). As seen from the spin-polarization of the vacuum LDOS (Fig. 9b) and the position dependent spin-averaged LDOS at the atoms (Fig. 9c) there is a spin-polarized edge state also at this boundary (for band structure see Supplementary Figure S9 and for SP-STM simulations see Supplementary Figure S13). Interestingly, the spin polarization of the LDOS is very similar for the ↑↓-edge (Fig. 9b) and the ↑↑-edge (Fig. 8i) and both curves show the characteristic shift towards the ML. The edge state decays exponentially in both directions and in addition displays oscillations in the ML (Fig. 9c), which leads also to an enhanced oscillation of the spin polarization in the ML (Fig. 9b). The effective decay constant is obtained from a fit to the spin-averaged LDOS of atom sites far from the boundary

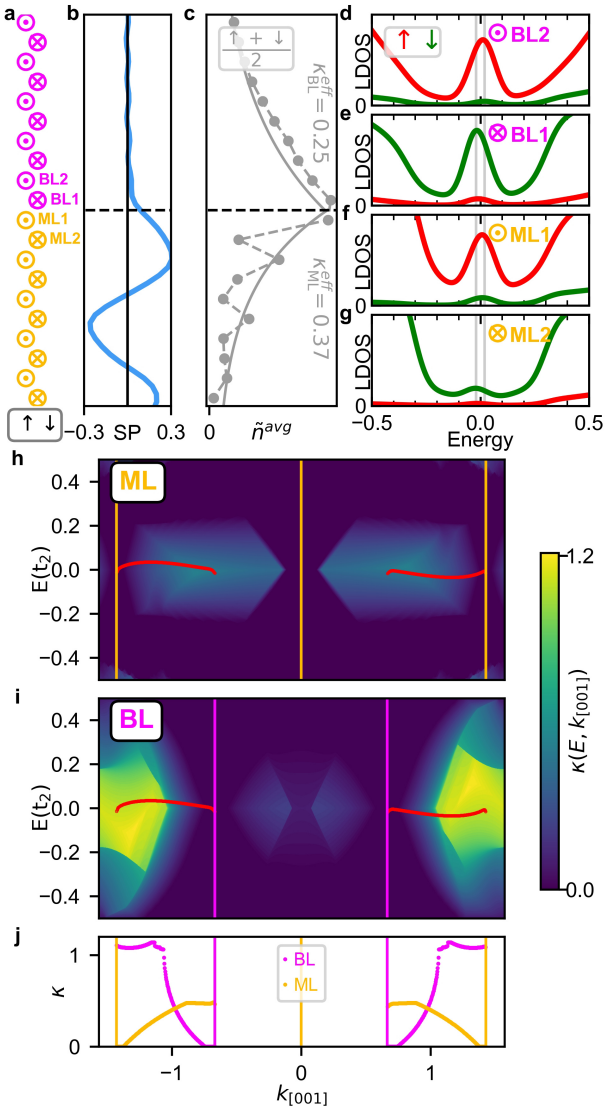

Figure 9. **LDOS for the ↑↓-edge and decay constants for surface states calculated from the complex band structure. a** Sketch of the spin structure close to the edge. **b** Spin polarization for the ↑↑-edge, calculated from the vacuum LDOS at 4 Å. **c** spin-averaged LDOS for lattice sites close to the boundary. The LDOS is integrated in an energy interval $E \in [-0.02, 0.02]$ around the Fermi energy. The solid line represents a fit, where the fitted decay values $\kappa^{\mathrm{eff}}_{\mathrm{BL}}$ and $\kappa^{\mathrm{eff}}_{\mathrm{ML}}$ are noted. The dashed line is a guide to the eye. **d-g** LDOS for the spin-up (red) and spin-down (green) orbitals for the lattice sites BL2, BL1, ML1, and ML2, respectively, as defined in (**a**). The energy window used for the integration in (**c**) is marked by vertical gray lines. **h,i** Decay constant $\kappa(E, k_{[001]})$ as a function of the energy E and the wave vector $k_{[001]}$ of a surface state. **h** Decay constants for the ML and **i** for the BL. The edge mode from the ML/BL boundary (cf. Fig. 7a) is marked in red. The positions of the bulk nodal points of the ML and BL (cf. Fig. 6) are indicated by purple and yellow lines. **j** Decay constants for the edge modes from (**h, i**).

(starting from the outermost atoms from the interface visible in Fig. 9c) and it is larger in the ML ($\kappa^{\text{eff}}_{\text{ML}} = 0.37$) than in the BL ($\kappa^{\text{eff}}_{\text{BL}} = 0.25$) (cf. Supplementary Figure S14 and Supplementary Note 9).

The spin-resolved LDOS displayed in Fig. 9d-f for the atom sites closest to the edge (denoted according to the sketch in Fig. 9a) demonstrates that the edge mode is highly spin-polarized in the direction of the respective magnetic moment. When comparing the different spin channels for these four lattice sites one can see that the $\uparrow$ channel dominates, leading to a net spin polarization in the LDOS. Both spin contributions can compensate on an atomic scale in the BL as the edge state is only slowly decaying (Fig. 9b). Due to the faster decay of the edge state into the ML, the spin termination on the ML side defines the spin polarization of the edge mode and the maximum spin polarization is shifted into the ML (Fig. 9b).

In the case of surface states it is known that their decay into the bulk is an intrinsic material property and can be calculated via the complex band structure [28]. In our system that corresponds to the decay of the edge mode into the two adjacent antiferromagnetic MSH films. The decay constants are calculated individually for the ML and the BL as they stem from the respective bulk band structures (for details see the methods section). Fig. 9f shows the decay constants $\kappa_{\text{ML}}(E, k_{[001]})$ for the ML, which are universal for all possible boundaries. The edge mode at the $\uparrow\downarrow$-edge is marked in red and the positions of the bulk nodal points are indicated by vertical yellow lines. The areas of vanishing κ (dark blue) coincide with the bulk band structure (cf. Fig. 6c) and indicate an infinite decay length. Finite values for κ represent states which lie in the projected bulk band gap, resulting in a faster exponential decay. For the ML, the states of the edge mode (red line) have a small κ at the ML NPs, and it increases when moving towards the position of the BL NPs (see Fig. 6h). The decay constants for the BL (Fig. 9g) show a similar correlation with the projected bulk band structure (cf. Fig. 6e). Also here the edge mode states have the smallest κ near the respective NP, in this case the BL NP, and increase towards the NPs of the other MSH system (the ML), see Fig. 6h. This k-dependent decay of the edge mode can also be seen in the spectral function (Supplementary Figure 15).

The total decay of the edge state into each MSH system is given by an integration of all $k_{[001]}$ contributions, weighted with the spectral function. While the explicit calculation of the decay length for the whole edge mode is quite tedious, an effective decay constant of the edge state is obtained by a fit as in Fig. 9c, which reveals an overall faster decay into the ML. Different decay lengths can be expected in general for boundaries between any two systems, due to their different electronic structures. Consequently, any edge mode between two TNPSCs is expected to have a net spin polarization, independent of the details of the boundary and its specific termination. At an $\uparrow\uparrow$-edge the spin polarization can be further enhanced by the parallel spin termination at the boundary.

DISCUSSION

The experimental observation of a spin-polarized edge mode between the antiferromagnetic Mn ML and BL on a superconductor can be explained by our tight-binding model. The edge states connect NPs from the different TNPSCs, which are located at different positions on the BZ boundary. To investigate how general this finding is we have varied the coupling strengths JS, thereby continuously decreasing the difference between the two neighboring MSH systems until they become identical (Supp. Fig. S16, Supp. Fig. S17, Supp. Fig. S18, Supp. Note 10). In this scenario, the NP structure of one MSH transitions into that of the other MSH. Interestingly, edge states emerge even for small differences in the coupling strengths and for the same number of nodal points in both MSHs. The emergent different electronic structures directly lead to different decay lengths of the edge mode into the two adjacent MSH systems. This in turn facilitates the development of a net spin-polarization of the edge mode.

Based on these findings the formation of spin-polarized edge states at the boundary between two TNPSCs is expected to be a general phenomenon. A lateral change in the band structure might also be achieved in a single TPNSC film by external means such as applying local strain or electric fields. For example, a gate could be fabricated which covers one part of the TNPSC. An applied voltage would then change the electronic structure below the gate with respect to the uncovered TNPSC, allowing the formation of a spin-polarized edge mode at the boundary between gated and non-gated parts of the MSH. The combination of two or more antiferromagnetic layers with the same superconducting substrate represents a potential next step in the investigation of MSHs. The tailoring of boundaries between regions hosting different topological phases creates new possibilities for the manipulation of topological edge modes. This represents a new direction in the investigation of MSHs and opens the path to new discoveries and advanced functional design.

METHODS

Sample preparation

The sample preparation and experiments were done in ultra-high vacuum. The Ta(110) single crystal surface was cleaned by heating to temperatures >2300 K. This removes the oxygen reconstruction and reveals the unreconstructed (110) surface. For more details see [29]. Mn was evaporated from a PBN Knudsen cell at a temperature of 690° C at a flux of approx. 0.2 atomic layers per minute. For samples including both the Mn ML and Mn BL, the Mn was deposited starting 8-10 min after the last flash annealing. This means the Ta crystal was still at elevated temperatures of approx. 100-200° C during the deposition. For samples with sub-monolayer coverage the Mn was deposited after the Ta crystal had cooled to room temperature. The samples were

then cooled down to 4.2 K or 1.3 K within the STM.

STM measurements.

The STM measurements were performed using a Cr bulk tip, etched in 1M HCl solution. The tip was first cleaned via field emission and subsequently sharpened by voltage pulses and tip-sample contact. Even though Cr is antiferromagnetic the apex of our tip is not always magnetic as it can be covered by non-magnetic material. Gentle tip-surface collisions were performed to pick up Ta or Mn atoms to make the tip superconducting or magnetic.

For maps of differential tunnel conductance and tunnel spectroscopy both the current and voltage offsets were adjusted until the current was zero at zero bias (or very close i.e. $< 5 - 10\,\mu$V). The $\mathrm{d}I/\mathrm{d}U$-signal was measured using lock-in technique by modulating the bias across the tunnel junction with a modulation amplitude U_{mod} and a frequency of 4777 Hz or 4675 Hz. For the superconducting tunnel spectroscopy measurements the tip was stabilized at a stabilization bias U_{s} and stabilization current I_{s} before switching off the feedback loop. For spectroscopy a time constant of 30 ms was used. For the zero-bias $\mathrm{d}I/\mathrm{d}U$ maps it was 10 ms.

Zero-bias $\mathrm{d}I/\mathrm{d}U$ maps were measured in two distinct ways: In constant-height mode the tip was stabilized at the stabilization parameters and the feedback loop was disabled. The tip was then scanned across the surface on a plane parallel to the Mn film, i.e. parallel to the (110) plane of the Ta. The tilt of the sample was corrected using topographic measurements. In multi-pass mode the constant-current topography of each line was first measured at 4 mV (outside the superconducting gap) and then replayed during the zero-bias scan. This allows for scanning of more corrugated surface topographies as compared to constant-height measurements.

Tight-binding calculations

For the tight-binding calculations we used the Hamiltonian given by Eq. (1). We assumed two-site interactions (hopping term and Rashba-type SOC) up to third nearest neighbors. The used parameters are $\mu = -3.8, \Delta = 1, t_1 = 1.1, t_2 = 1.0, t_3 = 0.9, \lambda_1 = 0.55, \lambda_2 = 0.5, \lambda_3 = 0.45, JS_{\mathrm{ML}} = 4.0, JS_{\mathrm{BL}} = 2.5$. The hopping parameters and the Rashba parameters decrease with increasing distance. These values were motivated by parameters used in Ref. [18]. The ratio of JS_{ML} and JS_{BL} is given by $\frac{JS_{\mathrm{ML}}}{JS_{\mathrm{BL}}} = \frac{0.204}{0.125} \approx 1.63$, which is the ratio of the induced magnetic moments in the top Ta layer as calculated by DFT (see Supplementary Note 7). In addition, the parameters μ, JS_{ML}, and JS_{BL} have been chosen such that the ML and BL have a different number of nodal points. As shown in our work, a different number of nodal points in the two adjacent TNPSC is not a necessary condition for the emergence of edge states, but it allows to showcase both types of occurring edge states. Further we have used parameters which lead to a small amount of states within the superconducting gap of the pure Ta substrate in accordance with the experimental observations (for more details see Supplementary Figure 19 and Supplementary Note 11).

SP-STM simulations

For the SP-STM simulations the spin-polarized generalization [26, 27] of the Tersoff-Hamann model [30] was applied. The tunneling current is given by

$$I(\mathbf{r}_{\mathrm{T}}, V_{\mathrm{B}}) \propto n_{\mathrm{T}} \tilde{n}_{\mathrm{S}}(\mathbf{r}_{\mathrm{T}}, V_{\mathrm{B}}) + \mathbf{m}_{\mathrm{T}} \tilde{\mathbf{m}}_{\mathrm{S}}(\mathbf{r}_{\mathrm{T}}, V_{\mathrm{B}}), \quad (2)$$

where $\mathbf{r}_{\mathrm{T}}$ is the position of the tip, V_{B} the bias voltage, n_{S} (n_{T}) is the vacuum LDOS of the sample (tip), and $\mathbf{m}_{\mathrm{S}}$ and $\mathbf{m}_{\mathrm{T}}$ are the respective magnetization DOS. The tilde indicates an integration over energy. As a zero-bias STM measurement has only a small AC bias voltage and no DC voltage, we integrate the LDOS in a small energy range of $-0.02t \leq E \leq 0.02t$ around the Fermi energy. From the tight-binding calculations the LDOS of the sample is only known at the lattice sites and not in the vacuum at the tip position. For the wave functions an exponential decay into the vacuum can be assumed and the contributions of all atom sites $\mathbf{r}_i$ to the LDOS at the tip position are summed [27]

$$\tilde{n}_{\mathrm{S}}(\mathbf{r}_{\mathrm{T}}, V) = \sum_i [\tilde{n}_i^{\uparrow}(V) + \tilde{n}_i^{\downarrow}(V)] \mathrm{e}^{-2\gamma|\mathbf{r}_{\mathrm{T}} - \mathbf{r}_i|} \quad (3)$$

where $\tilde{n}_i^{\sigma}(V)$ is the integrated LDOS of spin channel σ at lattice site $\mathbf{r}_i$ obtained from the tight-binding model and the decay constant $\gamma = \sqrt{\frac{2m\phi}{\hbar^2}}$ with the work function ϕ. For the magnetization DOS one obtains:

$$\tilde{\mathbf{m}}_{\mathrm{S}}(\mathbf{r}_{\mathrm{T}}, V) = \sum_i \mathbf{e}_i [\tilde{n}_i^{\uparrow}(V) - \tilde{n}_i^{\downarrow}(V)] \mathrm{e}^{-2\gamma|\mathbf{r}_{\mathrm{T}} - \mathbf{r}_i|} \quad (4)$$

where $\mathbf{e}_i$ is a unit vector denoting the local spin direction at atom site i. For the tip we assume a magnetization direction defined by $\mathbf{e}_{\mathrm{T}}$ and a spin polarization given by $P_{\mathrm{T}} = \frac{n_{\mathrm{T}}^{\uparrow} - n_{\mathrm{T}}^{\downarrow}}{n_{\mathrm{T}}^{\uparrow} + n_{\mathrm{T}}^{\downarrow}}$. We chose an in-plane lattice constant of $2.87607\,\text{Å}$ (see Supplementary Note 7) and a tip height of $4\,\text{Å}$. A value of $\gamma = 1.0\,\text{Å}^{-1}$ was used as the decay constant.

Spectral function

The spectral function can be calculated from the solutions for the wavefunctions $|\Psi_{n,\mathbf{k}}\rangle$ as

$$A_i(\mathbf{k}, E) = \sum_n \delta(E_{\mathbf{k}} - \epsilon_{n,\mathbf{k}}) \langle i|\Psi_{n,\mathbf{k}}\rangle \langle \Psi_{n,\mathbf{k}}|i\rangle \quad . \quad (5)$$

The index i differentiates between the lattice sites, the spin and between electrons and holes. For the calculation of the spectral function in Fig. 7 the contributions of four lattice sites were summed. The spin channels were considered individually and only electronic orbitals were considered.

Complex band structure

When assuming the wave vector to have a complex value, i.e. $\mathbf{k} = \mathbf{k}_{\mathrm{Re}} + \mathbf{k}_{\mathrm{Im}} = \mathbf{k}_{\mathrm{Re}} + i\boldsymbol{\kappa}$, the Bloch theorem has the form

$$\Psi_{n,\mathbf{k}}(\mathbf{r}) = \Psi_{n,\mathbf{k}_{\mathrm{Re}},\boldsymbol{\kappa}}(\mathbf{r}) = \underbrace{\mathbf{e}^{i\mathbf{k}_{Re}\cdot\mathbf{r}}}_{\text{periodic}} \cdot \underbrace{\mathbf{e}^{-\boldsymbol{\kappa}\cdot\mathbf{r}}}_{\text{decaying}} \cdot u_{n,\mathbf{k}}(\mathbf{r}) \quad . \quad (6)$$

Solving the Schrödinger equation

$$\hat{H}\Psi_{n,\mathbf{k}_{\mathrm{Re}},\boldsymbol{\kappa}} = E(\mathbf{k}_{\mathrm{Re}},\boldsymbol{\kappa})\Psi_{n,\mathbf{k}_{\mathrm{Re}},\boldsymbol{\kappa}} \quad (7)$$

therefore leads to $E(\mathbf{k}_{\mathrm{Re}},\boldsymbol{\kappa})$. Taking $\mathbf{k}_{\mathrm{Re}}$ as a parameter and inverting E yields $\boldsymbol{\kappa}(E,\mathbf{k}_{\mathrm{Re}})$. The calculation unit cell contained 200 magnetic unit cells in the $[1\bar{1}0]$-direction and one in the $[001]$ direction. In both directions periodic boundaries were assumed. Now $\mathbf{k}_{\mathrm{Re}}$ was only varied along $[001]$, leading to $k_{[001]}$. Due to the large unit cell in the $[1\bar{1}0]$ direction, the dispersion is nearly flat in this direction and can be neglected. $\boldsymbol{\kappa}$ is assumed to decay perpendicular to the surface, leaving $\kappa||[1\bar{1}0]$. The inversion of the function $E(\mathbf{k}_{\mathrm{Re}},\boldsymbol{\kappa})$ was performed numerically. For a given value of κ the characteristic decay length is given by its inverse $\tau = \frac{1}{\kappa}$. This is the distance after which the signal decays to a value of $\frac{1}{e}$.

REFERENCES

* Email: felix.zahner@uni-hamburg.de
† Email: nickel@physik.uni-kiel.de

[1] F. Wilczek, Majorana returns, Nature Physics **5**, 614 (2009).
[2] S. Nadj-Perge, I. K. Drozdov, J. Li, H. Chen, S. Jeon, J. Seo, A. H. MacDonald, B. A. Bernevig, and A. Yazdani, Observation of Majorana fermions in ferromagnetic atomic chains on a superconductor, Science **346**, 602 (2014).
[3] A. Palacio-Morales, E. Mascot, S. Cocklin, H. Kim, S. Rachel, D. K. Morr, and R. Wiesendanger, Atomic-scale interface engineering of Majorana edge modes in a 2D magnet-superconductor hybrid system, Science Advances **5** (2019).
[4] R. Lo Conte, J. Wiebe, S. Rachel, D. K. Morr, and R. Wiesendanger, Magnet-superconductor hybrid quantum systems: a materials platform for topological superconductivity, La Rivista del Nuovo Cimento **47**, 453 (2024).
[5] K. von Bergmann, A. Kubetzka, O. Pietzsch, and R. Wiesendanger, Interface-induced chiral domain walls, spin spirals and skyrmions revealed by spin-polarized scanning tunneling microscopy, Journal of Physics: Condensed Matter **26**, 394002 (2014).
[6] B. Huang, M. A. McGuire, A. F. May, D. Xiao, P. Jarillo-Herrero, and X. Xu, Emergent phenomena and proximity effects in two-dimensional magnets and heterostructures, Nature Materials **19**, 1276 (2020).
[7] J. Li, T. Neupert, Z. Wang, A. H. MacDonald, A. Yazdani, and B. A. Bernevig, Two-dimensional chiral topological superconductivity in Shiba lattices, Nature Communications **7**, 12297 (2016).
[8] S. Rachel, E. Mascot, S. Cocklin, M. Vojta, and D. K. Morr, Quantized charge transport in chiral majorana edge modes, Phys. Rev. B **96**, 205131 (2017).
[9] J. Bedow, E. Mascot, T. Posske, G. S. Uhrig, R. Wiesendanger, S. Rachel, and D. K. Morr, Topological superconductivity induced by a triple-q magnetic structure, Physical Review B **102**, 180504(R) (2020).
[10] E. Mascot, J. Bedow, M. Graham, S. Rachel, and D. K. Morr, Topological superconductivity in skyrmion lattices, npj Quantum Materials **6**, 6 (2021).
[11] D. Steffensen, M. H. Christensen, B. M. Andersen, and P. Kotetes, Topological superconductivity induced by magnetic texture crystals, Physical Review Research **4**, 013225 (2022).
[12] T. Kieu, E. Mascot, J. Bedow, R. Wiesendanger, and D. K. Morr, Topological nodal point superconductivity in checkerboard magnet-superconductor hybrid systems, Physical Review B **108**, L060509 (2023).
[13] F. Nickel and S. Heinze, Topological properties of magnet-superconductor hybrid systems due to atomic-scale non-coplanar spin textures, npj Spintronics **3**, 13 (2025).
[14] G. C. Ménard, S. Guissart, C. Brun, R. T. Leriche, M. Trif, F. Debontridder, D. Demaille, D. Roditchev, P. Simon, and T. Cren, Two-dimensional topological superconductivity in Pb/Co/Si(111), Nature Communications **8**, 2040 (2017).
[15] S. Kezilebieke, M. N. Huda, V. Va?o, M. Aapro, S. C. Ganguli, O. J. Silveira, S. G?odzik, A. S. Foster, T. Ojanen, and P. Liljeroth, Topological superconductivity in a van der Waals heterostructure, Nature **588**, 424 (2020).
[16] S. Nakosai, Y. Tanaka, and N. Nagaosa, Two-dimensional p-wave superconducting states with magnetic moments on a conventional s-wave superconductor, Physical Review B **88**, 180503 (2013).
[17] K. Mæland and A. Sudbø, Topological superconductivity mediated by skyrmionic magnons, Phys. Rev. Lett. **130**, 156002 (2023).
[18] M. Bazarnik, R. Lo Conte, E. Mascot, K. von Bergmann, D. K. Morr, and R. Wiesendanger, Antiferromagnetism-driven two-dimensional topological nodal-point superconductivity, Nat. Commun. **14**, 614 (2023).
[19] M. O. Soldini, F. Küster, G. Wagner, S. Das, A. Aldarawsheh, R. Thomale, S. Lounis, S. S. P. Parkin, P. Sessi, and T. Neupert, Two-dimensional Shiba lattices as a possible platform for crystalline topological superconductivity, Nature Physics **19**, 1848 (2023).
[20] J. Zeng, J. J. He, Z. Ning, D.-H. Xu, and R. Wang, Spin signature of majorana fermions in topological nodal-point superconductors, npj Quantum Mater. **10**, 1 (2025).
[21] R. Bruning, J. Bedow, R. Lo Conte, K. von Bergmann, D. K. Morr, and R. Wiesendanger, The non-collinear path to topological superconductivity, arXiv:2405.14673v1 (2024).
[22] M. Sato, Nodal structure of superconductors with time-reversal invariance and Z_2 topological number, Phys. Rev. B **73**, 214502 (2006).
[23] Y. Baum, T. Posske, I. C. Fulga, B. Trauzettel, and A. Stern, Gapless topological superconductors: Model Hamiltonian and realization, Phys. Rev. B **92**, 045128 (2015).
[24] A. P. Schnyder and P. M. R. Brydon, Topological surface states in nodal superconductors, Journal of Physics: Condensed Matter **27**, 243201 (2015).
[25] S. Heinze, M. Bode, A. Kubetzka, O. Pietzsch, X. Nie, S. Blügel, and R. Wiesendanger, Real-space imaging of two-dimensional antiferromagnetism on the atomic scale, Science **288**, 1805 (2000).

[26] D. Wortmann, S. Heinze, P. Kurz, G. Bihlmayer, and S. Blügel, Resolving complex atomic-scale spin structures by spin-polarized scanning tunneling microscopy, Phys. Rev. Lett. **86**, 4132 (2001).

[27] S. Heinze, Simulation of spin-polarized scanning tunneling microscopy images of nanoscale non-collinear magnetic structures, Applied Physics A **85**, 407 (2006).

[28] X. Dang, J. D. Burton, A. Kalitsov, J. P. Velev, and E. Y. Tsymbal, Complex band structure of topologically protected edge states, Phys. Rev. B **90**, 155307 (2014).

[29] T. Eelbo, V. Zdravkov, and R. Wiesendanger, STM study of the preparation of clean Ta(110) and the subsequent growth of two-dimensional fe islands, Surface Science **653**, 113 (2016).

[30] J. Tersoff and D. R. Hamann, Theory and application for the scanning tunneling microscope, Phys. Rev. Lett. **50**, 1998 (1983).

ACKNOWLEDGMENTS

K.v.B. gratefully acknowledges financial support from the Deutsche Forschungsgemeinschaft (DFG, German Research Foundation) via projects no. 402843438 and no. 552644472. S.H. gratefully acknowledges financial support from the DFG via project no. 555842692. R.W. acknowledges funding by the European Research Council (ERC Advanced Grant No. 786020).

AUTHOR CONTRIBUTIONS

F.Z. prepared the samples, performed the experiments, and together with K.v.B. and R.L.C. analyzed the data. F.N. developed the tight-binding model, performed the tight-binding calculations and STM simulations and analyzed the data together with S.H. T.D. performed the DFT calculations. F.Z., F.N., R.L.C., S.H., and K.v.B. wrote the manuscript. All authors discussed the data and contributed to the final manuscript.

Supplementary Information for: Spin-polarized edge modes between different magnet-superconductor-hybrids

Felix Zahner,[1,2,*] Felix Nickel,[3,2,†] Roberto Lo Conte,[4] Tim Drevelow,[3]
Roland Wiesendanger,[1] Stefan Heinze,[3,5] and Kirsten von Bergmann[1]

[1]*Department of Physics, University of Hamburg, Jungiusstraße 11, 20355 Hamburg, Germany*
[2]*These authors contributed equally: Felix Zahner, Felix Nickel*
[3]*Institut für Theoretische Physik und Astrophysik, Christian-Albrechts-Universität zu Kiel, D-24098 Kiel, Germany*
[4]*Zernike Institute for Advanced Materials, University of Groningen, The Netherlands*
[5]*Kiel Nano, Surface, and Interface Science (KiNSIS), University of Kiel, Germany*

(Dated: June 16, 2025)

EXPERIMENTS

Supplementary Note 1: Magnetization Direction

To identify the magnetization axis of the antiferromagnetic (AFM) states in the Mn monolayer (ML) and Mn bilayer (BL) we use a soft-magnetic Fe/W-tip that typically has an in-plane magnetization in zero field, and aligns its magnetization with applied magnetic field. At zero field we observe no magnetic contrast, see Fig. S1a,b for a constant-current topographic image and current map, respectively. Note that the periodic oscillation in the Mn ML near the buried Ta step edge (upper center of Fig. S1c) originate from standing electron waves with a period of about $0.9\,$nm at this bias voltage. Upon applying an out-of-plane magnetic field of $+2.5\,$T the fine lines, indicative of the AFM state, are seen in both the Mn ML and Mn DL, see Fig. S1b. At this value of applied magnetic field the tip magnetization aligns itself with the magnetic field and is therefore out of plane. Reversing the field to -2.5 T shows an inversion of the magnetic line contrast, see Fig. S1d. This inversion of magnetic contrast can be best seen by comparing the interference pattern of the standing electron waves on the ML and the stripe magnetic contrast in b and d.

Supplementary Note 2: Magnetic ground state of the Mn ML.

The ground state of the extended Mn ML is a spin spiral, where the magnetic moments rotate along $[001]$, similar to the one in the Cr monolayer on W(110) [1]. In the $[1\bar{1}0]$-direction the magnetic moments invert from one atomic row to the next, resulting in a line contrast in the SP-STM images. For the undisturbed Mn ML region at the top of Fig. S2, this contrast vanishes periodically as the magnetic moments rotate to be oriented perpendicular to the tip magnetization. After about $18\,$nm one spin spiral period is completed. However, in small Mn ML patches and in particular in the vicinity to the Mn BL the rotation of the spin spiral is suppressed and the magnetic state is a collinear AFM state, see lower region in Fig. S2. The two layers have a strict phase relation between them, suggesting strong antiferromagnetic interlayer exchange coupling between the two AFM states, see inset in Fig. S2b.

Supplementary Note 3: Mn ML bulk in-gap states

To investigate the effect of the rotation of the AFM spin spiral on the superconducting gap of the Mn ML we measured equally spaced tunneling point spectra along the 30 nm long red line marked in Fig. S3a. The result is plotted as a waterfall-plot in Fig. S3b. We do not observe any modulation inside the gap across distances larger than the spin-spiral period (18.5 nm), indicating that in-gap states for the in-plane and out-of-plane areas of the AFM spin spiral do not differ measurably. This is different for the Fe/Ta(110) system were a ferromagnetic spin spiral was found to lead to a modulation inside the superconducting gap with the spin-spiral period [2].

Supplementary Note 4: Mn ML edge state

To investigate the edge mode at the edges between Mn ML and Ta substrate, we measure the $\mathrm{d}I/\mathrm{d}U$ signal at zero bias by first tracing the topography at a bias voltage outside the superconducting gap, typically 4 mV, and then replaying this topography signal for the zero bias measurement (also called multi-pass). We can show that the measured edge mode of the Mn ML is related to the superconductivity, as the edge mode contrast vanishes when the superconductivity is quenched at 200 mT, but reappears upon switching off the magnetic field, see Fig. S4. The measured intensity at zero bias at the edge depends on the edge direction. We observe the highest intensity at the $[001]$ edges and a much lower intensity at the $[1\bar{1}1]$ and $[1\bar{1}0]$ edges. Comparing point spectra taken on the different edges as well as the bare Ta and the Mn ML we find a clear peak for the $[001]$ edge close to zero bias for both the sample area shown in the main text Fig. 2 as well as for the sample area shown in Fig. S4a.

Supplementary Note 5: Mn BL morphology

The thin film morphology of the 1.25 AL sample (see Fig. 3 main text) is shown in Fig. S5. Here the SP-STM current map from Fig. 3 in the main text is shown next to the corresponding constant-current topography image. Estimating the position of

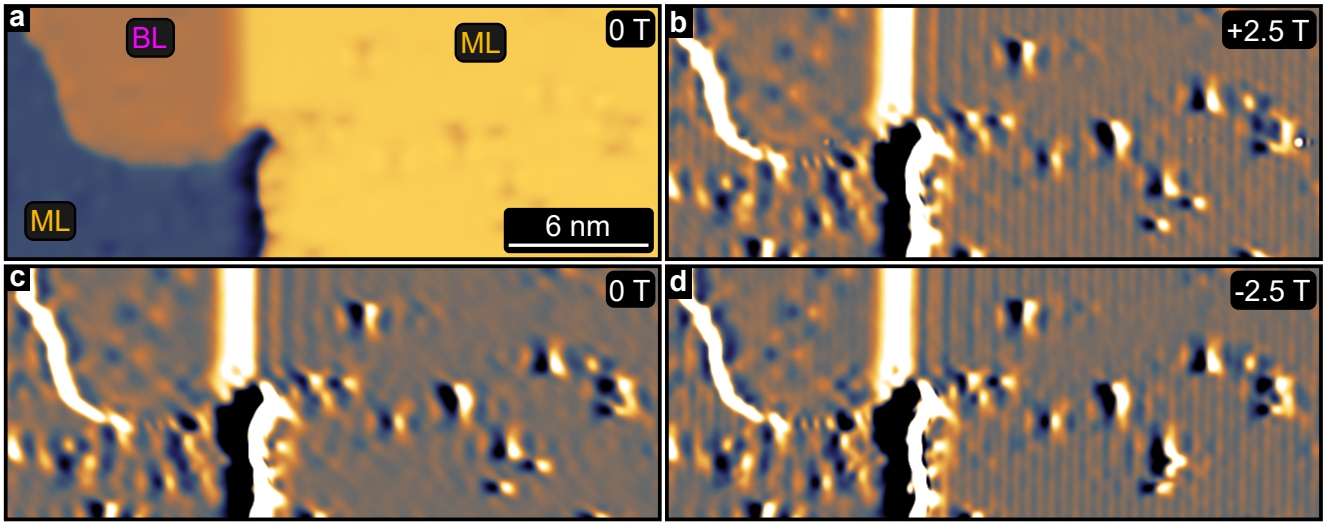

FIG. S1. **Magnetization Direction.**. **a,** STM topography image of a Mn BL area (top left) next to the Mn ML. **b-d,** STM current maps of the same area at the magnetic filed values indicated; because a soft magnetic Fe/W-tip is used the tip magnetization direction changes from in-plane in c, to opposite out-of-plane in b,d. High frequency noise was removed by low-pass filtering. Measurement parameters for all: $U = 10\,\mathrm{mV}$, $I = 1\,\mathrm{nA}$, Fe-coated W tip, $T = 8.7\,\mathrm{K}$.

the last row of atoms at the edge can be done by comparing the topography and simultaneously measured $\mathrm{d}I/\mathrm{d}U$ signal, see Fig. S6c. Here one needs to adjust for the delay of the $\mathrm{d}I/\mathrm{d}U$ signal due to the lock-in technique. The raw data from Fig. 4d,e in the main text is shown in Fig. S6a,b. For the figure in the main text each spectrum was normalized using the y-intercept of a line fitted to the data outside the gap.

Supplementary Note 6: Mn BL edge state

Similar to the edge mode at the boundary between Mn ML and Ta we find that the edge mode between Mn BL and Mn ML vanishes at an applied magnetic field of 200 mT, see Fig. S7. For each field value in Fig. S7b-d we show the topography, the zero bias multi-pass map and the zero bias constant height map. One can see an inversion in contrast in the topography for 200 mT compared to 0 mT seemingly indicating that the z-component of the tip magnetization has changed. This does, however, seem to happen at an unexpectedly low field. It seems more likely that the spin-polarization of the states near the Fermi energy is different for the superconducting and non-superconducting case. While we observe no contrast at the edge for the multi-pass mode at 200 mT we do observe a non-vanishing spin-polarized contrast in the constant height data at zero bias even when the superconductivity is quenched. This contrast is just a measurement of the spin-polarized LDOS near the Fermi-energy and similar to the contrast measured at the edges at a bias of 5 mV, see Fig. S5a. The difference between multi-pass and constant height data is not unexpected as the changing tip-sample distance in the multi-pass modes may exactly compensate this spin-polarization resulting in no observable contrast.

We performed zero bias measurements at the boundary between the Mn BL and the bare Ta substrate, see Fig S8. Constant height measurements across the vertical straight [001] edges show a strong $\mathrm{d}I/\mathrm{d}U$ signal at zero bias localized at the edge, see Fig. S8b,c. As we know the Ta substrate is in a trivial state, we conclude that the Mn BL is in a TNPSC phase. We have not observed straight edges between the Mn BL and Ta substrate along any other direction in our samples.

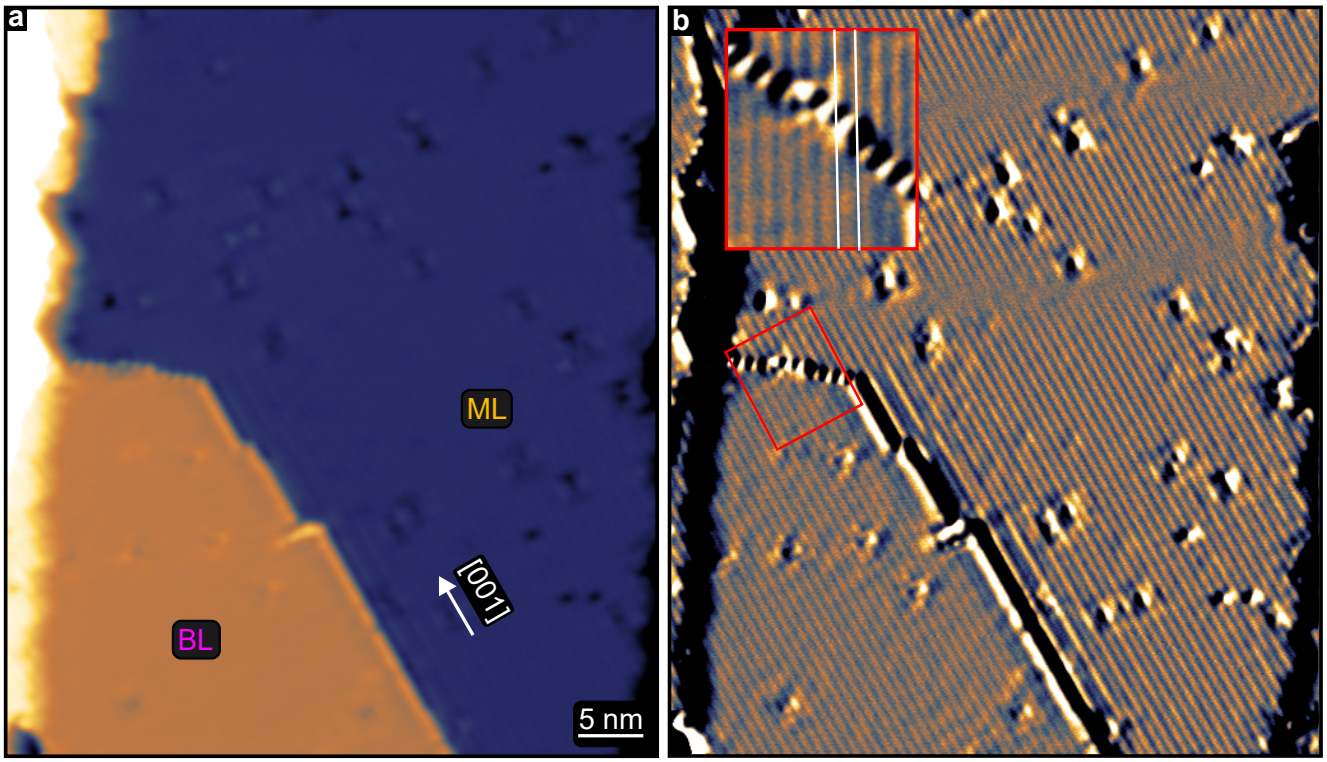

FIG. S2. **Magnetic ground state of the Mn ML. a,** STM constant-current topography image of a Mn BL area (bottom left) next to the Mn ML(right). **b,** Simultaneously measured STM current map of the same area showing magnetic contrast on both the BL and ML regions. Inset is a zoom-in of the area in the red rectangle. Measurement parameters for both: $U = -15\,\mathrm{mV}$, $I = 2\,\mathrm{nA}$, Cr bulk tip, $T = 4.2\,\mathrm{K}$.

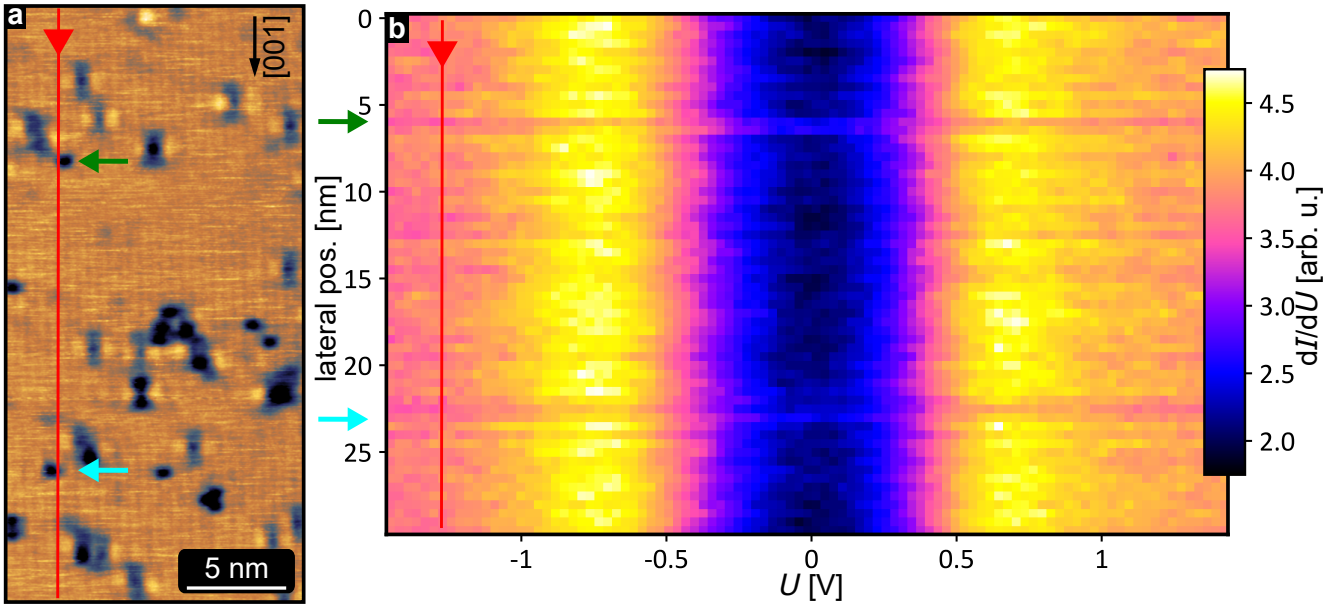

FIG. S3. **Tunneling spectra along a spin-spiral period. a,** STM current map of a Mn ML region showing the presence of the AFM spin-spiral with a period of 18.5 nm. **b,** 60 tunneling point spectra were taken along a 30 nm long red line shown in **a**. The green and cyan arrows indicate spectra taken near the defects marked by similar arrows in a. All spectra were taken with the following parameters: stabilization bias $U_\mathrm{s} = 4\,\mathrm{mV}$, stabilization current $I_\mathrm{s} = 1\,\mathrm{nA}$, modulation bias $U_\mathrm{mod} = 50\,\mu\mathrm{V}$, Cr bulk tip, $T = 1.3\,\mathrm{K}$.

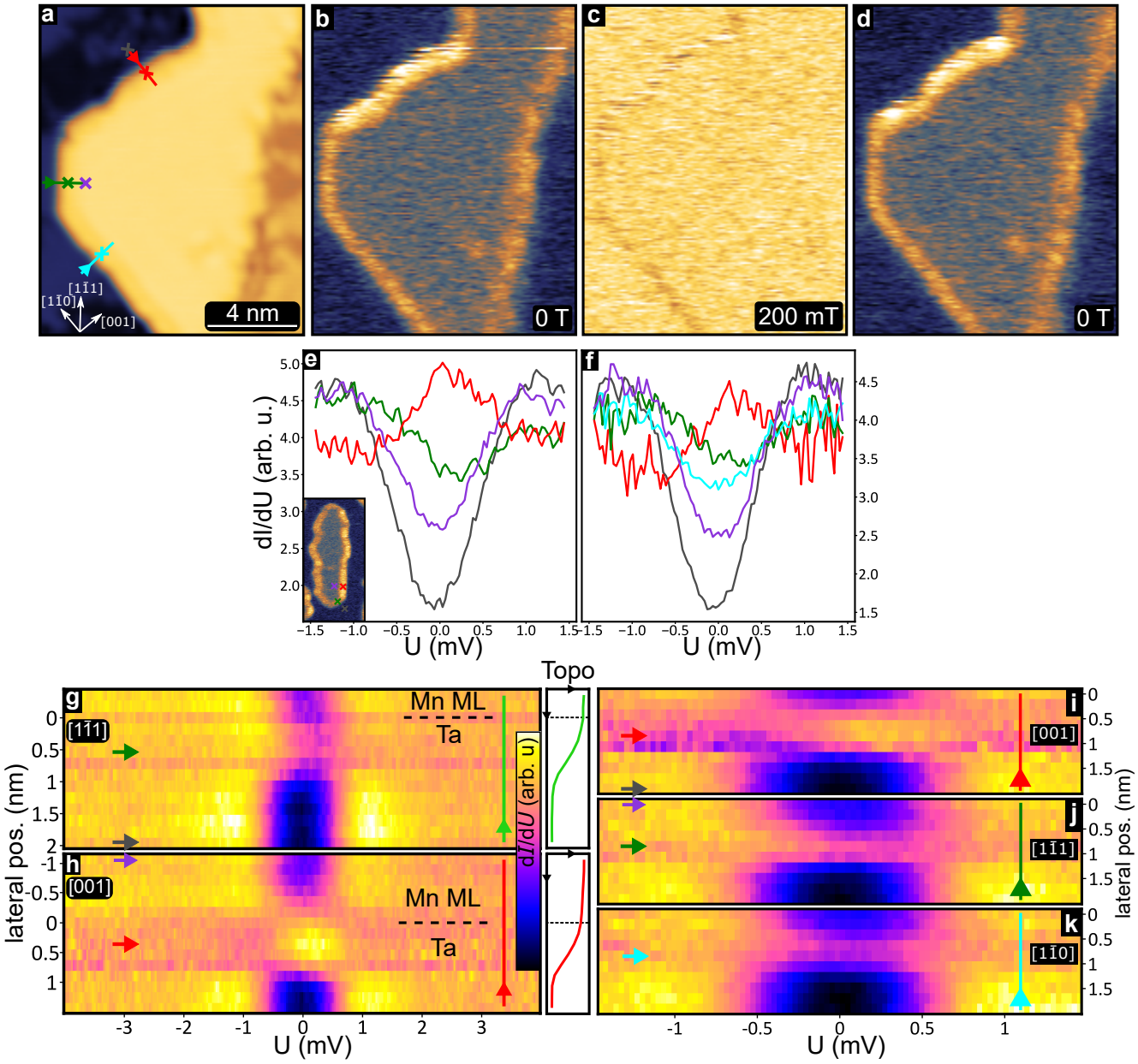

FIG. S4. **Mn ML edge state. a,** STM topography image of a Mn ML island grown from a Ta step edge. **b-d,** Maps of differential tunnel conductance ($\mathrm{d}I/\mathrm{d}U$) at zero bias of the same area as in (a) measured at the indicated applied magnetic field. **e,** Tunneling point spectra taken at the locations marked in inset (bottom left). Bare Ta (blue), Mn ML island (purple), [001]-edge (red) and [1$\bar{1}$1]-edge (green). **f,** Tunneling point spectra taken at the locations marked (cross) in (a). Bare Ta (blue), Mn ML island (purple), [001]-edge (red), [1$\bar{1}$1]-edge (green) and [1$\bar{1}$0]-edge (cyan). **g-h,** Raw data corresponding to the waterfall plots in Fig. 2d,e of the main text. For the main text figure each spectrum was normalized using the y-intercept of a line fitted to the data outside the gap. Graphs on the right show the height the tip was stabilized at before each spectrum, which was used to estimate the position of the last row of atoms at the ML edge. **i-k,** Waterfall plots of tunnel spectra taken along the colored lines marked in (a). Colored arrows indicate spectra shown in (e) and (f) recorded at the marked locations in (a). Measurement parameters: a-d: $U = 4\,\mathrm{mV}$, $I = 1\,\mathrm{nA}$, $U_{\mathrm{mod}} = 50\,\mu\mathrm{V}$; for all spectra: stabilization bias $U_{\mathrm{s}} = 4\,\mathrm{mV}$, stabilization current $I_{\mathrm{s}} = 1\,\mathrm{nA}$, modulation bias $U_{\mathrm{mod}} = 50\,\mu\mathrm{V}$; all: Cr bulk tip, $T = 1.3\,\mathrm{K}$.

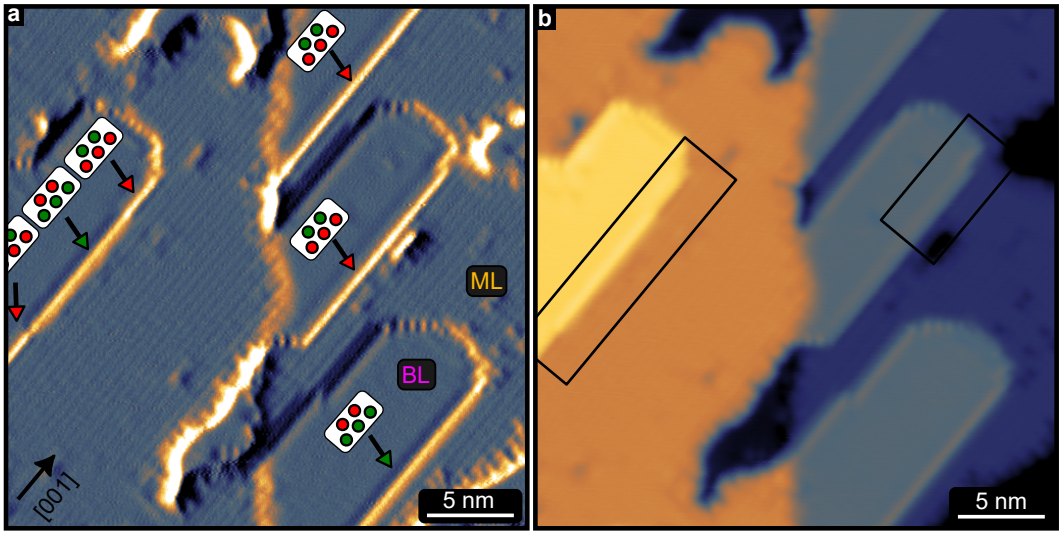

FIG. S5. **BL thin film morphology. a,** SP-STM current map of 1.25 AL of Mn on Ta(110), directly corresponding to Fig. 3a in the main text. **b,** Constant-current STM image of the same region as in a. Black rectangles indicate regions shown Fig. 3c,d in the main text. Measurement parameters: a,b: $U = +5$ mV, $I = 1$ nA, $T = 1.3$ K, Cr bulk tip.

THEORY

Supplementary Note 7: DFT calculations

Based on density functional theory (DFT) we have calculated the Ta bulk lattice constant and performed structural relaxations of the Mn ML and Mn BL on the Ta(110) surface using the VASP code [3–6] and applying the PBE [7] GGA exchange-correlation functional. The obtained theoretical Ta lattice constant was 3.321 Å which deviates by only 0.6% from the experimental value of 3.30 Å. Based on this lattice constant, a symmetric slab made from 13 Ta layers and with a (110) surface and a Mn ML/BL on each side was structurally relaxed to determine the interlayer distances. Relaxations were performed for the FM state and the RW-AFM state in each layer. For the BL, there was always an antiferromagnetic alignment between two Mn layers. The RW-AFM configurations are always preferred, by 243 meV/unit cell for the ML and 173 meV/unit cell for the BL. The interlayer distances between the Mn layers and the topmost Ta layers of the surface are given in Tab. I for the RW-AFM states of ML and BL. The magnetic moments obtained for the Mn and Ta surface layers are given in Tab. II. The calculated work function is 4.23 eV for the Mn ML on Ta(110) and 4.45 eV for the Mn BL on Ta(110).

ML		BL	
		$Mn_{top} - Mn_{bottom}$	1.430
$Mn - Ta_1$	1.869	$Mn_{bottom} - Ta_1$	1.857
$Ta_1 - Ta_2$	2.247	$Ta_1 - Ta_2$	2.237

TABLE I. **Interlayer distances for the Mn ML and BL on Ta(110).** The interlayer distances obtained from structural relaxations performed in DFT calculations between the Mn layers and the two topmost Ta layers of the surface. All values are given in Å.

ML		BL	
		Mn_{top}	2.74
Mn	2.78	Mn_{bottom}	1.03
Ta_1	0.21	Ta_1	0.15
Ta_2	0.02	Ta_2	0.04

TABLE II. **Magnetic moments for the Mn ML and BL on Ta(110).** The magnetic moments calculated via DFT are given for the Mn atoms (top and bottom layer for the BL) and for the two upmost Ta layers of the surface. All values are given in μ_B.

Supplementary Note 8: Tip spin polarization

For the SP-STM simulations shown in the main text (Fig. 8) we assumed a 100% spin polarization of the tip. Fig. S11 shows the same type of simulations as in the main text, but with a 50% spin polarization. In Fig. S11d the ↑ and the ↓ contributions approach the spin-averaged value. This leads to a small peak also in the ↓ signal close to the maximum of the spin polarization. The spin polarization in Fig. S11e displays a maximum value of 27% which is around half the value obtained for the 100% spin polarized tip cf. Fig. 8 of the main text). If one would assume a 7% tip polarization, the peak of the spin polarization would have about the same height as in the experiment. Note, that in this comparison the spin polarization incorporates the effect of a non-collinear alignment of the tip and sample magnetization direction. Therefore, the small value of the effective spin polarization needed for a quantitative agreement with the experiment still seems

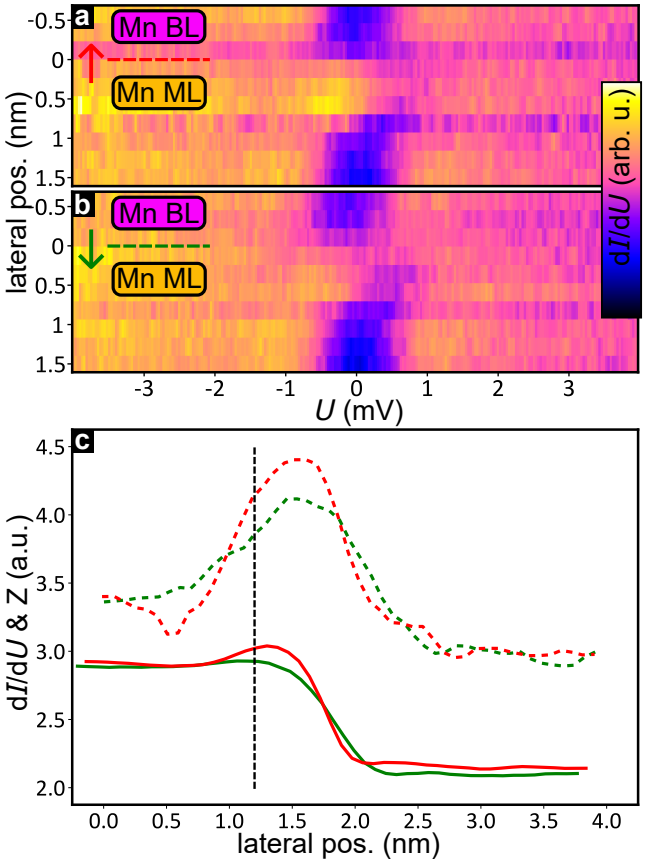

FIG. S6. **BL edge state. a-b,** Waterfall plots of tunneling spectra taken across two BL-ML edges with opposite magnetization., directly corresponding to Fig. 4c,d in the main text and plotted using the raw data here. Experimental parameters: stabilization bias $U_\mathrm{s} = 4\,\mathrm{mV}$, stabilization current $I_\mathrm{s} = 1\,\mathrm{nA}$, modulation bias $U_\mathrm{mod} = 50\,\mu\mathrm{V}$. **c,** Line profiles of the same edges measured in a $\mathrm{d}I/\mathrm{d}U$ map by retracing the topography measured at 4 mV. After adjusting for lock-in delay we can estimate the position of the last row of Mn atoms in the BL using the topography line profiles and compare them to the $\mathrm{d}I/\mathrm{d}U$ line profiles plotted using full/dotted lines respectively.

reasonable.

Supplementary Note 9: Lateral decay of the vacuum LDOS

In the main text the decay parameter is calculated for each surface state by the complex band structure (cf. Fig. 9). Further exponential functions are fitted to the spin-averaged LDOS at the lattice site. Here we discuss the fit to the lateral decay of the vacuum LDOS of the spin-up, spin-down and spin averaged data. Fig. S14 shows the integrated vacuum LDOS from Fig. S13. For each direction from the boundary we fit the function

$$A = A_0\,\mathrm{e}^{-\kappa^\mathrm{eff}(x-x_0)} + C \qquad (1)$$

to the vacuum LDOS. Here x represents the distance, x_0 is the position of the maximal value, A_0 is the amplitude and C an offset. The lateral decay of the vacuum LDOS towards the side of the BL or the ML is very similar to that at the lattice sites shown in the main text (Fig. 9c). The lateral decay parameter into the ML is around 0.36 and larger than that for the BL which is 0.26. Furthermore, the values are very similar between both spin channels and the spin-averaged signal. As expected from the complex band structure, the lateral decay seems not to depend on the spin channel. Also the decay of the edge state into the vacuum does not affect the lateral decay into the BL or ML. This shows that the intrinsic decay from the edge state is also detectable by STM.

Supplementary Note 10: transformation of nodal points

Topological nodal points are protected against spontaneous annihilation. The ML and BL are simulated by sets of parameters, which differ only in the value of JS. Therefore both systems can be transformed into each other by a continuous transformation of JS from $JS_\mathrm{BL} = 2.5$ to $JS_\mathrm{BL} = 4.0$. In Fig. S16 the positions of bulk nodal points are marked in the 2D-BZ, where the color encodes the value of JS. When the parameter is varied from 2.5 to 4.0 the nodal points on the boundary of the BZ shift further to the corner. These nodal points are considered equivalent nodal points, as they can be transformed into each other. At a critical value of $JS = 2.9$ two new nodal points form in the center of the BZ and split for an increased value of JS. These new nodal points, which exist in the ML have no equivalent correspondent in the BL.

The edge modes, which were observed in Fig. 7 of the main text, form between the equivalent nodal points on the boundary of the BZ. This shows, that edge modes cannot only occur, if the number of nodal points changes, but also if the nodal points are just slightly shifted in one domain. To test the robustness of the edge mode observed in Fig. 7 of the main text, Fig. S18 shows the band structure for a stripe geometry in the $[001]$ direction, where one domain is formed by the BL and in the other domain the parameter JS is varied. Fig. S18p corresponds to the same band structure as in the main text and Fig. S18a resembles the BL bulk band structure. For a value of $JS_\mathrm{mod} = 2.6$ the nodal points become wider and even for $JS_\mathrm{mod} = 2.7$ four distinct nodal points with edge states between them can be observed. For further increasing values of JS, the nodal points are separating more, while the edge mode is still connecting two equivalent nodal points. The emerging nodal points in the middle of the BZ for $JS \geq 2.9$ are not involved in the edge mode formation. Beside the edge modes in the $[001]$ direction, also a stripe geometry in $[1\bar{1}0]$ direction shows edge modes.

The band structure for a stripe geometry of alternating ML and BL stripes, equivalent to Fig. 7 of the main text, is shown in Fig. S10a. An edge mode connects the two bulk nodal points of the ML, indicated by yellow vertical lines. Differing for the stripes in $[001]$ direction, here two nodal points

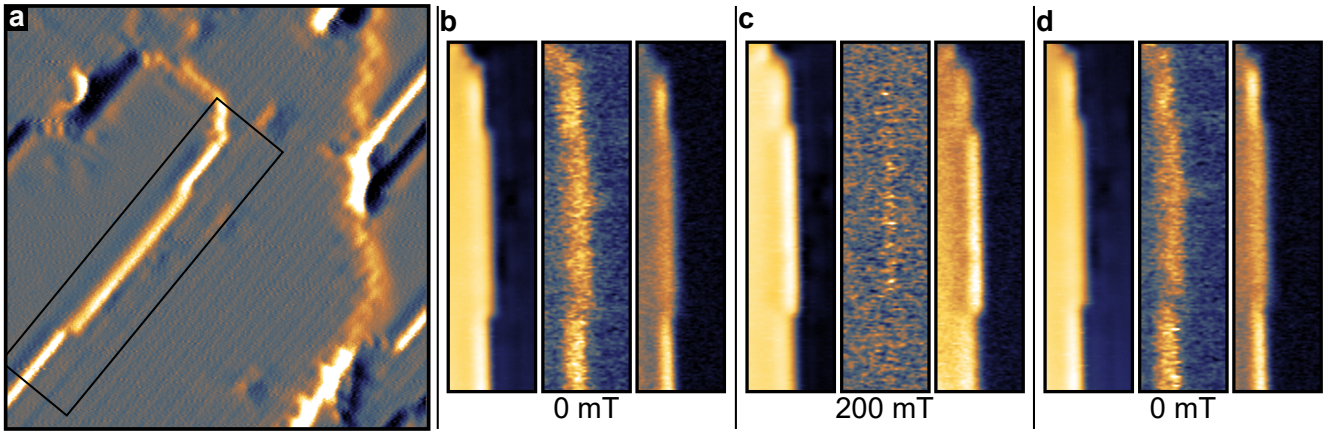

FIG. S7. **BL edge state in magnetic field. a,** SP-STM current image of an area of Mn BL (left) next to Mn ML; $U = 5\,\mathrm{mV}$, $I = 1\,\mathrm{nA}$. **b-d,** Mn BL edge along the [001] direction at 0 mT and 200 mT. For each field value the topography at 4 mV and 1 nA (left), $\mathrm{d}I/\mathrm{d}U$ at 0 mV (multi-pass, middle) and $\mathrm{d}I/\mathrm{d}U$ at 0 mV (constant height, right) are shown. All the $\mathrm{d}I/\mathrm{d}U$ maps were recorded with a bias modulation of $50\,\mu$V.

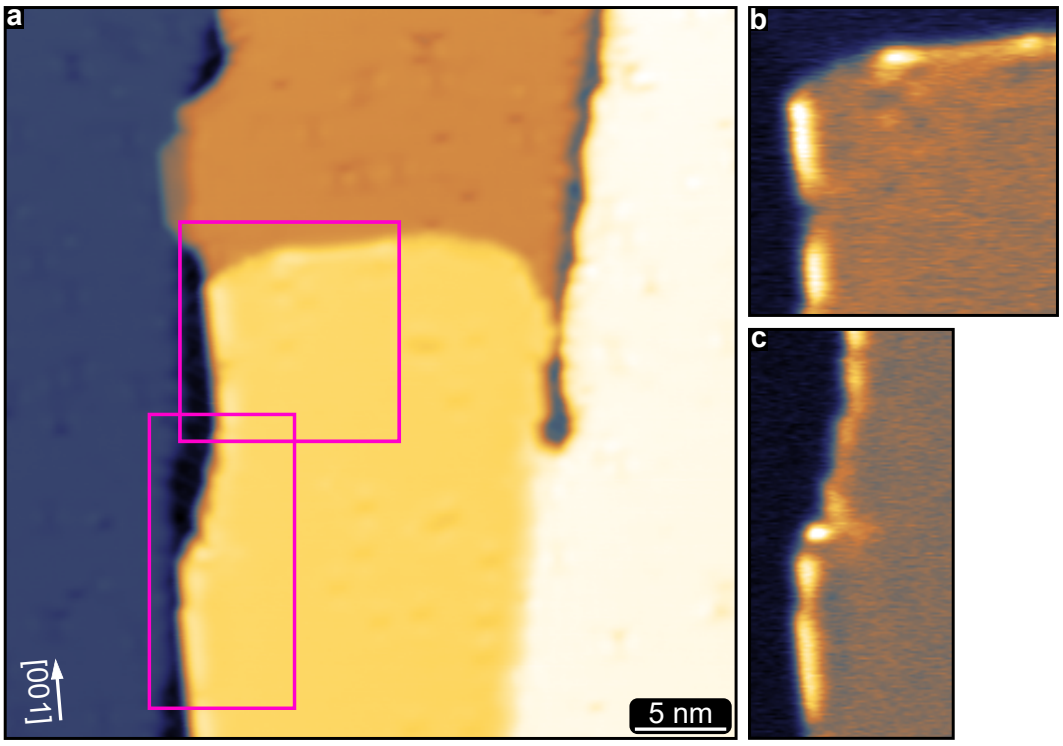

FIG. S8. **BL edge state at BL-Ta edge. a,** STM topography image of 1.25 ML of Mn on Ta(110). The regions within the pink rectangles show vertical edges from the BL directly to the bare Ta substrate running along the [001] direction. **b-c,** Constant height $\mathrm{d}I/\mathrm{d}U$ images measured in the regions of the pink rectangles in **a** at 0 mV. The tip was stabilized at 4 mV, 1 nA.

are connected which belong to the same domain. The spectral function at the boundary for electronic spin-up (↑) and spin-down (↓) orbitals are shown in Fig. S10b,c. Here it can be seen that the mode is indeed an edge mode and that it is spin-polarized. Thereby, it can be concluded that a spin-polarization of the edge mode can also occur when two nodal points of the same domain are connected as at the boundary to a trivial state. Fig. S10d summarizes the emerging edge modes from Fig. 7 of the main text and Fig. S10a.

The $[1\bar{1}0]$ boundary between the ML and the BL has an edge mode, similar to the edge mode between the ML and the bare Ta surface (cf. Fig. 6 of the main text). The ML nodal points in the middle of the BZ have no equivalent partner in the BL, as both nodal points meet and retract from the Fermi

surface at $JS = 2.9$. The edge modes between two TNPSCs can be of two types: (i) edge modes between equivalent nodal points (nodal points that can be transformed into each other) and (ii) edge modes between a pair of nodal points of one domain, when no equivalent nodal points exist. These edge modes also occur for boundaries to trivial states, as they host no topological nodal points and subsequently can not have equivalent nodal points. The novel implications of the first mechanism are that only a small local disturbance of one MSH system can lead to the formation of edge modes between perturbed and unperturbed regions. A spin polarization of the edge mode is a general effect that can be found in both scenarios. Both mechanisms can also be transformed into each other as shown in Fig. S17. Here, a stripe geometry is shown in $[1\bar{1}0]$ direction for a ML and a modified layer similar to Fig. S18. The parameter JS in the modified domain is varied in the range $2.5 \leq JS_{\mathrm{mod}} \leq 4.0$. Fig. S18a corresponds to the ML bulk. For increasing JS_{mod} the nodal points split and are connected by an edge mode of mechanism (i). At the value of $JS_{\mathrm{mod}} = 2.9$, two edge modes meet and vanish as JS_{mod}. Now the edge modes are connected and form a single edge mode connecting a pair of nodal points following mechanism (ii).

Supplementary Note 11: Choice of TB parameters

For the tight-binding (TB) calculations, we have used the hopping parameter t and the Rashba-SOC parameter α according to Ref. [8]. The superconducting order parameter has been set to $\Delta = 1$. For other spin structures it has been shown that the results are qualitatively robust against the superconducting order parameter [9, 10]. For the chemical potential μ and the coupling to the magnetic state JS three considerations were made: (1) The number of nodal points in the ML and the BL should differ. (2) The number of states in the band gap of the ML should change as little as possible for an orientation of the magnetic moments in the AFM state chosen along the $[001]$ (in-plane) and the $[110]$ (out-of-plane) direction. (3) The number of states for $JS \neq 0$ should be small compared to the band gap of Ta with $JS = 0$. Note that a different number of nodal points is not a necessary condition for the existence of edge modes as shown in the main text. However, if the ML and BL have a different number of nodal points, both types of edge states (between two ML nodal points and between ML and BL nodal points) can be observed. The second point is motivated by a spin spiral, observed in the experiment, where the $\frac{\mathrm{d}I}{\mathrm{d}U}$ signal is nearly constant along the spin spiral (see Fig. S3). The third condition relies also on experimental observations. Further the ratio of $\frac{JS_{\mathrm{ML}}}{JS_{\mathrm{BL}}} \approx 1.63$ is chosen according to the ratio of magnetic moments found via DFT.

Fig. S19a shows the number of nodal points in the BZ obtained in the tight-binding calculations as a function of chemical potential μ and coupling strength JS. The squared difference in the LDOS for an orientation of the magnetic moments

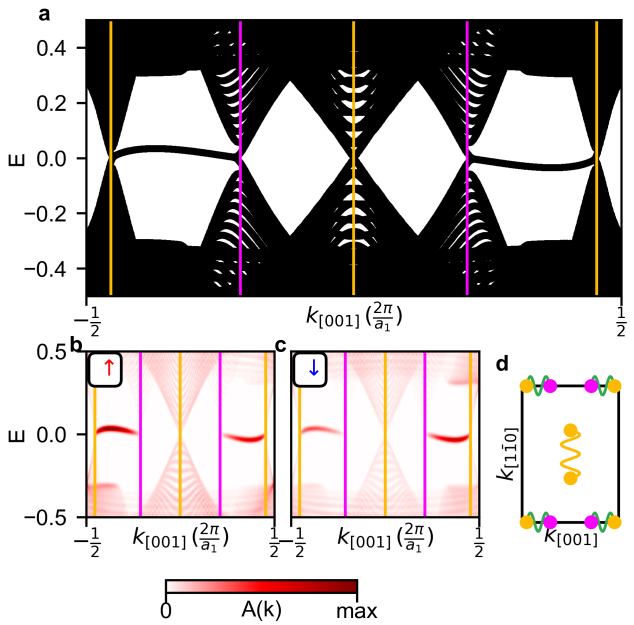

FIG. S9. **Band structure for the ML/BL stripe geometry with an ↑↓ edge.** **a** Band structure along $k_{[001]}$ for ribbons, which are periodic in this direction. The positions of the nodal points from the ML bulk and the BL bulk are marked by vertical lines (cf. Fig- 6 of the main text). **b,c** Spectral functions of the first two rows of the ML and the first two rows of the BL counting from the boundary. The spectral function is shown for the electron spin-up orbitals (**b**) and the electron spin-down orbitals (**c**). **d** Sketches of the 2D-BZ with the positions of the bulk nodal points of the ML and BL. Nodal points which are connected by edge modes for the $[001]$ or $[1\bar{1}0]$ geometry are indicated by wavy lines.

in the AFM state along the $[001]$ and a $[110]$ direction is given by

$$\zeta = \int_{-1}^{1} [n_{[001]}(E) - n_{[110]}(E)]^2 \mathrm{d}E \tag{2}$$

and is displayed in Fig. S19b. The integral over the LDOS within the band gap is calculated via

$$\eta = \int_{-1}^{1} [n_{[110]}(E)]^2 \quad dE. \tag{3}$$

and shown in Fig. S19c. The values ζ and η are smaller for $\mu < 0$ than for $\mu > 0$. For a value of $\mu = -3.8$ two values, $JS_{\mathrm{BL}} = 2.5$ and $JS_{\mathrm{ML}} = 4.0$, can be found with four and six nodal points. Thereby, all three conditions are fulfilled for this set of parameters.

* Email: felix.zahner@uni-hamburg.de
† Email: nickel@physik.uni-kiel.de

[1] B. Santos, J. M. Puerta, J. I. Cerda, R. Stumpf, K. von Bergmann, R. Wiesendanger, M. Bode, K. F. McCarty,

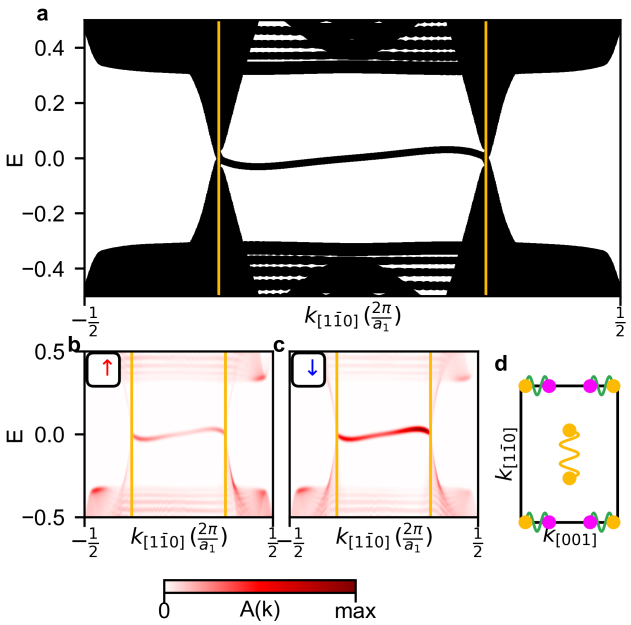

FIG. S10. **Band structure for the ML/BL stripe geometry along** $[1\bar{1}0]$**. a** Band structure along $k_{[1\bar{1}0]}$ for ribbons, which are periodic in this direction. The positions of the nodal points from the ML bulk and the BL bulk are marked by vertical lines (cf. Fig- 6 of the main text). **b,c** Spectral functions of the first two rows of the ML and the first two rows of the BL counting from the boundary. The spectral function is shown for the electron spin-up orbitals (**b**) and the electron spin-down orbitals (**c**). **d** Sketches of the 2D-BZ with the positions of the bulk nodal points of the ML and BL. Nodal points, which are connected by edge modes for the $[001]$ or $[1\bar{1}0]$ geometry are connected by wavy lines.

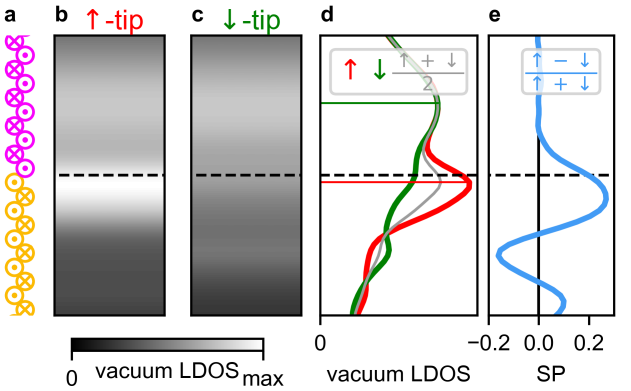

FIG. S11. **Simulated zero-bias SP-STM images for a ↑↑-edge at the ML/BL boundary with** 50% **tip polarization. a** Sketch of the magnetic moment for a ↑↑ edge in the $[001]$-direction between the ML and BL. **b, c** Simulated zero-bias SP-STM contrast for a 100% spin polarized tip, which is ↑ polarized (**b**) or ↓ polarized (**c**). The boundary between both domains is displayed as a black dashed line. The tip height is 4 Å and the averaged voltage interval is $[-0.02, 0.02]$. **d** Integrated SP-STM signal along $[001]$ for spin-up (red), spin-down (green) and spin-averaged (gray). The position of the maximum intensity is marked by a thin solid line. **e** Spin polarization of the SP-STM signal calculated from the values shown in **d**.

and J. de la Figuera, Structure and magnetism of ultra-thin chromium layers on w(110), New Journal of Physics **10**, 013005 (2008).
[2] R. Brüning, J. Bedow, R. Lo Conte, K. von Bergmann, D. K. Morr, and R. Wiesendanger, The non-collinear path to topological superconductivity, arXiv:2405.14673v1 https://doi.org/10.48550/arXiv.2405.14673 (2024).
[3] See `https://www.vasp.at`.
[4] G. Kresse and J. Furthmüller, Efficient iterative schemes for ab initio total-energy calculations using a plane-wave basis set, Phys. Rev. B **54**, 11169 (1996).
[5] G. Kresse and D. Joubert, From ultrasoft pseudopotentials to the projector augmented-wave method, Phys. Rev. B **59**, 1758 (1999).
[6] P. E. Blöchl, Projector augmented-wave method, Phys. Rev. B **50**, 17953 (1994).
[7] J. P. Perdew, K. Burke, and M. Ernzerhof, Generalized gradient approximation made simple, Phys. Rev. Lett. **77**, 3865 (1996).
[8] M. Bazarnik, R. Lo Conte, E. Mascot, K. von Bergmann, D. K. Morr, and R. Wiesendanger, Antiferromagnetism-driven two-dimensional topological nodal-point superconductivity, Nat. Commun. **14**, 614 (2023).
[9] J. Bedow, E. Mascot, T. Posske, G. S. Uhrig, R. Wiesendanger, S. Rachel, and D. K. Morr, Topological superconductivity induced by a triple-q magnetic structure, Physical Review B **102**, 180504(R) (2020).
[10] F. Nickel and S. Heinze, Topological properties of magnet-superconductor hybrid systems due to atomic-scale non-coplanar spin textures, npj Spintronics **3**, 13 (2025).

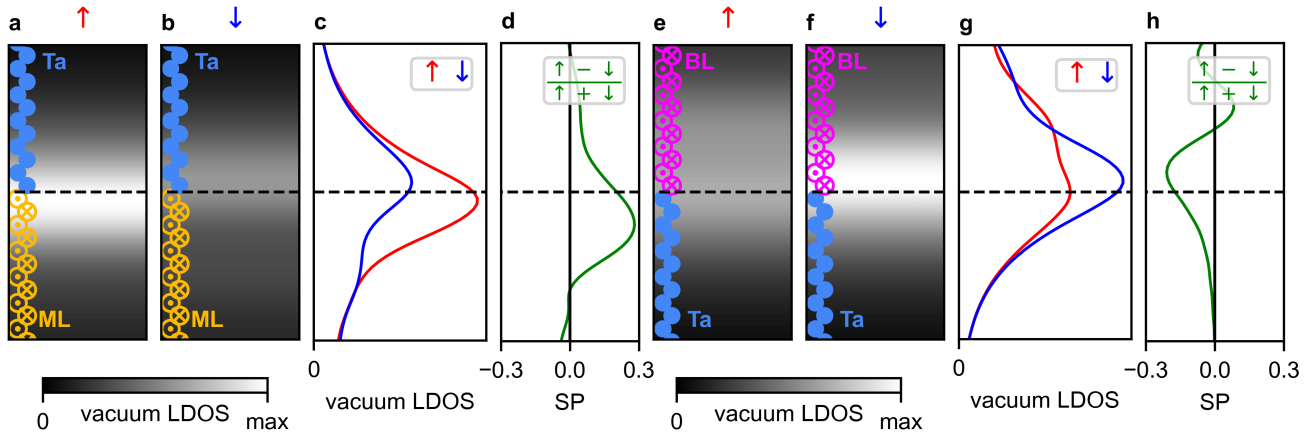

FIG. S12. **SP-STM simulations for the ML/Ta and BL/Ta edge. a-d** Simulations for a boundary between the ML and the bare Ta surface. **e-h** Simulations for a boundary between the BL and the bare Ta surface. **a+e** (**b+f**) show the spin-up (spin-down) contributions. **c+g** display the integrated signal and **d+h** the spin polarization. The simulations were performed for an energy range of $[-0.02, 0.02]$, reflecting zero-bias SP-STM measurements. SP-STM simulations for a ML (a, b, c) and a BL (d, e, f) adjacent to a Ta(110) surface.

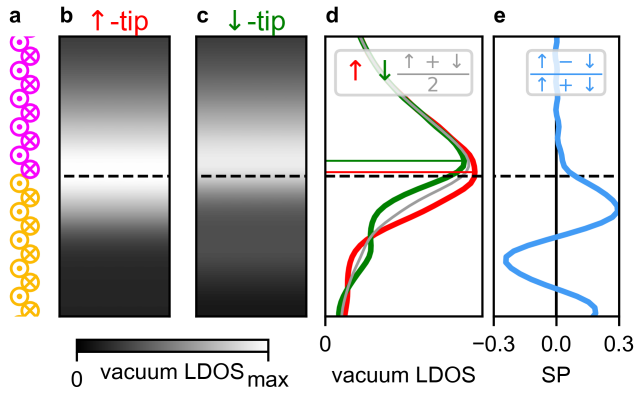

FIG. S13. **Simulated zero-bias SP-STM images for a ↑↓-edge at the ML/BL boundary. a** Sketch of the magnetic moments for a ↑↓ edge in the [001]-direction between the ML and BL. **b, c** Simulated zero-bias SP-STM contrast for a 100% spin polarized tip, which is ↑ polarized (**b**) or ↓ polarized (**c**). The boundary between both domains is displayed as a black dashed line. The tip height is 4 Å and the averaged voltage interval is $[-0.02, 0.02]$. **d** Integrated SP-STM signal along [001] for spin-up (red), spin-down (green) and spin-averaged (gray). The position of the maximum intensity is marked by a thin solid line. **e** Spin polarization of the SP-STM signal calculated from the values shown in **d**.

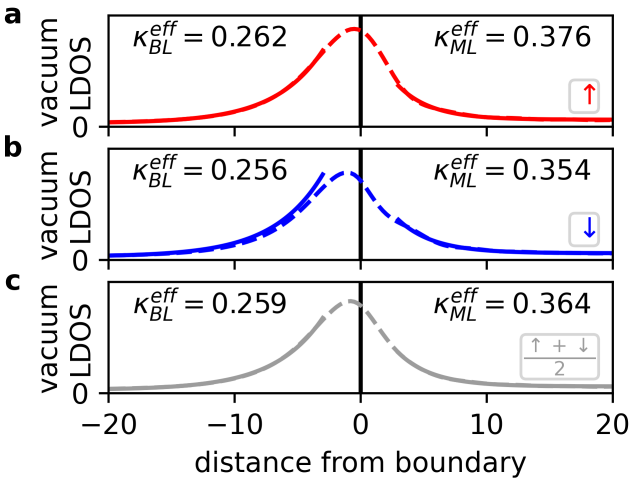

FIG. S14. **Vacuum LDOS for the ↑↓-edge at the ML/BL interface.** The vacuum LDOS from Supplementary Figure S13 is shown for the **a** spin-up channel, **b** spin-down channel and **c** spin averaged by a dashed line. An exponential function is fitted to the signal (solid line) individually in both directions from the boundary. The effective fit parameters are indicated.

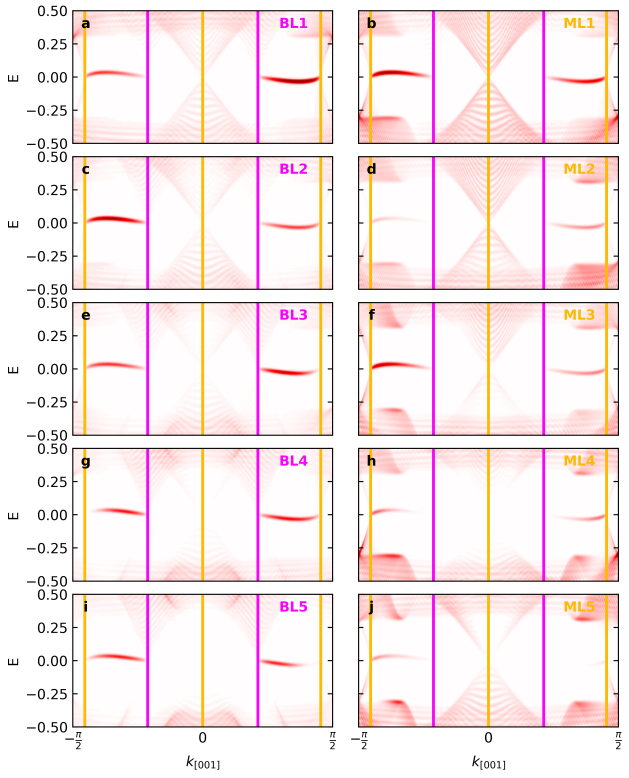

FIG. S15. **Spectral function for the ML/BL boundary with an ↑↓ edge.** The spectral functions of the electronic states (↑ + ↓) are shown for the five BL and ML atoms closest to the boundary of a stripe geometry in the $[1\bar{1}0]$ direction. The positions of the bulk nodal point are marked.

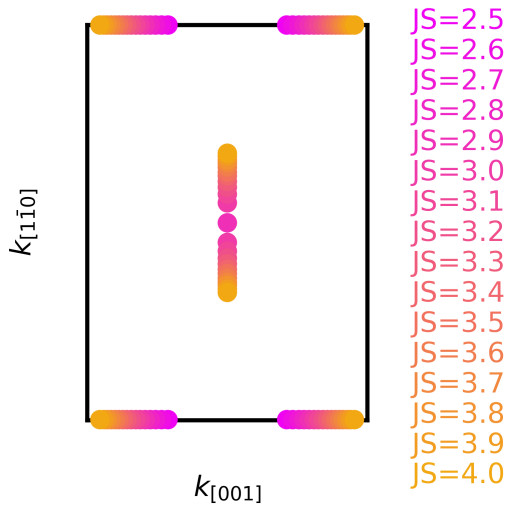

FIG. S16. **Position of nodal points.** The positions of nodal points, obtained from bulk calculations are marked in the 2D-BZ. The coupling to the magnetic layer is varied in the range $2.5 \leq JS \leq 4.0$. All other parameters are as described in the methods section of the main text. The parameters $JS = 2.5$ and $JS = 4.0$ correspond to the BL and ML, respectively. The varying parameters model therefore a continuous transformation from the BL to the ML.

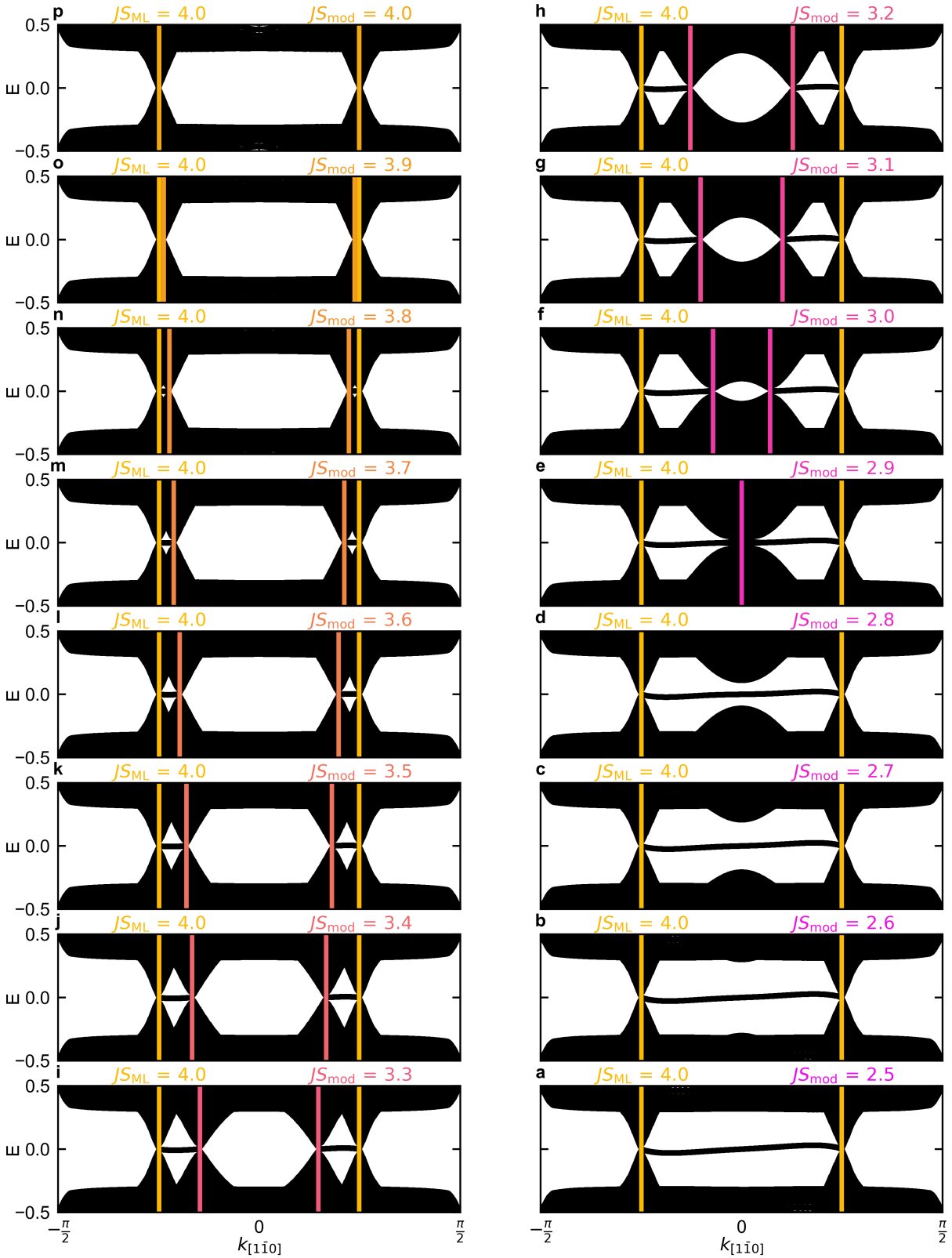

FIG. S17. **Band structures for a stripe geometry with an ↑↓ edge for alternating domains of ML and a modified layer with varied** $2.5 \leq JS_{\mathrm{mod}} \leq 4.0$**.** The value of JS_{mod} is varied from **a** to **f** in 0.1 increments. The stripe is oriented along the $[1\bar{1}0]$ direction. The position of the ML bulk nodal points and of the bulk nodal points of the modified layer (cf. Fig. S16) are marked by vertical lines.

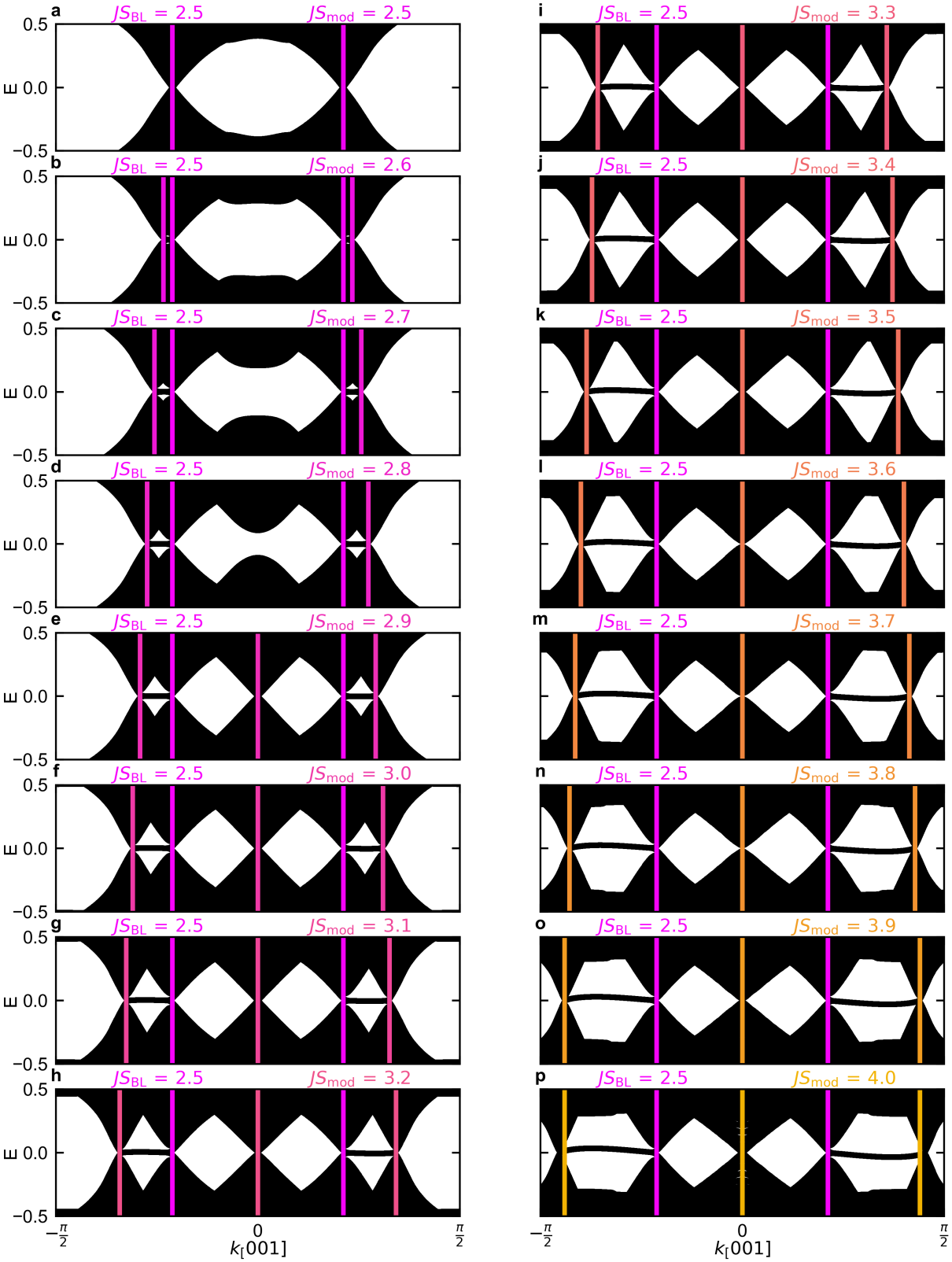

FIG. S18. **Band structures for a stripe geometry with an ↑↓ edge for alternating domains of BL and a modified layer with varied** $2.5 \leq JS_{\mathrm{mod}} \leq 4.0$**.** The value of JS_{mod} is varied from **a** to **f** in 0.1 increments. The stripe is oriented along the [001] direction. The position of the BL bulk nodal points and of the bulk nodal points of the modified layer (cf. Fig. S16) are marked by vertical lines.

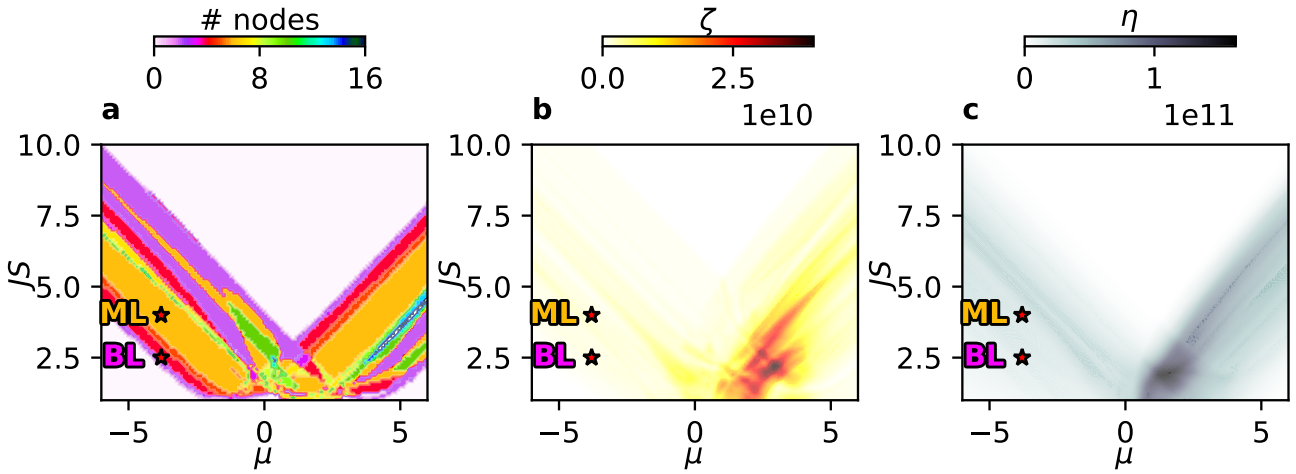

FIG. S19. **Nodal points and number of in-gap states in the tight-binding model for different parameters.** The chemical potential and the coupling to the magnetic state are varied between $-6 \leq \mu \leq 6$ and $1 \leq JS \leq 10$. (a) Number of nodal points in the BZ. (b) Difference ζ for a AFM state oriented along the [110] and the [001] direction. (c) Square of LDOS η within the Ta(110) bandgap for a AFM state in [110] direction. The stars mark the parameters used for the ML and the BL.

Bibliography

[1] P. Grünberg, R. Schreiber, Y. Pang, M. B. Brodsky, and H. Sowers, "Layered Magnetic Structures: Evidence for Antiferromagnetic Coupling of Fe Layers across Cr Interlayers", Phys. Rev. Lett. **57**, 2442–2445 (1986).

[2] M. N. Baibich et al., "Giant Magnetoresistance of (001)Fe/(001)Cr Magnetic Superlattices", Phys. Rev. Lett. **61**, 2472–2475 (1988).

[3] I. Žutić, J. Fabian, and S. Das Sarma, "Spintronics: Fundamentals and applications", Rev. Mod. Phys. **76**, 323–410 (2004).

[4] J. Brede, B. Chilian, A. A. Khajetoorians, J. Wiebe, and R. Wiesendanger. "Atomic-Scale Spintronics". In: Handbook of Spintronics. Ed. by Y. Xu, D. D. Awschalom, and J. Nitta. Dordrecht: Springer Netherlands, 2016, pp. 757–784. ISBN: 978-94-007-6892-5.

[5] S. Bader and S. Parkin, "Spintronics", Annual Review of Condensed Matter Physics, **1**, 71–88 (2010).

[6] A. Fert, "Nobel Lecture: Origin, development, and future of spintronics", Rev. Mod. Phys. **80**, 1517–1530 (2008).

[7] S. A. Wolf et al., "Spintronics: A Spin-Based Electronics Vision for the Future", Science, **294**, 1488–1495 (2001).

[8] B. Göbel, I. Mertig, and O. A. Tretiakov, "Beyond skyrmions: Review and perspectives of alternative magnetic quasiparticles", Physics Reports, **895**, 1–28 (2021).

[9] B. Behin-Aein, J.-P. Wang, and R. Wiesendanger, "Computing with spins and magnets", MRS Bulletin, **39**, 696–702 (2014).

[10] J. Grollier et al., "Neuromorphic spintronics", Nature Electronics, **3**, 360–370 (2020).

[11] D. P. DiVincenzo, "The Physical Implementation of Quantum Computation", Fortschritte der Physik, **48**, 771–783 (2000).

[12] M. AbuGhanem, "IBM quantum computers: evolution, performance, and future directions", The Journal of Supercomputing, **81**, 687 (2025).

[13] B. Schumacher, "Quantum coding", Phys. Rev. A, **51**, 2738–2747 (1995).

[14] F. Arute et al., "Quantum supremacy using a programmable superconducting processor", Nature, **574**, 505–510 (2019).

[15] M. Kjaergaard et al., "Superconducting Qubits: Current State of Play", Annual Review of Condensed Matter Physics, **11**, 369–395 (2020).

[16] B. Trauzettel, D. V. Bulaev, D. Loss, and G. Burkard, "Spin qubits in graphene quantum dots", Nature Physics, **3**, 192–196 (2007).

[17] D. Loss and D. P. DiVincenzo, "Quantum computation with quantum dots", Phys. Rev. A, **57**, 120–126 (1998).

[18] L. M. K. Vandersypen and M. A. Eriksson, "Quantum computing with semiconductor spins", Physics Today, **72**, 38–45 (2019).

[19] J. I. Cirac and P. Zoller, "Quantum Computations with Cold Trapped Ions", Phys. Rev. Lett. **74**, 4091–4094 (1995).

[20] S. A. Moses et al., "A Race-Track Trapped-Ion Quantum Processor", Phys. Rev. X, **13**, 041052 (2023).

[21] S. J. Devitt, W. J. Munro, and K. Nemoto, "Quantum error correction for beginners", Reports on Progress in Physics, **76**, 076001 (2013).

[22] D. G. Cory et al., "Experimental Quantum Error Correction", Phys. Rev. Lett. **81**, 2152–2155 (1998).

[23] J. Chiaverini et al., "Realization of quantum error correction", Nature, **432**, 602–605 (2004).

[24] V. Lahtinen and J. K. Pachos, "A Short Introduction to Topological Quantum Computation", SciPost Phys. **3**, 021 (2017).

[25] A. Kitaev, "Fault-tolerant quantum computation by anyons", Annals of Physics, **303**, 2–30 (2003).

[26] C. Nayak, S. H. Simon, A. Stern, M. Freedman, and S. Das Sarma, "Non-Abelian anyons and topological quantum computation", Rev. Mod. Phys. **80**, 1083–1159 (2008).

[27] R. Raussendorf, J. Harrington, and K. Goyal, "Topological fault-tolerance in cluster state quantum computation", New Journal of Physics, **9**, 199 (2007).

[28] D. Crawford, R. Wiesendanger, and S. Rachel, "Preparation and readout of Majorana qubits in magnet-superconductor hybrid systems", Phys. Rev. B, **110**, L220505 (2024).

[29] M. Sato and Y. Ando, "Topological superconductors: a review", Reports on Progress in Physics, **80**, 076501 (2017).

[30] V. Levajac et al., "Subgap spectroscopy along hybrid nanowires by nm-thick tunnel barriers", Nature Communications, **14**, 6647 (2023).

[31] M. Aghaee et al., "Interferometric single-shot parity measurement in InAs–Al hybrid devices", Nature, **638**, 651–655 (2025).

[32] V. Mourik et al., "Signatures of Majorana Fermions in Hybrid Superconductor-Semiconductor Nanowire Devices", Science, **336**, 1003–1007 (2012).

[33] R. M. Lutchyn, J. D. Sau, and S. Das Sarma, "Majorana Fermions and a Topological Phase Transition in Semiconductor-Superconductor Heterostructures", Phys. Rev. Lett. **105**, 077001 (2010).

[34] G. C. Ménard et al., "Two-dimensional topological superconductivity in Pb/-Co/Si(111)", Nature Communications, **8**, 2040 (2017).

[35] G. C. Ménard et al., "Isolated pairs of Majorana zero modes in a disordered superconducting lead monolayer", Nature Communications, **10**, 2587 (2019).

[36] A. Palacio-Morales et al., "Atomic-scale interface engineering of Majorana edge modes in a 2D magnet-superconductor hybrid system", Science Advances, **5**, eaav6600 (2019).

[37] J. J. Goedecke et al., "Correlation of Magnetism and Disordered Shiba Bands in Fe Monolayer Islands on Nb(110)", ACS Nano, **16**, 14066–14074 (2022).

[38] S. Kezilebieke et al., "Moiré-Enabled Topological Superconductivity", Nano Letters, **22**, 328–333 (2022).

[39] M. Bazarnik et al., "Antiferromagnetism-driven two-dimensional topological nodal-point superconductivity", Nature Communications, **14**, 614 (2023).

[40] D. Aasen et al. Roadmap to fault tolerant quantum computation using topological qubit arrays. 2025. arXiv: `2502.12252 [quant-ph]`.

[41] S. Heinze et al., "Spontaneous atomic-scale magnetic skyrmion lattice in two dimensions", Nature Physics, **7**, 713–718 (2011).

[42] A. Fert, N. Reyren, and V. Cros, "Magnetic skyrmions: advances in physics and potential applications", Nature Reviews Materials, **2**, 17031 (2017).

[43] A. N. Bogdanov and U. K. Rößler, "Chiral Symmetry Breaking in Magnetic Thin Films and Multilayers", Phys. Rev. Lett. **87**, 037203 (2001).

[44] N. Nagaosa and Y. Tokura, "Topological properties and dynamics of magnetic skyrmions", Nature Nanotechnology, **8**, 899–911 (2013).

[45] R. Wiesendanger, "Nanoscale magnetic skyrmions in metallic films and multilayers: a new twist for spintronics", Nature Reviews Materials, **1**, 16044 (2016).

[46] A. Soumyanarayanan et al., "Tunable room-temperature magnetic skyrmions in Ir/Fe/Co/Pt multilayers", Nature Materials, **16**, 898–904 (2017).

[47] N. Romming et al., "Writing and Deleting Single Magnetic Skyrmions", Science, **341**, 636–639 (2013).

[48] W. Legrand et al., "Room-Temperature Current-Induced Generation and Motion of sub-100 nm Skyrmions", Nano Letters, **17**, 2703–2712 (2017).

[49] W. Jiang et al., "Blowing magnetic skyrmion bubbles", Science, **349**, 283–286 (2015).

[50] A. Fert, V. Cros, and J. Sampaio, "Skyrmions on the track", Nature Nanotechnology, **8**, 152–156 (2013).

[51] F. Jonietz et al., "Spin Transfer Torques in MnSi at Ultralow Current Densities", Science, **330**, 1648–1651 (2010).

[52] H. Wang, Y. Dai, G.-M. Chow, and J. Chen, "Topological hall transport: Materials, mechanisms and potential applications", Progress in Materials Science, **130**, 100971 (2022).

[53] P. Bruno, V. K. Dugaev, and M. Taillefumier, "Topological Hall Effect and Berry Phase in Magnetic Nanostructures", Phys. Rev. Lett. **93**, 096806 (2004).

[54] R. Lo Conte, J. Wiebe, S. Rachel, D. K. Morr, and R. Wiesendanger, "Magnet-superconductor hybrid quantum systems: a materials platform for topological superconductivity", La Rivista del Nuovo Cimento, **47**, 453–554 (2024).

[55] S.-C. Chang and P. Hosur, "Spontaneous time-reversal symmetry breaking without magnetism in an $S = 1$ spin chain", Phys. Rev. B, **102**, 174404 (2020).

[56] S. Grytsiuk et al., "Topological–chiral magnetic interactions driven by emergent orbital magnetism", Nature Communications, **11**, 511 (2020).

[57] M. dos Santos Dias, J. Bouaziz, M. Bouhassoune, S. Blügel, and S. Lounis, "Chirality-driven orbital magnetic moments as a new probe for topological magnetic structures", Nature Communications, **7**, 13613 (2016).

[58] M. Gutzeit et al., "Nano-scale collinear multi-Q states driven by higher-order interactions", Nature Communications, **13**, 5764 (2022).

[59] M. Gutzeit, T. Drevelow, M. A. Goerzen, S. Haldar, and S. Heinze, "Spontaneous square versus hexagonal nanoscale skyrmion lattices in Fe/Ir(111)", Phys. Rev. B, **108**, L060405 (2023).

[60] M. Gutzeit. "Nanoscale spin structure as surfaces driven by exchange frustration and higher-order exchange interactions". dissertation. Christian-Albrechts-University Kiel, 2023.

[61] S. Paul, S. Haldar, S. von Malottki, and S. Heinze, "Role of higher-order exchange interactions for skyrmion stability", Nature Communications, **11**, 4756 (2020).

[62] D. Steffensen, M. H. Christensen, B. M. Andersen, and P. Kotetes, "Topological superconductivity induced by magnetic texture crystals", Phys. Rev. Res. **4**, 013225 (2022).

[63] M. Leijnse and K. Flensberg, "Introduction to topological superconductivity and Majorana fermions", Semiconductor Science and Technology, **27**, 124003 (2012).

[64] E. Majorana, "Teoria simmetrica dell'elettrone e del positrone", Il Nuovo Cimento (1924-1942), **14**, 171–184 (1937).

[65] F. Wilczek, "Majorana returns", Nature Physics, **5**, 614–618 (2009).

[66] P. Wölfle, "Quasiparticles in condensed matter systems", Reports on Progress in Physics, **81**, 032501 (2018).

[67] L. N. Cooper, "Bound Electron Pairs in a Degenerate Fermi Gas", Phys. Rev. **104**, 1189–1190 (1956).

[68] A. Y. Kitaev, "Unpaired Majorana fermions in quantum wires", Physics-Uspekhi, **44**, 131 (2001).

[69] R. S. K. Mong and V. Shivamoggi, "Edge states and the bulk-boundary correspondence in Dirac Hamiltonians", Phys. Rev. B, **83**, 125109 (2011).

[70] T. Fukui, K. Shiozaki, T. Fujiwara, and S. Fujimoto, "Bulk-Edge Correspondence for Chern Topological Phases: A Viewpoint from a Generalized Index Theorem", Journal of the Physical Society of Japan, **81**, 114602 (2012).

[71] L. P. Gor'kov and E. I. Rashba, "Superconducting 2D System with Lifted Spin Degeneracy: Mixed Singlet-Triplet State", Phys. Rev. Lett. **87**, 037004 (2001).

[72] A. Mackenzie and Y. Maeno, "p-wave superconductivity", Physica B: Condensed Matter, **280**, 148–153 (2000).

[73] S. Nakosai, Y. Tanaka, and N. Nagaosa, "Two-dimensional *p*-wave superconducting states with magnetic moments on a conventional *s*-wave superconductor", Phys. Rev. B, **88**, 180503 (2013).

[74] D. Crawford, E. Mascot, D. K. Morr, and S. Rachel, "High-temperature Majorana fermions in magnet-superconductor hybrid systems", Phys. Rev. B, **101**, 174510 (2020).

[75] D. Crawford et al., "Majorana modes with side features in magnet-superconductor hybrid systems", npj Quantum Materials, **7**, 117 (2022).

[76] H. Jang et al. Robustness of Majorana modes to potential disorder in Fe chains on a superconducting Rashba alloy. 2025. arXiv: `2506.17414 [cond-mat.supr-con]`.

[77] S. Nadj-Perge, I. K. Drozdov, B. A. Bernevig, and A. Yazdani, "Proposal for realizing Majorana fermions in chains of magnetic atoms on a superconductor", Phys. Rev. B, **88**, 020407 (2013).

[78] S. Rachel and R. Wiesendanger, "Majorana quasiparticles in atomic spin chains on superconductors", Physics Reports, **1099**, 1–28 (2025).

[79] D. Crawford et al., "Increased localization of Majorana modes in antiferromagnetic chains on superconductors", Phys. Rev. B, **107**, 075410 (2023).

[80] L. Schneider et al., "Precursors of Majorana modes and their length-dependent energy oscillations probed at both ends of atomic Shiba chains", Nature Nanotechnology, **17**, 384–389 (2022).

[81] H. Kim et al., “Toward tailoring Majorana bound states in artificially constructed magnetic atom chains on elemental superconductors”, Science Advances, **4**, eaar5251 (2018).

[82] S. Nadj-Perge et al., “Observation of Majorana fermions in ferromagnetic atomic chains on a superconductor”, Science, **346**, 602–607 (2014).

[83] S. Rachel, E. Mascot, S. Cocklin, M. Vojta, and D. K. Morr, “Quantized charge transport in chiral Majorana edge modes”, Phys. Rev. B, **96**, 205131 (2017).

[84] R. M. Menezes, J. F. S. Neto, C. C. d. S. Silva, and M. V. Milo ševi ć, “Manipulation of magnetic skyrmions by superconducting vortices in ferromagnet-superconductor heterostructures”, Phys. Rev. B, **100**, 014431 (2019).

[85] A. P. Petrovi ć et al., “Skyrmion-(Anti)Vortex Coupling in a Chiral Magnet-Superconductor Heterostructure”, Phys. Rev. Lett. **126**, 117205 (2021).

[86] M. Garnier, A. Mesaros, and P. Simon, “Topological superconductivity with deformable magnetic skyrmions”, Communications Physics, **2**, 126 (2019).

[87] G. Yang, P. Stano, J. Klinovaja, and D. Loss, “Majorana bound states in magnetic skyrmions”, Phys. Rev. B, **93**, 224505 (2016).

[88] J. Bedow et al., “Topological superconductivity induced by a triple-q magnetic structure”, Phys. Rev. B, **102**, 180504 (2020).

[89] E. Mascot, J. Bedow, M. Graham, S. Rachel, and D. K. Morr, “Topological superconductivity in skyrmion lattices”, npj Quantum Materials, **6**, 6 (2021).

[90] Y. Baum, T. Posske, I. C. Fulga, B. Trauzettel, and A. Stern, “Gapless topological superconductors: Model Hamiltonian and realization”, Phys. Rev. B, **92**, 045128 (2015).

[91] T. Kieu, E. Mascot, J. Bedow, R. Wiesendanger, and D. K. Morr, “Topological nodal point superconductivity in checkerboard magnet-superconductor hybrid systems”, Phys. Rev. B, **108**, L060509 (2023).

[92] R. Brüning et al. The Non-collinear Path to Topological Superconductivity. 2024. arXiv: `2405.14673 [cond-mat.supr-con]`.

[93] K. H. Wong et al., “Higher order topological superconductivity in magnet-superconductor hybrid systems”, npj Quantum Materials, **8**, 31 (2023).

[94] R.-X. Zhang, W. S. Cole, X. Wu, and S. Das Sarma, “Higher-Order Topology and Nodal Topological Superconductivity in Fe(Se,Te) Heterostructures”, Phys. Rev. Lett. **123**, 167001 (2019).

[95] K. H. Wong et al., “Competing higher order topological superconducting phases in triangular lattice magnet-superconductor hybrid systems”, Phys. Rev. B, **109**, 144521 (2024).

[96] Y. Wang, M. Lin, and T. L. Hughes, "Weak-pairing higher order topological superconductors", Phys. Rev. B, **98**, 165144 (2018).

[97] J. Neuhaus-Steinmetz, E. Y. Vedmedenko, T. Posske, and R. Wiesendanger, "Complex magnetic ground states and topological electronic phases of atomic spin chains on superconductors", Phys. Rev. B, **105**, 165415 (2022).

[98] J. Neuhaus-Steinmetz, T. Matthies, E. Y. Vedmedenko, T. Posske, and R. Wiesendanger, "Large diversity of magnetic phases in two-dimensional magnets with spin-orbit coupling and superconductivity", Phys. Rev. B, **110**, 155427 (2024).

[99] K. Mæland and A. Sudbø, "Quantum fluctuations in the order parameter of quantum skyrmion crystals", Phys. Rev. B, **105**, 224416 (2022).

[100] K. Mæland and A. Sudbø, "Topological Superconductivity Mediated by Skyrmionic Magnons", Phys. Rev. Lett. **130**, 156002 (2023).

[101] L. Schneider et al., "Proximity superconductivity in atom-by-atom crafted quantum dots", Nature, **621**, 60–65 (2023).

[102] L. Schneider et al., "Scanning tunneling spectroscopy study of proximity superconductivity in finite-size quantized surface states", Phys. Rev. B, **110**, L100505 (2024).

[103] J. Spethmann et al., "Discovery of Magnetic Single- and Triple-**q** States in Mn/Re(0001)", Phys. Rev. Lett. **124**, 227203 (2020).

[104] S. Haldar, S. Meyer, A. Kubetzka, and S. Heinze, "Distorted 3Q state driven by topological-chiral magnetic interactions", Phys. Rev. B, **104**, L180404 (2021).

[105] J. Tersoff and D. R. Hamann, "Theory and Application for the Scanning Tunneling Microscope", Phys. Rev. Lett. **50**, 1998–2001 (1983).

[106] D. Wortmann, S. Heinze, P. Kurz, G. Bihlmayer, and S. Blügel, "Resolving Complex Atomic-Scale Spin Structures by Spin-Polarized Scanning Tunneling Microscopy", Phys. Rev. Lett. **86**, 4132–4135 (2001).

[107] S. Heinze, P. Kurz, D. Wortmann, G. Bihlmayer, and S. Blügel, "Complex magnetism in ultra-thin films: atomic-scale spin structures and resolution by the spin-polarized scanning tunneling microscope", Applied Physics A, **75**, 25–36 (2002).

[108] P. Marra, "Majorana nanowires for topological quantum computation", Journal of Applied Physics, **132**, 231101 (2022).

[109] R. Aguado and L. P. Kouwenhoven, "Majorana qubits for topological quantum computing", Physics Today, **73**, 44–50 (2020).

[110] V. L. Ginzburg and L. D. Landau, "On the Theory of superconductivity", Zh. Eksp. Teor. Fiz. **20**, 1064–1082 (1950).

[111] J. R. Schrieffer, "Theory of superconductivity", Il Nuovo Cimento (1955-1965), **7**, 377–385 (1958).

[112] D. van Delft, "Little cup of helium, big science", Physics Today, **61**, 36–42 (2008).

[113] J. Bardeen, L. N. Cooper, and J. R. Schrieffer, "Theory of Superconductivity", Phys. Rev. **108**, 1175–1204 (1957).

[114] J. Bardeen, L. N. Cooper, and J. R. Schrieffer, "Microscopic Theory of Superconductivity", Phys. Rev. **106**, 162–164 (1957).

[115] A. M. Kadin, "Spatial Structure of the Cooper Pair", Journal of Superconductivity and Novel Magnetism, **20**, 285–292 (2007).

[116] A. Einstein, "Quantentheorie des einatomigen idealen Gases. (German) [Quantum Theory of Monatomic Ideal Gases]", 261–267 (1924).

[117] W. Meissner and R. Ochsenfeld, "Ein neuer Effekt bei Eintritt der Supraleitfähigkeit", Naturwissenschaften, **21**, 787–788 (1933).

[118] K. Fossheim, A. Sudbø, and A. Sudboe. "Superconductivity : physics and applications". eng. In: XIV, 427 S. Weinheim [u.a.]: Wiley, 2004. ISBN: 0470844523.

[119] M. Tinkham. "Introduction to superconductivity". eng. In: 2. ed. International series in pure and applied physics. XXI, 454 S. New York [u.a.]: McGraw-Hill, 1996. ISBN: 0070648786.

[120] A. A. Abrikosov, "Nobel Lecture: Type-II superconductors and the vortex lattice", Rev. Mod. Phys. **76**, 975–979 (2004).

[121] N. N. Bogoliubov, "A New Method in the Theory of Superconductivity", Soviet Physics JETP, **7**, 41–46 (1958).

[122] P. de Gennes. Superconductivity of Metals and Alloys. Frontiers in physics. W.A. Benjamin, 1966.

[123] J.-X. Zhu. "Bogoliubov-de gennes method and its applications". eng. In: vol. volume 924. Lecture notes in physics ; volume 924. xi, 188 Seiten. Switzerland: Springer, 2016. ISBN: 9783319313122.

[124] N. Mohanta, R. Soni, S. Okamoto, and E. Dagotto, "Majorana corner states on the dice lattice", Communications Physics, **6**, 240 (2023).

[125] M. Sato and S. Fujimoto, "Existence of Majorana Fermions and Topological Order in Nodal Superconductors with Spin-Orbit Interactions in External Magnetic Fields", Phys. Rev. Lett. **105**, 217001 (2010).

[126] B. Huang, X. Yang, N. Xu, and M. Gong, "Type-I and type-II topological nodal superconductors with *s*-wave interaction", Phys. Rev. B, **97**, 045142 (2018).

[127] J. Zeng, J. J. He, Z. Ning, D.-H. Xu, and R. Wang, "Spin signature of majorana fermions in topological nodal-point superconductors", npj Quantum Materials, **10**, 48 (2025).

[128] E. P. Wigner and E. P. Wigner. "Group theory and its application to the quantum mechanics of atomic spectra". eng. In: Expanded and improved ed. Vol. 5. Pure and applied physics ; 5. XI, 372 S. New York, NY [u.a.]: Academic Press, 1959. ISBN: 0127505504.

[129] M. R. Zirnbauer, "Riemannian symmetric superspaces and their origin in random-matrix theory", Journal of Mathematical Physics, **37**, 4986–5018 (1996).

[130] A. Altland and M. R. Zirnbauer, "Nonstandard symmetry classes in mesoscopic normal-superconducting hybrid structures", Phys. Rev. B, **55**, 1142–1161 (1997).

[131] A. P. Schnyder, S. Ryu, A. Furusaki, and A. W. W. Ludwig, "Classification of topological insulators and superconductors in three spatial dimensions", Phys. Rev. B, **78**, 195125 (2008).

[132] A. P. Schnyder and P. M. R. Brydon, "Topological surface states in nodal superconductors", Journal of Physics: Condensed Matter, **27**, 243201 (2015).

[133] M. Stone and S.-B. Chung, "Fusion rules and vortices in $p_x + ip_y$ superconductors", Phys. Rev. B, **73**, 014505 (2006).

[134] L. Fu and C. L. Kane, "Superconducting Proximity Effect and Majorana Fermions at the Surface of a Topological Insulator", Phys. Rev. Lett. **100**, 096407 (2008).

[135] L. Schneider et al., "Probing the topologically trivial nature of end states in antiferromagnetic atomic chains on superconductors", Nature Communications, **14**, 2742 (2023).

[136] S. Kezilebieke et al., "Topological superconductivity in a van der Waals heterostructure", Nature, **588**, 424–428 (2020).

[137] A. Andreev, "Thermal conductivity of the intermediate state of superconductors", Soviet Physics JETP, **20**, B864–B871 (1965).

[138] J. A. Sauls, "Andreev bound states and their signatures", Philosophical Transactions of the Royal Society A: Mathematical, Physical and Engineering Sciences, **376**, 20180140 (2018).

[139] J. Alicea, Y. Oreg, G. Refael, F. von Oppen, and M. P. A. Fisher, "Non-Abelian statistics and topological quantum information processing in 1D wire networks", Nature Physics, **7**, 412–417 (2011).

[140] F. Wilczek, "Anyons", Scientific American, **264**, 58–65 (1991).

[141] T. I. Andersen et al., "Non-Abelian braiding of graph vertices in a superconducting processor", Nature, **618**, 264–269 (2023).

[142] M. Ruelle et al., "Time-domain braiding of anyons", Science, **389**, eadm7695 (2025).

[143] J. Bedow and D. K. Morr. Majorana Edge Modes as Quantum Memory for Topological Quantum Computing. 2025. arXiv: 2505.08888 [cond-mat.mes-hall].

[144] J.-Y. Ge et al., "Nanoscale assembly of superconducting vortices with scanning tunnelling microscope tip", Nature Communications, **7**, 13880 (2016).

[145] J. C. Slater and G. F. Koster, "Simplified LCAO Method for the Periodic Potential Problem", Phys. Rev. **94**, 1498–1524 (1954).

[146] N. W. Ashcroft and N. D. Mermin. "Solid state physics". eng. In: XXI, 826 S. New York [u.a.]: Holt, Rinehart and Winston, 1976. ISBN: 0030839939.

[147] C. M. Goringe, D. R. Bowler, and E. Hernández, "Tight-binding modelling of materials", Reports on Progress in Physics, **60**, 1447 (1997).

[148] W. E. Pickett. "Tight Binding" Method: Linear Combination of Atomic Orbitals (LCAO). 2014.

[149] J. Li et al., "Two-dimensional chiral topological superconductivity in Shiba lattices", Nature Communications, **7**, 12297 (2016).

[150] D.-L. Deng, S.-T. Wang, and L.-M. Duan, "Systematic construction of tight-binding Hamiltonians for topological insulators and superconductors", Phys. Rev. B, **89**, 075126 (2014).

[151] H. J. Monkhorst and J. D. Pack, "Special points for Brillouin-zone integrations", Phys. Rev. B, **13**, 5188–5192 (1976).

[152] Z.-H. Wang, E. V. Castro, and H.-Q. Lin, "Strain manipulation of Majorana fermions in graphene armchair nanoribbons", Phys. Rev. B, **97**, 041414 (2018).

[153] M. Eliashvili, G. I. Japaridze, G. Tsitsishvili, and G. Tukhashvili, "Edge States in 2D Lattices with Hopping Anisotropy and Chebyshev Polynomials", Journal of the Physical Society of Japan, **83**, 044706 (2014).

[154] T. Fukui, "Theory of edge states based on the Hermiticity of tight-binding Hamiltonian operators", Phys. Rev. Res. **2**, 043136 (2020).

[155] A. Kubetzka, J. M. Bürger, R. Wiesendanger, and K. von Bergmann, "Towards skyrmion-superconductor hybrid systems", Phys. Rev. Mater. **4**, 081401 (2020).

[156] M. M. Odashima, B. G. Prado, and E. Vernek, "Pedagogical introduction to equilibrium Green's functions: condensed-matter examples with numerical implementations", Revista Brasileira de Ensino de Física, **39** (2017).

[157] E. N. Economou. "Green's functions in quantum physics". eng. In: vol. 7. Springer series in solid-state sciences ; 7. IX, 251 S. Berlin [u.a.]: Springer, 1979. ISBN: 3540091548.

[158] J. Bedow. "Edge Modes in Magnet-Superconductor Hybrid structures". Available at `https://cmt.physik.tu-dortmund.de/storages/cmt-physik/r/uhrig/master/master-jasmin-bedow.pdf`. Master's thesis. Technische Universität Dortmund, 2020.

[159] T. Fukui, Y. Hatsugai, and H. Suzuki, "Chern Numbers in Discretized Brillouin Zone: Efficient Method of Computing (Spin) Hall Conductances", Journal of the Physical Society of Japan, **74**, 1674–1677 (2005).

[160] R. Zhao et al., "First-principle calculation of Chern number in gyrotropic photonic crystals", Opt. Express, **28**, 4638–4649 (2020).

[161] K. Kang, "U(1) gauge symmetry free of redundancy and a generalized Byers-Yang theorem", Journal of Physics Communications, **3**, 105008 (2019).

[162] R. Bianco and R. Resta, "Mapping topological order in coordinate space", Phys. Rev. B, **84**, 241106 (2011).

[163] X. Dang, J. D. Burton, A. Kalitsov, J. P. Velev, and E. Y. Tsymbal, "Complex band structure of topologically protected edge states", Phys. Rev. B, **90**, 155307 (2014).

[164] F. Bloch, "Über die Quantenmechanik der Elektronen in Kristallgittern", Zeitschrift für Physik, **52**, 555–600 (1929).

[165] V. Hoffstein and D. Boudreaux, "Calculation of complex band structures", Surface Science, **21**, 99–108 (1970).

[166] Y.-C. Chang and J. N. Schulman, "Complex band structures of crystalline solids: An eigenvalue method", Phys. Rev. B, **25**, 3975–3986 (1982).

[167] M. G. Reuter, "A unified perspective of complex band structure: interpretations, formulations, and applications", Journal of Physics: Condensed Matter, **29**, 053001 (2016).

[168] I. Hargittai, "Walter Kohn Centennial—Nobel laureate for density functional theory", Structural Chemistry, **34**, 2375–2377 (2023).

[169] S. Blinder. "Chapter 1 - Introduction to the Hartree-Fock method". In: Mathematical Physics in Theoretical Chemistry. Ed. by S. Blinder and J. House. Developments in Physical & Theoretical Chemistry. Elsevier, 2019, pp. 1–30. ISBN: 978-0-12-813651-5.

[170] K. Capelle, "A bird's-eye view of density-functional theory", Braz. J. Phys. **36** (2002).

[171] R. G. Parr. "Density Functional Theory of Atoms and Molecules". In: Horizons of Quantum Chemistry. Ed. by K. Fukui and B. Pullman. Dordrecht: Springer Netherlands, 1980, pp. 5–15. ISBN: 978-94-009-9027-2.

[172] E. Engel and R. M. Dreizler. Density Functional Theory. Sprimnger Berlin, Heidelberg, 2011. ISBN: 978-3-642-26718-5.

[173] M. Born and R. Oppenheimer, "Zur Quantentheorie der Molekeln", Annalen der Physik, **389**, 457–484 (1927).

[174] P. Hohenberg and W. Kohn, "Inhomogeneous Electron Gas", Phys. Rev. **136**, B864–B871 (1964).

[175] W. Kohn and L. J. Sham, "Self-Consistent Equations Including Exchange and Correlation Effects", Phys. Rev. **140**, A1133–A1138 (1965).

[176] P. Kurz. "Non-Collinear Magnetism at Surfaces and in Ultrathin Films". dissertation. Forschungszentrum Jülich, 2000.

[177] M. Weinert, E. Wimmer, and A. J. Freeman, "Total-energy all-electron density functional method for bulk solids and surfaces", Phys. Rev. B, **26**, 4571–4578 (1982).

[178] P. Kurz, F. Förster, L. Nordström, G. Bihlmayer, and S. Blügel, "Ab initio treatment of noncollinear magnets with the full-potential linearized augmented plane wave method", Phys. Rev. B, **69**, 024415 (2004).

[179] P. Kurz, G. Bihlmayer, K. Hirai, and S. Blügel, "Three-Dimensional Spin Structure on a Two-Dimensional Lattice: Mn /Cu(111)", Phys. Rev. Lett. **86**, 1106–1109 (2001).

[180] D. D. Koelling and B. N. Harmon, "A technique for relativistic spin-polarised calculations", Journal of Physics C: Solid State Physics, **10**, 3107 (1977).

[181] A. Oswald, R. Zeller, P. J. Braspenning, and P. H. Dederichs, "Interaction of magnetic impurities in Cu and Ag", Journal of Physics F: Metal Physics, **15**, 193 (1985).

[182] A. Liechtenstein, M. Katsnelson, V. Antropov, and V. Gubanov, "Local spin density functional approach to the theory of exchange interactions in ferromagnetic metals and alloys", Journal of Magnetism and Magnetic Materials, **67**, 65–74 (1987).

[183] M. Heide, G. Bihlmayer, and S. Blügel, "Describing Dzyaloshinskii–Moriya spirals from first principles", Physica B: Condensed Matter, **404**, 2678–2683 (2009).

[184] S. H. Vosko, L. Wilk, and M. Nusair, "Accurate spin-dependent electron liquid correlation energies for local spin density calculations: a critical analysis", Can. J. Phys. **58**, 1200–1211 (1980).

[185] J. P. Perdew, K. Burke, and M. Ernzerhof, "Generalized Gradient Approximation Made Simple", Phys. Rev. Lett. **77**, 3865–3868 (1996).

[186] D. M. Ceperley and B. J. Alder, "Ground State of the Electron Gas by a Stochastic Method", Phys. Rev. Lett. **45**, 566–569 (1980).

[187] The FLEUR project. `https://www.flapw.de/`.

[188] D. Wortmann et al. FLEUR. Zenodo. May 2023.

[189] E. Wimmer, H. Krakauer, M. Weinert, and A. J. Freeman, "Full-potential self-consistent linearized-augmented-plane-wave method for calculating the electronic structure of molecules and surfaces: O_2 molecule", Phys. Rev. B, **24**, 864–875 (1981).

[190] D. J. Singh and L. Nordstrom. Planewaves, Pseudopotentials and the LAPW Method, Second Edition. , Berlin, Germany, Jan. 2005.

[191] O. K. Andersen, "Linear methods in band theory", Phys. Rev. B, **12**, 3060–3083 (1975).

[192] H. Krakauer, M. Posternak, and A. J. Freeman, "Linearized augmented plane-wave method for the electronic band structure of thin films", Phys. Rev. B, **19**, 1706–1719 (1979).

[193] VASP. `https://www.vasp.at`.

[194] G. Kresse and J. Furthmüller, "Efficient iterative schemes for ab initio total-energy calculations using a plane-wave basis set", Phys. Rev. B, **54**, 11169–11186 (1996).

[195] G. Kresse and D. Joubert, "From ultrasoft pseudopotentials to the projector augmented-wave method", Phys. Rev. B, **59**, 1758–1775 (1999).

[196] P. E. Blöchl, "Projector augmented-wave method", Phys. Rev. B, **50**, 17953–17979 (1994).

[197] P. E. Blöchl, J. Kästner, and C. J. Först. "Electronic Structure Methods: Augmented Waves, Pseudopotentials and The Projector Augmented Wave Method". In: Handbook of Materials Modeling: Methods. Ed. by S. Yip. Dordrecht: Springer Netherlands, 2005, pp. 93–119. ISBN: 978-1-4020-3286-8.

[198] D. R. Hamann, M. Schlüter, and C. Chiang, "Norm-Conserving Pseudopotentials", Phys. Rev. Lett. **43**, 1494–1497 (1979).

[199] P. Schwerdtfeger, "The Pseudopotential Approximation in Electronic Structure Theory", ChemPhysChem, **12**, 3143–3155 (2011).

[200] C. L. Reis, J. M. Pacheco, and J. L. Martins, "First-principles norm-conserving pseudopotential with explicit incorporation of semicore states", Phys. Rev. B, **68**, 155111 (2003).

[201] B. Dupé, M. Hoffmann, C. Paillard, and S. Heinze, "Tailoring magnetic skyrmions in ultra-thin transition metal films", Nature Communications, **5**, 4030 (2014).

[202] O. Eriksson, A. Bergman, L. Bergqvist, and J. Hellsvik. Atomistic Spin Dynamics: Foundations and Applications. Oxford University Press, Feb. 2017. ISBN: 9780198788669.

[203] W. Heisenberg, "Zur Theorie des Ferromagnetismus", Zeitschrift für Physik, **49**, 619–636 (1928).

[204] S. Blundell. Magnetism in condensed matter. eng. Oxford master series in condensed matter physics. 1 Online-Ressource (xii, 238 Seiten). Oxford: Oxford University Press, 2001. ISBN: 9780191586644.

[205] S. von Malottki, B. Dupé, P. F. Bessarab, A. Delin, and S. Heinze, "Enhanced skyrmion stability due to exchange frustration", Scientific Reports, **7**, 12299 (2017).

[206] S. Meyer et al., "Isolated zero field sub-10 nm skyrmions in ultrathin Co films", Nature Communications, **10**, 3823 (2019).

[207] M. A. Ruderman and C. Kittel, "Indirect Exchange Coupling of Nuclear Magnetic Moments by Conduction Electrons", Phys. Rev. **96**, 99–102 (1954).

[208] T. Kasuya, "A Theory of Metallic Ferro- and Antiferromagnetism on Zener's Model", Progress of Theoretical Physics, **16**, 45–57 (1956).

[209] K. Yosida, "Magnetic Properties of Cu-Mn Alloys", Phys. Rev. **106**, 893–898 (1957).

[210] F. Nickel. "Dichtefunktionaltheorie-basierte Untersuchung nicht-kollinearer Spinstrukturen in Übergangsmetall-Multilagen". Master's thesis. Christian-Albrechts-University Kiel, 2020.

[211] S. Meyer. "Complex spin structures in frustrated ultrathin films". dissertation. Christian-Albrechts-University Kiel, 2023.

[212] T. Momoi, K. Kubo, and K. Niki, "Possible Chiral Phase Transition in Two-Dimensional Solid ^{3}He", Phys. Rev. Lett. **79**, 2081–2084 (1997).

[213] M. Hoffmann and S. Blügel, "Systematic derivation of realistic spin models for beyond-Heisenberg solids", Phys. Rev. B, **101**, 024418 (2020).

[214] M. Bode et al., "Chiral magnetic order at surfaces driven by inversion asymmetry", Nature, **447**, 190–193 (2007).

[215] T. Moriya, "Anisotropic Superexchange Interaction and Weak Ferromagnetism", Phys. Rev. **120**, 91–98 (1960).

[216] I. Dzyaloshinsky, "A thermodynamic theory of "weak" ferromagnetism of antiferromagnetics", Journal of Physics and Chemistry of Solids, **4**, 241–255 (1958).

[217] P. M. Levy and A. Fert, "Anisotropy induced by nonmagnetic impurities in Cu Mn spin-glass alloys", Phys. Rev. B, **23**, 4667–4690 (1981).

[218] D. Smith, "New mechanisms for magnetic anisotropy in localised S-state moment materials", Journal of Magnetism and Magnetic Materials, **1**, 214–225 (1976).

[219] J. B. Staunton, B. L. Gyorffy, J. Poulter, and P. Strange, "A relativistic RKKY interaction between two magnetic impurities-the origin of a magnetic anisotropic effect", Journal of Physics C: Solid State Physics, **21**, 1595–1611 (1988).

[220] G. Jackeli and G. Khaliullin, "Mott Insulators in the Strong Spin-Orbit Coupling Limit: From Heisenberg to a Quantum Compass and Kitaev Models", Phys. Rev. Lett. **102**, 017205 (2009).

[221] F. R. Lux, F. Freimuth, S. Blügel, and Y. Mokrousov, "Engineering chiral and topological orbital magnetism of domain walls and skyrmions", Communications Physics, **1**, 60 (2018).

[222] B. Berg and M. Lüscher, "Definition and statistical distributions of a topological number in the lattice O(3) σ-model", Nuclear Physics B, **190**, 412–424 (1981).

[223] X. G. Wen, F. Wilczek, and A. Zee, "Chiral spin states and superconductivity", Phys. Rev. B, **39**, 11413–11423 (1989).

[224] G. Tatara and H. Kohno, "Permanent current from noncommutative spin algebra", Phys. Rev. B, **67**, 113316 (2003).

[225] Y. Taguchi, Y. Oohara, H. Yoshizawa, N. Nagaosa, and Y. Tokura, "Spin Chirality, Berry Phase, and Anomalous Hall Effect in a Frustrated Ferromagnet", Science, **291**, 2573–2576 (2001).

[226] M. Hoffmann et al., "Topological orbital magnetization and emergent Hall effect of an atomic-scale spin lattice at a surface", Phys. Rev. B, **92**, 020401 (2015).

[227] G. Binnig, H. Rohrer, C. Gerber, and E. Weibel, "Tunneling through a controllable vacuum gap", Applied Physics Letters, **40**, 178–180 (1982).

[228] G. Binnig, H. Rohrer, C. Gerber, and E. Weibel, "Surface Studies by Scanning Tunneling Microscopy", Phys. Rev. Lett. **49**, 57–61 (1982).

[229] G. Binnig, H. Rohrer, C. Gerber, and E. Weibel, "7 × 7 Reconstruction on Si(111) Resolved in Real Space", Phys. Rev. Lett. **50**, 120–123 (1983).

[230] R. Wiesendanger. "Scanning probe microscopy and spectroscopy : methods and applications". eng. In: 1. publ. XXII, 637 S. Cambridge [u.a.]: Cambridge Univ. Press, 1994. ISBN: 0521418100.

[231] C. J. Chen, "Origin of atomic resolution on metal surfaces in scanning tunneling microscopy", Phys. Rev. Lett. **65**, 448–451 (1990).

[232] C. J. Chen. Introduction to Scanning Tunneling Microscopy. Oxford University Press, Sept. 2007. ISBN: 9780199211500.

[233] S. Heinze, "Simulation of spin-polarized scanning tunneling microscopy images of nanoscale non-collinear magnetic structures", Applied Physics A, **85**, 407–414 (2006).

[234] R. Wiesendanger, "Spin mapping at the nanoscale and atomic scale", Rev. Mod. Phys. **81**, 1495–1550 (2009).

[235] D. Serrate et al., "Imaging and manipulating the spin direction of individual atoms", Nature Nanotechnology, **5**, 350–353 (2010).

[236] M. Bode, M. Getzlaff, and R. Wiesendanger, "Spin-Polarized Vacuum Tunneling into the Exchange-Split Surface State of Gd(0001)", Phys. Rev. Lett. **81**, 4256–4259 (1998).

[237] M. Bode, "Spin-Polarized Scanning Tunneling Microscopy: Breakthroughs and Highlights", CHIMIA, **66**, 56 (2012).

[238] M. Bode et al., "Magnetization-Direction-Dependent Local Electronic Structure Probed by Scanning Tunneling Spectroscopy", Phys. Rev. Lett. **89**, 237205 (2002).

[239] C. Gould et al., "Tunneling Anisotropic Magnetoresistance: A Spin-Valve-Like Tunnel Magnetoresistance Using a Single Magnetic Layer", Phys. Rev. Lett. **93**, 117203 (2004).

[240] K. von Bergmann et al., "Tunneling anisotropic magnetoresistance on the atomic scale", Phys. Rev. B, **86**, 134422 (2012).

[241] S. Haldar, M. Gutzeit, and S. Heinze, "Tunneling anisotropic magnetoresistance of Pb and Bi adatoms and dimers on Mn/W(110): A first-principles study", Phys. Rev. B, **100**, 094412 (2019).

[242] C. Hanneken et al., "Electrical detection of magnetic skyrmions by tunnelling non-collinear magnetoresistance", Nature Nanotechnology, **10**, 1039–1042 (2015).

[243] P. Weiss. Scanning Probe Microscopy and Spectroscopy. Theory, Techniques, and Applications. Vol. 123. 39. 2nd Edition Edited by D. W. Bonnell (University of Pennsylvania). Washington, DC: American Chemical Society, 2001, p. 9725. ISBN: 0-471-24824-X.

[244] S. Heinze. "First-Principles Theory of Scanning Tunneling Microscopy Applied to Transition-Metal Surfaces". dissertation. 2000.

[245] N. D. Lang, "Spectroscopy of single atoms in the scanning tunneling microscope", Phys. Rev. B, **34**, 5947–5950 (1986).

[246] J. Bardeen, "Tunnelling from a Many-Particle Point of View", Phys. Rev. Lett. **6**, 57–59 (1961).

[247] S. Meyer, M. Schmitt, M. Vogt, M. Bode, and S. Heinze, "Dead magnetic layers at the interface: Moment quenching through hybridization and frustration", Phys. Rev. Res. **2**, 012075 (2020).

[248] S. Heinze, S. Blügel, R. Pascal, M. Bode, and R. Wiesendanger, "Prediction of bias-voltage-dependent corrugation reversal for STM images of bcc (110) surfaces: W(110), Ta(110), and Fe(110)", Phys. Rev. B, **58**, 16432–16445 (1998).

[249] S. Heinze et al., "Real-Space Imaging of Two-Dimensional Antiferromagnetism on the Atomic Scale", Science, **288**, 1805–1808 (2000).

[250] P. Park et al., "Tetrahedral triple-Q magnetic ordering and large spontaneous Hall conductivity in the metallic triangular antiferromagnet Co1/3TaS2", Nature Communications, **14**, 8346 (2023).

[251] H. Takagi et al., "Spontaneous topological Hall effect induced by non-coplanar antiferromagnetic order in intercalated van der Waals materials", Nature Physics, **19**, 961–968 (2023).

[252] I. Martin and C. D. Batista, "Itinerant Electron-Driven Chiral Magnetic Ordering and Spontaneous Quantum Hall Effect in Triangular Lattice Models", Phys. Rev. Lett. **101**, 156402 (2008).

[253] J.-P. Hanke et al., "Role of Berry phase theory for describing orbital magnetism: From magnetic heterostructures to topological orbital ferromagnets", Phys. Rev. B, **94**, 121114 (2016).

Acronyms

AFM antiferromagnet

APW augmented plane wave

ASE anisotropic symmetric exchange

BCS Bardeen-Cooper-Schrieffer

BdG Bogoliubov de Gennes

BL bilayer

BZ Brillouin zone

DFT density functional theory

DMI Dzyaloshinskii-Moriya interaction

DOS density of states

FLAPW full-potential linearized augmented plane wave

FM ferromagnet

GGA generalized gradient approximation

GMR giant magneto resistance

HOI higher-order exchange interactions

HOTSC higher order topological superconductor

LAPW linearized augmented plane wave

LDA local density approximation

LDOS local density of states

LSDA local spin density approximation

MAE magnetocrystalline anisotropy energy

MBS Majorana bound state

ML monolayer

MSH magnet-superconductor-hybrid

MT muffin-tin

MZM Majorana zero mode

NCMR non-collinear magneto resistance

PAW projector augmented wave

RKKY Rudermann-Kittel-Kasuya-Yosida

RW-AFM row-wise antiferromagnet

SOC spin-orbit coupling

SP-STM spin-polarized scanning tunneling microscope

STM scanning tunneling microscopy

STS scanning tunneling spectroscopy

TAMR tunneling anisotropic magnetic resistance

TNPSC topological nodal point superconductor

TOM topological orbital moment

XC exchange-correlation

A Appendix

A.1 Pauli spin matrices

Here the explicit forms of the Pauli spin matrices are given.

$$\sigma_x = \sigma_1 = \begin{pmatrix} 0 & 1 \\ 1 & 0 \end{pmatrix}, \quad \sigma_y = \sigma_2 = \begin{pmatrix} 0 & -\mathrm{i} \\ \mathrm{i} & 0 \end{pmatrix}, \quad \sigma_z = \sigma_3 = \begin{pmatrix} 1 & 0 \\ 0 & -1 \end{pmatrix} \quad . \tag{A.1}$$

In the context of electronic models for topological superconductivity often the (2×2) unity matrix is often defined as

$$\sigma_0 = \begin{pmatrix} 1 & 0 \\ 0 & 1 \end{pmatrix} \quad . \tag{A.2}$$

These four matrices now build a full basis.
Often a vector containing the Pauli spin matrices

$$\boldsymbol{\sigma} = \begin{pmatrix} \sigma_x \\ \sigma_y \\ \sigma_z \end{pmatrix} \tag{A.3}$$

is used.

A.2 Effective p-wave pairing

The Hamiltonian for a periodic square lattice is given by

$$\underline{H}(\mathbf{k}) = \begin{pmatrix} JS & -2\alpha(\sin(k_y a) + \mathrm{i}\sin(k_x a)) & 0 & \Delta_0 \\ -2\alpha(\sin(k_y a) - \mathrm{i}\sin(k_x a)) & -JS & -\Delta_0 & 0 \\ 0 & -\Delta_0 & -JS & -2\alpha(\sin(k_y a) - \mathrm{i}\sin(k_x a)) \\ \Delta_0 & 0 & -2\alpha(\sin(k_y a) + \mathrm{i}\sin(k_x a)) & JS \end{pmatrix}, \tag{A.4}$$

where Δ_0 represents s-wave superconductivity, JS a homogeneous magnetic field and α Rashba-SOC (cf. Eq. (2.43)). The electronic part of the Hamiltonian following Eq. (2.8) is

$$\underline{H^e}(\mathbf{k}) = \begin{pmatrix} JS & -2\alpha(\sin(k_y a) + \mathrm{i}\sin(k_x a)) \\ -2\alpha(\sin(k_y a) - \mathrm{i}\sin(k_x a)) & -JS \end{pmatrix} . \tag{A.5}$$

This electronic Hamiltonian can be diagonalized via

$$\mathcal{U}_e^\dagger \underline{H^e}(\mathbf{k}) \mathcal{U}_e \tag{A.6}$$

with

$$\mathcal{U}_e = \begin{pmatrix} \chi_- & \chi_+ \\ 1 & 1 \end{pmatrix} \tag{A.7}$$

and the definition

$$\chi_\pm = \frac{1}{2\alpha} \frac{JS \pm \sqrt{4\alpha^2 \sin^2(k_x a) + 4\alpha^2 \sin^2(k_y a) + (JS)^2}}{\mathrm{i}\sin(k_x a) - \sin(k_y a)} . \tag{A.8}$$

Now a unitary matrix

$$\mathcal{U} = \begin{pmatrix} \mathcal{U}_e & 0 \\ 0 & -\mathcal{U}_e^* \end{pmatrix} = \begin{pmatrix} \chi_- & \chi_+ & 0 & 0 \\ 1 & 1 & 0 & 0 \\ 0 & 0 & -\chi_-^* & -\chi_+^* \\ 0 & 0 & 1 & 1 \end{pmatrix} \tag{A.9}$$

can be defined. This unitary matrix can be used to perform a basis transformation

$$\underline{\widetilde{H}}(\mathbf{k}) = \mathcal{U}^\dagger \underline{H}(\mathbf{k}) \mathcal{U} . \tag{A.10}$$

This transformation diagonalized the electronic and hole sub-matrices $\underline{H^e}(\mathbf{k})$ and $\underline{H^h}(\mathbf{k})$, but it does not mix electronic and hole states. The off-diagonal terms $\underline{H}^{(e-h)}(\mathbf{k})$ and $\underline{H}^{(h-e)}(\mathbf{k})$ can therefor still be associated with the superconducting pairing. This new effective pairing matrix is now given by

$$\underline{\widetilde{H}}^{(e-h)}(\mathbf{k}) = \frac{-\Delta_0}{\alpha(\mathrm{i}\sin(k_x a) + \sin(k_y a))} \begin{pmatrix} JS & JS - \beta \\ JS + \beta & JS \end{pmatrix} \tag{A.11}$$

with the definition

$$\beta = \sqrt{4\alpha^2 \sin^2(k_x a) + 4\alpha^2 \sin^2(k_y a) + (JS)^2} \quad . \tag{A.12}$$

The entry $\underline{\widetilde{H}}^{(e-h)}(\mathbf{k})$ follows from Eq. (2.38). The effective pairing matrix is now dependent on $\mathbf{k}$. It contains real values, which are k_y-dependent and imaginary values, which are k_x-dependent. This represents an effective p-wave pairing of the type $p_y + \mathrm{i}p_x$, which can induce topological superconductivity.
With the definition

$$\zeta = \frac{-\Delta_0}{\alpha(\mathrm{i}\sin(k_x a) + \sin(k_y a))} \tag{A.13}$$

the effective paring matrix from Eq. (A.11) can be written in terms of the vector $\mathbf{d}(\mathbf{k})$ and $\Delta(\mathbf{k})$, following Eq. (2.15) as

$$\Delta(\mathbf{k}) = -\beta\zeta \quad \text{and} \quad \mathbf{d}(\mathbf{k}) = \begin{pmatrix} 0 \\ -\mathrm{i}\zeta JS \\ \zeta JS \end{pmatrix} \quad . \tag{A.14}$$

As the non-zero vector $\mathbf{d}(\mathbf{k})$ shows, that effective triplet pairing exists. This minimal example shows, that the combination of magnetic moments and Rashba-SOC can lead to effective triplet-pairing. An effective Rashba-SOC can also be induced by a non-collinear spin structure and spin-conserving hopping [73]. This can be shown by local unitary transformations, that rotate the spin-quantization axis along the magnetic moment (cf. Sec. 2.2.3). Therefore, a non-collinear spin structure, providing magnetic moments and spin-mixing can induce topological superconductivity.

A.3 Introduction of the tight-binding model

The tight-binding approximation assumes that electrons can be described in an appropriate way by atomic orbitals, which are located at the lattice sites of a crystal. For each individual atom a set of atomic orbitals Φ_n exists. The energy of the electrons is given by the solution of the Schrödinger equation

$$H_{at}\Phi_n = \epsilon_n^{at}\Phi_n \tag{A.15}$$

using the atomic Hamiltonian H_{at}. Note that although all atoms are described individually the underlying potential $V(\mathbf{r})$ has a periodic form

$$V(\mathbf{r}) = V(\mathbf{r} - \mathbf{R}_0) \quad , \tag{A.16}$$

where $\mathbf{R}_0$ is a lattice vector. To find an eigen state which can describe the lattice these single atom orbitals Φ_n can be combined in a so-called Bloch sum, which fulfills the Bloch condition

$$B_{n,\mathbf{k}}(\mathbf{r}) = \frac{1}{\sqrt{N}} \sum_{\mathbf{R}} e^{\mathrm{i}\mathbf{k}\mathbf{R}}\Phi_n(\mathbf{r} - \mathbf{R}) \quad . \tag{A.17}$$

Here $\mathbf{k}$ is the wave vector and $\mathbf{R}$ sums over all lattice sites. The index n denotes a specific orbital. As interactions between different types of orbitals are possible the wavefunctions are expanded in Bluch sums by

$$\Psi_{\mathbf{k}}(\mathbf{r}) = \sum_n b_n(\mathbf{k}) B_{n,\mathbf{k}}(\mathbf{r}) \quad , \tag{A.18}$$

where $b_n(\mathbf{k})$ are the expansion coefficients, which fulfill

$$\sum_n |b_n(\mathbf{k})|^2 = 1 \quad . \tag{A.19}$$

These $\Psi_{\mathbf{k}}$ now form a basis wavefunction for the whole crystal and the Schrödinger equation for the crystal has the form

$$H\Psi_{\mathbf{k}} = \epsilon_k \Psi_{\mathbf{k}} \quad . \tag{A.20}$$

When using the wavefunction $\Psi_{\mathbf{k}}$ from Eq. (A.18) this becomes

$$H \sum_n b_n(\mathbf{k}) B_{n,\mathbf{k}}(\mathbf{r}) = \epsilon_{\mathbf{k}} \sum_n b_n(\mathbf{k}) B_{n,\mathbf{k}}(\mathbf{r}) \quad . \tag{A.21}$$

When multiplying with $B^*_{m,\mathbf{k}}(\mathbf{r})$ from the left and integrating over d$\mathbf{r}$ it follows

$$\sum_n b_n(\mathbf{k}) \underbrace{\int B^*_{m,\mathbf{k}}(\mathbf{r}) H B_{n,\mathbf{k}}(\mathbf{r}) \mathrm{d}\mathbf{r}}_{\langle m|H|n\rangle = H_{m,n}(\mathbf{k})} = \epsilon_\mathbf{k} \sum_n b_n(\mathbf{k}) \underbrace{\int B^*_{m,\mathbf{k}}(\mathbf{r}) B_{n,\mathbf{k}}(\mathbf{r}) \mathrm{d}\mathbf{r}}_{\langle m|n\rangle = S_{m,n}(\mathbf{k})} \quad . \tag{A.22}$$

Here $H_{m,n}(\mathbf{k})$ is the matrix element of the Hamilton matrix and $S_{m,n}(\mathbf{k})$ the matrix element of the overlap matrix. With these two definitions, the equation looks like

$$\sum_n b_n(\mathbf{k}) H_{m,n}(\mathbf{k}) = \epsilon_\mathbf{k} \sum_n b_n(\mathbf{k}) S_{m,n}(\mathbf{k}) \quad . \tag{A.23}$$

When $\mathbf{b}(\mathbf{k})$ is a vector with the components $b_n(\mathbf{k})$ for all orbitals n, one can write Eq. (A.22) as

$$\underline{H}\mathbf{b}(\mathbf{k}) = \epsilon_\mathbf{k} \underline{S}\mathbf{b}(\mathbf{k}) \quad , \tag{A.24}$$

where $\underline{H}$ is a matrix with the elements $H_{m,n}(\mathbf{k})$ and $\underline{S}$ is a matrix with the elements $S_{m,n}(\mathbf{k})$. For known matrices $\underline{H}$ and $\underline{S}$ this is a generalized eigenvalue problem of the form

$$\{\underline{H} - \epsilon_\mathbf{k} \underline{S}\}\mathbf{b}(\mathbf{k}) = 0 \quad . \tag{A.25}$$

To solve this generalized eigenvalue problem the matrix element $H_{m,n}(\mathbf{k})$ and $S_{m,n}(\mathbf{k})$ need to be known. With the definition of Eq. (A.17) one can write

$$H_{m,n}(\mathbf{k}) = \langle m|H|n\rangle = \int B^*_{m,\mathbf{k}}(\mathbf{r}) H B_{n,\mathbf{k}}(\mathbf{r}) \mathrm{d}\mathbf{r} \tag{A.26}$$

$$= \frac{1}{N} \sum_{\mathbf{R}_1,\mathbf{R}_2} e^{-\mathrm{i}\mathbf{k}\mathbf{R}_1} e^{\mathrm{i}\mathbf{k}\mathbf{R}_2} \int \Phi^*_m(\mathbf{r}-\mathbf{R}_1) H \Phi_n(\mathbf{r}-\mathbf{R}_2) \mathrm{d}\mathbf{r} \tag{A.27}$$

$$= \frac{1}{N} \sum_{\mathbf{R}_1,\mathbf{R}_2} e^{\mathrm{i}\mathbf{k}(\mathbf{R}_2-\mathbf{R}_1)} H_{m,n}(\mathbf{R_2}-\mathbf{R}_1) \tag{A.28}$$

and

$$S_{m,n}(\mathbf{k}) = \langle m|S|n\rangle = \int B^*_{m,\mathbf{k}}(\mathbf{r}) B_{n,\mathbf{k}}(\mathbf{r}) \mathrm{d}\mathbf{r} \tag{A.29}$$

$$= \frac{1}{N} \sum_{\mathbf{R}_1,\mathbf{R}_2} e^{-\mathrm{i}\mathbf{k}\mathbf{R}_1} e^{\mathrm{i}\mathbf{k}\mathbf{R}_2} \int \Phi^*_m(\mathbf{r}-\mathbf{R}_1) \Phi_n(\mathbf{r}-\mathbf{R}_2) \mathrm{d}\mathbf{r} \tag{A.30}$$

$$= \frac{1}{N} \sum_{\mathbf{R}_1,\mathbf{R}_2} e^{\mathrm{i}\mathbf{k}(\mathbf{R}_2-\mathbf{R}_1)} S_{m,n}(\mathbf{R_2}-\mathbf{R}_1) \quad . \tag{A.31}$$

Because of the periodicity of the atomic orbitals both matrix elements depend only on the difference between $\mathbf{R}_1$ and $\mathbf{R}_2$. So with the definition $\mathbf{R} = \mathbf{R}_2 - \mathbf{R}_1$ it follows

$$H_{m,n}(\mathbf{k}) = \sum_\mathbf{R} e^{\mathrm{i}\mathbf{k}(\mathbf{R}} H_{m,n}(\mathbf{R}) \tag{A.32}$$

with

$$H_{m,n}(\mathbf{R}) = \int \Phi_m^*(\mathbf{r}) H \Phi_n(\mathbf{r} - \mathbf{R}) \quad . \tag{A.33}$$

These matrix elements can be parametrized. As an example are the contributions of the chemical potential and the hopping term derived. The Hamiltonian for the kinetic energy and the chemical potential ϵ has the form

$$H_0 = \frac{\hat{p}^2}{2m} - \epsilon \quad . \tag{A.34}$$

The matrix element is now given as

$$H_{m,n}(\mathbf{R}_2 - \mathbf{R}_1) = \int \Phi_m^*(\mathbf{r} - \mathbf{R}_1) \left[\frac{\hat{p}^2}{2m} - \epsilon \right] \Phi_n(\mathbf{r} - \mathbf{R}_2) \mathrm{d}\mathbf{r} \quad , \tag{A.35}$$

which becomes on a discrete lattice

$$H_{m,n}(\mathbf{R}) = \sum_{\mathbf{R}} \Phi_m^*(\mathbf{r}) \left[\frac{\hat{p}^2}{2m} - \epsilon \right] \Phi_n(\mathbf{r} - \mathbf{R}) \quad , \tag{A.36}$$

where **R** is a vector connecting two lattice points.

Momentum operator on a discrete lattice: The momentum operator has the form

$$\hat{p} = -\mathrm{i}\hbar \frac{\mathrm{d}}{\mathrm{d}x} \tag{A.37}$$

where x represents an arbitrary direction. This makes the square of the operator

$$\hat{p}^2 = \hbar^2 \frac{\mathrm{d}^2}{\mathrm{d}x^2} \quad . \tag{A.38}$$

On a discrete lattice is the derivation after the direction x

$$\frac{\mathrm{d}}{\mathrm{d}x}\Phi(x) = \frac{\Phi(x+a) - \Phi(x)}{a} \tag{A.39}$$

where a is the distance between neighboring lattice points in the direction x. Now follows

$$\frac{\mathrm{d}^2}{\mathrm{d}x^2}\Phi(x) = \frac{\Phi(x+2a) - \Phi(x+a) - \Phi(x+a) + \Phi(x)}{a^2} \quad . \tag{A.40}$$

When summing over all lattice sites, one can shift the index by a and obtain

$$\sum_{\mathbf{R}} \frac{\mathrm{d}^2}{\mathrm{d}x^2}\Phi(x) = \sum_{\mathbf{R}} \frac{\Phi(x+a) - 2\Phi(x) + \Phi(x-a)}{a^2} \quad . \tag{A.41}$$

With the momentum operator on the discrete lattice Eq. (A.36) can be written as

$$H_{m,n}(\mathbf{R}) = \sum_{\mathbf{R}} \left[\left(-2\frac{\hbar^2}{2ma^2} - \epsilon \right) \Phi_m^*(\mathbf{r})\Phi_n(\mathbf{r}-\mathbf{R}) + \frac{\hbar^2}{2ma^2} \left(\Phi_m^*(\mathbf{r})\Phi_n(\mathbf{r}-\mathbf{R}-a) + \Phi_m^*(\mathbf{r})\Phi_n(\mathbf{r}-\mathbf{R}-a) \right) \right] \quad . \tag{A.42}$$

With the definition of

$$t := \frac{\hbar^2}{2ma^2} \tag{A.43}$$

this becomes

$$H_{m,n}(\mathbf{R}) = \sum_{\mathbf{R}} \left[(-2t - \epsilon)\, \Phi_m^*(\mathbf{r})\Phi_n(\mathbf{r}-\mathbf{R}) + t \left(\Phi_m^*(\mathbf{r})\Phi_n(\mathbf{r}-\mathbf{R}-a) + \Phi_m^*(\mathbf{r})\Phi_n(\mathbf{r}-\mathbf{R}-a) \right) \right] \quad . \tag{A.44}$$

and when assuming that

$$\Phi_m^*(\mathbf{r})\Phi_n(\mathbf{r}-\mathbf{R}) = \delta(\mathbf{R}) \tag{A.45}$$

it follows that

$$H_{m,n}(\mathbf{R}) = \begin{cases} -2t - \epsilon & , \mathbf{R} = 0 \\ t & , \mathbf{R} = \pm a \end{cases} \quad . \tag{A.46}$$

With the definition of $\mu = -2t - \epsilon$ it follows

$$H_{m,n}(\mathbf{R}) = \begin{cases} \mu & , \text{onsite term} \\ t & , \text{interaction with the next neighbor} \end{cases} \quad . \tag{A.47}$$

The onsite term corresponds to the eigenenergy of the atomic orbitals and t is called a hopping term.

A.4 SkX state

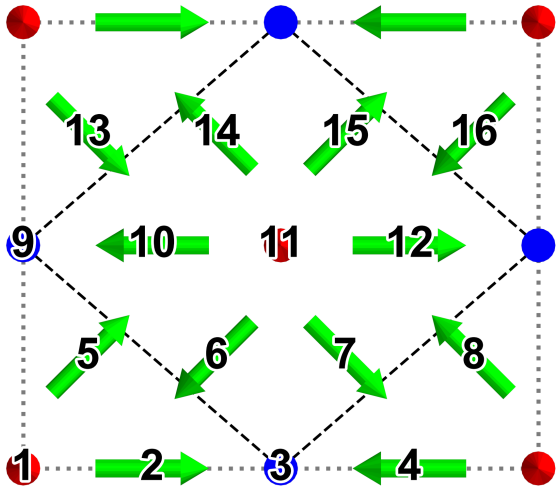

Figure A.1: SkX state. The arrows represent the direction of the local magnetic moment. The green arrows are in the plane of the magnetic layer, the red arrows point outward and the blue arrows point inward. The magnetic unit cell is indicated by black dashed lines and the unit cell used for the calculations is marked by gray dotted lines. The lattice sites are numerated and the positions and directions af the magnetic moments are given in Tab. A.1.

The SkX state (Fig. A.1) is an atomic-scale skyrmionic lattice, which has been investigated in Pub. II (referred to as s-SkX state) and in Pub. III. It is also used for exemplary calculations in Sec. 2.2. To make it possible to reproduce these examples the explicit orientations of the normalized magnetic moments are given in Tab. A.1. The position $\mathbf{r}_i$ of the lattice site i is given in units of the lattice vectors $\mathbf{a}_1$ and $\mathbf{a}_2$ by

$$\mathbf{r}_i = n_i\mathbf{a}_1 + m_i\mathbf{a}_2 = n_i \begin{pmatrix} \frac{1}{2} \\ -\frac{\sqrt{3}}{2} \\ 0 \end{pmatrix} + m_i \begin{pmatrix} \frac{1}{2} \\ \frac{\sqrt{3}}{2} \\ 0 \end{pmatrix} \quad . \tag{A.48}$$

Note that Fig. A.1 displays twice the magnetic unit cell. The magnetic unit cell is marked by a black dashed line, while the unit cell used for the calculation is indicated by a gray dotted line. The larger unit cell has been used in order to achieve a direct comparability with the multi-Q state and the d-SkX state (see Pub. II), which have the larger unit cell.

	n	m	S_x	S_y	S_z
0	0	0	0	0	1
1	1	1	1	0	0
2	2	2	0	0	-1
3	3	3	-1	0	0
4	0	1	$\frac{1}{\sqrt{2}}$	$\frac{1}{\sqrt{2}}$	0
5	1	2	$-\frac{1}{\sqrt{2}}$	$-\frac{1}{\sqrt{2}}$	0
6	2	3	$\frac{1}{\sqrt{2}}$	$-\frac{1}{\sqrt{2}}$	0
7	3	4	$-\frac{1}{\sqrt{2}}$	$\frac{1}{\sqrt{2}}$	0
8	-1	1	0	0	-1
9	0	2	-1	0	0
10	1	3	0	0	1
11	2	4	1	0	0
12	-1	2	$\frac{1}{\sqrt{2}}$	$-\frac{1}{\sqrt{2}}$	0
13	0	3	$-\frac{1}{\sqrt{2}}$	$\frac{1}{\sqrt{2}}$	0
14	1	4	$\frac{1}{\sqrt{2}}$	$\frac{1}{\sqrt{2}}$	0
15	2	5	$-\frac{1}{\sqrt{2}}$	$-\frac{1}{\sqrt{2}}$	0

Table A.1: Magnetic moments of the SkX state. The numerating corresponds to Fig. A.1. The positions are given by n, m and Eq. (A.48). The normalized magnetic moment is $\mathbf{s} = (S_x, S_y, S_z)^T$).

A.5 Conference contributions

Talks

- **26.7.2022** Complex spin structures of ultrathin Fe/Ir films on Re(0001)
  Felix Nickel, Soumyajyoti Haldar, Kirsten von Bergmann
  13th Joint European Magnetic Symposia – JEMS 2022, Warsaw

- **28.3.2023** Lifting the frustration of higher-order exchange interactions in ultrathin films
  Felix Nickel, Soumyajyoti Haldar, Roland Wiesendanger, Stefan Heinze, Kirsten von Bergmann
  DPG-meeting, Dresden

- **30.8.2023** Observation of the Ideal Triple-Q State in Pd/Mn/Re(0001)
  Felix Nickel, André Kubetzka, Soumyajyoti Haldar, Roland Wiesendanger, Stefan Heinze, Kirsten von Bergmann
  13th Joint European Magnetic Symposia – JEMS 2023, Madrid

- **14.9.2023** Coupling of the Triple-Q State to the Atomic Lattice by Anisotropic Symmetric Exchange
  Felix Nickel, André Kubetzka, Soumyajyoti Haldar, Roland Wiesendanger, Stefan Heinze, Kirsten von Bergmann
  SPP 2137 Meeting, Hamburg

- **7.3.2024** Coupling of the Triple-Q State to the Atomic Lattice by Anisotropic Symmetric Exchange
  Felix Nickel, André Kubetzka, Soumyajyoti Haldar, Roland Wiesendanger, Stefan Heinze, Kirsten von Bergmann
  APS-march meeting, Minneapolis

- **17.3.2025** Antiferromagnetic order of topological orbital moments in atomic-scale skyrmion lattices
  Felix Nickel, André Kubetzka, Mara Gutzeit, Roland Wiesendanger, Kirsten von Bergmann, Stefan Heinze
  APS-march meeting, Anaheim

Posters

- **28.8.2021** First-principles study of DMI mechanisms and exchange frustration in Rh/Co/Fe/Ir multilayers
  Felix Nickel, Sebastian Meyer, Stefan Heinze
  DPG-meeting, online

- **20.9.2021** First-principles study of DMI mechanisms and exchange frustration in Rh/Co/Fe/Ir multilayers
  Felix Nickel, Sebastian Meyer, Stefan Heinze
  The European School on Magnetism, Cluj-Napoca

- **24.8.2022** Complex spin structures of ultrathin Fe/Ir films on Re(0001)
  Felix Nickel, Soumyajyoti Haldar, Stefan Heinze
  PSI-K, Lausanne

- **9.7.2024** Coupling of the triple-Q state to the atomic lattice by anisotropic symmetric exchange
  Felix Nickel, André Kubetzka, Soumyajyoti Haldar, Roland Wiesendanger, Stefan Heinze, Kirsten von Bergmann
  ICM-FS, Perugia

Acknowledgments

I really enjoyed my time as a PhD student. Having an own project and the freedom to choose how to advance and how to tackle issues and problems is great. But throughout the research also a lot of challenges arise. Many people helped me to pursue my research, either by scientific advice or by moral support. This section is dedicated to express my thankfulness to all these people.
Firstly I thank Stefan Heinze for creating very good work environment, making it possible for me to attend many conferences and always having good advice. Kirsten von Bergmann I want to thank for the nice collaborations and many in-depth discussions on various projects.
I want to thank the whole group, namely Hendrik Schrautzer, Moritz Goerzen, Tim Drevelow, Soumyajyoti Haldar, Leo Kollwitz, Bjarne Beyer, Mara Gutzeit and Eike Tessars, for discussions about any scientific or non-scientific problems, lunch breaks, collaborations for publications, fun travels to conferences and the wordle challenge. The good mood and great willingness to help others makes working in this group really great.
Further I would like thank my experimental collaborators from the University of Hamburg: André Kubetzka, Felix Zahner and Roland Wiesendanger as well as Roberto Lo Conte.
For the possibility to present and discuss my work I thank Thore Posske and Jannis Neuhaus-Steinmetz.
For the great support throughout my life and especially my time as a PhD student I want to thank Louisa Lagmöller, Birgit Nickel, Gerald Nickel, Erik Nickel, Kateryna Hanina, the rest of my family, all my friends and the Schwammtisch.

Erklärung

Ich versichere, dass diese Arbeit, abgesehen von der Beratung durch meine Betreuer Stefan Heinze, nach Inhalt und Form meine eigene Arbeit ist. Diese Arbeit oder Teile der Arbeit haben nicht an anderer Stelle einem Prüfungsverfahren vorgelegen. Die Arbeit beinhaltet Veröffentlichungen in Fachzeitschriften. Dabei sind drei Artikel veröffentlicht und einer eingereicht. Es ist in der Arbeit klar kenntlich gemacht, wo diese Artikel erschienen sind. Mein Anteil an den Veröffentlichungen ist kenntlich gemacht. Diese Arbeit ist unter der Einhaltung der Regeln guter wissenschaftlicher Praxis der Deutschen Forschungsgemeinschaft entstanden. Mir wurde nie ein akademischer Grad entzogen.

Ort, Datum

Felix Nickel